THÈSE

Présentée à

L'Université de Lille Sciences et Technologies

Laboratoire de PhysicoChimie des Processus de Combustion et de l'Atmosphère

En vue de l'obtention du grade de

Docteur de l'Université de Lille Sciences et Technologies

École Doctorale des Sciences de la Matière, du Rayonnement et de l'Environnement

Par

Emmanuel Assaf

Kinetic study of reactions with interest to atmospheric chemistry by simultaneous detection of OH and RO_2 radicals coupled to laser photolysis

Soutenue le 03 Octobre 2017 devant la commission d'examen composée de :

Geoffrey Tyndall	Directeur de Recherche	Rapporteur
David Rowley	Professeur	Rapporteur
Dwayne Heard	Professeur	Examinateur
Yoshizumi Kajii	Professeur	Examinateur
Thérèse Huet	Professeur	Examinateur
Elena Jimenez	Professeur	Examinateur
Ondrej Votava	Chercheur	Examinateur
Christa Fittschen	Directrice de Recherche CNRS	Directrice de thèse

Résumé

Les radicaux hydroxyle OH et hydroperoxyle HO_2 jouent un rôle essentiel dans de nombreux processus d'oxydation dans l'atmosphère. La dégradation des composés organiques volatils dans les conditions troposphériques est généralement initiée par la réaction avec les radicaux OH, suivie par la réaction des produits d'oxydation avec l'oxygène. Dans le cadre de cette thèse, des études on été menées afin de mieux comprendre les mécanismes d'oxydation d'espèces d'intérêt atmosphérique. Pour cela, un dispositif expérimental composé d'une photolyse laser couplée à des techniques spectroscopiques de détection résolues dans le temps: Laser Induced Fluorescence Induite par Laser (LIF, pour la détection des radicaux OH) et continuous-wave Cavity Ring-Down Spectroscopy (cw-CRDS, pour la détection des radicaux OH, HO_2 et RO_2) a été utilisé.

Après avoir mesuré le spectre ainsi que les sections efficaces d'absorption de quelques raies sélectionnées de OH, HO_2 et RO_2 dans la région du proche infrarouge, quatre systèmes ont été étudiés avec les techniques mentionnées ci-dessus: CH_3O_2 + OH, $C_2H_5O_2$ + OH, $C_3H_7O_2$ + OH et $C_4H_9O_2$ + OH. La constante de vitesse ainsi que le rendement de HO_2 ont été déterminés pour ces quatre réactions. En outre, les constantes de vitesse de réactions secondaires telles que CH_3O + HO_2, CH_3O + CH_3O ou OH + HO_2 ont été déterminées.

Mots-clés: Chimie atmosphérique, radical, photolyse laser, fluorescence induite par laser, continuous–wave cavity ring-down spectroscopy, hydroxyle, peroxy, hydroperoxyle

Abstract

The hydroxyl radical OH and hydroperoxy radical HO_2 are key species in many oxidation processes in the atmosphere. The degradation of volatile organic compounds under tropospheric conditions is induced by reactions with hydroxyl radicals followed by the subsequent chemistry of the initial OH oxidation products with O_2. This thesis was focused on the kinetic study of some of these atmospherically relevant reactions to better understand their oxidation mechanisms using an experimental system of laser photolysis coupled to Laser Induced Fluorescence (LIF, for OH radical) and continuous-wave Cavity Ring-Down Spectroscopy (cw-CRDS, for OH, HO_2 and RO_2 radicals) detection techniques.

After determining the infrared spectrum of OH, HO_2 and CH_3O_2 radicals in the near infrared region and the absorption cross-sections of few selected lines, four systems were studied with the above mentioned techniques: CH_3O_2 + OH, $C_2H_5O_2$ + OH, $C_3H_7O_2$ + OH and $C_4H_9O_2$ + OH. The rate constant and the HO_2 yield of the four reactions were determined. In addition, the rate constants of few secondary reactions such as CH_3O + HO_2, CH_3O + CH_3O or OH + HO_2 have been determined.

Keywords: Atmospheric chemistry, radicals, laser photolysis, laser induced fluorescence, continuous–wave cavity ring-down spectroscopy, hydroxyl, peroxy, hydroperoxyl

List of Publications

(i) E. Assaf and C. Fittschen, "Cross Section of OH Radical Overtone Transition near 7028 cm^{-1} and Measurement of the Rate Constant of the Reaction of OH with HO_2 Radicals," *J. Phys. Chem. A*, vol. 120, no. 36, pp. 7051–7059, Sep. 2016. (Impact Factor 2.847)

(ii) E. Assaf, B. Song, A. Tomas, C. Schoemaecker, and C. Fittschen, "Rate Constant of the Reaction between CH_3O_2 Radicals and OH Radicals Revisited," *J. Phys. Chem. A*, vol. 120, no. 45, pp. 8923–8932, Nov. 2016. (IF 2.847)

(iii) E. Assaf, L. Sheps, L. Whalley, D. Heard, A. Tomas, C. Schoemaeker, C. Fittschen, "The Reaction between CH_3O_2 and OH Radicals: Product Yields and Atmospheric Implications," *Environmental Science & Technology*, vol. 51, no. 4, pp. 2170–2177, Feb. 2017. (IF 6.198)

(iv) D. Liu, F. Khaled, B. R. Giri, E. Assaf, C. Fittschen, and A. Farooq, "H-Abstraction by OH from Large Branched Alkanes: Overall Rate Measurements and Site-Specific Tertiary Rate Calculations," *J. Phys. Chem. A*, vol. 121, no. 5, pp. 927–937, Feb. 2017. (IF 2.847)

(v) C. Fittschen, E. Assaf, and L. Vereecken, "Experimental and Theoretical Investigation of the Reaction NO + OH + O_2 → HO_2 + NO_2," *J. Phys. Chem. A*, vol. 121, no. 24, pp. 4652–4657, Jun. 2017. (IF 2.847)

(vi) E. Assaf, S. Tanaka, Y. Kajii, C. Schoemaecker, and C. Fittschen, "Rate Constants of the Reaction of C_2–C_4 Peroxy Radicals with OH Radicals," *Chemical Physics Letters*, vol. 684, pp. 245–249, Sep. 2017. (IF 1.815)

(vii) E. Assaf, O. Asvany, O. Votava, S. Batut, C. Schoemaecker, and C. Fittschen, "Measurement of line strengths in the Ã $^2A'$ ← $^2A''$ transition of HO_2 and DO_2," *Journal of Quantitative Spectroscopy and Radiative Transfer*, vol. 201, pp. 161–170, Nov. 2017. (IF 2.419)

Contents

À mes parents et à Michel

À Marion

Acknowledgement/Remerciements

Mes plus sincères remerciements sont tout d'abord adressés à ma directrice de thèse Christa Fittschen pour avoir dirigé ces travaux. Merci pour sa confiance, ainsi que sa présence et sa bienveillance accordées tout au long de ma thèse. Je vous suis extrêmement reconnaissant pour tout ce que vous m'avez appris, ce fut un plaisir de travailler avec vous. Je m'excuse pour les quelques comptes rendus que je n'ai pas rédigés mais j'essaierai de m'améliorer pendant cette année de post-doc. Je voudrais également remercier Coralie de m'avoir encadré ainsi que Laure pour sa grande sympathie, tous ses conseils et enseignements.

Je tiens à remercier les différents membres du jury d'avoir accepté d'évaluer ce travail de thèse. Merci à Thérèse Huet de m'avoir fait l'honneur de présider ce jury. Merci Geoffrey Tyndall et David Rowley d'avoir rapporté mes travaux de thèse. Leurs remarques et commentaires ont ajouté une valeur à mon manuscrit. Merci aux examinateurs Dwayne Heard, Yoshizumi Kajii, Elena Jimenez et Ondrej Votava pour les échanges que nous avons eus lors de nos rencontres et lors de la soutenance.

Je remercie Laurent Gasnot, directeur de laboratoire PC2A, pour son accueil ainsi que tout le personnel administratif et technique qui m'ont permis de travailler dans de très bonnes conditions. Je voudrais en particulier remercier Sébastien et Pascal pour leurs disponibilité, conseils et nombreuses interventions, et sans qui la manip n'aurait pas aussi bien fonctionné.

Je voudrais ensuite remercier toutes les personnes qui ont fait que cette thèse a été fructueuse et ont fait que j'ai pu évoluer dans une ambiance de travail très saine et amicale. À tous ceux que j'oublie, la page blanche suivante vous est dédiée. Mes pensées vont tout d'abord à Michael, Marion, Patrice, Ahmad, Damien, Florent, Christopher. Merci pour trois années faites de discussions aussi bien philosophiques que scientifiques, sorties resto/ciné/bar/foot, karting, bowling, futsal. Je continuerais

avec toutes les autres personnes du laboratoire, Nicolas, Mohamad, Lucia, Sympho, Momo, Junteng, et quelques personnes du LASIR Lucie, Samantha, Cécilia. Merci pour tous nos bons moments passés ensemble.

Sur un plan plus personnel, je dois évidemment cette réussite à mes parents qui ont consacrés toute leur vie à l'éducation et au bien-être de leurs deux fils. Je leur adresse ma plus tendre gratitude. Je remercie également mon frère qui m'a aidé à devenir l'homme que je suis aujourd'hui. Merci également à toute ma famille et belle-famille qui m'ont soutenu toutes ces années.
Enfin, mes pensées se tournent vers Marion dont j'ai le bonheur de partager la vie depuis plusieurs années et à qui je dois cette réussite dans mon travail. Je n'aurai jamais assez de mots pour lui témoigner toute l'admiration et la reconnaissance de m'avoir supporté pendant ces trois années ainsi que pour les sacrifices que nous avons dû faire. Nous pouvons maintenant suivre nos désirs d'évasions et de découvertes.

Encore merci à tous,
Emmanuel

Introduction

The worldwide interest to investigate atmospheric chemistry has been increased during the last decades. Chemical compounds are released permanently by biogenic sources and anthropogenic activities and the extent to which environmental pollution is irreversibly affecting the quality of life because of its contribution to smog conditions, acid rain, stratospheric ozone depletion and global warming are rapidly becoming more apparent. The pressure being put to act and restrain the rise in greenhouse gases and pollutants with policy change is directed by complex climate model that aim to predict the future of the climate. These models rely on various physical and chemical processes at work in the atmosphere. A detailed understanding of the oxidative species and reactions in the atmosphere is important to improve to models and to develop optimum strategies to deal with these worldwide challenges.

Hydroxyl radicals OH play a key role in the atmosphere as they act as the primary daytime oxidant, initiating the degradation of most trace gases, greenhouse gases and anthropogenic pollutants emitted into the atmosphere, which can then form an array of secondary species, thereby controlling the concentrations and lifetimes of many volatile organic compounds (VOCs). Hydroxyl radicals OH are linked to hydroperoxy HO_2 and peroxy RO_2 radicals through a series of oxidation steps that depend on the local environment. These highly reactive radicals, known as HO_x = OH + HO_2, have short tropospheric lifetimes (~ 1 s and ~ 100 s for OH and HO_2 respectively) and their low ambient steady state concentrations (~ 10^6 and ~ 10^8 cm^{-3} for OH and HO_2 respectively) are therefore uninfluenced by transport processes. While the influence of RO_2 in polluted environment is well known and numerous experimental results are available, the reaction scheme in clean environment is much less known. Under low NO_x conditions the RO_2 self- and cross-reactions become predominant and RO_2 can also react with OH radicals. However, until recently no experimental or theoretical data were found in the literature about RO_2 + OH reactions and these reactions were

not included in atmospheric chemistry models. Their impact on atmospheric chemistry is however critically dependent on the nature and yields of the products.

This thesis concentrates on kinetic studies of relevant reactions including OH, HO_2 and RO_2 radicals to better understand their oxidation mechanisms in low NO_x environment. Two well-known techniques, namely Laser Induced Fluorescence (LIF, for OH radical) and continuous-wave Cavity Ring-Down Spectroscopy (cw-CRDS, for OH, HO_2 and RO_2 radicals) coupled to a laser photolysis reactor have been used as the measurement tools for the kinetic measurements of OH, HO_2 and RO_2 radicals.

The Chapter 1 is a short overview of the role of peroxy radicals in the photochemistry of the troposphere highlighting the role of HO_2 radicals as intermediates of reactions and their interconversion with OH radicals. Existing techniques used for the detection of these three radicals are described briefly, taking into account the strengths and weaknesses of each technique.

The Chapter 2 is dedicated to the theoretical and experimental description of the two detection systems: continuous-wave Cavity Ring Down Spectroscopy (cw-CRDS) and high repetition rate Laser Induced Fluorescence (LIF). In the frame of this thesis, two such detection techniques were coupled to a photolysis cell. The results of the characterization of each technique are also developed.

In Chapter 3, the first determination of the absolute cross-section of an overtone transition of OH radicals in the near-infrared region at 7028.830 cm^{-1} was performed and the impact of broadening gas on this line was determined. The absorption spectrum and the absorption cross-section of H_2O_2, used as precursors for OH radicals, have been measured. Then the two cw-CRDS absorption paths have been used to simultaneously measure OH and HO_2 profiles and deduce the absolute concentrations of OH and H_2O_2 from subsequent modeling of the concentration time profiles, and the rate constant of the very fast reaction between OH and HO_2 radicals has been determined.

In Chapter 4, the absorption cross-sections of HO_2 and DO_2 radicals in the near infrared region between 6940 and 7080 cm^{-1} were determined. In this range it is

possible to detect the three radicals HO_2, DO_2 and OH with the same DFB laser diode and mirror set. The absorption spectra of DO_2 and HO_2 radical and CH_3OH, CD_3OD molecules, used as precursors were studied. Absolute absorption cross-sections of HO_2 and DO_2 will allow selective quantification of both radicals while tuning the laser source within a small wavelength range.

In the Chapter 5 it will be shown that measuring time-resolved HO_2 profiles at different O_2 concentrations will allow retrieving the yield of CH_3O and CH_2OH in the reaction of F atoms with methanol following the photolysis of XeF_2. The rate constants of both CH_3O self-reaction and $CH_3O + HO_2$ cross-reaction will then be experimentally determined using low O_2 concentrations. While the agreement with literature data for the CH_3O self-reaction was found satisfying, the rate constant for the reaction of $CH_3O + HO_2$ differed by several orders of magnitude with the two only literature values. In order to better understand this strong disagreement, this reaction was again investigated by theoretical methods in collaboration with L. Vereecken.

Finally, in Chapter 6 new experiments for determining the reactivity of CH_3O_2, $C_2H_5O_2$ and the next larger peroxy radicals, $C_3H_7O_2$ and $C_4H_9O_2$, with OH radicals are presented. Experiments have been carried out using different precursors than in the previous studies. Experiments for the determination of the yields of the possible products have also been carried out. The results of the experiments on the reaction $CH_3O_2 + OH$ have been implemented in a collaboration with D. Heard and L. Whalley into a box model utilizing the MCM, and the impact on the composition of the remote atmosphere has been determined. In addition, the absorption cross-section of CH_3O_2, a parameter on which the rate constant $CH_3O_2 + OH$ directly depends during the experiment, has also been remeasured because available literature data were not in agreement.

Chapter 1 HO_X and RO_2 radicals: chemistry and detection techniques

1.1 Radical photochemistry in the troposphere

A layer called the atmosphere, composed of solid, liquid and mainly gas constituents, surrounds the Planet Earth. The atmosphere consists of different layers namely troposphere, stratosphere, mesosphere and thermosphere divided by temperature inversion profiles. The Earth atmosphere is composed of 78% N_2, 20.9% O_2, 1% Ar and 0.036% CO_2 [1]. The water vapor concentration, which is the next most ambient constituent, is variable and can be up to 3%. The remaining gas constituents called trace gases are composed of volatile components with concentrations below 1 %. These trace gases are either of biogenic origin and emitted from sources such as forests and oceans or of anthropogenic origin released due to human activities. After being emitted in the atmosphere, these trace gases can be transformed or removed through different processes: wet or dry deposition, transport or chemical transformation. For example, the atmospheric lifetimes of certain greenhouse gases, in particular methane, are controlled by chemical oxidation, while anthropogenic emissions of some particulate matter and gaseous species in densely populated areas have adverse effects on human health. The chemical ageing of particulates and gases through oxidation and photolysis can enhance the production of aerosols and toxic products, and thus it is important to understand the oxidative species and reactions in the atmosphere in furthering the ability to model the chemistry in order to better predict the evolution of the oxidizing capacity of the atmosphere.

Peroxy radicals RO_2 (with R = H, CH_3, C_2H_5, etc.) are key species in the chemistry of Earth atmosphere. They are formed as intermediate species of the oxidation process of VOCs in the atmosphere. The VOCs can be removed in the atmosphere by photolysis, by solar radiation and by reaction with other species such as OH radical or to a minor extend to Cl atoms, NO_3 or O_3 for example. One of the simplest oxidation

mechanisms leading to the formation of the smallest peroxy radical, i.e. the hydroperoxy radical HO_2, is the reaction of OH radicals with CO in presence of O_2. A general and simplified scheme of the closely linked chemistry between OH and HO_2 radicals and involving peroxy radicals RO_2 is shown in Figure 1.

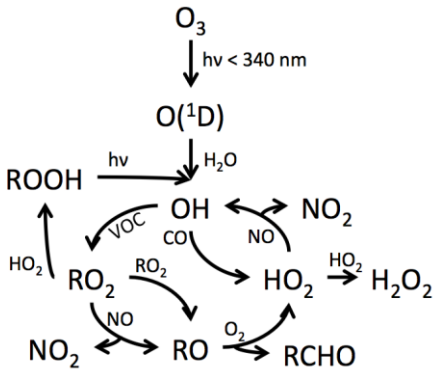

Figure 1: Reactions and key species involved in the chemistry of OH, HO_2 and RO_2 radicals

The tropospheric chemistry of OH, HO_2 and RO_2 radicals has been described in recent reviews [2]–[4] in the literature and a full description is beyond the scope of this introduction. Thus, only key reactions will be shown here. The main source of daytime OH is through the photochemical production from the photolysis of ozone O_3 ($\lambda < 310$ nm) to form an electronically excited oxygen atom $O(^1D)$ that reacts with water vapor to form OH.

$$O_3 + h\upsilon_{<310nm} \rightarrow O(^1D) + O_2(^1\Delta_g) \qquad (R\ 1)$$

$O(^1D)$ is metastable with a radiative lifetime of about 148 s because the transition between the excited singlet state to the triplet ground state is spin-forbidden. Most $O(^1D)$ atoms however are quenched by collisions with other molecules M, which are mostly N_2 and O_2 in the atmosphere:

$$O(^1D) + M \rightarrow O(^3P) + M \qquad (R\ 2)$$

This deactivation channel is in direct competition with the chemical reaction. In the lower troposphere for water mixing ratio equal to 1.5%, about 10% of the produced $O(^1D)$ reacts with H_2O to form two OH radicals [5], while $O(^3P)$ can react with O_2 to recycle O_3:

$$O(^1D) + H_2O \rightarrow 2\ OH \quad \text{(R 3)}$$

$$O(^3P) + O_2\ (+ M) \rightarrow O_3 \quad \text{(R 4)}$$

As mentioned above, various reaction pathways exist for OH including the reactions with CO to form HO_2 and the reactions with VOCs to form RO_2 radicals:

$$OH + CO + O_2 \rightarrow HO_2 + CO_2 \quad \text{(R 5)}$$

$$OH + RH + O_2 \rightarrow RO_2 + H_2O \quad \text{(R 6)}$$

The thus formed RO_2 radicals have two main destruction pathways, either the reaction with NO or the reaction with HO_2 or other RO_2 radicals depending on the NO_X conditions. In areas with high NO_X concentrations, typically when [NO] > 2×10^{10} cm^{-3}, RO_2 radicals react predominantly with NO forming NO_2 finally leading to the formation of O_3 through the photolysis of NO_2:

$$RO_2 + NO \rightarrow RO + NO_2 \quad \text{(R 7)}$$

$$HO_2 + NO \rightarrow OH + NO_2 \quad \text{(R 8)}$$

OH radicals are recycled at the same time through the production and destruction of HO_2. However, in absence of NO_X, loss of RO_2 is dominated by reaction with other RO_2 and HO_2 radicals and both HO_2 and RO_2 radicals can undergo chain termination reactions forming stable products ROOH and H_2O_2 or RO radicals:

$$RO_2 + RO_2 \rightarrow 2\ RO + O_2 \quad \text{(R 9)}$$

$$HO_2 + RO_2 \rightarrow ROOH + O_2 \quad \text{(R 10)}$$

$$HO_2 + HO_2 \rightarrow H_2O_2 + O_2 \quad \text{(R 11)}$$

$$HO_2 + OH \rightarrow H_2O + O_2 \quad \text{(R 12)}$$

The most important sink process for OH in polluted environments is the reaction of OH with NO_2, resulting in the production of nitric acid HNO_3:

$$NO_2 + OH\ (+ M) \rightarrow HNO_3 \quad \text{(R 13)}$$

The high reactivity of OH and HO_2 radicals leads to short atmospheric lifetime with respectively ~ 1 s and ~ 100 s. Their chemistry does not involve transport and their steady state concentrations depend on the chemical composition and on the balance between the sources and sinks of the local environment. Thus, OH and HO_2 concentrations in the troposphere vary depending on the location as well as meteorological conditions. The range of OH concentrations are from 10^5 up to 10^7 cm^{-3}, while for HO_2 the range of concentrations are from 10^7 to 10^8 cm^{-3}. The ratio of $[HO_2]/[OH]$ is an important parameter to quantify the oxidizing capacity of the atmosphere, i.e. the quantity of OH effectively available to initiate the destructive reactions of many hydrocarbons.

1.2 Techniques for HO_X and RO_2 radical measurements

As mentioned above, the atmosphere is a very complex system and understanding all its processes is very difficult from only one type of study. Therefore, atmospheric studies are subdivided into several areas such as field measurement, emission/deposition/transport studies or model studies. Field measurements and models are intertwined as they contribute to improve the knowledge of tropospheric chemistry. Measurements have demonstrated a lack of understanding in tropospheric chemistry models, while models pointed out measurement errors. In recent field campaigns in biogenic environments, an overestimation of the measurements over the models indicate that the chemistry of peroxy radicals in low NO_X environments is not

well understood [6]. In order to understand these discrepancies, laboratory kinetic measurements have to be carried out. Different measurement techniques for the quantification of OH and HO_2 were reviewed in details [4]. The measurement of radicals is difficult because of their high reactivity with gases and surfaces. Highly sensitive detection techniques are needed in field measurements to determine the low concentrations of peroxy radicals, which are typically on the order of 10^8 cm^{-3} during the day.

Few measurement techniques allows the quantification of OH in the atmosphere and are based either on spectroscopic techniques with Fluorescence Assay by Gas Expansion (FAGE) and Differential Optical Absorption Spectroscpy (DOAS), or on chemical techniques with Chemical Ionizaton Mass Spectrometry (CIMS, temporal resolution 30 s to 1 min), ^{14}CO oxydation (temporal resolution 5 min), scrubbing using salicylic acid (temporal resolution 30 min to 90 min) or spin trapping (20 to 30 min [4]). It should be noted that for the chemical techniques, only the CIMS allows measuring with a high temporal resolution necessary to identify phenomena involving OH radicals because they have a short lifetime (on the order of a second) and a regenerated rapidly. Thus, only the FAGE, DOAS and CIMS techniques, which have similar performances in terms of limit of detection and temporal resolution, will be described below. Several measurement techniques exist for HO_X measurements such as continuous-wave Cavity Ring-Down spectroscopy (cw-CRDS) or the chemical amplification methods with Peroxy Radical Chemical Amplification (PERCA). Most also allows the measurement of RO_2 radicals according to the conditions of use. The Matrix Isolation Electron Spin Resonance Spectroscopy (MIESR) technique makes it possible to measure simultaneously and selectively different types of radicals such as HO_2 or the sum of RO_2 after the collection of the radicals on a cold matrix and, even if it is a sensitive method, this method is ex situ and will not be developed here. From all above techniques, only the three FAGE, PerCIMS and PERCA techniques have yet been deployed for measurement campaigns.

The above experimental techniques allowing the quantification of HO_X and RO_2 radicals are presented in the following section with their advantages, disadvantages and limits of detection and are summarized in Table 1.

1.2.1 Chemical amplifier and mass spectroscopy systems

1.2.1.1 Peroxy Radical Chemical Amplifier (PERCA)

The PERCA technique allows measuring the sum of HO_2 and RO_2 radicals and is used by various groups for field measurements. However, the discrimination between different species is not done. The ambient air is sucked into a chamber where a reaction cycle between OH and HO_2 is initiated by the reaction of HO_2 with NO followed by the addition of CO to convert OH back to HO_2:

$$RO_2 + NO \rightarrow RO + NO_2 \quad \text{(R 14)}$$

$$RO + O_2 \rightarrow R'O + HO_2 \quad \text{(R 15)}$$

$$HO_2 + NO \rightarrow OH + NO_2 \quad \text{(R 16)}$$

$$OH + CO \rightarrow H + CO_2 \quad \text{(R 17)}$$

$$H + O_2 (+M) \rightarrow HO_2 \quad \text{(R 18)}$$

NO_2 is formed in the reaction (R 16) and amplified by the reaction cycle up to 50 to 150 times compared to the initial concentration of RO_2 + HO_2. NO_2 concentration is usually measured by a chemiluminescence detector with luminol, by CRDS or by LIF. The signal caused by NO_2 present in ambient air has to be subtracted from the signal due to NO_2 concentration produced in the amplification process. The cycling between OH and HO_2 radicals is fast because of the high CO mixing ratio around 10% in the reaction cell. The most problematic issue concerning PERCA instruments is the sensitivity to the relative water vapor content in sampled air [7], [8]. The interference

of water in the response of the PERCA can be up to 50% of the signal if the relative humidity changes about 50%.

A new method [9] was developed in order to selectively measure HO_2 and RO_2 radicals based on a PERCA/LIF instrument. This method is based on the fact that losses through heterogeneous reactions are more important for HO_2 compared to other peroxy radicals. The air is pumped through a pre-inlet filled with spherical glass beads where 90% of HO_2 radicals are removed whereas the RO_2 loss is only around 15%. The alternating measurement through the pre-inlet or not allows measuring either RO_2 or the sum of RO_2 + HO_2. The detection limit for the concentration of RO_2 for this instrument is around 0.25 to 1×10^7 cm^{-3} for 1 min of acquisition.

1.2.1.2 Peroxy Radical Chemical Ionization Mass Spectroscopy (PerCIMS, ROxMas)

In contrast to the PERCA instrument, the CIMS technique is based on the chemical conversion of OH into H_2SO_4 and HO_2 by adding isotopically labeled SO_2 instead of CO in presence of O_2 through the reaction mechanism:

$$OH + SO_2 (+M) \rightarrow HSO_3 \qquad (R\ 19)$$

$$HSO_3 + O_2 \rightarrow SO_3 + HO_2 \qquad (R\ 20)$$

$$SO_3 + 2\ H_2O \rightarrow H_2SO_4 + H_2O \qquad (R\ 21)$$

During each cycle, one H_2SO_4 molecule is formed and converted into HSO_4^- by chemical ionization by NO_3^-, which are generated separately from the sample air and drawn through the sample by an electric field. The HSO_4^- and NO_3^- concentrations are then measured by MS, establishing an indirect method for OH radical concentration measurement. OH measurement time resolution with this system is typically 30 s with detection limit about 1×10^5 cm^{-3} [10] based on 5 min signal integration. With the FAGE technique, the CIMS is the only other technique deployed during field

campaigns for the measurement of OH. This technique is very sensitive to variation of NO concentration that converts HO_2 into OH, and thus may overestimate the OH concentration, but this phenomenon is negligible at low NO concentration < 10 ppb.

However, the PerCIMS instrument could also be used to measure the sum of HO_2 + RO_2 radical concentration using the same amplification conversion process of HO_2 and RO_2 into H_2SO_4 by combining above reactions with NO (R 14)-(R 16) and SO_2 (R 19) to (R 21). Here also, H_2SO_4 concentration is measured by CIMS. It is possible to differentiate HO_2 and RO_2 radicals using the dependence of the conversion efficiency of RO_2 as a function of O_2 and NO concentrations, allowing to measure the sum of HO_2 + RO_2 or only HO_2. The detection sensitivity is independent of the water vapor concentration and a detection limit around 1×10^7 cm^{-3} [11] is reached at a temporal resolution of 10 s to 120 s. This method was used during a field campaign [12] in a forest and allowed to identify missing RO_2 sources.

1.2.2 Spectroscopic methods

1.2.2.1 Differential Optical Absorption Spectroscopy (DOAS)

The quantification of OH radicals by DOAS technique is based on the extinction of UV light passing through a gas mixture. The concentration of OH is obtained via the Beer-Lambert law:

$$[OH] = \frac{\ln\left(\frac{I_0}{I}\right)}{\sigma_{OH,\lambda} L} \qquad \text{Equation 1}$$

With I_0 and I are the light intensity before and after transmission through the gas mixture, $\sigma_{OH,\lambda}$ is the absorption cross-section of OH at the wavelength and spectral resolution used and L is the path length

The DOAS technique is composed of four elements: a light source whose luminance should be high enough due to the length of the absorption path and should have a homogeneous spectral profile in order to be selective, a multiple-reflection cell to improve the spatial resolution with a distance of several meters between the different mirrors allowing an absorption path length of several km in order to obtain a low limit of detection, a high resolution spectrograph to discriminate the different OH absorption lines, and a photodiode for the light detection. This technique is self-calibrating, the absorption cross-sections of OH are known and thus the concentration of OH is obtained by the difference of light intensity before and after transmission. The absolute accuracy of this method is limited only by the accuracy of $\sigma_{OH,\lambda}$ and L. The absorption cross-section $\sigma_{OH,\lambda}$ is a function of the pressure, temperature and instrumental resolution and the value is known for OH with an accuracy of at minimum 8% [13], giving the accuracy of the DOAS technique. This technique needs a very long absorption path length to reach detection limits around 10^6 cm^{-3}, resulting in a less spatially resolved technique than the FAGE. Only one DOAS instrument, installed in the SAPHIR chamber in Jülich, is currently operational in the world with a limit of detection of 7×10^6 cm^{-3} using a 20 m long optical multiple-reflection cell [14].

1.2.2.2 Laser Induced Fluorescence (LIF) and Fluorescence Assay by Gas Expansion (FAGE)

The LIF technique has been used for indirect detection of HO_2 and RO_2. This technique is the basis of the FAGE technique where OH radicals are detected by LIF. In order to freeze all reactions of OH radicals and to have a sufficiently long fluorescence lifetime that depends strongly on quenching, the measurements are carried out at low pressure and low laser pulse energy, but high repetition rate. The FAGE technique uses 308 nm radiation to excite OH radicals, and the resulting fluorescence is detected also at 308 nm and applied to measure OH radicals

concentration as described in more details in Chapter 2. HO_2 radicals cannot be detected directly by LIF and have to be converted into OH, which is detected with a high sensitivity by LIF. Thus, HO_2 is measured simultaneously in a second detection cell where excess NO is added to the sampled gas leading to the conversion of HO_2 into OH. The organic peroxy radicals have also the potential to be chemically converted to OH via the reaction with NO producing HO_2, which will further be converted to OH. The detection limit is typically around as 10^5 cm^{-3} for ambient OH radicals and 10^6 cm^{-3} for HO_2 radicals [15], which makes the FAGE a well-adapted technique for field measurements due to its high sensitivity.

1.2.2.3 Cavity Ring-Down Spectroscopy (CRDS)

In the past, laboratory experiments have mostly used UV absorption for the detection of RO_2 radicals. For example, the absorption spectrum of CH_3O_2 has been measured several times [16], [17] and a maximal absorption coefficient of 4.6×10^{-18} cm^2 at 240 nm has been obtained. However, the absorption spectra of RO_2 radicals in the UV region are broad and unstructured and do not offer a selective detection in the presence of other species. Another technique used for the detection of specific organic peroxy radicals is CRDS. This technique has only been applied in laboratory kinetics studies so far. CRDS is a specific kind of long path absorption spectroscopy where the transient absorption in a resonator is observed following the Beer-Lambert's law. The long path improves the sensitivity of this technique, which is higher than that of conventional absorption spectroscopy. Peroxy radicals have a more structured and characteristic absorption features in the near-infrared region due to an A ← X transition [18]. The CH_3O_2 spectrum has already been measured in the wavelength range 7470 - 7500 cm^{-1} corresponding to the ν_{12} transition with a maximum absorption cross-section of 4.38×10^{-20} cm^2 at 7488.18 cm^{-1} [19]. Since then, the weak absorption spectra and cross-sections of many stables [20]–[23] and unstable species [24], [25] have been measured in the near-infrared region. The absorption spectrum

of the $^2\nu_1$ band of HO_2 radicals have been measured in the wavelength range 6604 – 6696 cm^{-1} and the strongest line observed in this region at 6638.20 cm^{-1} has an absorption cross-section of 2.72×10^{-19} cm^2 at 50 Torr Helium. However, the absorption cross-sections of OH radicals in this wavelength range have not yet been determined and only theoretically obtained values are tabulated in the HITRAN database [26]. Neither a possible application of the CRDS in field measurement nor expected detection limits are discussed in the literature for RO_2, HO_2 or OH radicals. However, it is assumed that an identification of different organic peroxy radicals in a mixture can be achieved because of the specific structures of their absorption spectra in the near-infrared region. This is the main technique used during this work and its functioning principle will be described in details in Chapter 2.

Table 1: Non-exhaustive list of field measurement techniques for detection of HO_X (HO_2 + OH) and RO_2 [4]

Instrument	Measured Species	Time Resolution / s	Uncertainty / %	Detection Limit / 10^6 cm^{-3}	Ref.
PERCA	HO_2, RO_2	60	20-40	100	[27]
PerCIMS	HO_X, RO_2	30-60	15-30	OH: 0.1 HO2: 10	[28]
DOAS	OH	200-600	8-30	0.5-2	[29]
LIF (or FAGE)	HO_X, RO_2	30-60	10-35	OH: 0.1-0.3 HO_2: 0.1-3.6	[15]
MIESR	HO_X, RO_2,	1800	5	50	[30]

1.2.3 Techniques for rate constant measurements in complex systems

1.2.3.1 Discharge Flow technique

The radical species are produced continuously with electric or microwave discharge within a fast flow system. The radicals are generated within a moveable injector and

then mixed with the reaction partner in the reactor. Both are highly diluted with the gas bath and are pumped at a high-speed through the injector and reactor. If the flow velocity along the tube is known, then changing the position of the movable injector into the flow tube controls the reaction time between the radical and the reactant. The radical concentration is detected at the end of the reactor, enabling the measurement the time-resolved concentration profiles. The reaction conditions are generally set such that the reaction occurs under pseudo first-order conditions: one of the reactant is in large excess over the second reactant and thus it can be considered that its concentration will be constant during the reaction. A major advantage of this technique is that the detection method does not need to be time resolved. However a drawback of this method is to well define the time zero of the reaction because of the undefined mixing time between the injector and reactor flows, and thus only slow reactions can be measured in order to keep this mixing time short compared to the time scale of the reaction. Also, this technique is limited to low-pressure experiments to obtain a laminar, well-mixed flow. Contributions from heterogeneous reactions on the wall can complicate the experiment and have to be taken into account, but can be minimized by coating the inner surface with an unreactive substance or by varying the diameter of the flow tube.

1.2.3.2 Flash photolysis technique

The reactant and the precursors are mixed and introduced into the photolysis cell at an appropriate pressure depending on the detection techniques. The radicals are formed in the cell from the precursors through a photolysis pulse, either by a pulsed laser or a pulsed flash lamp. The evolution of their concentration can subsequently be followed by time-resolved detection techniques. The time scale of the reaction to be studied is determined by the duration of the photolysis pulse which must be short compared to the reaction time. It can be in a nanosecond time scale in the case of laser pulse or millisecond time scale for UV lamps. For studying extremely fast

reaction such as electron transfer processes, laser pulses as short as few femtoseconds may be also used. The advantage of this method is that the reactants are produced from well-mixed precursors and thus there is no mixing time reducing the time resolution. The time zero is easier to determine and correspond to the photolysis pulse. Also, because the reactants are generated and monitored at the center of the cell, the wall reactions are generally minimized. However, a suitable precursor is not always easily available and co-photolysis products may lead to complications. This is the technique employed during this work and will be described in details in Chapter 2.

1.2.3.3 Relative rate technique

This method is based on the simultaneous monitoring of two or more reactant species relative to each other. The ratio of the decay rate of the investigated reactant with a given radical, for example RO_X or HO_X, is compared to the decay rate with a reference compound:

$$HO_X \text{ or } RO_X + \text{Reactant} \rightarrow \text{Products 1} \qquad \text{(R 22)}$$

$$HO_X \text{ or } RO_X + \text{Reference} \rightarrow \text{Products 2} \qquad \text{(R 23)}$$

$[HO_X]$ or $[RO_X]$ is considered as constant between the reactions (R 22) and (R 23) and the rates can be written as:

$$\frac{-\mathrm{d}[\text{Reactant}]}{\mathrm{dt}} = k(\text{R 22})\,[\text{Radical}][\text{Reactant}] \qquad \text{Equation 2}$$

$$\frac{-\mathrm{d}[\text{Reference}]}{\mathrm{dt}} = k(\text{R 23})\,[\text{Radical}][\text{Reference}] \qquad \text{Equation 3}$$

The integration and the combination of Equation 2 and Equation 3 lead to

$$\ln\left\{\frac{[\text{Reactant}]_{t=0}}{[\text{Reactant}]_t}\right\} = \frac{k(R\ 22)}{k(R\ 23)} \ln\left\{\frac{[\text{Reference}]_{t=0}}{[\text{Reference}]_t}\right\} \qquad \text{Equation 4}$$

During the measurements, the concentration of the reactant and the reference species are followed as a function of the time. A plot of $\ln\left\{\frac{[\text{Reactant}]_{t=0}}{[\text{Reactant}]_t}\right\}$ as a function of $\ln\left\{\frac{[\text{Reference}]_{t=0}}{[\text{Reference}]_t}\right\}$ should give a straight line with the slope being $\frac{k(R\ 22)}{k(R\ 23)}$. Thus, if the rate constant of the reference reaction k(R 23) is known, then it is possible to determine k(R 22). The disadvantage of this method is that heterogeneous or unknown secondary reactions could occur leading to systematic errors in the rate constant. Also, the uncertainty in the rate constant of the reference reaction has to be taken into account. This experimental technique is often used in simulation chambers for kinetic measurements.

In this thesis, a time-resolved experimental device has been set up for the measurement of RO_2, HO_2 and OH radicals in order to study the kinetics of elementary reactions involving them. A laser photolysis cell, which initiates the reaction by pulsed photolysis of a suitable precursor (e.g. H_2O_2 to form the OH radical), is coupled to two detection techniques: (i) OH radicals are detected by high repetition (10 kHz) LIF technique: this technique makes it possible to follow the evolution of the OH radicals concentration after the pulse of the photolysis laser with a temporal resolution of 100 μs. The use of such a high repetition laser for time-resolved measurements is still rare in the world. (ii) RO_2, HO_2 and OH radicals are detected by the cw-CRDS (continous-wave Cavity Ring-Down Spectroscopy) technique. This technique is a very sensitive absorption technique, based on the measurement of the rate decay of a light pulse trapped in an optical cavity. This ring-down time depends on the reflectivity of the mirrors (generally higher than 99.99%: the higher the reflectivity, the longer is the ring-down time because the photons make more round trip before escaping from the cavity), and on the concentration of absorbing species being present between the mirrors. The measurement of these ring-down times occurring at different delays with respect to the photolysis laser pulse makes it possible to determine the temporal profile of absorbing species, in out case

radicals. The coupling of these two techniques with an initiation of the reaction by laser pulse photolysis is unique in the world.

Chapter 2 Experimental Technique

2.1 General principles of the experimental techniques

Absorption spectroscopy is a well-adapted technique for the quantification of radicals inside a gaseous mixture. In order to carry out selective and sensitive measurements, it is judicious to operate in the near IR domain with a device including a multi-pass cell. This type of cell increases the distance traveled by the light through a gaseous mixture and amplifies the sensitivity of the absorbance measurement. The absorption path length is then a few tens of meters. Another approach is to employ high finesse optical cavities in order to increase the absorbance path length of the spectrometer to few kilometers. This chapter is dedicated to the description of one of such techniques: the continuous-wave Cavity Ring Down Spectroscopy (cw-CRDS). In the frame of this thesis, two such spectrometers were coupled to a photolysis cell, and a third detection system based on high repetition rate Laser Induced Fluorescence (LIF) was installed in the same photolysis reactor. The main approach developed for the measurements of radicals or molecular species will be described with notions of the absorption spectroscopy, optical cavity and cavity modes.

2.1.1 Laser Induced Fluorescence technique (LIF)

Laser Induced Fluorescence is one of the most sensitive and selective analytical technique and is applied widely for the measurements of atmospheric trace gases such as Cl, OH, NO_X, HCHO or SO_2. In this chapter, the fundamental principles of the LIF technique for the time resolved measurement of OH radicals is described.

Most atoms and small molecules absorb strongly in the ultraviolet region resulting from their excitation from the ground electronic state S_o to excited electronic states S_n. The phenomenon of photoluminescence during the relaxation can be divided in

two categories, phosphorescence and fluorescence depending on the electronic configuration of the excited states. Fluorescence is the spontaneous emission of a photon between states with the same spin $S_n \rightarrow S_o$. The lifetime of fluorescence is in general very short, 10^{-9} to 10^{-7} s. If the excited species undergoes first relaxation to a state of different spin, called intersystem crossing (ISC), then the photon emission occurs between two states with different spin. This emission is called phosphorescence and lasts longer, 10^{-3} to 10^{2} s. Non-radiative deactivation processes including internal conversion (IC), vibrational relaxation or quenching can also occur in the time range, 10^{-14} to 10^{2} s.

Absorption and fluorescence spectra are unique and are used to characterize selectively individual compounds. However, fluorescence techniques are in general less efficient for large molecules because quenching, IC and ISC relaxations are competitive with spontaneous emission. A Jablonski diagram given in Figure 2 can summarize these different excitation and relaxation processes.

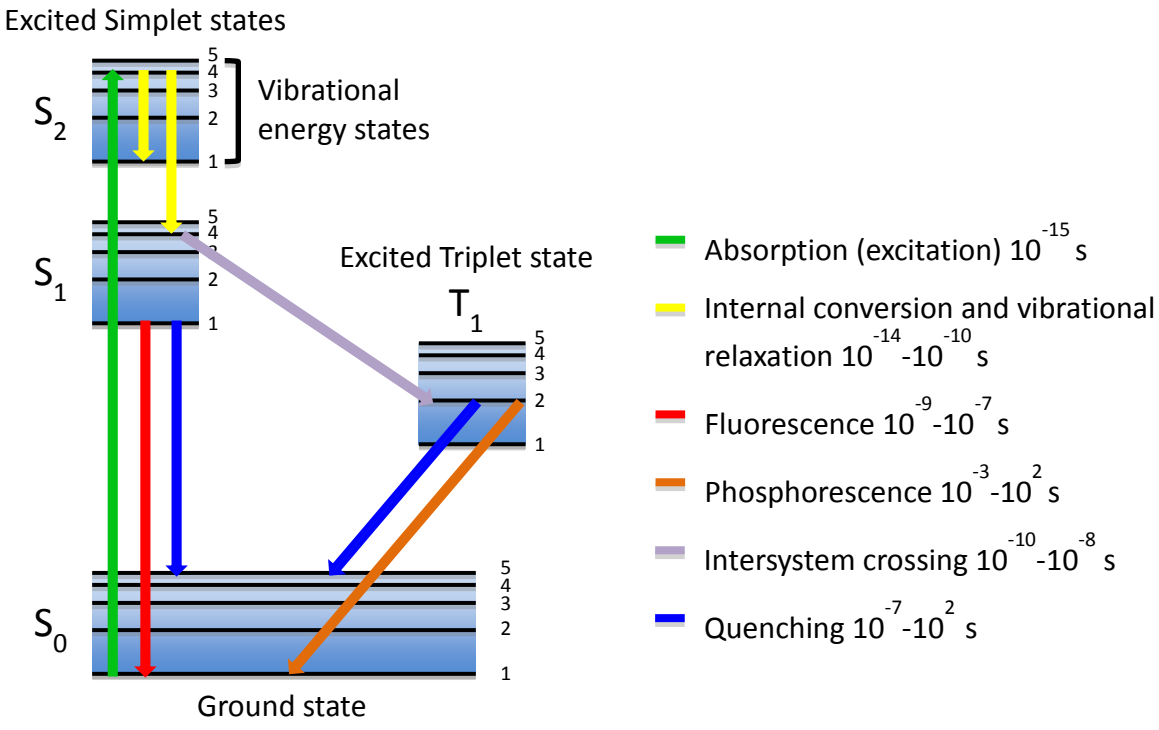

Figure 2: Jablonski energy diagram [31]

In the present work, LIF technique has been used to detect OH radicals. OH is excited from the v" = 0 vibrational bands of the ground electronic state $X^2\pi$ to the excited vibrational bands v' = 1 of the first electronically excited state $A^2\Sigma$ near 282 nm. Two red shifted fluorescence bands can be detected near 308 nm and 315 nm (0-0 and 1-1 A-X transitions respectively). A schematic diagram of the OH detection by LIF is shown in Figure 3.

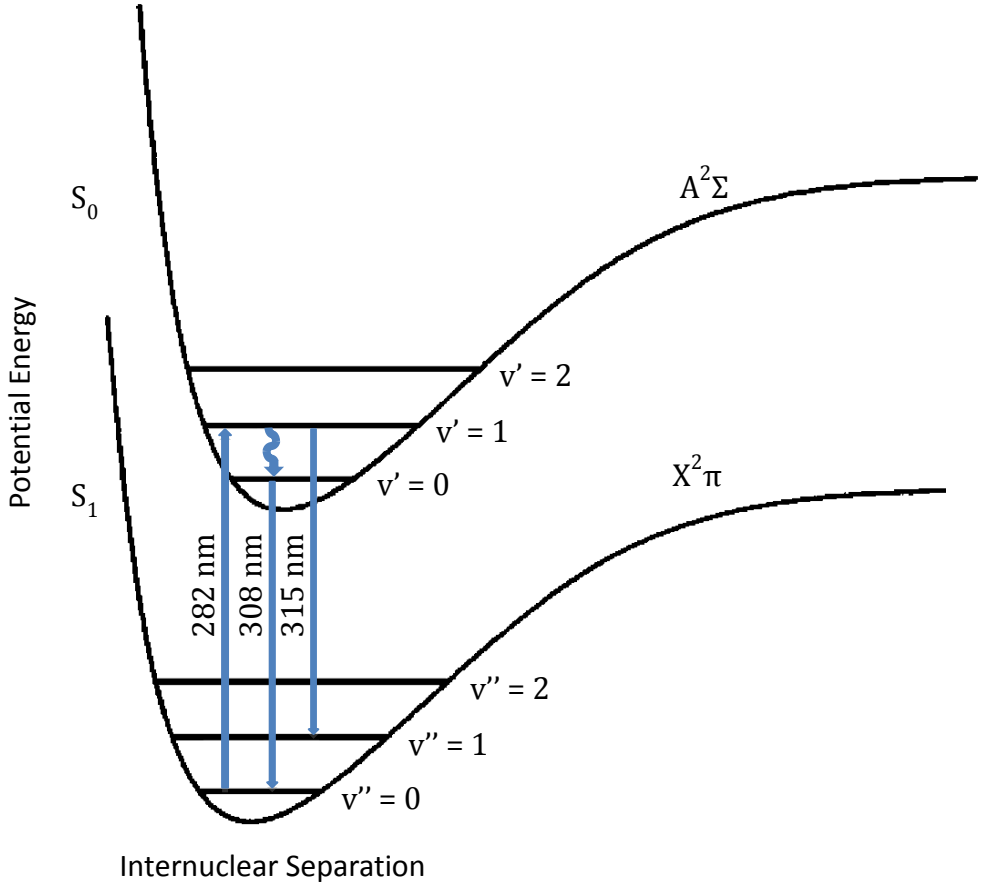

Figure 3: Schematic diagram of the potential energy curves of the OH radical. Excitation and fluorescence (0-0 and 1-1) are represented at 282 nm, 308 nm and 315 nm respectively (adapted from [32])

The observed intensity of the fluorescence signal I_{LIF} following the fluorescence excitation laser pulse depends on various parameters and can be linked to the concentration with the Equation 5 described by [33]:

$$I_{LIF} \propto I_{Laser}\theta[OH]\sigma G \qquad \text{Equation 5}$$

with θ the fluorescence quantum yield; σ the absorption cross-section of the absorbing species; [OH] concentration; G the light collection efficiency; I_{Laser} the laser intensity

The fluorescence quantum yield θ is the fraction of molecules in an excited electronic state that decay to ground state by fluorescence. θ depends on the spontaneous emission of fluorescence A, the quenching Q and other relaxation processes and can be defined with the Equation 6:

$$\theta = \frac{A}{A + Q + \Sigma \text{ other relaxation processes}} \qquad \text{Equation 6}$$

Most of the time, LIF technique is used as a relative technique because performing quantitative fluorescence measurements of a given species requires detailed knowledge about the quenching of all the species present in the gas mixture. However, LIF is a very sensitive technique with a limit of detection around 10^6-10^7 molecules cm^{-3}. It requires a basic setup: a laser source for excitation, optics to align the laser beam in the absorption medium, collection optics and a detector.

2.1.2 Cavity Ring-Down Spectroscopy techniques (CRDS)

2.1.2.1 Introduction to optical cavity and cavity modes

An optical cavity (or resonator) is the arrangement of different optical components (e.g. mirrors, optical fibers or lens, filters, etc.) making the light circulating within a closed path. The simplest optical cavity is the linear cavity. It consists of two mirrors with a reflectivity *R*, a radius of curvature *Rc*, separated by a distance *L* and facing each other along the *z*-axis. The confinement of the light in this system imposes three conditions because the light must be identical during each return trip: (1) the

wavefront of the beam should spread along the *z*-axis, (2) the maximum of energy should be at the center of the mirror to neglect the losses by diffraction due to the finite size of the mirrors and (3) the covering of the light should be constructive for each path at certain wavelengths.

As part of the paraxial approximation and from the Maxwell equations, the beam shape can be described as Gaussian beams and remains Gaussian during its propagation. Depending on the coordinate systems, higher-order transverse modes can be either Hermite-Gauss modes (for rectangular symmetry) or Laguerre-Gauss modes (for circular symmetry). The intensity distribution of the modes is described in the Figure 4. The cavity modes of the resonator TEM with qmn orders (m nodes in the *x*-direction, n nodes in the *y*-direction and q the fundamental mode number) are obtained by the approximation solutions. The mode with the lowest order in the transverse direction (m = n = 0) is called fundamental transverse mode or TEM_{qoo}.

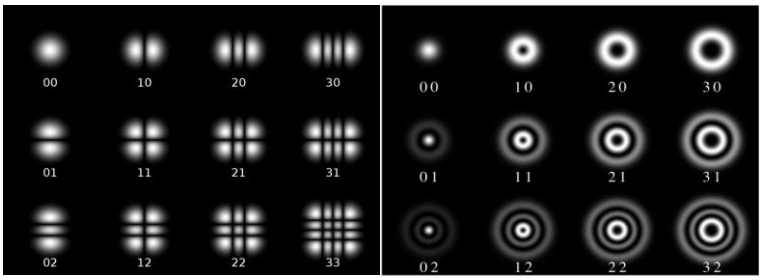

Figure 4: Spatial repartition of the energy of high-order modes with rectangular symmetry (left) and circular symmetry (right) [34]

The solutions obtained from Maxwell's equations answered to the two first conditions of the modes of the cavity: the maximum of energy would spreads around the z-axis and at the center of the mirrors. The TEM_{oo} is the mode with the lowest spatial shift limiting the losses by absorption, diffraction and diffusion. It can be considered that it has the highest lifespan, allowing the best spatial resolution and the maximum of sensitivity. Few parameters are necessary to describe the geometry of a fundamental mode TEM_{oo} inside a linear optical cavity and to realize the mode matching: the beam waist dimension ω_o, the radius of the beam on the mirrors surface ω_m and the Rayleigh range z_o indicating the length of collimation of the beam.

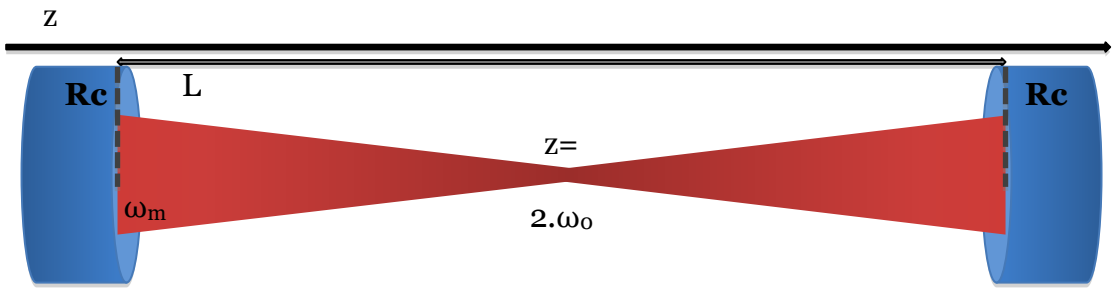

Figure 5: Schematic shape of the fundamental mode TEM_{00} inside a linear optical cavity

For a confocal cavity composed of two identical mirrors illustrated in Figure 5, these three parameters are given in Equation 7 to Equation 9:

$$\omega_0 = \sqrt{\frac{\lambda}{\pi}}\left[\frac{L}{4}(2R_c - L)\right]^{1/4} \qquad \text{Equation 7}$$

$$\omega_m = \omega_0 \frac{2R_c}{2R_c - L} \qquad \text{Equation 8}$$

$$z_0 = \frac{\pi {\omega_0}^2}{\lambda} \qquad \text{Equation 9}$$

When a laser beam with the energy E_{inc} is injected into the cavity, it is decomposed in different transverse modes at the energy $E_{m,n}$ weighted by the spatial coupling coefficient $\varepsilon_{m,n}$ though the Equation 10:

$$E_{inc}(x,y,z) = \sum_{m,n} \varepsilon_{m,n} E_{m,n}(x,y,z) \qquad \text{Equation 10}$$

The perfect mode matching of the TEM_{00} is for a spatial coupling $\varepsilon_{(0,0)} = 1$.

The third condition is that the covering of the light interferes constructively at each round trip inside the cavity. Thus, the phase difference at each crossing of the resonator should be an integer multiple of π. This frequency of resonance $\nu_{q,lm}$

depends on the m and n orders of the transverse mode and can be calculated from the Equation 11:

$$\nu(q, mn) = \frac{c}{2L}\left[q + \frac{1}{\pi}(m + n + 1).\arccos\left(\pm\sqrt{g_1 g_2}\right)\right] \qquad \text{Equation 11}$$

With c the velocity of light

For each transverse mode (m,n) exists an infinity of longitudinal modes q. The difference of frequency between two successive fundamental modes of the cavity ($TEM_{q,mn}$ and $TEM_{q+1,mn}$) is called Free Spectral Range (FSR). The FSR can be determined as shown in Equation 12:

$$FSR = \Delta\nu = \frac{C}{2n_g L} \qquad \text{Equation 12}$$

With n_g the group index

If the cavity length L is a multiple of half the wavelength λ, then the light trapped inside the cavity follows constructive interferences, meaning that at least one mode of the cavity will be in resonance with the wavelength of the beam.

$$L = n_g \frac{\lambda}{2} \qquad \text{Equation 13}$$

A simple schematic of the mode structure inside the cavity is shown in Figure 6.

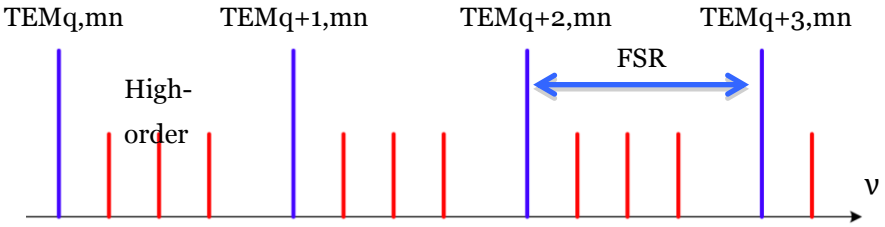

Figure 6: Mode structure inside a cavity.

For the light to be confined at the center of the cavity, its geometry should respect some stability criterions. The cavity parameters g_1 and g_2 are defined as a function of the cavity length L and the radius of curvature of the mirrors Rc_1 and Rc_2 through the Equation 14:

$$g_1 = 1 - \frac{L}{R_{c1}} \quad \text{and} \quad g_2 = 1 - \frac{L}{R_{c2}} \qquad \text{Equation 14}$$

It can be noted that R_{c1} and R_{c2} are positive for concave mirrors and negative for convex mirrors. The condition of stability of an optical linear cavity with two mirrors can be obtained from transfer matrices (or ABCD law) in Equation 15:

$$0 \leq g_1 g_2 \leq 1 \qquad \text{Equation 15}$$

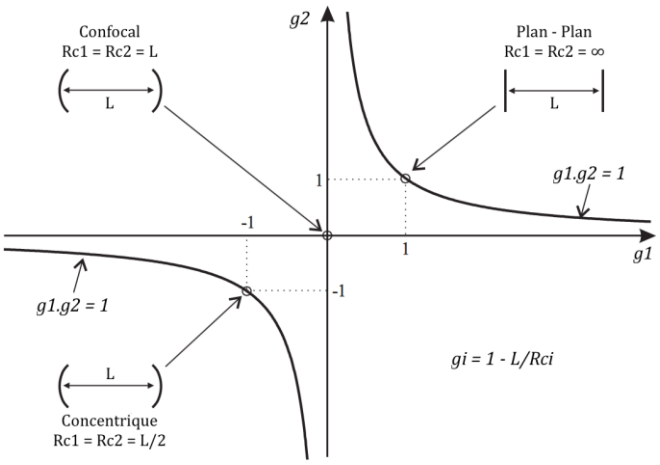

Figure 7: Conditions of stability of a linear optical cavity. g1 and g2 represents the geometrical parameters of the cavity.

The different stable configurations can be visualized for different types of cavities in Figure 7. The zone of stability is between the curves $g_1.g_2 = 1$ and g_1 and g_2 axes. Three configurations can be distinguished at the limit of stability: plan-plan with $R_{c1} = R_{c2} = \infty$, confocal with $R_{c1} = R_{c2} = L$ and concentric with $R_{c1} = R_{c2} = L/2$. Thus, for a linear cavity made with two mirrors with the same radius of curvature $R_{c1} = R_{c2}$, the cavity stays stable if its length is lower than twice the radius of curvature $L \leq 2R_c$.

2.1.2.2 Principles of Cavity Ring-Down Spectroscopy

The Cavity Ring-Down Spectroscopy (CRDS) is a highly sensitive technique developed with the emergence of high reflectivity dielectric mirrors. The first studies using this type of mirrors in an enhanced cavity configuration were designed to accurately measure their reflectivity. In 1984, Anderson et al. [35] observed for the first time the exponential decrease of the light intensity transmitted by a resonant cavity. They established the connection between the light decay of the cavity and the losses through the mirrors allowing determining their reflectivity. This work was followed by the first study on cavity ring-down spectroscopy in 1988 by O'Keefe and Deacon [36] who experimentally verified that the light decay is not only due to the losses through the mirrors but also to absorption of species inside the cavity. Using a pulsed laser they showed that this technique could be used to measure precisely and directly the absorption coefficient of a given species. Thus, compared to the majority of absorption spectroscopic techniques where the molecular absorption is deduced from the variation of light intensity between the entrance and the exit of an absorbing cell, in the case of CRDS it is the decay rate of light inside an enhanced absorption cavity that is measured. In 1996, Lehmann [37] proposed the possibility to use continuous light sources such as diode lasers. Compared to pulse lasers, diode lasers are spectrally finer which allow the mono-mode excitation in an optical cavity. This technique also presents the advantages to increase the selectivity of detection and make more compact systems. In the present thesis, cw-CRDS coupled to laser photolysis is used to detect different peroxy radicals (RO_2 with R = H, D, CH_3, C_2H_5, etc.), hydroxyl radical OH, or stable molecules. The basic theory of CRDS technique is explained here.

2.1.2.2.1 CRDS in an empty cavity

The principle of the cavity ring-down spectroscopy is based on the measurement of the lifetime of photons from a pulsed or a continuous laser trapped into an enhanced optical cavity composed of two mirrors M (with a reflectivity Rc) separated by a distance L. This principle is illustrated in Figure 8.

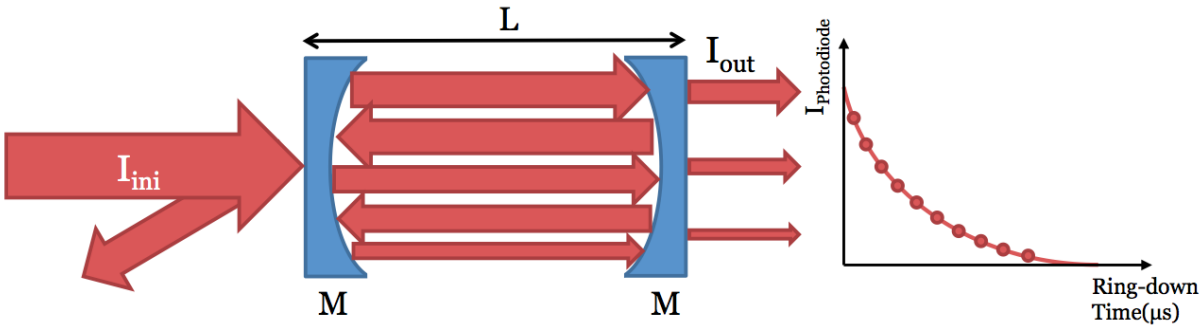

Figure 8: Schematic of principle of the CRDS technique

The incoming laser beam with an intensity I_{ini} is injected thought the front mirror and only a small fraction of the photons enter inside the cavity. The other part is reflected at the entrance. Then, the beam is reflected on both mirrors and at each round trip a part of the light is transmitted through both mirrors. In the ideal case where the beam loss is only due to the transmission through the mirrors, the intensity exiting at the cavity through the rear mirror I_{out} can be characterized by a succession of n impulsions decreasing exponentially. It can be defined as the Equation 16:

$$I_{out} = I_{laser} T^2 R_c^{2n} = I_{in} R_c^{2n}$$

$$I_{out} = I_{in} \exp(2n \ln(R_c)) \qquad \text{Equation 16}$$

With R_c = 1-T and n the number of round trips

Because the coefficient of reflectivity R_c is close to 1 it is possible to use the approximation $\ln(R_c) \approx -(1-R_c)$. The Equation 16 can then be written as:

$$I_n = I_{out} \exp\left(-2n(1 - R_c)\right) \qquad \text{Equation 17}$$

The number of round trips n can be defined as a function of the time t:

$$n = \frac{t}{t_{rt}} = \frac{t\,c}{2L} \qquad \text{Equation 18}$$

With the round trip time $t_{rt} = \frac{2L}{c}$

Thus, substituting n into Equation 17 gives:

$$I_n = I_{out} \exp\left(-\frac{tc}{L}(1 - R_c)\right)$$

$$I_n = I_{out} \exp\left(-\frac{t}{\tau_0}\right) \qquad \text{Equation 19}$$

The residence time or ring-down time τ corresponds to the time when the intensity I_{out} is divided by e. This ring-down time statistically represents the average residence time of a photon inside the cavity. In an empty cavity, the ring-down time τ_0 (in s) is equal to:

$$\tau_0 = \frac{L}{c(1 - R_c)} \qquad \text{Equation 20}$$

This parameter τ_0 is directly measured during the CRDS experiments.

2.1.2.2.2 CRDS in a cavity containing an absorbent

If absorbing species are present inside the cavity, additional losses due to absorption result in a faster exponential decay. Considering species with a concentration N (in

molecules.cm^{-3}) and an absorption cross-section σ (in cm^2), the ring-down time τ_{abs} (in s) can be written as:

$$\tau_{abs} = \frac{L}{c} \frac{1}{(1 - R_c) + N.\sigma.l} \qquad \text{Equation 21}$$

With l the absorption path length in cm

Using the Equation 20 and Equation 21, the absorption coefficient α can be obtained as:

$$\alpha = N\sigma = \frac{R_l}{c}\left(\frac{1}{\tau_{abs}} - \frac{1}{\tau_0}\right) \qquad \text{Equation 22}$$

With R_l the ratio between the cavity length L and the absorption path length l

The absorption spectrum can be obtained by measuring the absorption coefficient α as a function of the wavelength for tunable lasers. Knowing the absorption cross-section of a given compound at a particular wavelength, its absolute concentration can be calculated by measuring τ_{abs} and τ_0.

2.2 Instrumentation and development

The experimental technique has been improved in the frame of this thesis and is based on a version of a setup that has been described in previous publications [38]–[40]. The experiment consists of a photolysis cell coupled to high repetition laser induced fluorescence (LIF) and the continuous wave cavity ring-down spectroscopy (cw-CRDS) measurement techniques. The reaction cell is a stainless steel cross, coated internally with Teflon, with on the vertical plan four short arms (two used for passing the LIF excitation laser and one for detection of fluorescence) and on the horizontal plan two long arms (total length of 70 cm) where the photolysis beam propagates and where the cw-CRDS techniques are installed. The radicals are generated inside the reactor by laser photolysis and three species can be detected

simultaneously by LIF and cw-CRDS. A detailed schematic view of the set-up is represented in Figure 9.

The aim of this chapter is to provide a detailed description of the three main parts of the instruments and experimental techniques: (i) the photolysis system materialized by the excimer laser and the reactor, (ii) the LIF system and (iii) the two cw-CRDS systems.

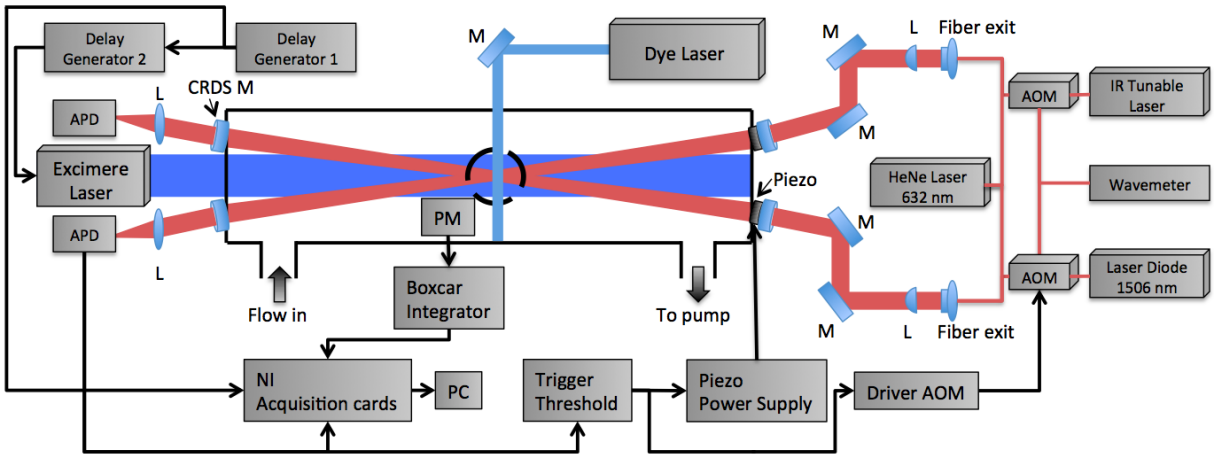

Figure 9: Schematic view of the experimental set-up: APD: Avalanche Photo Diode; AOM: Acousto-Optic Modulator; M: Mirror; L: Lens; PM: PhotoMultiplier. Separate but identical trigger circuits and data acquisition systems are used for both cw-CRDS systems but are shown for only one path in the figure for clarity

2.2.1 Reactor and photolysis system

2.2.1.1 Photolysis cell

The photolysis cell is built with six stainless steel tubes assembled according to three perpendicular axes XYZ, one long (X = 71.8 cm) and two short (Y and Z = 27 cm), forming a three dimensional cross. The tubes are connected through a cubic central structure. The internal diameter of each tube is 6 cm and they are internally coated with Teflon to reduce deterioration of the surface due to aggressive chemicals. The conception of the extremities of the tubes seals the reactor and fulfills more specific

functions detailed below. The schematic representation of the photolysis cell is shown in Figure 10.

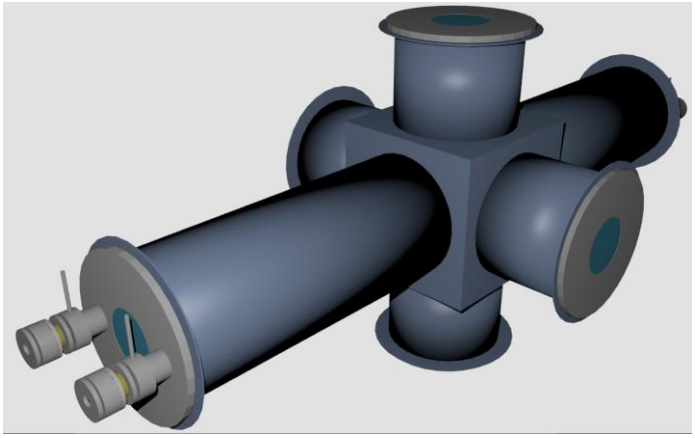

Figure 10: Schematic representation of the photolysis cell

The X-axis is used for the CRDS detection and the photolysis laser and the Y and Z-axis are used for the LIF excitation and detection, respectively. The flanges at the end of the X-axis were redesigned as shown in Figure 11. Besides sealing the cell, they allow the entrance of the photolysis beam though a 3 cm diameter quartz window, transparent for UV. The junction between the CRDS mirror and the flange has an angle of 4°. The flange was conceived to maximize the overlap distance between the volume where the radicals are generated by laser photolysis and the inner-cavity CRDS laser beam. The geometrical calculated overlap distance is 36 cm. A constant flow of helium passes though an additional tube of 2 mm inner diameter soldered to the part 1 to protect the mirrors from dust or corrosive gases. Two CRDS mirror holders (part 2) can now be fixed directly on the flange and not to the optical table as in the earlier version, which improves the stability of the CRDS. The connection between parts 1 and 2 uses an O-ring to seal the cell. Four screws are pushing on the O-ring, allowing enough movement to align the CRDS mirrors. The alignment procedure of the CRDS cavity is described below. The piezo (described below) links the mirror holder (part 2) and the mirror box (part 3). The mirror box can be removed for cleaning purposes without changing the alignment of the CRDS cavity.

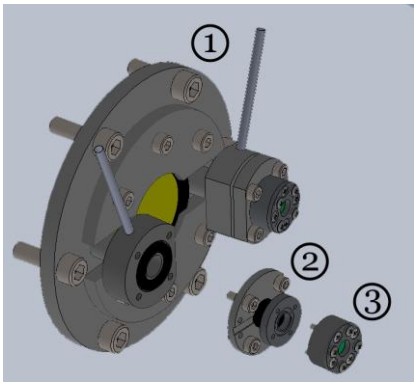

Figure 11: The end flange of the X-axis of the photolysis cell showing the different parts

The flange of the Y-axis contains a 2.5 cm diameter quartz window at the center to allow the LIF excitation laser beam to enter into the photolysis cell. The upper flange of the Z-axis is also equipped with a 6 cm diameter quartz window allowing the detection of the fluorescence photons. A set of two lenses (Thor labs, focal length 75 mm) is placed between the center of the cell and the quartz window to focus the fluorescence signal at the surface of a photomultiplier (PM) fixed above the flange. An interference filter is placed between the window and the PM: this filter is optimized for transmission of OH fluorescence photons (310±10nm) and will filter most of the light scattered by the photolysis and LIF lasers as well as daylight entering the cell through the divers windows. The LIF laser beam is aligned at the center of the photolysis beam to have the highest possible sensitivity.

2.2.1.2 Photolysis laser

The radicals are generated by laser photolysis. For this purpose we have at our disposal an excimer laser Lambda Physic LPX 202i series emitting a pulsed radiation in the UV. This laser source owes its name to the presence of excited state dimers present inside the laser cavity and behind the radiation. The excimer gain medium typically contains a noble gas (argon, krypton or xenon) combined with a halogen

(fluorine, chlorine or bromine). During this work two gas mixtures have been used to work at two different wavelengths:

248 nm with a Krypton/Fluorine mixture

351 with a Xenon/Fluorine mixture

The emitted laser beam has a rectangular profile of dimension 16 mm x 28 mm at the exit of the laser but is cut at the entrance of the reactor (16 mm x 25 mm). The pulse duration is 10 ns, which is much shorter than the time scale of the reactions of interest encountered during this work (in the msec range). The repetition rate is 1 Hz or less to allow the gases to be renewed inside the reactor. The energy measured at the exit of the laser can vary over a large range from 200 to 600 mJ/pulse (leading to energies from 50 to 150 mJ/cm^2 inside the reactor) depending on the gas mixture and on age of the gas mixture.

2.2.1.3 Uniformity of the photolysis laser

In the frame of this work, radical-radical reactions have been studied and hence it is important to characterize the uniformity of energy distribution within the photolysis laser beam and try to generate a distribution of energy (and thus radicals) as homogeneous as possible. This value of the absorption path length is important especially for the measurement of radical-radical reactions. There are several points that could include systematic errors in our setup and are schematized on the Figure 12: (i) the photolysis laser should enter into the reactor perfectly parallel without even a small angle, because this would have an influence on the absorption path length, i.e. the overlap between the cw-CRDS beam and the photolysis laser beam, inducing errors on the calculation of concentrations, (ii) a divergent photolysis beam would have two effects: a longer overlap region compared to a collimated beam and an inhomogeneous radical distribution along the photolysis cell with a higher radical concentration at the entrance windows compared to the exit windows due to a decrease of the laser energy per cm^2, and (iii) an inhomogeneous distribution of the

laser energy within the beam leading to an inhomogeneous distribution of the radical concentration and thus volumes with faster and slower rates for radical-radical reactions. This last point will not be revealed by the CRDS or LIF techniques because they both probe the full width of the laser beam and thus only average concentrations are observed.

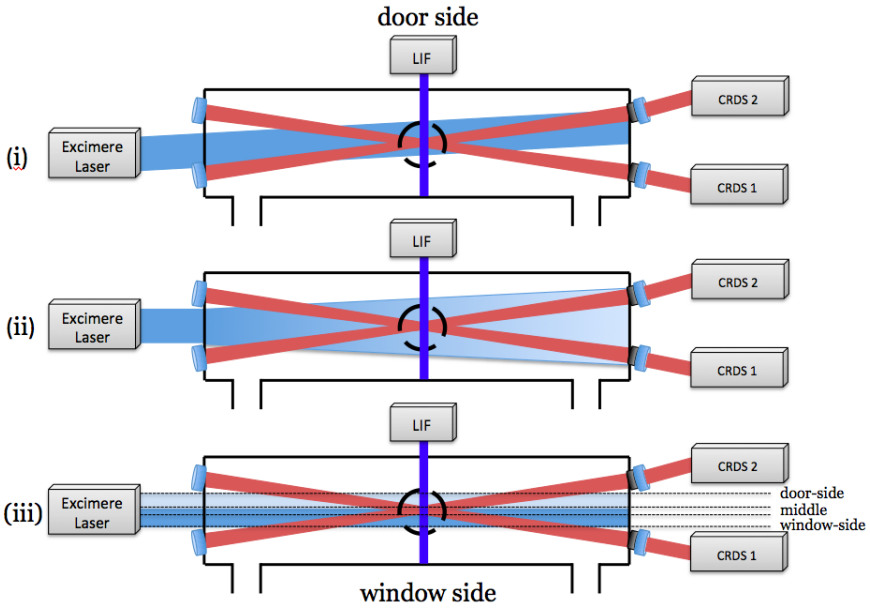

Figure 12: Three possible problems with the photolysis laser: (i) the laser enters with an angle into the reactor, (ii) a divergence of the laser beam induces an inhomogeneity of energy from the entrance to the back of the cell as well as an increase in absorption path length, (iii) an inhomogeneity on the beam profile induces volumes with different radical concentrations

To quantify these uniformities, several tests were carried out by taking advantage of the two identical but opposite cw-CRDS paths. (i) To align the photolysis beam as straight as possible, HO_2 concentration time profiles were measured simultaneously on both cw-CRDS paths. If the laser beam enters with a small angle, the absorption path length would be longer on one path than on the other leading to a higher absorption of HO_2. Simultaneously measured HO_2 absorptions were equivalent to better than 5%, showing that the photolysis beam was well aligned. (ii),(iii) A first preliminary test was carried to test the possible divergence and distribution of energy of the laser beam. An impact of the beam was taken on a photosensitive paper at

different distance of the entrance of the cell, and the size of the beam was measured. Inspecting visually the impact of on the photosensitive paper, a homogeneous distribution was found and only a barely quantifiable divergence was observed in agreement with the speciation given by the constructor Lambda Physik (a divergence of 0.17°). The distribution of energy was also mapped through a mask of 0.5 x 0.5 cm using a power meter (Newport). The energy was evenly distributed within the uncertainty of the power meter. (ii), (iii) A second test was carried out to measure in a more precise way the distribution of energy and the divergence. Only a fraction of the photolysis beam was allowed to enter the cell by dividing it in four parts as indicated in Figure 12: 0.5 or 1 cm at the two extremities marked “door-side” and “window-side”, 0.5 cm in the middle, and the entire beam 2.5 cm. For example, when photolysing the “door-side” the CRDS 1 will probe a volume at the entrance of the cell while CRDS 2 sees the volume at the exit. Any divergent in the laser beam would lead to a lower radical concentration in volume 1 than volume 2. Furthermore, comparing the volume probed by the CRDS 1 and the CRDS 2 at the entrance of the cell, i.e. using “door-side” for CRDS 1 and “window-side” for CRDS 2, would show information on the homogeneity of the distribution of the photolysis energy.
For these tests, HO_2 radicals were generated by photolysing $(COCl)_2$ in the presence of CH_3OH and O_2. The different masks have been applied on the photolysis beam with 0.5 or 1 cm at each extremity of the photolysis beam (named door and windows-side), 0.5 cm in the middle and the entire beam 2.5 cm. For each configuration CH_3OH and O_2 have been kept constant, while $(COCl)_2$ was varied. HO_2 radicals have been quantified on both CRDS paths.

For the first two series, the two 0.5 cm at each extremity were used. The Figure 13 shows the increase of the absorbance of HO_2 (α_{HO2}) at t = 0 s obtained within the four volumes (door and window-sides at the entrance and exit) for five concentrations of $(COCl)_2$. The results are fitted by a linear regression forced through zero and the obtained values of the slopes are 9.61, 9.45, 8.39, 9.06×10^{-22} for the door-side entrance and exit and the window-side entrance and exit, respectively. The four absorbance α_{HO2} diverge by less than 5% except for the window-side entrance that seems around 10% lower for all the $(COCl)_2$ concentrations. This may be due to a

slight inhomogeneity of the distribution of energy on the window side of the excimer laser beam.

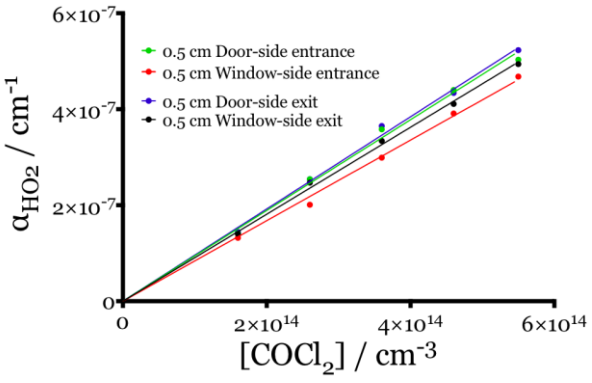

Figure 13: Two series of experiments using 0.5 cm at each extremity of the photolysis beam (marked door and windows-side). For each series four different concentrations of $(COCl)_2$ have been used, keeping all other flows and the photolysis energy constant

Experiments have then been carried out with four series: either 1 cm at each extremity, 0.5 cm in the middle or 2.5 cm for the entire beam and the results are presented in Figure 14. Again, the door and window series are identical, confirming the good homogeneity of the photolysis beam. The slope of the four series should change proportional to the absorption path length. The obtained values of the slope are nearly proportional with 1.17, 2.10, 2.26 and 5.01 for 0.5, 1 door, 1 window and 2.5 cm respectively, but a better linearity is obtained by taking into account a slight divergence. Indeed, the divergence has a stronger impact on the absorption path length for the 0.5 cm than for the 2.5 cm beam. Increasing the geometrically calculated overlap by 1.7 cm (i.e. 37.7 cm instead of 36 cm for 2.5 cm beam and 8.9 instead of 7.2 cm for 0.5 cm beam) leads to a better proportionality of the observed absorbance. Such an increase corresponds to a divergence of 0.7° which is slightly larger than the value given by Lambda Physik (0.17°).

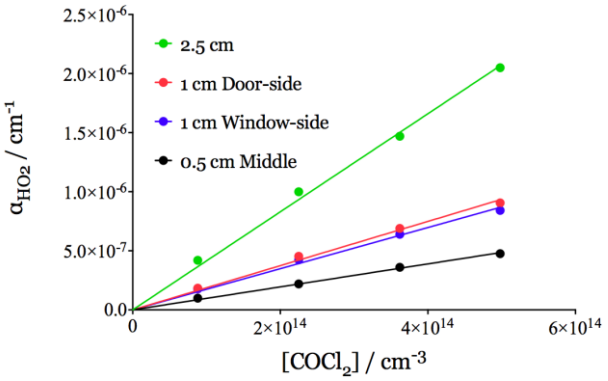

Figure 14: Four series of experiments using 1 cm at each extremity of the photolysis beam (marked door and windows-side), 0.5 cm in the middle and the entire beam of 2.5 cm. For each series the same conditions than in Figure 13 have been used

2.2.2 The LIF system

During this work, the Laser Induced Fluorescence (LIF) technique has been used to detect OH radicals. OH is excited from the ground vibrational level of electronic ground state to the first excited vibrational level of excited electronic state (from $X^2\Pi$ to $A^2\Sigma$) at 282 nm. The excitation beam is achieved from a frequency doubled dye laser (Sirah Laser PrecisionScan PRSC-24-HPR) pumped by a frequency-doubled output of a YAG (Spectra Physics Navigator II YHP40-532QW) laser. The excitation beam enters the photolysis cell perpendicular to the photolysis beam along the Y-axis. The red shifted fluorescence is collected perpendicular to the photolysis and excitation beams near 308 nm using two lenses and an interference filter (310 ± 10 nm) and detected by a photomultiplier (Hamatsu R212). The electrical signal generated by the photomultiplier is fed into a boxcar integrator (EG&G Model 4121B) and transferred to the A/D convertor of a data acquisition card (National Instruments PCI-6221). The boxcar is triggered by a photodiode using a reflection of the YAG laser. Since the OH fluorescence decay under the experimental conditions of this work is a few hundred of nanoseconds, the signal is integrated within a gate of 100 ns positioned 80 ns after the YAG laser pulse. A Labview based acquisition program retrieves the signal every 100 µs and converts it into a digital signal.

2.2.2.1 High repetition rate laser and fluorescence detection in the LIF system

As mentioned above, the dye laser is pumped by the frequency doubled output of a Nd :YVO_4 laser (emission at 532 nm, after doubling). The Nd:YVO_4 laser is pumped using laser diodes. The 532 nm wavelength is then used to pump a dye system. The emission of the dye laser is produced with a mixture of rhodamine 6G diluted into methanol which fluoresces at 564 nm when excited with light of a suitable frequency. The dye solution is rapidly flowed through a quartz cuvette from a large reservoir to avoid heating, and with this the degradation of the solution under the influence of the light. The dye fluorescence emission is then doubled using a doubling crystal (e.g. BBO: Beta Barium Borate) to obtain a wavelength of 282 nm. The dye laser passes through optics as shown on a schematic diagram Figure 15 to ensure a narrow line width. The average output of the dye laser is 35-40 mW at 10 kHz with a pulse width of 30 ns and a bandwidth of 20 MHz. The choice of the repetition rate depends on the temporal resolution required for the measurement and was generally 10 kHz.

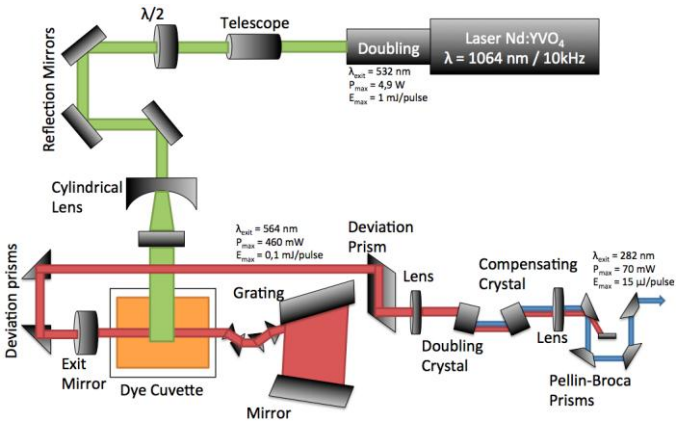

Figure 15: Schematic diagram of a dye laser pumped by a Nd :YVO4 laser [41]

The tunable output from the dye laser excites OH radicals in the (1-0) vibrational band Q1(4) of the A-X transition at 282.522 nm marked with an arrow on the Figure 16. This A-X 1-0 line is chosen because it corresponds to one of the most intense in

this wavelength range and the structure of the spectrum is easily identifiable. The Figure 16 presents a portion of the OH spectrum scanned between 282 and 283 nm. The line strengths from the HITRAN database of the corresponding A-X 1-0 transition lines are also presented as red dots.

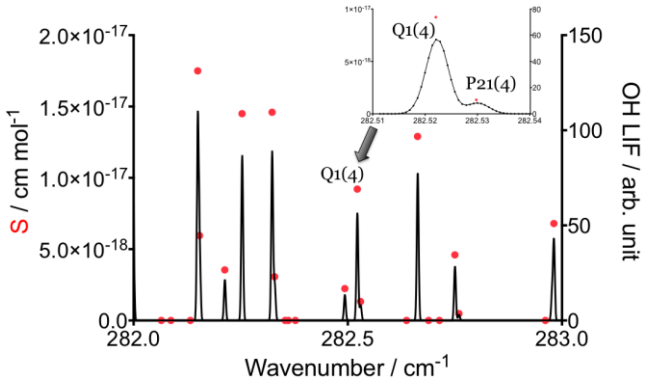

Figure 16: Scan of the excitation spectrum of OH around 282 nm (black line) and corresponding line strength (red dots) from the HITRAN database [42]

The red shifted OH fluorescence is collected at a wavelength (310±10 nm) different of the wavelength of excitation to minimize the influence of the laser pulse on the detector and avoid its saturation by stray light. The optical system presented in Figure 17 is optimized in order to collect the maximum of the OH fluorescence light. The OH fluorescence is collected perpendicular to the laser beam and collimated using two plano-convex lenses. Then it passes through a band pass filter with a maximum of transmission near the OH fluorescence wavelengths, $\lambda \approx 310\pm10$ nm. The filter reduces any interference lights, i.e. solar light, stray light from the excitation laser, and potential fluorescence of other chemical species [43].

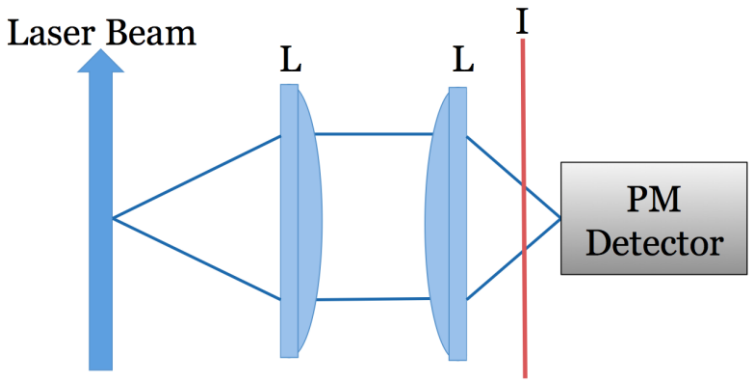

Figure 17: Simplified OH fluorescence collection. I, the band pass interferometer; L, the lenses

A photomultiplier PM (Hamamatsu R212) supplied by high voltage (Stanford Research System PS325) is used to detect the emitted OH fluorescence. Detectors are usually composed of 3 elements: (1) a photocathode converts the photon into electrons. (2) Electrons are then accelerated using a high-voltage potential between the photocathode and an electron multiplier made of discrete dynodes. (3) The electrons are then amplified and detected on an anode. The collection of the signal is done with a boxcar average (EG&G Model 4121B), connected to an A/D converter of a National Instrument acquisition card.

2.2.2.2 The etalon

A rapid drift of the excitation wavelength has been observed on the LIF Sirah laser which resulted in a rapid decrease of the fluorescence intensity. The use of a temperature-controlled etalon placed at the exit of the Sirah laser was necessary to lock the laser at the OH excitation wavelength around 282 nm. The etalon represented in Figure 18 is based on a Fabry-Pérot interferometer (or etalon). The LIF laser beam is injected into the etalon and passes though a 6.3 mm thick window where around 96% of the light intensity is sent to the experiment for the OH excitation. The remaining 4% are reflected into two beams by the front and back

surface of the window. A neutral-density filter reduces the light intensity. The two reflected beams are then aligned using a quartz prism. The first reflection is injected onto a photodiode to normalize the transmission to the incoming laser intensity, while the second reflection is sent to the photodiode 2 through a Farby-Pérot etalon.

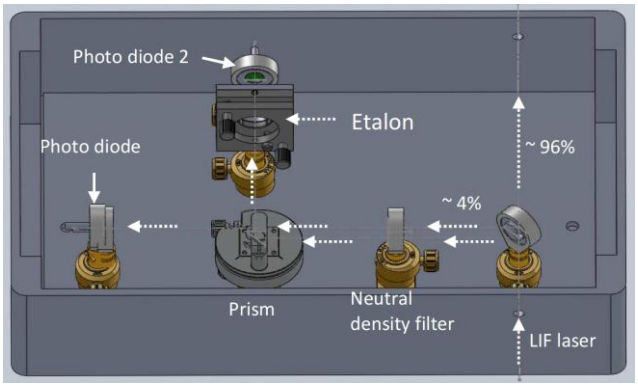

Figure 18: Schematic representation of the etalon system [44]

A Fabry-Pérot etalon in Figure 19 consists of two parallel semi-transparent flat mirrors with a high reflectivity coefficient, separated by a fixed distance.

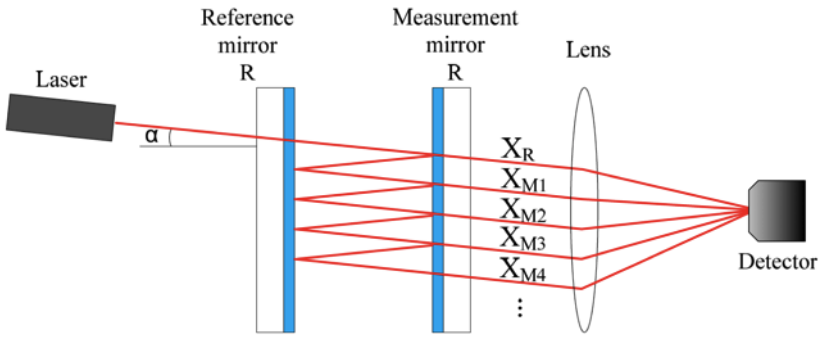

Figure 19: Schematic of the working principle of the Fabry-Pérot interferometer [45]

A monochromatic light incident upon the etalon at an angle α to the normal of the mirror surface undergoes multiple internal reflections within the mirrors. The transmitted light from the etalon depends on whether constructive or destructive interferences occur within the etalon, resulting respectively to high or low

transmission as shown in Figure 20. The reflections inside the etalon depend on the wavelength of the light, the entering angle of the light, the distance between the two reflecting surfaces and the refractive index of the material.

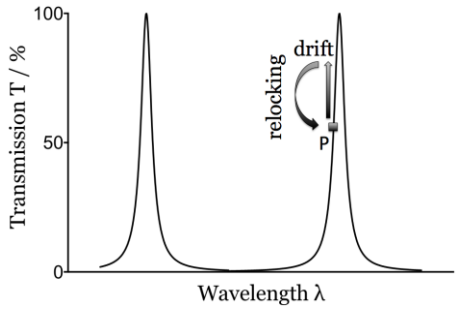

Figure 20: Transmittance of the Fabry-Pérot etalon as a function of the wavelength, locking of the LIF laser

In practice, the excitation beam enters perpendicular to the etalon. The intensity of the exiting beam will depend on whether the reflections undergo constructive or destructive interferences. The intensity of the transmission depends on the distance between the two reflecting surfaces, which is strongly linked to the temperature. The Farby-Pérot etalon is placed inside a temperature-controlled box where the temperature is stabilized at ±0.1 K with a servoloop system. Thus, the wavelength of the LIF laser is tuned to the maximum of the OH-absorption peak by measuring the fluorescence intensity. The temperature is then adjusted to place the transmitted intensity though the etalon at roughly half of the maximal transmission peak (position noted P in Figure 20). The temperature of the box is then kept constant so any drift in the wavelength will result in a decrease or increase of the transmission of the resonator. A homemade Labview program will relock the laser wavelength depending on the direction of the drift.

2.2.3 The CRDS system

Several improvements to the experimental setup such as described in earlier publications [38]–[40] have been realized in the frame of this thesis: (i) a second cw-CRDS absorption path in the near infrared has been installed, both absorption paths installed in a small angle (4°) to the excimer laser beam, (ii) the change of the cw-CRDS mirrors from a plane to a wedged external surface, which made it necessary to change the alignment procedure with the addition of a He/Ne laser aligned collinear to the near-IR laser, (iii) the change to an entirely fibered experiment, including the acousto-optic modulator (AOM) and (iv) an improved way of tracking the movement of the piezo has been developed to increase the occurrence of ring-down events and thus the sensitivity of the measurements.

The near-IR cw-CRDS system is formed by two highly reflective mirrors with a reflectivity R>99.995 % (Layertec). Three sets of mirrors are available with the maximum reflectivity in different ranges (1280 nm, 1392 nm and 1510 nm) allowing the detection of several species. The mirror at the entrance of the cavity is glued to a piezo-electric transducer (P-010-00H), which has a full range of displacement of 5 µm (0-1000V). The goal of the piezo is to modulate the length of the cavity with a high voltage triangular signal. The amplitude of the signal is set to cover one free spectral range (described in Equation 12) of the cavity. The TEM_{00} mode is then excited twice per period, once on the positive slope and once on the negative slope. Two folding mirrors and one focal lens (10 or 12 cm) ensure the spatial coupling.

Three distributed feed-back (DFB) laser diodes provide near-IR laser beams with an output power of 1 to 20 mW in different wavelength range: at 6629±17 cm^{-1} (Fitel FOL15DCWB-A81-W1509), at 7014±18 cm^{-1} (NEL NLK1E5GAAA) and at 7480±20 cm^{-1} (NEL NLK1B5EAAA). A laser diode module (Agilent mainframe 8164B with laser module 81600B), borrowed from the Gerätezentrum ”Cologne Center for Terahertz Spectroscopy” was also used in the frame of this thesis. This laser module was able to cover a wide tuning range between 6200 to 8000 cm^{-1}. It was equipped with a built-in wavemeter with a wavelength accuracy of ±0.005 cm^{-1}. The spectral width of all the

lasers is less than 2 MHz. The laser diode emission passes through a fibred optical isolator. The role of the isolator is to prevent reflection problems that can disturb the stability of the laser diode. The laser beam is then injected into an acousto-optical modulator (AOM, AA optoelectronics MT110-IIR25-3Fio-PM0,5-J3-A). The AOM is a rapid switch; it is composed of a TeO_2 crystal and a frequency switch at 100 MHz. When a trigger signal is sent to the AOM, an acoustic wave is sent to the crystal, which will behave like a diffraction grating. Exploiting the order 1 thus enables the propagation of the radiation to be interrupted within 350 ns with respect to the trigger signal. The order 1 from the AOM is injected into the cavity, while the order 0 of the diffraction pattern is injected into a wavemeter (Burleigh WA-1100) having an accuracy of 0.01 cm^{-1}.

The laser beam transmitted by the cavity is focused by a lens (5 cm) on an avalanche photodiode (Perking Elmer C30662E), converting the signal into current. The transmitted intensity, and thus the signal, increases when cavity comes into resonance. As soon as the photodiode signal passes a user-defined threshold, the trigger to the AOM is interrupted, thus completely removing the order 1 at the exit of the AOM. The Figure 9 shows a schematic diagram of the cw-CRDS technique used in the present work.

2.2.3.1 Laser in the CRDS system

As described in the previous section, a distributed feedback (DFB) laser diode is the source of the near-infrared light for the cw-CRDS system. DFB lasers are based on semiconductor gain media [46]. The gain is achieved by stimulated emission via interband transition between a conduction band and a valence band. The Figure 21 shows a schematic diagram of the laser gain in a semiconductor laser diode. The laser diodes are pumped using an electrical current that is higher than the band gap voltage between n-doped and a p-doped semiconductor materials, resulting in population

inversion. The electron in the conduction band will fall back to the valence band, emitting a photon with the excess of energy causing the laser action.

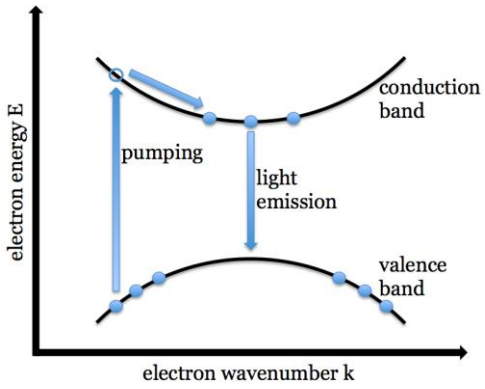

Figure 21: Laser action in a semiconductor diode laser [47]

The DFB laser is built with a grating structure incorporated to the semiconductor chip, restricting the laser emission wavelength. A controller (Thorlabs ITC502) powers the DFB laser by adjusting the temperature and current. These two parameters determine the laser power and the laser wavelength along a given range (typically 25cm^{-1}). The DFB lasers used in this work have an output power around 15 mW with a fluctuation of 2% at 25°C and a bandwidth of the laser emission around 2 MHz.

2.2.3.2 Procedure of alignment of the cavity

A near-infrared laser (between around 1300-1500nm) and a He-Ne laser (at 632nm) are coupled together into one optical fiber at the exit of the acousto-optic modulator. In order to realize the mode matching, i.e. excite only the TEM_{00} mode, a lens (f = 10 mm) is positioned on a X-Y-Z stage closed to the exit of the fiber. Two folding mirrors are placed between the lens and the cavity to control the propagation of the laser beam. Concretely, the procedure is to obtain the beam waist at the center of the cavity

and the same beam diameter on the surface of both CRDS mirrors. Wedge mirrors are used in order to avoid interferences, possibly generated by building a cavity between the back surface of the mirror and another optical surface such as the mode-matching lens. At the exit of the cavity, a photodiode is placed on a X-Y-Z stage after a focalization lens.

The first step consists of working without any cavity mirrors and only the He-Ne laser. By adjusting the folding mirrors, we make sure that the beam is passing through the center of the CRDS mirror positions. Besides the positioning of the beam, the focalization of the laser at the center of the cavity and the position of the photodiode at the exit of the cavity are also adjusted by observing the intensity of the radiation signal on the oscilloscope.

For the second step, the CRDS mirror at the exit of the cavity is placed and the incident and reflected beams are made collinear. To do that a pinhole is place before the entrance of the cavity. Two reflected beams will be visible, an unfocused beam from the wedged surface and a focused beam from the concave surface of the CRDS mirror. The orientation of the mirror can be changed with screws compressing more or less an O-ring. Once found the two spots, the rear mirror will be aligned such that the focused reflected spot will pass through the pinhole and be collinear with the incident beam with a maximum of precision.

A third step is realized now placing also the CRDS mirror at the entrance of the cavity. The length of the cavity is modulated by applying a triangular signal to a piezoelectric transducer on which is mounted the entrance CRDS mirror. The modulation of the distance between the two mirrors allows to periodically having resonance conditions – the length of the cavity should be a multiple of half of the wavelength – by sweeping the cavity modes in an interval higher than the free spectral range. This time the reflected beams from the convex surface of the CRDS mirror will be defocused and the reflection from the wedged surface will be unfocused. The adjustment procedure of the entrance mirror is the same as the one described for the exit mirror: the orientation of the mirror is changed until the defocused beam goes through the pinhole. After this procedure, the two convex surfaces of the mirrors are parallel to each other and perpendicular to the incent beam. However, due to the wedged surface

of the mirror, the beam is bent inside the cell and is not going through the center of the exit CRDS mirror anymore. The first step and then the third step are repeated to position again the beam at the center of both CRDS mirrors and have collinear reflections. While tending to this alignment, the signal of the photodiode is observed on the oscilloscope over an interval of time equal to the modulation period of the piezo. A series of constructive interference waves from the He-Ne laser can be observed as shown in Figure 22. The numbers of waves are directly proportional to the modulation length of the cavity.

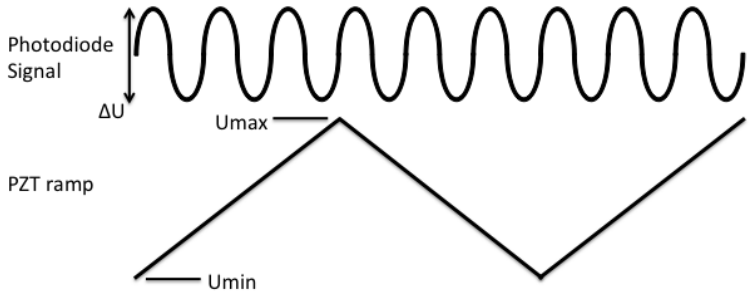

Figure 22: Piezo voltage and observed interferences from the He-Ne laser on the photodiode signal

The last step is to align the cavity by observing the photodiode signal. The goal is to maximize the peak-to-peak ΔU voltage signal of the photodiode by adjusting the orientation of the entrance and exit CRDS mirrors. Once maximized, the IR laser is turned on and the mode-matching lens is positioned such that the IR beam is focalized at the center of the cavity instead of the He-Ne laser. In the ideal case, only the fundamental mode TEM_{00} is excited. In practice however, higher modes are commonly excited as well, and the cavity is finally aligned such as to obtain the maximum of intensity for this mode and the minimum intensity for the others. In general, the intensity gap allows to easily suppressing the higher modes by setting the trigger threshold well above the intensity of the higher mode ring-down events.

2.2.3.3 The event filter

The event filter is an improved version of a setup that has been described in previous works [38], [48]. The photodiode and the AOM trigger signals are both connected to a National Instruments acquisition cards (two PCI-6259 for both cw-CRDS), with an acquisition frequency of 1.25 MHz, thus sampling the photodiode signal every 800 ns. The signal from the photodiode contains noises coming from many sources such as stray light, interferences from the deviation of the laser by the AOM, and lower modes of the cavity. The Labview acquisition program works as an event filter that only acquires the photodiode signal when the AOM trigger signal is at 5 V, i.e. when the laser has been deviated, and keeps the photodiode signal at 0 V the rest of the time. In order to filter the higher cavity modes, i.e. the TEM_{00} mode, it is also possible with a threshold to select the ring-down events by putting the threshold value higher than the maximum of intensity of the lower modes. This results in the photodiode signal being cleaned as shown in Figure 23.

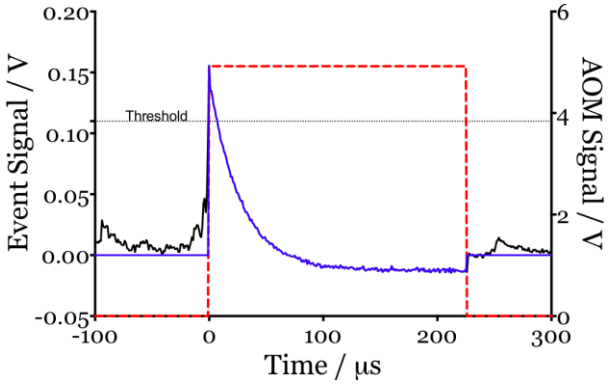

Figure 23: Schematic of the filtering of the photodiode signal. In black the signal acquired by the photodiode, in blue the signal obtained after the filtering procedure, in red the AOM signal

2.2.3.4 The piezo tracking servo

As mentioned earlier, one of the two CRDS mirrors is glued to a piezoelectric transducer. The piezo periodically modulates the length of the cavity using a triangular voltage ramp to achieve the resonance between the cavity modes and the IR laser. A piezo tracking servo unit was home-designed [39] in order to improve the signal to noise ratio by bringing the cavity into resonance more frequently and thus acquiring more ring-down events per time unit. This piezo servo has two modes: (i) full scan mode and (ii) a tracking mode. The piezo full scan brings the cavity modes and the laser mode into resonance with each ramp, once on the forward scan and once on the backward scan. With this mode, time is lost between the two resonances on the two ramps.

Using the piezo tracking servo mode, the piezo tracks the position of a cavity mode on the ramp and reverses the direction of the piezo movement as soon as an event occurred without completing the full scan. The position of the event is found when the signal from the photodiode passes a user-defined threshold. When the position of the resonance is detected, the piezo continues to scan for a short time (a little longer than the ring-down time) and reverses its direction to find the same resonance again, thus reducing the time between two resonant positions. This tracking continues until the position of the resonance is lost due to mechanical instabilities of the cavity. In this case, the length of the piezo scan will increase gradually following a back and forth movement until the event is detected again. This tracking procedure reduces the time taken by the piezo for a full scan and hence increases the number of detected ring-down events for a given acquisition time. The numbers of ring-down events can be increased by a factor of up to 200 compared to the number obtained with the full scan. The Figure 24 shows the piezo ramp and the corresponding photodiode signal with and without tracking.

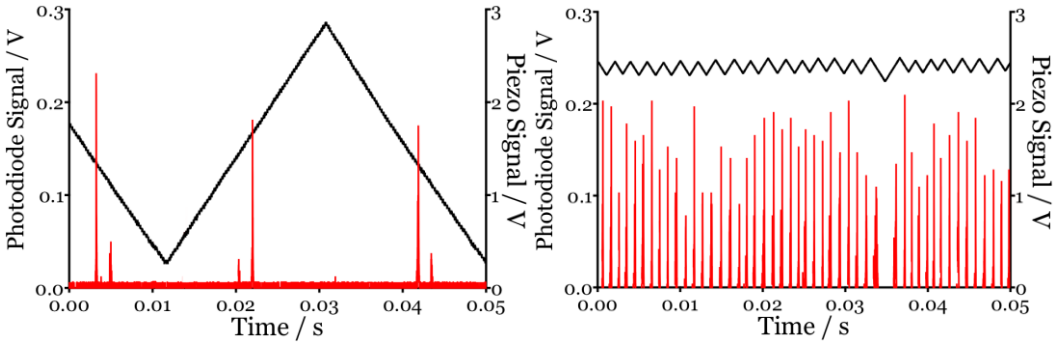

Figure 24: Piezo signal (black) and corresponding photodiode signal (red) without (left) and with (right) piezo tracking

An example of kinetic measurement of HO_2 recorded for only one photolysis pulse during the photolysis of H_2O_2 at 248 nm and 50 Torr of helium is shown in Figure 25.

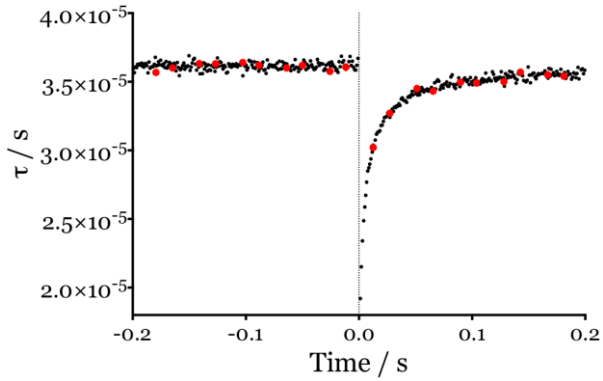

Figure 25: HO_2 kinetics with (black dots) and without (red dots) piezo tracking acquired for one photolysis pulse

2.2.3.5 The cw-CRDS measurement techniques

This experimental setup can be used for two distinct applications: (i) kinetics applications where the concentration profiles of radical or molecular species are followed as a function of the time with the goal to measure rate constants or product yields, and (ii) spectroscopic applications with the goal to determine the spectroscopic

parameters of species as a function of the wavelength. Spectroscopic applications can be divided into two modes, either in continuous mode for stable species, or in pulsed mode for radicals using the synchronization of the acquisition of the ring-down events with the laser photolysis pulse.

The synchronization of the experiment is achieved with two delay generators (DG1 and DG2). The master clock of the entire experiment is a delay generator (Quantum Composers 9300 series) running at 10 kHz (noted DG1). This DG1 has two tasks: (i) triggering the YAG laser to get a time resolution of 100 μs for the LIF signal and (ii) triggering a second delay generator (Princeton Research 9650) (noted DG2). The repetition rate of the DG2 is decreased to typically 0.33 to 1 Hz by setting a delay of 1 to 3 seconds onto an unused channel. In this way, DG2 considers a new trigger pulse from DG1 only once the delays of all output channels have been fulfilled. The acquisition cards for the LIF and both cw-CRDS (National Instrument PCI-6221 and PCI-6259, respectively) are triggered at this reduced repetition rate, using the t_0 output of DG2 as t_0 of the acquisition. The photolysis laser is then triggered by DG2 by setting a user set delay (generally 0.5 s), allowing the acquisition of a baseline, either ring-down events or the LIF signal before the photolysis pulse, i.e. without species generated by the photolysis pulse in the cell.

2.2.3.5.1 Kinetic applications

For the kinetic measurements, the signal of the photodiode is registered with a resolution of 800 ns by the PC, generally for a total of 1.5 s: 0.5 s before and 1 s after the photolysis pulse. The acquisition of the photodiode signal is triggered by DG2. Thus, the delay of each ring down event relative to the photolysis laser pulse can be determined from its position within the acquisition time window. This way, a variable number of ring-down events occur at a random, but well determined delay, for each photolysis pulse. Accumulating ring-down events over several photolysis pulses

(typically 20 to 50) leads to relatively evenly distributed data points in the entire time window.

The ring-down time τ of each individual event is obtained in a two step process by a homemade Labview program. A numerical filter sets the signal of the photodiode to zero when no events occur (as described above), i.e. as long as the photodiode signal does not exceed a user-set threshold value and the trigger circuit does not deviate the AOM. This way, the Labview program can unequivocally recognize the occurrence of a ring-down event in the data stream. The ring-down time is fitted with a Levenberg-Marquardt [49] method with an exponential decay over 7 lifetimes (determined in a quick pre-fit). The ring-down time together with the delay relative to the photolysis laser is then recorded.

The number of ring-down events obtained per photolysis shot over the time window depends strongly on the quality of the alignment and on the user-set trigger threshold. For each photolysis shot, between around 100 to 2000 events are typically obtained in a 1 s time window. A typical time-resolved kinetic signal is presented in left graph of Figure 26, obtained by accumulating ring-down events over 100 photolysis shots, leading to a total of up to 50000 ring-down events randomly scattered over a 1 s time window (0.5 s before and 0.5 s after the photolysis shot).

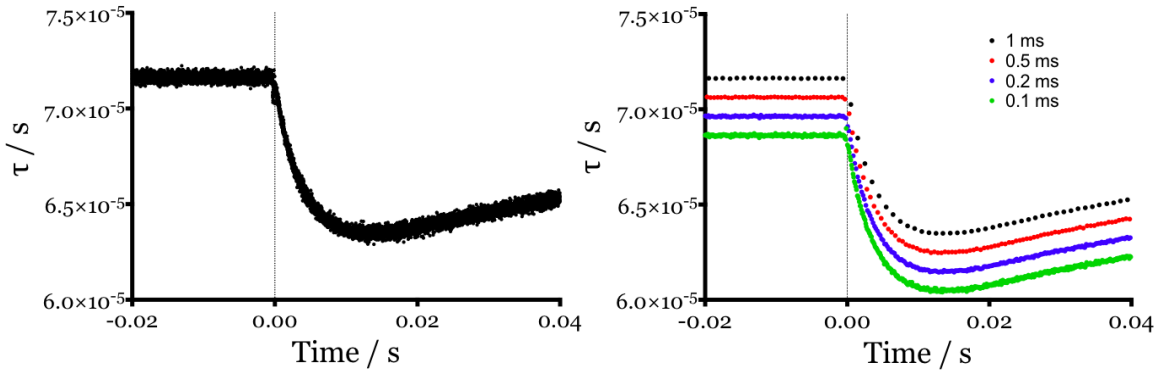

Figure 26: Left graph: Typical time-resolved kinetic measurement of HO_2 with the ring-down time as a function of the delay with respect to the photolysis pulse (t = 0 s) following the 248 nm photolysis of H_2O_2. Right graph: Comparison of different HO_2 signal from left graph averaging from 0.1 ms to 1 ms to get a better signal-to-noise ratio. The averaged signals are deliberately shifted for a better view

When a better signal-to-noise ratio is desired, then all the ring-down events occurring in the same user-defined time window can be average by a Labview program. The right graph of Figure 26 shows a comparison of four different (1, 0.5, 0.2 and 0.1 ms) time window averages from the raw HO_2 signal on the left graph. The averaged signals are deliberately shifted for a better view. The average is then done accordingly to the dynamic of the signal. A too large time windows will end up with less number of points. It is thus important to keep enough points to describe well the time resolution of the concentration.

While measuring kinetics of HO_2, a pattern in the value of the ring-down times just before the photolysis pulse is systematically observed. The Figure 27 shows an example of the pattern (with in the red circle) with first a decay, and then an increase of the ring-down time compared to the average value of the baseline (τ = 71.58 µs).

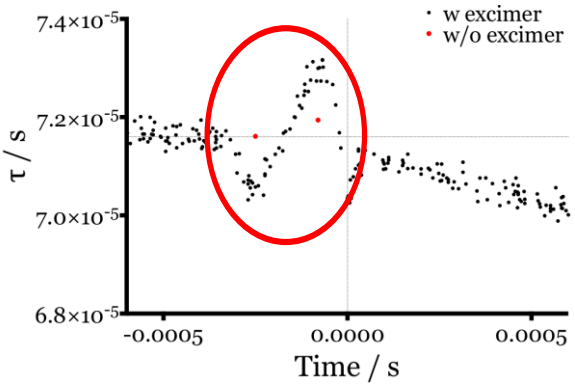

Figure 27: Kinetic measurement signal 500 µs before and after the photolysis pulse showing the effect of the photolysis pulse occurring after the start of the ring-down event. In red, two dots have been fitted after removing the effect of the pulse

In order to search for the reason of this pattern, the raw data of all the ring-down events traces having occurred 500 µs before the photolysis laser were recorded. The Figure 28 presents an event occurring 80 µs before the photolysis pulse. It was observed that the light intensity slightly increases just after the excimer pulse, possibly because the excimer laser beam is being reflected by the metallic pieces at the entrance of the photolysis cell and detected by the photodiode. As the ring-down events are fitted during 7 lifetimes (in this case 500 µs), it happens that the photolysis

pulse occurs during the ring-down event. The photolysis pulse induces a bump in the ring-down event decay. Fitting such a signal was done in two ways in Figure 28. First the ring-down event was fitted with the bump as done by the Labview program, leading to a value of τ = 72.95 µs, which is higher than the baseline average. Then the data points corresponding to the bump are removed and the ring-down event is fitted again. The obtained value τ = 72.06 µs is closer to the average baseline. The same procedure was repeated for an event positioned 250 µs before the photolysis pulse and again the value is closer to the average baseline. The two new values are reported on the Figure 27 as red dots. All the ring-down events inside this pattern are removed before calculating the value of τ_0 by averaging all ring-down events before the photolysis pulse.

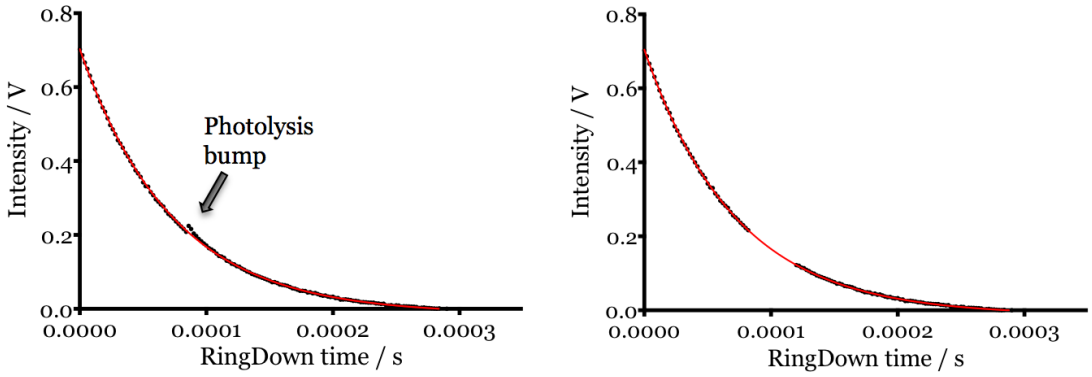

Figure 28: Decay of a ring-down event positioned 80 µs before the photolysis pulse. On the left the excimer laser pulse induce a bump in the ring-down time (τ = 72.95 µs), on the right the bump is removed (τ = 72.06 µs)

2.2.3.5.2 Spectroscopic applications

The cw-CRDS technique can also be used for measuring absorption spectra in two configurations: (i) a non-time resolved configuration to measure stables species and (ii) a time resolved configuration coupled to the laser photolysis to measure reactive species. In this section, the two configurations will be described.

2.2.3.5.2.1 Non time-resolved measurements

The spectrum of a stable species is measured with the non time-resolved measurement configuration. The photolysis laser is not required to measure this spectrum, thus the baseline τ_0 should be first measured separately in the absence of the stable species. Then, the absorption of the stable species is recorded in the same wavelength range. The wavelength is incremented repeatedly through the range of interest, and for each wavelength a user defined number of ring-down events is averaged. Typically, 100 ring-down events are average before tuning the diode laser to the next wavelength. The wavelength of the diode laser is slowly incremented by applying a voltage between 0 and 5 V in small increments (depending on the desired resolution) to the laser diode controller unit using the data acquisition card via the Labview program. The precision of the wavemeter is limited to ±0.01 cm^{-1}, however a higher resolution is usually desired. In order to improve the precision of the wavelength measurement, the wavenumber is recorded by the Labview program each 10 increments only and a polynomial fit through all the data points leads to a relation between voltage and wavelength. This relation is used to calculate the precise wavelength for each individual measurement.

2.2.3.5.2.2 Time-resolved measurements

The time-resolved measurement configuration is used to measure the spectrum of labile species formed by laser photolysis. A time resolved kinetic of the labile species is measured for each wavelength. The user defines a number of ring-down events required within a specific time window after the photolysis pulse before going to the next wavelength. This time window depends on the kinetic decay of the species of interest. Typically, 20 to 200 events are asked for within the first tens of milliseconds before the Labview program increments the wavelength and starts the next kinetic measurement. Figure 29 shows a typical time-resolved kinetic of HO_2 signal recorded for one wavelength during the photolysis of H_2O_2. Two different time windows are

used. The first time window in red averages all the ring-down events before the photolysis pulse to get the baseline τ_0. The second time window in green contains the number of required ring-down events. In a next step, the kinetic trace from each wavelength is fitted either to an exponential decay where the ring down time τ is obtained by extrapolation of the fitted curve to t = 0 s (right graph), or to an exponential association and the ring down time τ is obtained by the value of the plateau (left graph).

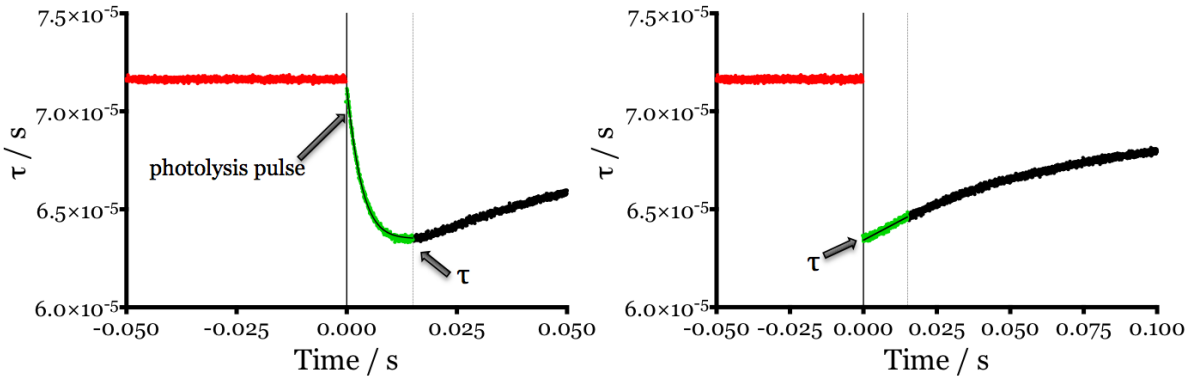

Figure 29: Typical kinetic signal obtained for one wavelength, in red the average of the baseline gives τ_0, and in green the windows with the number of needed events to be fitted to get τ. On the left exponential association fit: $\tau = \tau_{plateau}$, on the right exponential decay: $\tau = \tau_{t=0}$. Usually 20-200 points are accumulated over 15 ms after the photolysis pulse (here 200 points were asked)

Chapter 3 Kinetic and spectroscopic study of OH radicals

3.1 Introduction

Hydroxyl radicals OH dominate the daytime chemistry of the troposphere. The high reactivity of OH radicals with respect to a wide range of chemical species leads to oxidation and chemical conversion of most components that have a sufficient lifetime in the troposphere. OH radicals are key species in oxidation reactions in atmospheric chemistry but also in combustion. Most experiments designed to study OH radicals use laser induced fluorescence (LIF) as detection techniques [50]–[52]. LIF technique is very sensitive but it is only a relative technique. It is not straightforward to convert LIF signals into absolute concentrations because of the competition between fluorescence and quenching that makes the calibration fastidious and uncertain [53]. The use of the LIF technique is sufficient for measuring rate constants of reactions involving OH radicals. Indeed, under pseudo-first order conditions OH decays become exponential and measuring their relative concentration with a better S/N ratio is the best approach [54], [55]. However, with applications such as the determination of the product yields, a quantitative detection of OH radicals is required.

A first example is the determination of product yields is the reaction between peroxy radicals RO_2 and HO_2. It was supposed that this class of reaction is chain terminating and leads to the formation of stable products, when in 2004 a study [56] showed for the first time experimental and theoretical evidences of OH formation in the reaction between acetylperoxy radicals CH_3COO_2 and HO_2. An OH yield of 0.4 was deduced from the measurements of stable products in an atmospheric pressure photoreactor. A second study [57] using direct measurements by LIF determined a yield of 0.5, but in a most recent paper [50] by the same group, the yield was revised to 0.61 still using LIF with independent calibration. The yield of this reaction is still uncertain and a

more direct measurement of the absolute concentration of OH should be very useful to determine such yields in a more precise way.

A second example of product yields is the reaction between peroxy radicals and OH. Only very recently this type of reaction was found to be very fast [58], [59] and to be an important sink for peroxy radicals in remote environment such as the remote Marine Boundary Layers (MBL) [60]. In a modeling study [61], the impact of this reaction on the composition of the atmosphere was shown to be strongly dependent on the branching ratio between possible pathways. Thus, the absolute concentration of OH has to be known in order to convert product concentrations into product yields. The study of four peroxy radicals (CH_3O_2, $C_2H_5O_2$, $C_3H_7O_2$ and $C_4H_9O_2$) with OH and the determination of product yields has been carried out in the frame of this work and is described in a next chapter.

OH radicals have absorption lines in the near IR region between 6600 and 7300 cm^{-1} due to vibrational overtone absorption (v'=2, v"=0) in the electronic ground state $X^2\Pi$ as tabulated in the HITRAN database [62]. Overtone absorption lines are generally rather weak, but because of its very high sensitivity the cavity ring-down spectroscopy can be used to detect these lines even with their small absorption cross-sections [63]. The weak absorption spectra and the determination of absorption cross-sections of many stables [20]–[23] and unstable species [19], [24], [25], [64] have been done in the near infrared region, but the absorption cross-section of OH radicals have not yet been determined and only theoretical values are tabulated in the HITRAN database.

In this chapter, the first determination of the absolute cross-section of an overtone transition of OH radicals in the near-infrared region at 7028.830 cm^{-1} was performed and the impact of pressure broadening on this line was determined. The absorption spectrum and the absorption cross-section of H_2O_2 used as precursors for OH radicals was first determined. Then the two cw-CRDS absorption paths have been used to simultaneously measure OH and HO_2 profiles and deduce the absolute concentrations of OH and H_2O_2 from subsequent modeling of the concentration time profiles. The rate constant of the very fast reaction between OH and HO_2 radicals has also been determined. The results of this work will allow in future experiments the

measurements of absolute OH radical concentrations by cw-CRDS, thus facilitating the determination of branching ratios.

3.2 H_2O_2 spectrum and absorption cross-section determination

Hydrogen peroxide is an important component for atmospheric chemistry. It is present both in the gas and in the aqueous phase. H_2O_2 is one of the final products of oxidants in the gas-phase atmospheric chemistry and its concentration in the gas and liquid phases may give indication on the oxidizing power of the atmosphere. H_2O_2 is linked to the phenomena of acid fog and acid rain [5]. The principal source of upper tropospheric and stratospheric H_2O_2 is the self-reaction of HO_2:

$$HO_2 + HO_2 (+M) \rightarrow H_2O_2 + O_2 \qquad (R\ 24)$$

The reaction (R 24) is a sink for HO_X in the troposphere because of the H_2O_2 scavenging by aerosols and clouds. However, in the stratosphere H_2O_2 acts as a temporary reservoir for HO_X.

H_2O_2 has been used as precursor to generate OH radicals in all the following experiments. Usually, H_2O_2 is introduced into the cell by bubbling carrier gas through a 50% H_2O_2/H_2O solution. But, for generating a water-free stable concentration of H_2O_2, a new method described previously [65], [66] has been put in place. A mixture of roughly half and half H_2O_2-Urea (Aldrich) with SiO_2 (Aldrich) has been thermally stabilized in a water bath to temperature between 35 and 50°C. The increase of temperature leads to a faster decomposition of the H_2O_2-Urea complex and thus to a change in the H_2O_2 concentration in the gas phase. A flow of 200 cm^3 per minute STP of a carrier gas (helium (Air Liquide alphagaz 2) or oxygen (Air Liquide alphagaz 2) or nitrogen (Air Liquid alphagaz 1)) passes over the mixture to carry the H_2O_2 into the photolysis cell. This method is proved to be extremely stable and simple to use as source of H_2O_2. The precursor has to be replaced only every few weeks.

The photolysis of H_2O_2 at 248 nm leads to the formation of two OH radicals through the reaction (R 25):

$$H_2O_2 + h\nu_{248nm} \rightarrow 2\ OH \qquad (R\ 25)$$

The quantum yield of this reaction was previously studied [67], [68] and the IUPAC recommends a quantum yield of $\Phi=2$ for OH for a wavelength higher than $\lambda = 230$ nm [69]. The subsequent reaction of OH radicals with excess H_2O_2 leads to the formation of HO_2 radicals

$$H_2O_2 + OH \rightarrow HO_2 + H_2O \qquad (R\ 26)$$

which can reliably be quantified in our setup by cw-CRDS on the well-characterized absorption line at 6638.21 cm^{-1} [64], [70]–[73]. The rate constant of the reaction (R 26) is well-known [69] with $k(R\ 26) = 1.7\times10^{-12}$ $cm^3\ s^{-1}$, and therefore the concentration of H_2O_2 can be determined by measuring the OH decay under pseudo-first order conditions. However, the subsequent rapid reaction

$$HO_2 + OH \rightarrow O_2 + H_2O \qquad (R\ 27)$$

has to be taken into account, especially when using high photolysis energies. An absorption cross-section of $\sigma_{HO_2,6638.205\ cm^{-1}} = 2.72\times10^{-19}$ cm^2 has been used for all experiments in this work for converting α_{HO_2}, obtained from Equation 22, into absolute HO_2 concentrations. The uncertainty of the absorption cross-section of this HO_2 line is less than 10%.

In the first part, the measurement of the H_2O_2 spectrum will be presented, and then the absolute absorption cross-sections of two selected lines will be retrieved from the time-resolved absolute concentration of HO_2 measured by cw-CRDS and the relative concentration of OH measured by LIF after the photolysis of H_2O_2.

3.2.1 Measurement of the H_2O_2 spectrum

The H_2O_2 spectrum at 13 Torr helium has been recorded in Figure 30 using the cw-CRDS technique in the wavelength range 7023.5 to 7030.5 cm^{-1}. The line strength of the water absorption lines given by the HITRAN database [42] in this range are also represented by red dots.

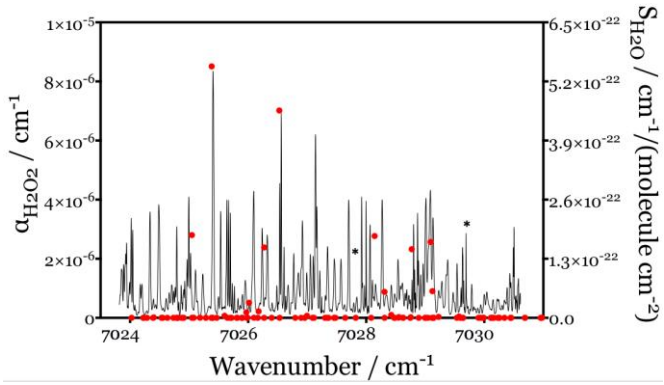

Figure 30: Absorption spectrum of H_2O_2 between 7023.5 and 7030.5 cm^{-1} at 13 Torr helium. The line strength S of the water lines given from the HITRAN database are represented by red dots

The absorption spectrum has been obtained by recording and averaging 100 ring-down events τ at each wavelength before incrementing the wavelength of the laser diode with steps of 0.001 cm^{-1}. The baseline τ_0 has to be measured in the absence of H_2O_2 due to the dense absorption spectrum. Indeed, the H_2O_2 peaks are not isolated, i.e. the absorption is not going back to zero between two peaks. If the ring-down time τ_0 is taken before or after the peak as baseline then it will induce error in the calculation of the absorption coefficient α_{H2O2}. Water peaks with a strong absorption lines are present in the same wavelength range. Therefore, two absorption lines of H_2O_2 isolated from water line and from other H_2O_2 lines have been selected to measure their absorption cross-section. These two peaks are marked with an asterisk on the Figure 30 at 7027.852 and 7029.727 cm^{-1}.

3.2.2 Determination of the H_2O_2 absorption cross-section

The two previously selected H_2O_2 absorptions lines at 7027.852 and 7029.727 cm^{-1} have been scanned in Figure 31 for four initial H_2O_2 concentrations at 50 Torr helium. The concentration of H_2O_2 was varied by changing the temperature of the water bath between 35 and 36.5°C each 0.5°C.

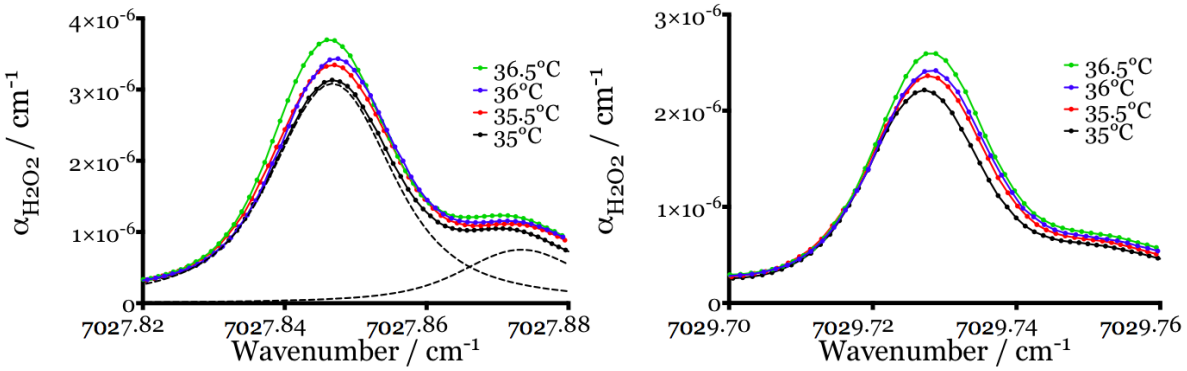

Figure 31: Absorption spectra of two H_2O_2 lines at 7027.852 (left) and 7029.727 cm^{-1} (right) at 50 Torr helium. The full lines: fits to a Voigt profile using the Fityk software. Dashed black lines: example of deconvolution of the two overlapping lines for 35°C around 7027.852 cm^{-1}

The Figure 31 shows that the absorption coefficient of the two H_2O_2 lines increases with the increasing H_2O_2 concentrations. The different spectra were fitted to a Voigt profile using the software Fityk [74] and the absorption coefficients at the maximum of the line were obtained. In order to determine the H_2O_2 concentration, measurements of OH by LIF and of HO_2 by cw-CRDS at 6638.205 cm^{-1} were performed after the photolysis of H_2O_2. OH radicals were measured by LIF only and not by cw-CRDS because due to their low concentration the S/N ratio for OH by cw-CRDS was poor. The OH and HO_2 profiles are shown in Figure 32 with on the left the OH decays for the four H_2O_2 concentrations and on the right the simultaneous formation of HO_2 from the reaction (R 26).

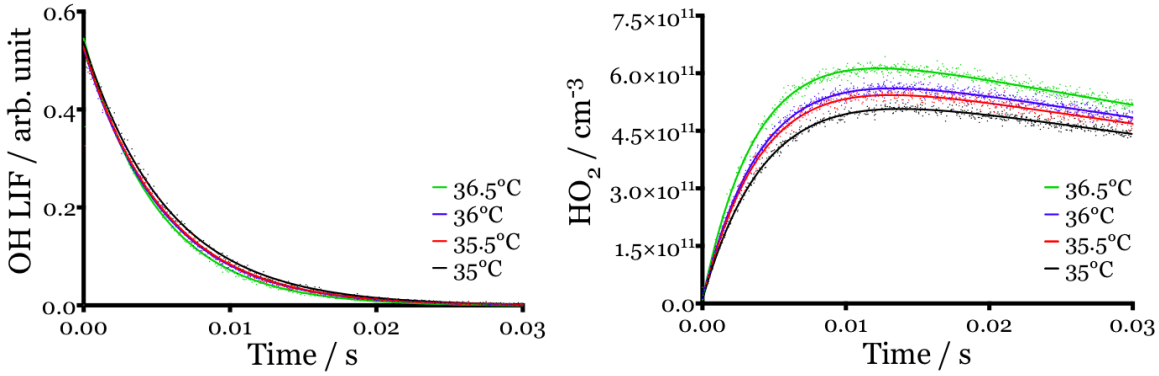

Figure 32: OH (left) and HO_2 (right) time-resolved profiles measured by LIF and cw-CRDS respectively at four different concentration of H_2O_2. The full lines present the concentration profiles obtained from the model

The OH decay rates increase with the increasing H_2O_2 concentration, which is obtained through a two-steps procedure: a first guess of the H_2O_2 concentration was obtained by fitting the decay of OH by assuming pseudo-first order conditions. OH will predominantly react with H_2O_2 to form HO_2 radicals through (R 26). This step leads directly to the H_2O_2 initial concentration. However, as the reaction advances and the HO_2 concentration increases, the OH decay is also influenced by the fast reaction (R 27). The formation rate of HO_2 depends on the decay rate of OH, i.e. on the initial H_2O_2 concentration, and the HO_2 yield depends on the initial OH concentration. The increase in OH initial concentration, i.e. with increasing photolysis energy, results in an increase in the HO_2 concentration but also in a deviation from an exponential decay for the OH due to a faster (R 27). This fit of the HO_2 profile returns the initial OH concentration. The H_2O_2 initial concentration is now changed to re-fit the OH decays with another iteration. The initial concentrations of H_2O_2 and OH have been used as input parameters for modeling the OH and HO_2 profiles on Figure 32 using the simple model given in Table 2:

Table 2: Reaction mechanism used to fit the OH and HO_2 concentration time profiles

No.	Reaction	Rate constant / $cm^3\ s^{-1}$	Reference
(R 25)	$H_2O_2 + h\upsilon_{248nm} \rightarrow 2\ OH$	$\Phi = 2$	[67], [68]
(R 26)	$H_2O_2 + OH \rightarrow HO_2 + H_2O$	1.7×10^{-12}	[69]
(R 27)	$HO_2 + OH \rightarrow O_2 + H_2O$	1.02×10^{-10} (discussed below)	[69], [75]
(R 28)	$OH + OH\ (+M) \rightarrow H_2O_2$	1.48×10^{-13}	[69]
(R 24)	$HO_2 + HO_2\ (+M) \rightarrow H_2O_2 + O_2$	1.6×10^{-12}	[69]
(R 29)	$HO_2 \rightarrow$ diffusion	$8\ s^{-1}$	This work
(R 30)	$OH \rightarrow$ diffusion	$13\ s^{-1}$	This work

OH and HO_2 radicals are also lost due to diffusion out of the photolysis volume. This diffusion is taken into account in the mechanism as a unimolecular reaction. The diffusion represents only a minor contribution for OH radicals. For HO_2 radicals the diffusion can be obtained experimentally by fitting the decay at long reaction time and was for all the experiments $k_{diff,HO2} = 8\ s^{-1}$. However, it is not possible to fit OH at long reaction time because the decay is rapidly going to zero and it is not straightforward to separate the loss through reaction from the loss through diffusion. Therefore the OH diffusion was set to be proportional from the HO_2 diffusion by calculating the respective diffusion coefficients $D_{OH\text{-}He} = 662\pm33$ Torr $cm^3\ s^{-1}$ and $D_{HO2\text{-}He} = 430\pm30$ Torr $cm^3\ s^{-1}$, leading to $k_{diff,OH} = 13\ s^{-1}$ [76]. However, during this experiment the influence of the diffusion on the OH decay is very minor. The influence of the self reaction of OH has also been tested and found to be negligible due to the low concentration of OH, with k(R 28) being nearly 100 times slower than k(R 27). The rate constant of (R 27) has been measured several times, and the recommended value is $k(R\ 27) = 1.1\times10^{-10}\ cm^3\ s^{-1}$ [69] with an uncertainty of ±25%. While modeling the OH and HO_2 profiles, it turned out that the concentration of OH and HO_2 and the quality of the fits were very sensitive to the value of k(R 27). The value of this rate constant used in the mechanism was deduced from different series of experiments performed in parallel from this work, which will be described in the following part.

The measurement of the absolute cross-section of H_2O_2 on the two selected lines is now determined by plotting the absorption coefficient α_{H2O2} obtained from the scans of H_2O_2 as a function of the concentration of H_2O_2 obtained from the fit of OH and HO_2 profiles as shown in Figure 33.

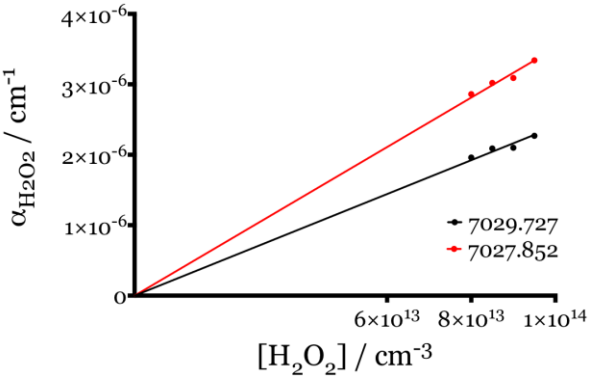

Figure 33: Absorption coefficient at the maximum of the two H_2O_2 absorption lines as a function of the H_2O_2 concentration

Using the slopes of the plots forced through zero, the absorption cross-sections of the lines at 7027.852 and 7029.727 cm^{-1} at 50 Torr helium were calculated to be $(3.52\pm0.53)\times10^{-20}$ and $(2.40\pm0.36)\times10^{-20}$ cm^2 respectively. The errors represent the 95% confidence level between the experimental data and the fit and an additional error due to the absorption cross-section of HO_2 radicals estimated to be less than 10%.

3.2.3 Direct measurement of the rate constant of the OH+HO_2 reaction

As described previously, the rate constant of the reaction (R 27) has a strong impact on the profiles of OH and HO_2 during the photolysis of H_2O_2. Using this setup, the rate constant k(R 27) can be determined in a direct way. OH and HO_2 radicals have been generated simultaneously by photolysing at 248 nm at 50 Torr helium a mixture

of H_2O_2, $(COCl)_2$, CH_3OH and O_2. The photolysis of $(COCl)_2$ in the presence of CH_3OH and O_2 was used to generate HO_2 radicals through the following sequence:

$$(COCl)_2 + h\upsilon_{248nm} \rightarrow 2\ Cl + 2\ CO \qquad (R\ 31)$$

$$Cl + CH_3OH \rightarrow CH_2OH + HCl \qquad (R\ 32)$$

$$CH_2OH + O_2 \rightarrow HO_2 + CH_2O \qquad (R\ 33)$$

Oxalyl chloride $(COCl)_2$ was used as precursor for chlorine because this compound is known to be an efficient chlorine precursor by photo-dissociation at 248 nm [77]. The concentration of each of the reactants during the measurement was: $O_2 = 2\times10^{17}$ cm^{-3}, $CH_3OH=6\times10^{14}$ cm^{-3} and $(COCl)_2$ in the range $3\text{-}5\times10^{14}$ cm^{-3}. The radiation energy of photolysis was estimated to be at 72 mJ/pulse leading to HO_2 concentrations around $0.7\text{-}1.1\times10^{13}$ cm^{-3}. The different concentrations were adapted such that the HO_2 concentration was in large excess over OH radicals and thus the pseudo-first order assumption can be applied. $(COCl)_2$ was prepared as diluted mixture in helium inside a glass balloon. A small flow of this mixture (typically 10 cm^3 per minute STP) was added to the main flow through a calibrated flowmeter. Liquid methanol was thermostated in a water bath at 10°C, and a small flow of helium passed through the bottle and was also controlled by a calibrated flowmeter.

As for the determination of H_2O_2 absorption cross-section, OH radicals were detected by LIF, and HO_2 by cw-CRDS. The left graph on Figure 34 shows a typical result with the OH concentration decaying rapidly, while in the same time range the HO_2 concentration is decaying slowly. The HO_2 decay is roughly in equal fractions due to the diffusion and to the self-reaction. On the right graph of Figure 34, the pseudo-first order rate constants obtained from the fit of the OH decays are plotted as a function of the HO_2 concentrations. In order to take into account the decay of HO_2 within the time window of the OH decay, the HO_2 concentration present at time $t([OH]_0/2)$ (corresponding to a loss of 2-4% of the initial HO_2 concentration) has been used as y-axis. Using this method, a rate constant of $k(R\ 27) = (1.02\pm0.06)\times10^{-10}$ cm^3 s^{-1} is obtained with the error being statistical only. This value is slightly lower than the

current recommended value by IUPAC at k(R 27) = 1.1×10^{-10} cm^3 s^{-1} [69], but still in very good agreement.

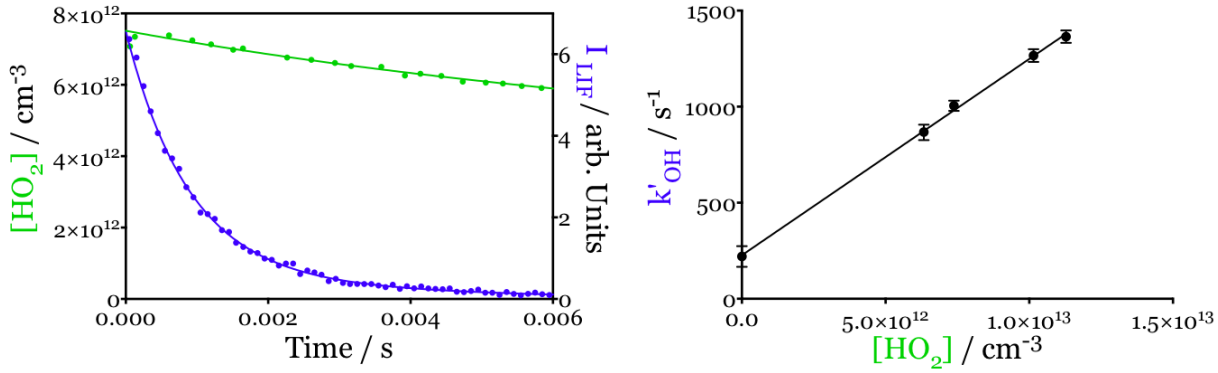

Figure 34: Decay of OH radicals (blue) in presence of an excess of HO_2 radicals (green) (left graph). Pseudo-first order decay rates as a function of the HO_2 concentration (right graph)

3.3 OH spectrum and absorption cross-section determination

In the first part the measurement of the absorption spectrum will be presented, and in the second part the different experimental approaches that have allowed retrieving the absolute OH concentration, and with it the absolute absorption cross-section, will be described.

3.3.1 Measurement of the OH spectrum

According to the HITRAN database [62], only two absorption lines of OH are accessible within the wavelength range of the laser diode (6996 to 7032 cm^{-1}). The overtone absorption spectrum of OH radicals (v' = 2, v" = 0) has been measured between 7028.7 and 7028.9 cm^{-1}, where the ground state $X^2\Pi1/2$ rotational Λ-doublet transitions R(0.5)e and R(0.5)f are tabulated at 7028.749 and at 7028.831 cm^{-1} respectively. The line strengths of these doublet peaks are at around S = 4.48×10^{-21}

cm. These line strengths are roughly a factor of 2 smaller than the line strengths of the nearby and lowest fine structure of the ground state transitions $X^2\Pi 3/2$ at 7049.118 (R(2.5)e) and 7049.234 cm^{-1} (R(2.5)f).

The absorption spectrum of the OH radicals has been obtained by measuring kinetic decays for different wavelength between 7028.7 and 7028.9 cm^{-1}. In this spectral range, 200 kinetic decays were recorded giving a resolution of 0.001 cm^{-1}.

The absorption spectrum is shown in Figure 35 by plotting the ring-down time τ_o (black dots) before the photolysis pulse, the ring-down time $\tau_{t=o}$ (red dots) obtained from an extrapolation to t = 0 s after the photolysis pulse, and the absorption coefficient α_{OH} (blue dots) as a function of the wavenumber from applying the Equation 22 to each pair of ring-down times. The wavenumber plotted in Figure 35 has been obtained as described in the previous chapter: the wavenumber of the laser diode is measured using the wavemeter every 10 increments of the wavelength. The wavenumber for each data point is then extrapolated from a polynomial fit. The peak wavenumbers obtained with this method are 7028.743 and 7028.831 cm^{-1} and are in excellent agreement with the wavenumbers tabulated in HITRAN (7028.749 and 7028.831 cm^{-1}).

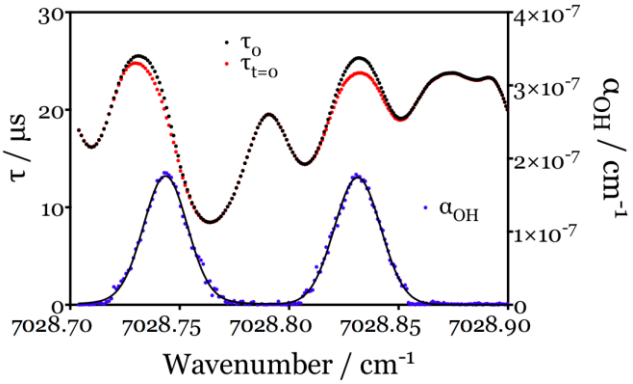

Figure 35: Ring-down time τ_o (black dots) and $\tau_{t=o}$ (red dots), such as obtained from Figure 29 type of signals, and the absorption coefficient α (blue dots) as a function of the wavenumber. The full lines represent a fit of the lines to a Voigt profile

The baseline τ_0 is not flat and its structure is due to the absorption of the precursor H_2O_2. This absorption can be a problem if too much H_2O_2 is photolysed. Indeed the value of τ_0 would increase after the photolysis pulse due to a lower concentration of H_2O_2. However, this has no impact on the measurements of the OH absorption spectrum. Only 1-2% of the precursor is photolysed in this experiment and therefore the same absorption, within the experiment uncertainty, due to H_2O_2 is seen for both τ_0 and τ. The intensity of the two OH absorption lines is very similar such as expected from doublet peaks and a fit to a Voigt profile with Fityk software leads to very similar relative line strengths for both peaks. The relative line strengths can be converted into absolute line strengths by using the peak absorption cross-section $\sigma_{OH} = 1.54\times10^{-19}$ cm² measured for the peak at 7028.831 cm^{-1} as described in the next paragraph. The obtained line strength $S = 4.07\times10^{-21}$ cm is in very good agreement with the line strength predicted by HITRAN with $S = 4.48\times10^{-21}$ cm.

The OH peak centered at 7028.831 cm^{-1} has been chosen to carry out all following kinetic measurements because this peak is perfectly located in a minimum of the H_2O_2 absorption structure. This position is advantageous for several reasons: (i) the value of the ring-down time is higher, leading to a better sensitivity, (ii) a small change in the wavelength of the laser diode or in the concentration of H_2O_2 during the kinetic measurements does not lead to a large change in the ring-down time as it would be the case for the peak at 7028.748 cm^{-1}, and (iii) for practical reasons it is simpler to precisely adjust the wavelength of the laser diode beyond the precision of the wavemeter and without generating OH radicals by fine tuning the current applied to the laser diode in order to obtain the longest τ_0. For these reasons, the absorption cross-section of the OH line at 7028.831 cm^{-1} was measured.

3.3.2 Determination of the OH absorption cross-section

In order to measure the absorption cross-section of the OH line at 7028.831 cm^{-1} and to verify the value of the rate constant k(R 27) of the cross-reaction OH +

HO_2 determined above, several series of experiments were carried out by either varying the H_2O_2 concentration with stable photolysis energy or stable H_2O_2 and varying the photolysis energy.

3.3.2.1 Data set with varying [H_2O_2] and stable photolysis energy

Two sets (out of a series of six) of simultaneous measurements of OH and HO_2 by cw-CRDS for different H_2O_2 concentrations using identical photolysis energy of 72 mJ cm^{-2} are presented in Figure 36. It can be seen that the OH decay and the HO_2 rise times are faster for the higher H_2O_2 concentration (in red), just as expected.

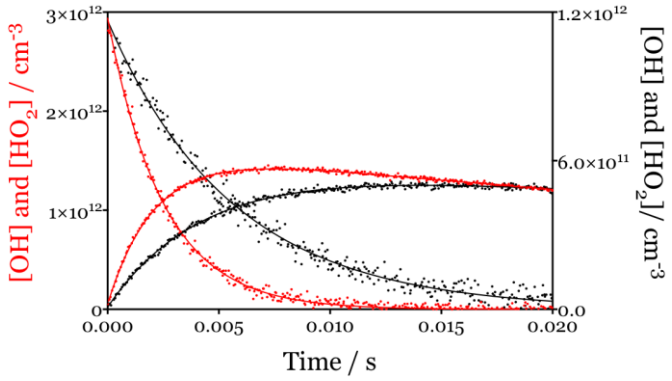

Figure 36: OH decaying and HO_2 rising concentration time profiles for two different initial [H_2O_2] (in red high, in black low) and using the same photolysis energy of 72 mJ cm^{-2}. The full lines represent the result from the model in Table 2 to retrieve the [H_2O_2]: left y-axis (red) 1.8×10^{14} and right y-axis (black) 0.7×10^{14} cm^{-3}

When fitting such signals using the model in Table 2 as described previously, there are initially two adjustable parameters: the H_2O_2 and OH initial concentrations, finally leading to the searched OH absorption cross-section σ_{OH} needed to convert the absorption coefficient into absolute concentration. Both parameters are not independent in these experiments. An increase in the initial H_2O_2 concentration will result in a faster OH decay, thus strongly limiting the range of adjustability of this

parameter. Due to an increase of H_2O_2 concentration, more OH radicals are converted into HO_2 because (R 26) becomes faster and (R 27) less efficient. Therefore, to reproduce the HO_2 concentration time profile, the initial OH concentration needs to be decreased in the model by increasing the absorption cross-section σ_{OH}, resulting in the conversion of the experimental α_{OH} into OH concentration through Equation 22. The experiment with the highest energy in Figure 36 has been modeled in Figure 37 using three different initial OH concentrations, so three different absorption cross-sections σ_{OH}. The value $\sigma_{OH} = 1.54\times10^{-19}$ cm², which fits the best all six experimental conditions, was varied by ±20% ($\pm0.3\times10^{-19}$ cm²). In order to reproduce correctly the corresponding HO_2 profile, the initial concentration of H_2O_2 needed to be adapted: for the lowest σ_{OH} (and hence the highest [OH] in red), the concentration of H_2O_2 is decreased to favor (R 27) leading to a decrease in the OH to HO_2 conversion. For the highest σ_{OH} (and hence the lowest [OH] in blue), the concentration of H_2O_2 is increased to favor (R 26) leading to an increase in the OH to HO_2 conversion. Doing so, the HO_2 concentration time profile can be correctly reproduced with all three σ_{OH} and H_2O_2 pairs ($[H_2O_2] = 1.25\times10^{14}$, 1.47×10^{14} and 1.95×10^{14} cm^{-3} for the red, black and blue traces, respectively). The OH decays however are only well reproduced for the black trace. The change in the H_2O_2 concentration necessary to reproduce the HO_2 profile is too big to be in agreement with the OH decay.

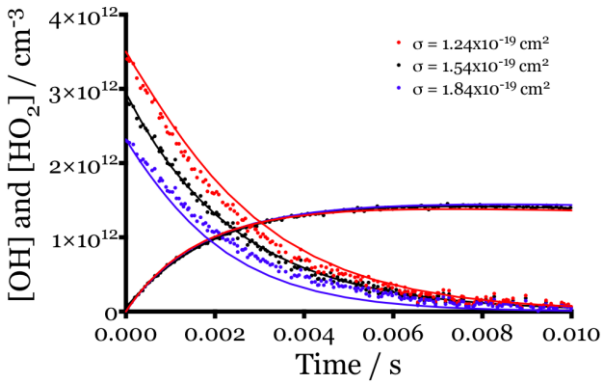

Figure 37: Same experiment than high $[H_2O_2]$ on Figure 36. Influence of σ_{OH} onto the initial $[H_2O_2]$ needed to reproduce the $[HO_2]$ time profile. The full lines represent the result from the model in Table 2 to retrieve the $[H_2O_2]$: 1.5×10^{14}, 1.8×10^{14} and 2.3×10^{14} cm^{-3} for the red, black and blue OH and HO_2 profiles, respectively

From the series of six different H_2O_2 concentrations, it was seen that the ratio OH/H_2O_2 was identical $((1.59\pm0.05)\times10^{-2})$ for all six experiments, as expected when using the same photolysis energy. A photolysis energy of 72 mJ cm^{-2} can be calculated, resulting in the photolysis of 0.8% of the initial H_2O_2. Only the value of σ_{OH} = $(1.54\pm0.1)\times10^{-19}$ cm^2 allowed to model all six OH and HO_2 profiles. The fraction of OH radicals converted into HO_2 radicals (0.47±0.03) does not change much in this series as seen on the Figure 36.

The other parameter that influences the OH and HO_2 profiles is the rate constant of (R 27). The experiment with the highest energy in Figure 36 has been modeled in Figure 38 using the rate constant k(R 27) determined above by direct experiments, which was varied by only ±10%. The OH absorption time profiles have been converted into concentration by using σ_{OH} = 1.54×10^{-19} cm^2. It can be seen that the OH decays are correctly reproduced for all three rate constant while the HO_2 maximum level is too high or too low in the case of too high or too low rate constant respectively. This result is in perfect agreement with the direct measurement of k(R 27) determined above.

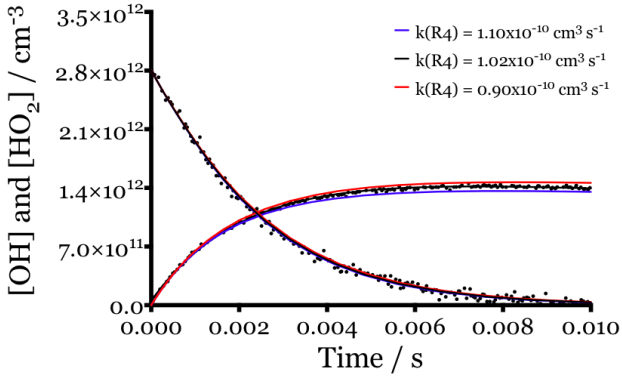

Figure 38: Same experiment than high $[H_2O_2]$ on Figure 36. Influence of k(R 27) on the modeling OH and HO_2 decays

3.3.2.2 Data set with stable [H_2O_2] and varying photolysis energy

Another series of six experiments has been carried out with a stable concentration of H_2O_2 and varying the photolysis energy by more than a factor of 10. The energy has been varied by changing the high voltage applied to the excimer discharge for the higher range of energy. For lower range, the energy has been varied by putting various layers of Teflon film into the excimer photolysis beam before the photolysis cell. The OH profiles have been obtained by LIF for all the conditions but the cw-CRDS has been employed only for the three highest photolysis energy when it was sensitive enough to give a good S/N ratio. This series of experiments has been fitted simultaneously in order to obtain a consistent set of parameters for all six conditions. The initial H_2O_2 concentration was first deduced from the lowest energy because (R 27) plays only a minor role and the OH decay is mostly due to (R 26). The concentration of H_2O_2 was found to be 1.85×10^{14} cm^2 and was kept constant for all six energy conditions.

The two extreme conditions of photolysis energy of 6 and 72 mJ cm^{-2} are illustrated in Figure 39. For the lowest energy (black symbols) the relative OH signal obtained by LIF is represented in absolute concentration using the OH such as finally obtained from the model. It can be very well seen that in this case the OH to HO_2 conversion decreases significantly in this series from 0.78 at the lowest energy to 0.47 at the highest energy. This is due to the fact that with the increasing energy (R 27) becomes more and more important while (R 26) stays constant due to the constant H_2O_2 concentration. The HO_2 profiles are very sensitive to the rate constant k(R 27), and in this series a consistent result was also obtained for all photolysis energy with k(R 27) = 1.02×10^{-10} cm^3 s^{-1}.

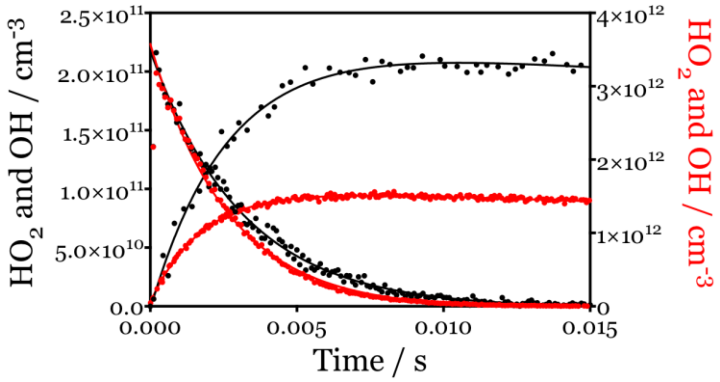

Figure 39: Two experiments (out of the six) with the same $[H_2O_2]$ but different photolysis energy: in left y-axis (black) 6 mJ cm^{-2} and in right y-axis (red) 72 mJ cm^{-2}. The full lines represent the result from the model in Table 2

OH profiles have been obtained by cw-CRDS for the three highest photolysis energies. The value of the absorption cross-section $\sigma_{OH} = 1.54\times10^{-19}$ cm^2 has been confirmed to be in agreement with the experiments with changing H_2O_2 concentrations.

It should finally be noted that the values for σ_{OH} and k(R 27) depend directly on the HO_2 concentration time profiles and with this on the absorption cross-section σ_{HO2} used to convert α_{HO2} into absolute concentrations. Sensitivity tests have been carried out by varying σ_{HO2} by ±10%, but this small change did not allow anymore to correctly reproduce the shape of the HO_2 signals. This shape is most sensitive to the two retrieved parameters, σ_{OH} and k(R 27), during experiments with the highest initial radical concentrations (up to 10^{13} cm^{-3}). The cw-CRDS set-up is very sensitive to the HO_2 radicals (S/N = 1 for $[HO_2] \approx 4\times10^{10}$ cm^{-3} in single shot but much better after averaging over several photolysis pulses). Therefore HO_2 concentration time profiles with very good S/N are obtained in all series with HO_2 concentration between 10^{11} and 10^{12} cm^{-3}.

3.3.3 Pressure broadening of the OH absorption cross-sections with different gas buffer

The profile of a line depicts the probability of interaction of a photon with a molecule as a function of the wavenumber. The shape of the absorption line spreads over a spectral width. The expression of the line profile depends on the nature of the cause of the broadening: (i) Natural broadening: originates from the uncertainty principle of Heisenberg applied from the initial and final energies of the transition, resulting in an uncertainty on the wavelength of the transition. The shape is represented by a Lorentzian function whose half-width at half-maximum (HWHM) is called the natural width of the transition. The natural broadening in the infrared region is generally negligible compared to other causes of broadening. (ii) Collisional/pressure broadening: collisions between the absorbing species and other species of the medium disrupt the initial and final energy states of the transition resulting to a line broadening. The shape of the profile is also Lorentzian. The HWHM is proportional to the pressure and depends on the collisional partners, the temperature and the considered transition. (iii) Doppler broadening: inhomogeneous broadening of the linewidth of transitions. A species having a velocity absorbs and emits at a wavenumber different of the wavenumber without any movements due to a light frequency shift when the source is moving toward, or away from the observer. The broadening depends only on the frequency of the spectral line, the mass of the emitting particles, and their temperature. The linewidth resulting from the Doppler effect is a Gaussian profile. The Doppler and the collisional broadenings are typically much larger than the natural linewidth.

Understanding the pressure broadening and the resulting lineshapes is important for the determination of the absorption cross-sections, and thus for a correct determination of the concentration, of selected spectral lines. Collisional and Doppler broadened spectral lines are approximated by a Voigt line profile. The Voigt profile is defined as a convolution between the Gaussian function and the Lorentzian function, caused by Doppler and pressure broadening respectively. At low pressure, the line width has a Gaussian shape due to the Doppler broadening. With the increasing

pressure, the line width increases and the shape changes from pure Gaussian to a complex line shape approximated by a Voigt line shape. The Gaussian contribution is characterized by the width parameter g while the Lorentzian contribution is characterized by the width parameter γ. Therefore the Voigt function can be expressed as in Equation 23:

$$\mathrm{V}(\mathrm{g},\gamma,\nu) = \int_{-\infty}^{\infty} G(g,x).L(\gamma,(\nu-\mathrm{x}))\,\mathrm{dx} \qquad \text{Equation 23}$$

The Gaussian and Lorentzian functions are conveniently defined as:

$$\mathrm{G}(\mathrm{g},\mathrm{x}) = \frac{1}{g\sqrt{\pi}}\, e^{-\left(\frac{x}{g}\right)^2} \; and \; L(\gamma,\mathrm{x}) = \frac{\gamma}{\pi}\frac{1}{x^2+\gamma^2} \qquad \text{Equation 24}$$

The Lorentzian Full-Width at Half-Maximum (L-FWHM) is related to the γ term by the relation:

$$\mathrm{L}-\mathrm{FWHM} = 2\gamma \qquad \text{Equation 25}$$

while the Gaussian Full-Width at Half-Maximum (G-FWHM) is related to g by the relation:

$$\mathrm{G}-\mathrm{FWHM} = 2\sqrt{\ln(2)\,g} \qquad \text{Equation 26}$$

The Doppler broadening G-FWHM can be derived from the Maxwell-Boltzman distribution of the velocities of mass M, and at a temperature T:

$$\mathrm{G}-\mathrm{FWHM} = \nu_0\frac{2}{c}\sqrt{\frac{2\ln(2)RT}{M}} = 7.1623\times10^{-7}\,\nu_0\sqrt{\frac{T}{M}} \qquad \text{Equation 27}$$

With the universal gas constant R and the speed of light c

The Fityk software is used during this work to fit the experimental line shape. Four fitting parameters are used in the built-in Voigt function of the software: height, center, gwidth and shape. The first two parameters represent the height and the

center frequency of the peak. The gwidth and shape parameters are defined as follows:

$$\text{gwidth} = g \quad \text{and} \quad \text{shape} = \frac{\gamma}{g} \qquad \text{Equation 28}$$

Combining the Equation 26 and Equation 27, the gwidth parameter corresponding to the Doppler width at a given temperature can be written as:

$$\text{gwidth} = \frac{G-FWHM}{2\sqrt{\ln(2)}} \approx 4.3014 \times 10^{-7}\, \nu_0 \sqrt{\frac{T}{M}} \qquad \text{Equation 29}$$

By nonlinear least squares fit using the Fityk software, the experimental line profile can be de-convoluted into the Gaussian and Lorentzian components. The Gaussian component reflects the Doppler broadened line shape at a given temperature, while the Lorentzian component is a linear function of the pressure. For the room temperature experiments, the Gaussian component was constrained to the room temperature Doppler width calculated with the Equation 29. In the present analysis, the line offset could not be determined.

In order to measure the variation of spectral width as a function of the pressure, the absorption spectrum of OH at 7028.830 cm^{-1} was scanned in several conditions carried out using three buffer gases helium, nitrogen or oxygen at five different pressures between around 10 and 90 Torr as shown in Figure 40, where all spectra have been normalized to the fitted surface area. The concentrations of the gas buffer were between 4×10^{17} to 3×10^{18} cm^3. All the scans have been fitted using the Fityk software with Voigt profile.

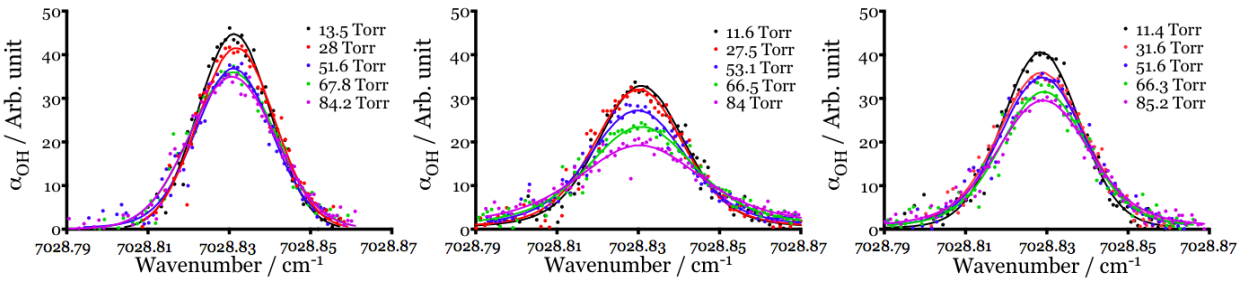

Figure 40: Absorption spectrum normalized to the fitted surface area of OH around 7028.830 cm^{-1} for different pressures between 10 and 90 Torr of He (left), N_2 (center) or O_2 (right). Dots are experimental values, lines represent the fits to Voigt profiles using Fityk software by fixing the Doppler width (gwidth) to its theoretical value

The Figure 41 shows the Lorentzian-half width at half maximum as a function of the pressure for the three broadening gases. The intercept of the linear regression, leading to the broadening coefficient, has been forced through zero.

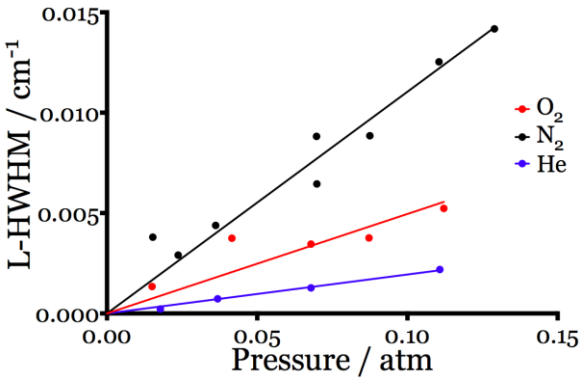

Figure 41: Lorentzian Half-Width at Half-Maximum (L-HWHM) as a function of the pressure for the three buffer gases (helium, nitrogen and oxygen). Regression lines have been forced through zero at zero pressure

The obtained broadening coefficients are listed in Table 3 for the three buffer gases. No measurement of the broadening coefficient is found in the current literature for this OH line in the near-infrared region but can be compared to the broadening coefficient obtained for the OH line at 118.455 cm^{-1} [50] with γ_{coll}^{He} = 0.018 cm^{-1} atm^{-1}, γ_{coll}^{O2} = 0.049 cm^{-1} atm^{-1} and γ_{coll}^{N2} = 0.091 cm^{-1} atm^{-1}. These values are consistent with the values for the line at 7028.830 cm^{-1} after an increase of 10%, but also consistent

with the value γ_{coll}^{air} = 0.95 cm^{-1} tabulated in HITRAN and the value calculated from the determined broadening coefficients 0.8 × γ_{coll}^{N2} + 0.2 × γ_{coll}^{O2} = γ_{coll}^{air} = 0.098 cm^{-1}.

Table 3: Pressure broadening coefficient measured for the 7028.830 cm^{-1} line of OH using different broadening gas

Broadening gas	γ_{coll} / cm^{-1} atm^{-1}
He	0.019
O_2	0.049
N_2	0.110

3.4 Conclusion

The absorption time profiles of OH and HO_2 following the 248 nm photolysis of H_2O_2 have been measured on the two cw-CRDS absorption paths. Taking advantage of the well-known absorption cross-sections of HO_2 radicals at 6638.21 cm^{-1}, allowing converting absorption coefficient to absolute HO_2 concentrations time profile, three parameters have been retrieved from consistent modeling of OH and HO_2 under a large range of conditions: (i) The absorption cross-section of two H_2O_2 lines have been determined, (ii) the rate constant of the reaction of OH and HO_2 profiles (R 27) proved to be very sensitive on the HO_2 profiles and was determined with k(R 27) = (1.02±0.06)×10^{-10} cm^3 s^{-1}. Using this rate constant it was possible to fit all experimental conditions but it was also confirmed in direct measurements by following the OH decays in the presence of a varying excess of HO_2. This rate constant is in good agreement with current recommendations by IUPAC at 1.1×10^{-10} cm^3 s^{-1}. (iii) The spectrum of OH radicals has been measured in the range of 7028.7 to 7028.9 cm^{-1} using several broadening gas (helium, oxygen and nitrogen). The overtone transition (v'=2, v''=0) in the ground state $X^2\Pi 1/2$ of OH radicals is observed as rotational Λ-doublet R(0.5)e at 7028.748 and R(0.5)f at 7028.831 cm^{-1}. The peak absorption cross-section at 7028.831 cm^{-1} has been determined at 50 Torr helium to

be σ_{OH} = (1.54±0.1) × 10^{-19} cm^2. Fitting the line to a Voigt profile resulted in a line strength S = 4.07×10^{-21} cm, in good agreement with the line strength tabulated in HITRAN database (S = 4.48×10^{-21} cm). The broadening coefficient of the OH line at 7028.831 cm^{-1} has been determined between 10 and 90 Torr in helium, oxygen and nitrogen with γ_{coll}^{He} = 0.019 cm^{-1} atm^{-1}, γ_{coll}^{O2} = 0.049 cm^{-1} atm^{-1} and γ_{coll}^{N2} = 0.110 cm^{-1} atm^{-1}. These values are in very good agreement with the literature for other OH absorption lines and with the γ_{coll}^{air} tabulated in HITRAN database. Knowledge of this absorption cross-section and these broadening coefficients will allow easy quantification of OH radicals in future experiments with the goal of studying branching ratios of atmospherically important reactions.

Chapter 4 Study of the DO_2 and HO_2 radicals and CH_3OH and CD_3OD molecules: measurement of the spectra and absorption cross-sections of selected peaks

4.1 Introduction

The hydroperoxy radical HO_2 is a key species in many chemical processes both in the gas phase and in the heterogeneous phase. They are involved in the oxidation of hydrocarbons in low temperature combustion but play also a central role in atmospheric chemistry. Their responsibility in cycles of destruction of stratospheric ozone as well as its ability to oxidize the main VOCs of the troposphere through its coupling with OH can be mentioned. Understanding the mechanisms involving HO_2 requires the development of tools capable of detecting and quantifying this radical in its environment. An example of mechanism can be the reaction of methylperoxy radicals CH_3O_2 with HO_2, which plays a key role in the oxidation of methane in the earth's atmosphere. At first it was thought that this reaction proceeded through one channel, via hydrogen abstraction mechanism, leading to CH_3OOH and O_2 as products. Direct experimental studies of the branching ratio showed that this reaction channel dominates at room temperature but also provided direct evidence for small contribution from another channel leading to O_2, HCHO and H_2O as products [79], [80]. This study has been possible thanks to the use of partially deuterated species. The DO_2 radical does not play any role in atmospheric chemistry, but a selective detection is nevertheless highly desired in laboratory studies for carrying out mechanistic studies, especially involving hydrogen abstraction mechanisms.

Many laboratory studies on peroxy radicals have been carried out using UV-absorption spectroscopy, which is a sensitive but highly unselective method due to the

very broad absorption features of these species [81]. On the contrary, the infrared region offers a very selective detection for both HO_2 [82] and DO_2 [83] radicals through diode laser absorption spectroscopy of vibrational transitions. Exploiting absorption spectroscopy with the aim of dosing species requires knowing their absorption spectrum in the considered spectral range. The absorption spectra of HO_2 and DO_2 in the near infrared region consist of vibrational overtone transitions as well as low-lying electronic transitions, typical for peroxides [84]. The overtone transition of HO_2 near 6638 cm^{-1} has been recorded in previous studies [64], [70], [72], [85], [86] and the well-described line at 6638.205 cm^{-1} has already been used for various laboratory studies [68], [87], [88]. Using FTIR emission spectroscopy, the low-lying rovibronic $\tilde{A} \rightarrow \tilde{X}$ 000-000 band has been recorded for both HO_2 [89] and DO_2 [90]. HO_2 and DO_2 are bent triatomic radicals that can be described as a light asymmetric top rotor with C_s symmetry, with irreducible representations A' and A". These two radicals have an unpaired electron, thus a total electron spin S = ½. They exhibit a doublet electronic structure in which the spin S couples to the rotational quantum number N to give the total angular momentum of J = N±½, usually called F_1 and F_2. Accurate spectroscopic data obtained previously [89], [90] are used in the frame of this work for simulating HO_2 and DO_2 spectra. Some lines of this transition have been characterized for HO_2 [91], [92] and DO_2 [93] in the near-infrared wavelength region and have been used for studying the reactivity of HO_2 [92], [94].

The setup of cw-CRDS coupled with laser photolysis is used to determine the absorption cross-section of HO_2 and DO_2 radicals in the near infrared region between 6940 and 7080 cm^{-1}. This wavelength range was accessible thanks to the loan of diode laser module from the Gerätezentrum "Cologne Center for Terahertz Spectroscopy". In this range it is possible to detect the three radical intermediates HO_2, DO_2 and OH (with the measurement of the OH absorption cross-section at 7028.831 cm^{-1} described in the previous chapter) with the same DFB laser diode and mirror set, which can be useful for future applications of the cw-CRDS technique. However, gaps in the spectroscopic database of these radicals in this region required first studying the absorption spectra of DO_2 and HO_2 radical and CH_3OH, CD_3OD molecules used as precursors. This work concentrates on the transition from the electronic ground state

$^2A''$ into the $^2A'$ excited state ($^2A'' \leftarrow {}^2A'$), and in particular on its vibrational 000–000 band. Absolute absorption cross-sections of HO_2 and DO_2 will allow selective quantification of both radicals while tuning the laser source within a small wavelength range.

4.2 Experimental conditions and measurement of CH_3OH and CD_3OD spectra

A continuous laser source (Agilent mainframe 8164B with laser module 81600B) has been used on one cw-CRDS path for measuring the absorption spectra of the different species while a DFB laser emitting around 6638 cm^{-1} was used on the other cw-CRDS path for calibration of the radical concentration. Depending on the mirror reflectivity in the two wavelength ranges, typical ring-down times for the empty cavity τ_0 were 80 µs around 6638 cm^{-1} and between 20 to 40 µs in the range 6957 to 7077 cm^{-1}. For obtaining the absorption spectra of HO_2 and DO_2, one time resolved kinetic trace has been registered for each wavelength for each radical. In order to have kinetic decays with comparable quality for all traces, 70 ring-down events occurring within 30 ms after the photolysis pulse were acquired before incrementing to the next wavelength with steps of 0.005 cm^{-1}. This was typically achieved after 3 to 5 laser photolysis pulses with a delay between two photolysis shots of three seconds. The ring-down time τ_0 was calculated by averaging the ring-down events before the photolysis pulse. The ring-down time τ was obtained by fitting the kinetics as described in Figure 29 and was converted to absorbance using Equation 22. This way, a total number of 28000 kinetic traces have been recorded for each radical during the three to four days of continuous measurements necessary to acquire one spectrum.

The absorption spectra have been recorded at a total pressure of 20 Torr. The main flow consisted of 40 cm^3 min^{-1} helium and 40 cm^3 min^{-1} O_2 (both Air liquid alphagaz 2). A second flow of helium was flown through a glass bottle containing liquid CH_3OH or CD_3OD kept at 12°C in a water bath. The pressure in the bottle was stabilized at

800 Torr. A flow of 0.5 cm^3 min^{-1} of this CH_3OH and helium mixture (0.8 cm^3 min^{-1} for CD_3OD) was added to the main flow leading to an absolute concentration of $[CH_3OH/CD_3OD] = 4.6\times10^{14}/7.2\times10^{14}$ cm^{-3} in the photolysis cell. $(COCl)_2$ was used as precursor for Cl atoms. It was prepared as a diluted mixture at 3.5% in helium. A flow of 0.5 cm^3 min^{-1} of this mixture was also added to the main flow. The absolute concentrations of $(COCl)_2$ during the measurement of the spectra were 1.35×10^{14} cm^{-3} for the measurement of HO_2 and 2.1×10^{14} cm^{-3} for the measurement of DO_2. The concentration of O_2 was 3.3×10^{17} cm^{-3} and 2.6×10^{17} cm^{-3} for the measurement of HO_2 and DO_2, respectively. A photolysis energy of 70 mJ cm^{-2} was calculated by measuring HO_2 and OH signals during the photolysis of H_2O_2 and thus retrieving the H_2O_2 and OH initial concentrations (whose ratio depends on the photolysis energy) by fitting the measured signals as described in the previous chapter. The photolysis leads to estimated initial Cl-atom concentrations of 7.3×10^{12} and 11.2×10^{12} cm^{-3} for HO_2 and DO_2 measurement, respectively. As in the previous chapter, HO_2 and DO_2 radicals have been generated through the following reaction sequence:

$$(COCl)_2 + h\upsilon_{248nm} \rightarrow 2\ Cl + 2\ CO \qquad (R\ 31)$$

$$Cl + CH_3OH\ (or\ CD_3OD) \rightarrow CH_2OH\ (or\ CD_2OD) + HCl\ (or\ DCl) \qquad (R\ 32)$$

$$CH_2OH\ (or\ CD_2OD) + O_2 \rightarrow HO_2\ (or\ DO_2) + CH_2O\ (or\ CD_2O) \qquad (R\ 33)$$

Under the experimental conditions, the (R 32) (R 33) reactions with rate constant k(R 32) = 5.5×10^{-11} cm^3 s^{-1} and k(R 33) = 9.6×10^{-12} cm^3 s^{-1} have pseudo-first order rates of k'(R 32) = 3.8×10^4 s^{-1} and k'(R 33) = 2.8×10^6 s^{-1}, and are thus completed within few 10 μs.

For CH_3OH and CD_3OD, which are stable molecules, the ring down time τ is equal to τ_0, i.e. the average of the ring-down time of the events before the photolysis pulse. The "real" ring-down time τ_0 of a totally empty cavity necessary to calculate the absorption coefficients $\alpha_{CH3OH/CD3OD}$ is then measured at the end of the acquisition of the spectrum with a rapid scan taking care that the alignment did not change in between.

Indeed, this ring-down time depends only on the reflectivity and on the alignment of the mirrors. The absorption spectra of CH_3OH and CD_3OD are presented in Figure 42. Low concentrations of water are always present in the photolysis cell, introduced by the carrier gas through permeation of ambient H_2O through the Teflon tubes or through small leaks. Thus, several H_2O absorption lines were seen on the CH_3OH and CD_3OD spectra. The H_2O concentration can be calculated from the integrated line strength from HITRAN database [42], and one finds $S = 6.58\times10^{-22}$ cm for the line at 7002.173 cm^{-1}, leading to $[H_2O] = 7.5\times10^{14}$ cm^{-3} during the CH_3OH measurement and $[H_2O] = 1.4\times10^{14}$ cm^{-3} during the CD_3OD measurement. Furthermore, it turned out during the data analysis that a good part of the observed absorption peaks during the measurement with CD_3OD were also due to the presence of HDO. The presence of this species results from the fact that a fast D/H exchange of the –OD in CD_3OD with H_2O leads to the partial conversion of CD_3OD to CD_3OH and to HDO. Therefore, the measured spectrum of CH_3OH was the sum of CH_3OH and H_2O and the measured spectrum of CD_3OD was the sum of CD_3OD, H_2O and HDO. The CH_3OH and CD_3OD pure spectra were thus obtained by substracting H_2O and HDO lines by setting their absorption to zero. The absorption spectra were converted into absorption cross-section using the calculated values of CH_3OH and CD_3OD concentrations from the flows.

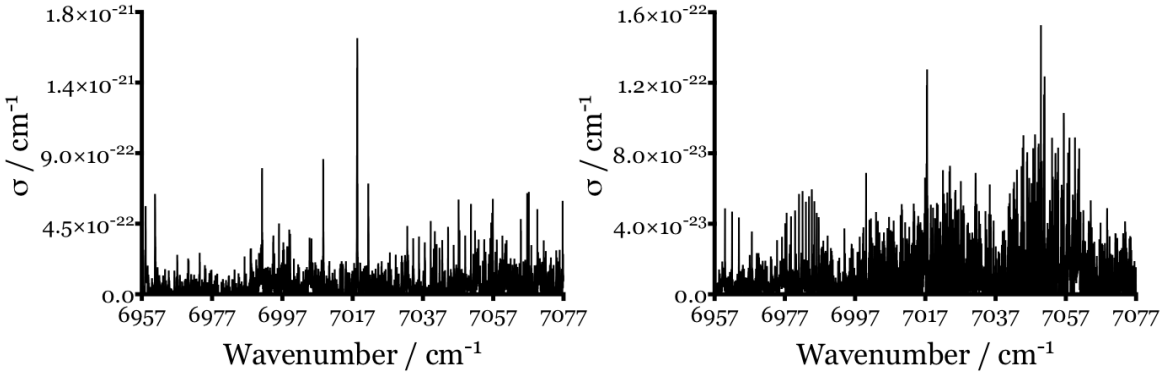

Figure 42: Absorption spectra of CH_3OH (left) and CD_3OD (right) recorded between 6957 and 7077 cm^{-1} at a total pressure of 20 Torr

4.3 HO_2 spectrum and absorption cross-section determination

4.3.1 Measurement of the HO_2 spectrum

A typical signal of HO_2 for one wavelength at 7000.27 cm^{-1} with the ring-down time as a function of the delay to the photolysis pulse is shown in the left graph of the Figure 43. The right graph shows the corresponding absorption coefficient signal after the application of the Equation 22. At time zero, the photolysis laser generates Cl atoms, which are immediately converted into HO_2 radicals on the time scale of the experiment and hence the ring-down time decreases due to the absorption. The ring-down time gets then slowly back to the initial value of the ring-down time before the photolysis pulse due to the loss of HO_2 radicals by either reactions or by diffusion and pumping out of the photolysis volume.

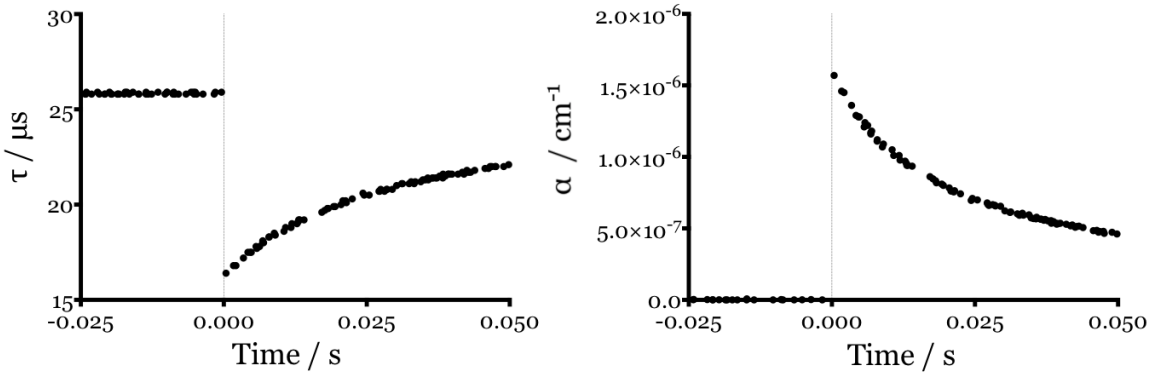

Figure 43: Typical signal of HO_2 obtained at 7000.27 cm^{-1}. Left graph: the ring-down time τ is plotted as a function of the delay with respect to the photolysis laser occurring at time t = 0 s. Right graph: ring-down times have been converted into absorbance α. $[(COCl)_2] = 1.4\times10^{14}$ cm^{-3}, $[CH_3OH] = 5\times10^{14}$ cm^{-3} and $[O_2] = 3.3\times10^{17}$ cm^{-3}, photolysis energy 70 mJ cm^{-2}

The full spectrum of HO_2 obtained from 28000 kinetic decays (such as shown in Figure 43) between 6940 and 7080 cm^{-1} with a resolution of 0.005 cm^{-1} is shown in Figure 52. A zoom of the HO_2 spectrum over 3 cm^{-1} between 7023 and 7026 cm^{-1} is shown in Figure 44 by plotting the ring-down time τ_0, i.e. the average of all ring-down

events having occurred before the photolysis pulse, the ring-down time $\tau_{t=0}$, i.e. the extrapolation of the time resolved decay to a zero delay relative to the photolysis laser, and absorbance α obtained by applying Equation 22 as a function of the wavelength. As described previously, low concentrations of water are always present in the photolysis cell. However, this is not perturbing the measurement of the HO_2 spectrum because the concentration of H_2O does not change before and after the photolysis and thus the corresponding absorbance α becomes zero.

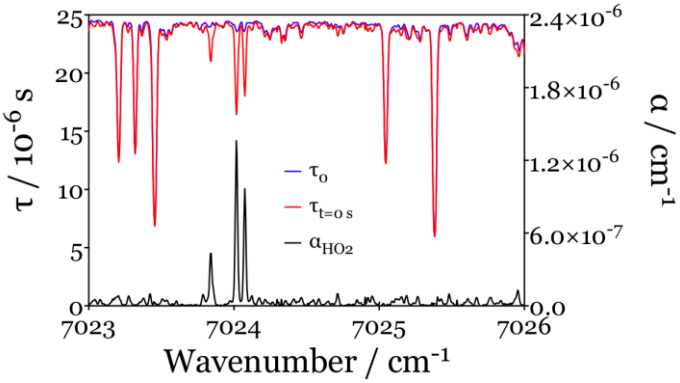

Figure 44: A zoom of the HO_2 spectrum. Blue line (in left y-axis): the ring-down time τ_0, i.e. the average of all ring-down events having occurred before the photolysis pulse. Red line (in left y-axis): the ring-down time $\tau_{t=0}$. The black line (in right y-axis): absorbance α obtained by applying Equation 22

The measurement of the full HO_2 spectrum shown in Figure 52 took a total time of 3 days. In order to control the stability of the radical concentration over the entire measurement period, the HO_2 absorption line at 7028.565 cm^{-1} has been scanned twice a day, as presented in Figure 45. This line consists of the sum of five absorption lines as indicated by black bars on Figure 45 from the results from PGOPHER (see further down). All the spectra have been fitted by Voigt profiles using Fityk software [74]. The total surface areas obtained for each fit were 5.42, 5.66, 5.65, 5.46, 5.94 and 5.73×10^{-9} cm^{-2}, indicating that the HO_2 concentration had varied by less than 5% over the 3 days. It will be then possible to convert the relative absorbance into absorption cross-section for the entire wavelength range using the calibration of only few selected lines over the entire spectrum.

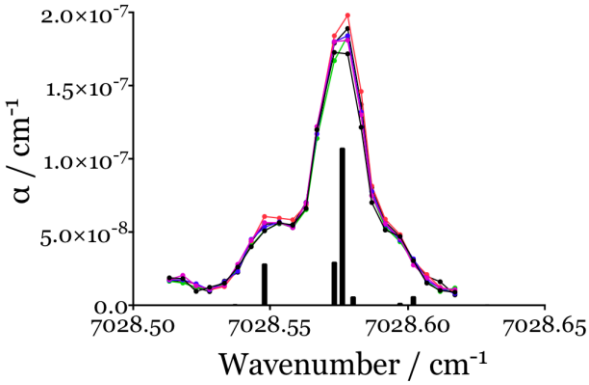

Figure 45: Selected HO_2 line at 7028.565 cm^{-1} measured twice per day to check the stability of HO_2 concentration over the entire spectrum time measurement. The integrated surface area agrees better than 5%. Bars represent line positions simulated with PGOPHER [95] using the spectroscopic data provided in the literature [89]

4.3.2 Calibration of the HO_2 spectrum

The concentration of HO_2 needs to be determined in order to convert the absorption coefficient α into absorption cross-section σ. For this purpose, one of the two CRDS path was set to determine the HO_2 radical concentration by measuring the kinetic decay on the well-characterized line at 6638.205 cm^{-1} [64], [70], [72], [73] in the overtone transition, while the other CRDS path was dedicated to the scan of five selected lines in the $\tilde{A}\ ^2A' \leftarrow \tilde{X}\ ^2A''$ 000-000 band. In order to check the value of HO2 absorption cross-section at 6638.205 cm^{-1}, a kinetic method was employed [19], [64] using two weak absorption lines at 6638.58 and 6637.46 cm^{-1}. The kinetic method is based on determining the time resolved decays of the radicals. During this experiment, one of the major removal mechanisms for HO_2 is the self-reaction:

$$HO_2 + HO_2 \rightarrow H_2O_2 + O_2 \qquad \text{(R 24a)}$$

$$HO_2 + HO_2 + M \rightarrow H_2O_2 + O_2 (+M) \qquad \text{(R 24b)}$$

HO_2 disappears also by diffusion:

$$HO_2 \rightarrow \text{diffusion} \qquad \text{(R 29)}$$

The HO_2 self-reaction has been widely studied. The IUPAC [69] recommends from several studies [16], [81] the rate constant to be:

$$k_{(\text{R }24)} = k_{(\text{R }24a)} + k_{(\text{R }24b)} = 1.6 \times 10^{-12} + 4.5 \times 10^{-32} \times [O_2] \qquad \text{Equation 30}$$

where the first term is the rate constant for bimolecular reaction and the second term is the pressure-dependent termolecular reaction.

However these studies have often used methanol CH_3OH as a precursor for HO_2. Laboratory experiments have shown that the observed rate constants k(R 24a) and k(R 24b) are enhanced by the presence of H_2O, CH_3OH and NH_3 [70], [96]–[98], especially at low temperature. The study [70] of the kinetic of the HO_2 self-reaction along with the H_2O or CH_3OH enhancement suggest a reinterpretation of the obtained experimental data. The rate constants k(R 24) should be multiplied by an enhancement coefficient of $1.58\times10^{-29}\times$ [CH_3OH] and $6.14\times10^{-30}\times$ [H_2O] at 298 K in presence of methanol and water respectively. Within the experimental conditions where [O_2] = 3.3×10^{17}, [CH_3OH] = 5×10^{14} and [H_2O] = 7.5×10^{14} cm^{-3}, the rate constant k(R 24) increases by 4.5×10^{-14} cm^3 s^{-1} at 298 K, being less than 2%. Only around 1% of the initial HO_2 is trapped by the formation of $HO_2.H_2O$ and $HO_2.CH_3OH$ complexes. Thus, even if the rate constants of the reactions of HO_2 with the two complexes are around 10 times higher than the HO_2 self-reaction, it is possible to neglect the effects from the complexes. Hence, the recommendation from IUPAC is taken for the rate constant of the HO_2 self-reaction k(R 24) = 1.6×10^{-12} cm^3 s^{-1}.

The formation of HO_2 due to the reaction sequence (R 31)-(R 33) appears instantaneously after the photolysis pulse. Then, the HO_2 decay occurs over tens of milliseconds as shown on Figure 46 for different $(COCl)_2$ concentrations between 1.7 and 4.8×10^{15} cm^{-3}. The diffusion can be approximated as an exponential loss k_{diff}. The

Equation 31 describes the HO_2 concentration time profiles using the rate constants k(R 24) and k_{diff}:

$$\frac{d[HO_2]}{dt} = -2k_{(R\ 24)}[HO_2]^2 - k_{diff}[HO_2] \qquad \text{Equation 31}$$

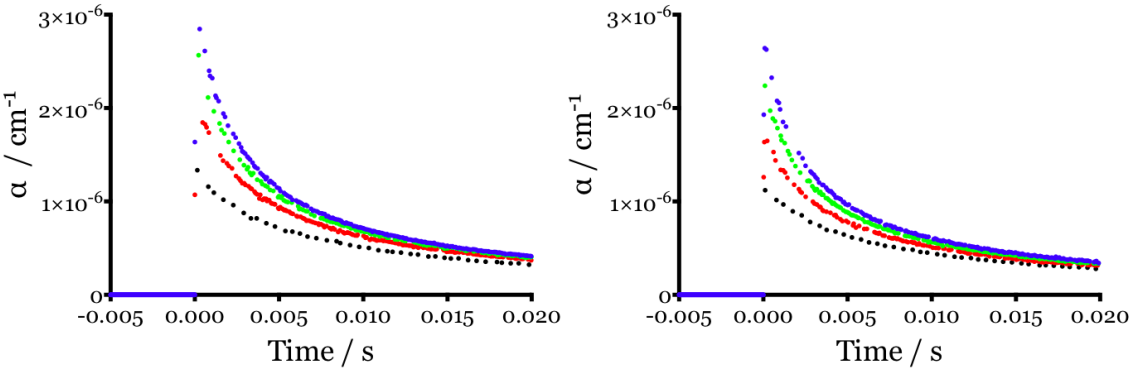

Figure 46: Absorption coefficient α plotted as a function of the photolysis delay at 50 Torr at 6638.58 cm^{-1} (left) and 6637.46 cm^{-1} (right) for four initial concentration of $(COCl)_2$: 1.7×10^{15} (black), 2.7×10^{15} (red), 3.8×10^{15} (green), and 4.8×10^{15} (blue) cm^{-3}

If the dominant process of consumption of HO_2 is the reaction (R 24) then it is possible to express the kinetics according to the Equation 32:

$$\frac{1}{[HO_2]_t} = \frac{1}{[HO_2]_0} + \left(\frac{k_{diff}}{[HO_2]_0} + 2k_{(R\ 24)}\right)t \qquad \text{Equation 32}$$

with $[HO_2]_t$ the radical concentration at time t after the photolysis pulse and $[HO_2]_0$ the initial radical concentration at time zero

The result of a plot of the Equation 32 with $1/[HO_2]_t = f(t)$ is a straight line with $m = (k_{diff}/[HO_2]_0 + 2k(R\ 24))$ as slope and $I = 1/[HO_2]_0$ as ordinate at the origin. By measuring kinetics with different HO_2 initial concentration, it is then possible to distinguish the contributions of the self-reaction (R 24) and the diffusion (R 29). Indeed, at high HO_2 initial concentration the term $k_{diff}/[HO_2]_0$ becomes smaller compare to 2k(R 24). The HO_2 decay is then reckoned to be only due to the self-

reaction. The goal of this experiment is to deduce the absorption cross-section σ knowing the apparent rate constant k(R 24) of the HO_2 self-reaction. To minimize the effect of the diffusion, the initial concentration of HO_2 is set to be high during this experiment. Thus, it is not possible to measure the HO_2 signal at 6638.21 cm^{-1}, which will be saturated. The absorption cross-section of two selected peaks at 6638.58 cm^{-1} and 6637.46 cm^{-1} have be measured and used to confirm the absorption cross-section of the HO_2 peak at 6638.21 cm^{-1} at lower HO_2 initial concentration. The concentration of HO_2 radical can be replaced by the absorption coefficient α in the Equation 32 to give:

$$f(t) = \frac{1}{\alpha} = \frac{1}{[HO_2]_t \sigma} \qquad \text{Equation 33}$$

leading to the slope m:

$$m = \frac{k_{diff}}{[HO_2]_0 \sigma} + \frac{2k_{4,obs}}{\sigma} \qquad \text{Equation 34}$$

and the intercept I:

$$I = \frac{1}{[HO_2]_0 \sigma} \qquad \text{Equation 35}$$

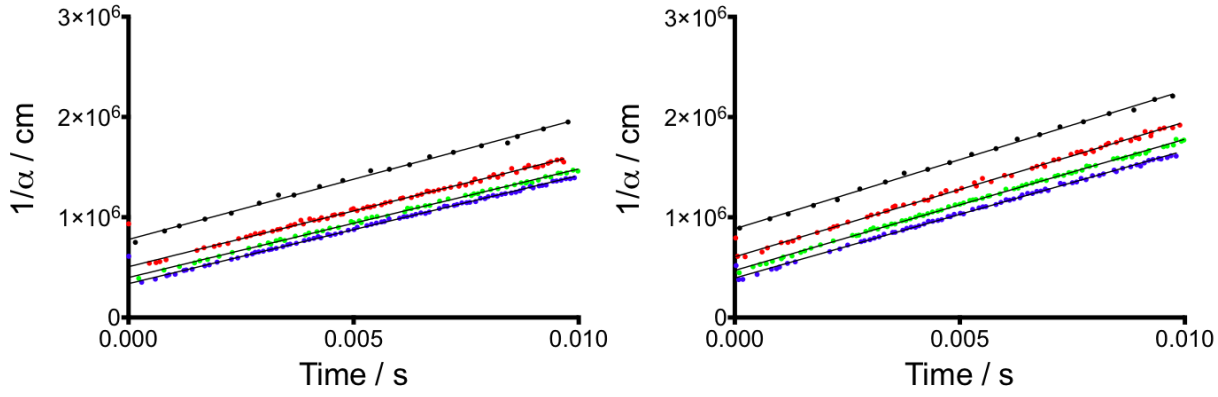

Figure 47: 1/α=f(t) for kinetics measurements at 50 Torr at 6638.58 cm^{-1} (left) and 6637.46 cm^{-1} (right) presented in Figure 46. Full lines are obtained from a linear regression of the data points between 0 and 10 ms following the photolysis pulse

The signals in Figure 47 are obtained by plotting $1/\alpha = f(t)$ at the top of the two absorption peaks at 6638.58 cm^{-1} and 6637.46 cm^{-1}. The full lines are derived from the linear fit of the data points between 0 and 10 ms after the photolysis pulse. During this time range the linear adjustment is well correlated with the data points. Thereby, the approximation introduced for the Equation 32 at high HO_2 initial concentration is validated. It can be noted that a slight increase in the slope m is observed when the HO_2 initial concentration becomes smaller. Indeed, the slope increases from $(1.035\pm0.372)\times10^8$ to $(1.152\pm0.590)\times10^8$ cm s^{-1} for the peak at 6638.58 cm^{-1} and $(1.233\pm0.545)\times10^8$ to $(1.312\pm0.580)\times10^8$ cm s^{-1} for the peak at 6637.46 cm^{-1}. This is due to the fact that the influence of the diffusion on the loss of HO_2 increases with decreasing HO_2 initial concentration. From these experiments, the slope m is plotted as a function of the intercept I, as shown in Figure 48.

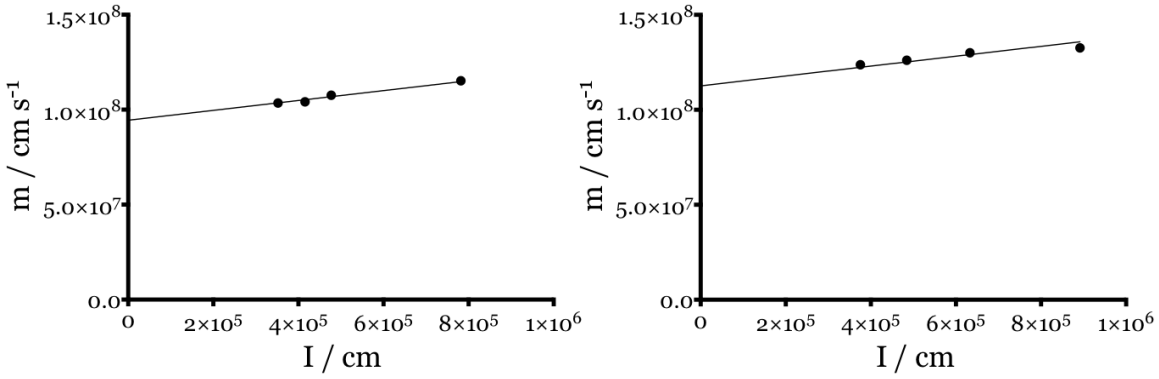

Figure 48: Plot of the slope m as a function of the intercept I obtained by the linear regression of the data of kinetics measurements at 50 Torr at 6638.58 cm^{-1} (left) and 6637.46 cm^{-1} (right) presented in Figure 47.

The extrapolation of the linear regression to I = 0, i.e. for an "infinite" concentration of HO_2, leads to a value of the slope m only due to the HO_2 self-reaction. As seen in the Equation 34, the slope is linked to the diffusion and should only depend on the pressure and not the wavelength. The linear regression is forced with the same value of the slope at 26 s^{-1} to get coherent values. This value is obtained by averaging the two value of the slope from unforced linear regressions and is consistent with the previous work on the HO_2 spectrum [64], namely 41 s^{-1} at the same pressure. Thus,

the linear regression gives the rate constant of diffusion k_{diff} = 26 s^{-1} from the slope, while the absorption cross-section σ_λ can be calculated from the intercept $m_{I=0} = 2k(R\ 24)/\sigma_\lambda$ using the rate constant k(R 24) = 1.6×10^{-12} cm^3 s^{-1}. These values are summarized in Table 4.

Table 4: HO_2 absorption cross-section from kinetics measurements at 50 Torr at 6637.46 cm^{-1} and 6638.58 cm^{-1}

ν / cm^{-1}	σ(HO_2,50 Torr) / 10^{-19} cm^2
6637.46	0.28±0.04
6638.58	0.34±0.05

The absorption cross-section of HO_2 at 6638.21cm^{-1} is then deduced with kinetics measurements at lower HO_2 initial concentration. To do so, the HO_2 absorption coefficient is measured at 6638.58 cm^{-1} and 6638.21 cm^{-1} at 50 Torr using around 10 times less $(COCl)_2$ as HO_2 precursor, $(COCl)_2 = 0.23\times10^{15}$ cm^{-3}.

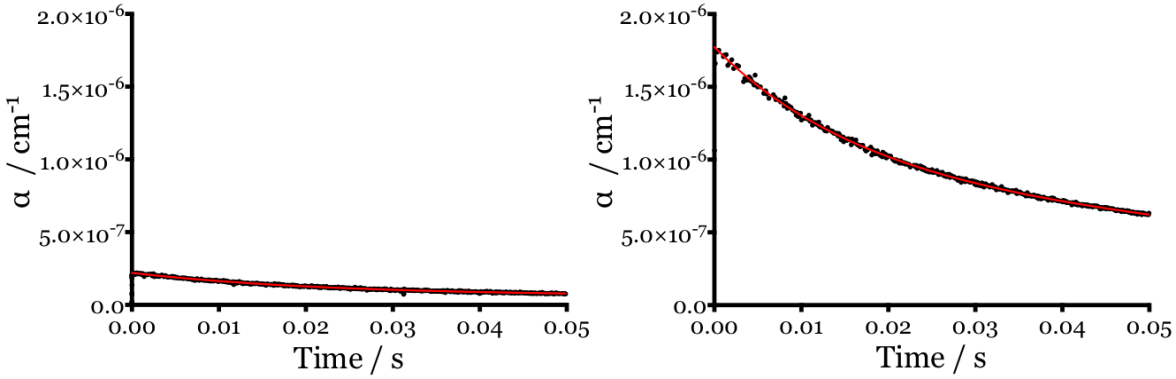

Figure 49: Kinetic measurements at 50 Torr at 6638.58 cm^{-1} (left) and 6638.21 cm^{-1} (right) for a concentration of $(COCl)_2 = 0.23\times10^{15}$ cm^{-3}. The absorption coefficient α plotted as a function of the photolysis delay. Red full lines are obtained by fitting the data with a bi-exponential decay

The ratio of absorption coefficients at time zero for the two wavelengths is then obtained by fitting the data with an exponential decay. At the same HO_2

concentration, the ratio of absorption coefficient and the ratio of absorption cross-section are equals. This way the absorption cross-section of HO_2 at 6638.21 cm^{-1} is extracted and tabulated in Table 5.

Table 5: Wavelength at the maximum of the peak and corresponding HO_2 absorption coefficient and absorption cross-section from kinetics measurements at 50 Torr at 6638.58 cm^{-1} and 6638.21 cm^{-1}

ν / cm^{-1}	$\alpha_{(HO2,50\ Torr)}$ / cm^{-1}	$\sigma_{(HO2,50\ Torr)}$ / 10^{-19} cm^2
6638.58	2.20×10^{-7}	0.34±0.05
6638.21	1.78×10^{-6}	2.73±0.04

The value of HO_2 absorption cross-section of the well-known absorption peak at 6638.21 cm^{-1} is in perfect agreement with the previously determined values [64], [70], [72], [85], [86] at 50 Torr, namely $\sigma_{HO2\ 6638.21cm^{-1}} = 2.72\times10^{-19}$ cm^2. The main uncertainties on the reported absorption coefficients are directly connected to the uncertainty in the rate constant k(R 24). In the latest IUPAC recommendation, the uncertainty for this rate constant at 298 K is estimated to be ±40%. However, a good agreement is found between the estimated initial HO_2 concentrations obtained from calculating the photolytic Cl-atom concentration and the one obtained from the intercept of Figure 47 plots, using the value 2.72×10^{-19} cm^2 as absorption cross-section.

Few HO_2 lines were selected in the range 6940 and 7080 cm^{-1} according to some criterions to determine their absorption cross-sections σ at 50 Torr relative to the value of the HO_2 absorption cross-section at 6638.21 cm^{-1}. The criterions of selection were to have a strong absorption and to be isolated enough from the neighbouring lines to avoid any problems of shouldering. All the selected lines are recorded with a higher resolution than the full spectrum (0.003 instead of 0.005 cm^{-1}) and are presented in Figure 50.

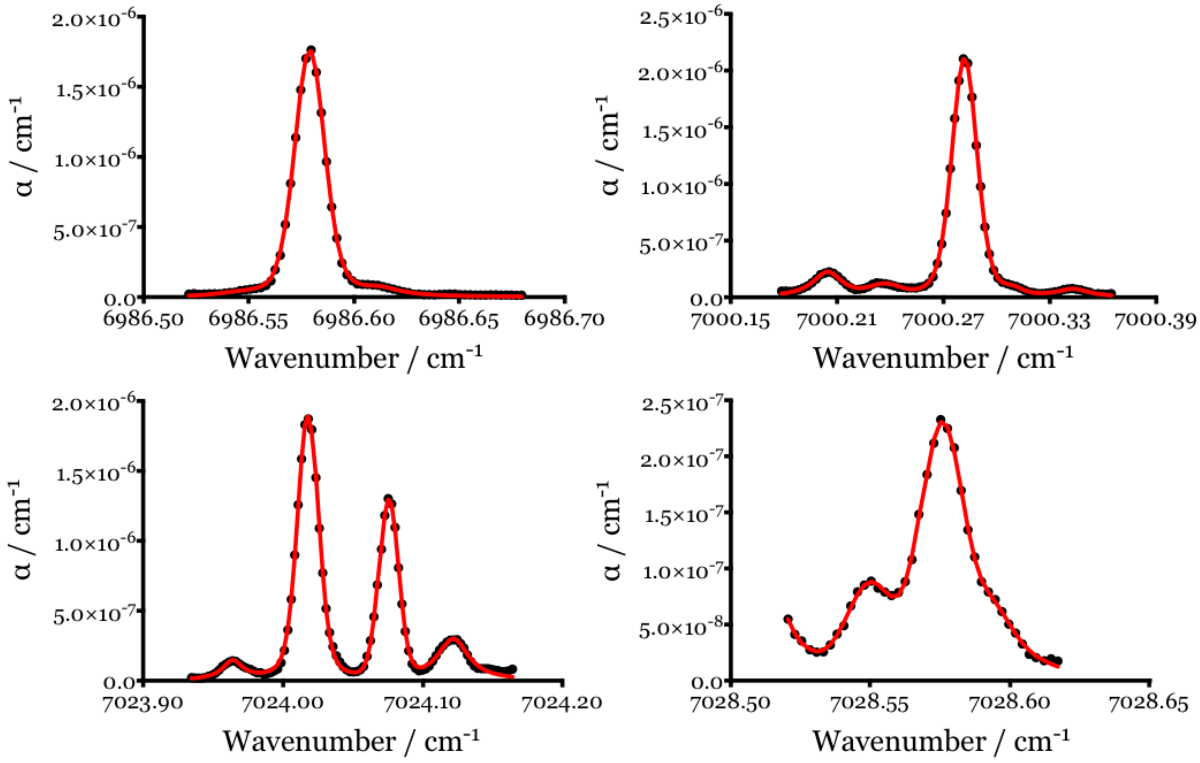

Figure 50: Absorption coefficient α of five selected HO_2 lines in different wavelength regions at 50 Torr. The red full lines represent Voigt adjustment

These five absorption lines are adjusted using a Voigt profile with the software Fityk and the value of absorption coefficient α at the maximum of each line was extracted from the fits. These values were then compared with the measurement of the absorption coefficient at 6638.21 cm^{-1} measured during the scans on the second cw-CRDS path.

Table 6: Absorption cross-section at 50 Torr helium for five selected lines of HO_2, obtained by simultaneous quantification of HO_2 through the well-characterized absorption line at 6638.21 cm^{-1} and the absorbance such as obtained during the measurement of the full spectrum Figure 52 at 20 Torr

ν / cm^{-1}	α / cm^{-1} at 50 Torr	σ / cm^2 at 50 Torr	α / cm^{-1} full spectrum
6638.21	2.80×10^{-6}	2.72×10^{-19}	-
6986.58	1.76×10^{-6}	1.75×10^{-19}	1.37×10^{-6}
7000.28	2.13×10^{-6}	2.12×10^{-19}	1.68×10^{-6}
7024.02	1.89×10^{-6}	1.88×10^{-19}	1.48×10^{-6}
7024.08	1.30×10^{-6}	1.29×10^{-19}	1.04×10^{-6}
7028.58	2.37×10^{-7}	2.36×10^{-20}	1.73×10^{-7}

In Figure 51 the absorbances from the full HO_2 spectrum are plotted as a function of the absolute absorption cross-section obtained from the scans for the five lines summarized in Table 6. From the slope of the linear regression it is possible to deduce the concentration of HO_2 radicals during the measurement of the full spectrum to be $[HO_2] = (7.87\pm0.04)\times10^{12}$ cm^{-3}. The given error is statistical only with an estimated uncertainty of 15%, which takes into account the variability of HO_2 concentration during the entire measurement period as well as the uncertainty of the absorption cross-section of the line at 6638.21 cm^{-1} used for calibration.

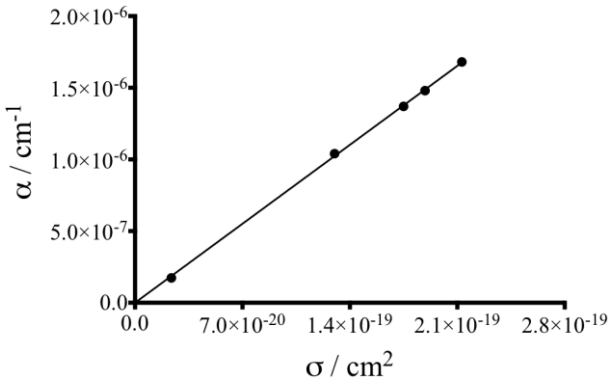

Figure 51: Absorption coefficient α measured during the full scan as a function of the absorption cross-section σ obtained from the comparison with the simultaneously measured absorption line at 6638.21 cm^{-1}

This concentration has been used to convert the absorbance α of the full spectrum into absorption cross-sections. The full spectrum of HO_2 is shown in Figure 52. Using the accurate spectroscopic parameters for the 000-000 vibrational band of the electronic transition $^2A' \leftarrow {}^2A''$ (with detailed spectroscopic parameters described in previous studies [89]), the absorption spectrum was simulated by the Gerätezentrum "Cologne Center for Terahertz Spectroscopy" using the program PGOPHER [95]. These simulations are compared to the measured data in Figure 52 for HO_2. The simulated band is of C-type and therefore has the selection rules $\Delta K_a = \pm 1$ and $\Delta K_c = 0$. Prominent lines are thus the Q- and R-branches of the sub-band $K_a' = 0 \leftarrow K_a'' = 1$ at about 7000 and 7020 cm^{-1}, as well as the Q- and R-branches of the sub-band $K_a' = 1 \leftarrow K_a'' = 0$ at about 7040 and 7060 cm^{-1}, respectively.

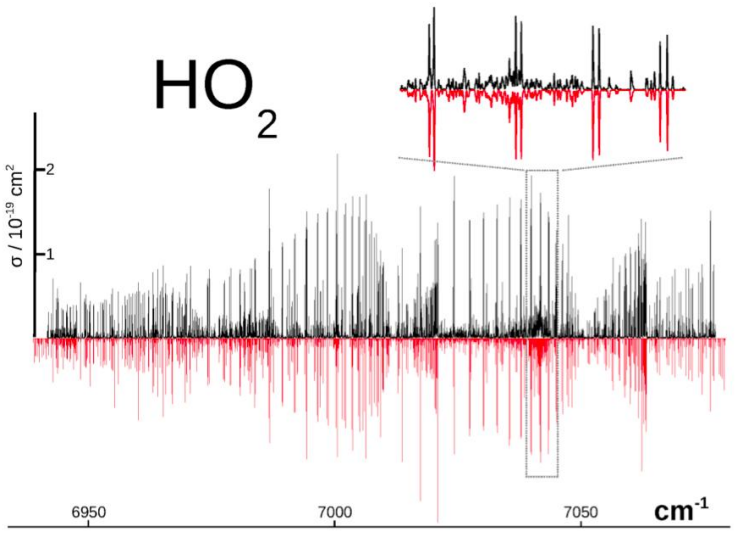

Figure 52: Measured (upper trace in black) and simulated (lower trace in red) spectra of HO_2 for the 000-000 band of the $^2A' \leftarrow {}^2A''$ electronic transition. The simulation has been performed with PGOPHER [95], based on the accurate molecular constants given in the literature [89]. The zoom in the range 7039 to 7045.2 cm^{-1} shows the strong C-type Q-branch transitions of the sub-band $K_a' = 1 \leftarrow K_a'' = 0$, which show up in pairs belonging to the two spin manifolds F_1 and F_2, as well as a dense forest of weak lines originating from the A-type ($\Delta K_a = 0$, $\Delta K_c = \pm 1$) magnetic dipole transitions [89]

By fitting the simulated spectrum obtained by PGOPHER, it is possible the check general parameters like the internal temperature and the average linewidth, as well as the internal calibration of the commercial diode laser system. With the intensity distribution corresponding to fitted temperatures of about T = 325 K, HO_2 was found to be colder during the full spectrum measurement compared to the corresponding measurements in the literature (350 K) [89]. A temperature close to room temperature is expected due to the fast collisional equilibrium with helium after the production of the investigated species. An average linewidth FWHM of about 0.019 cm^{-1} (600 MHz) is found. The linewidth is dominated by the Doppler broadening (451 MHz expected for 300 K, m = 33 u and at 7000 cm^{-1}) and the pressure broadening (20 Torr inside the cell), while the contribution of the Agilent laser (intrinsically narrow with a jitter of a few ~10 MHz) can be neglected. The comparison with the calibrated spectroscopic parameters [89] also allows correcting for a slight frequency shift of the Agilent laser which was found to be about 0.003 to 0.005 cm^{-1} too low.

The vast majority of the line positions and intensity were well reproduced by PGOPHER but some lines were slightly shifted or not predicted at all. A zoom between 7000.0 and 7001.5 cm^{-1} of the HO_2 full spectrum is presented in Figure 53. Arrows indicate the deviations from the simulation. Non-predicted transitions could principally originate from species present in the absorption cell other than HO_2. However, given that the spectrum is obtained from the change in absorbance following the photolysis pulse, only photolysis products are possible candidates, while absorption of the precursors or other impurities (such as water) will not show up in the absorption spectrum. The most likely photolysis product is formaldehyde CH_2O, co-product of HO_2 from the reaction (R 33). The absorption spectrum of CH_2O has recently been published [99], [100] and is added to the Figure 53. It can be seen that there is no agreement between the CH_2O spectrum and the non-predicted absorption lines. Besides, the absorption cross-sections for CH_2O are roughly 100 times smaller than those for HO_2, and given that both species are generated in equal amounts, it can be considered that CH_2O is not responsible for the unidentified absorption lines. Even though, CH_2O is a stable molecule and could to a certain extend accumulate in the cell, but only the absorption due to fresh molecules would be detected, all absorption due to molecules already present from earlier photolysis shots would also be detected in the baseline. The most probable explanation of this deviation is thus a known perturbation in the upper $^2A'$ state which is not captured by the standard spectroscopic constants and the corresponding simulation. More details about this perturbation can be found in the literature [89].

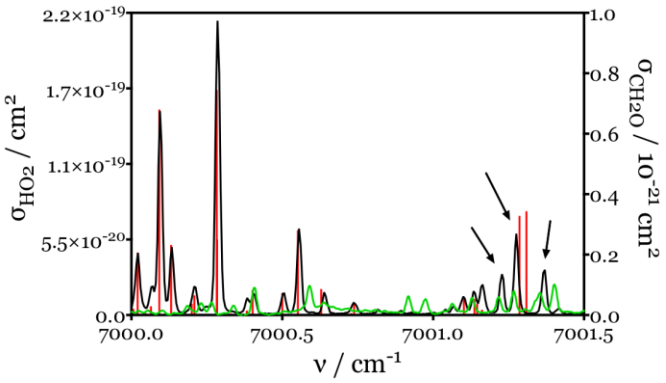

Figure 53: Zoom of the HO_2 spectrum between 7000.0 and 7001.5 cm^{-1}. Black line (left y-axis): HO_2 absorption spectrum measurement, red sticks (arb. units): prediction of HO_2 by PGOPHER, green line (right y-axis): CH_2O absorption spectrum

4.3.3 Pressure broadening of the HO_2 absorption cross-sections

The pressure broadening of HO_2 the line at 7000.28 cm^{-1} but also for the line at 6638.58 cm^{-1} used for calibration previously was investigated at four different pressures in helium: 21.4, 49.2, 73.8 and 100.1 Torr. The line at 7000.28 cm^{-1} is the strongest line in the full spectrum wavelength region and is hence susceptible to be used in laboratory studies for quantification, as it will lead to the best sensitivity. The lines were scanned with a resolution of 0.001 cm^{-1} for each pressure such as presented in Figure 54, where all spectra have been normalized to the fitted surface area. The lines were then reproduced by a fit to a Voigt profile using Fityk software by fixing the Doppler width to its theoretical value. These lines consist of a convolution of two nearly perfectly overlapping transitions, a strong one at 7000.283 cm^{-1} and a roughly four times weaker one at 7000.284 cm^{-1} as shown as dashed blue lines in Figure 54. The extracted following parameters can be used for practical purposes to retrieve peak absorption cross-sections using a Voigt profile: line strength $S = 4.0\times10^{-21}$ cm and a broadening of $\gamma = 4.0\times10^{-5} \times p/\text{Torr} + 9.02\times10^{-4}$ cm^{-1}.

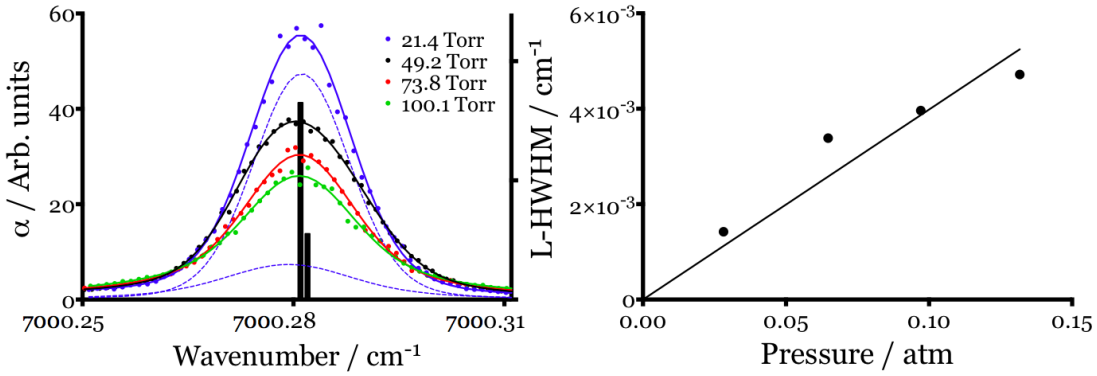

Figure 54: Left graph: absorption spectrum normalized to the fitted surface area of HO_2 at 7000.28 cm^{-1} for four different pressures between 21.4 and 100.1 Torr of He. Dots: experimental values, full lines: fits to Voigt profiles, dashed blue lines: deconvolution of the two overlapping lines for 21.4 Torr. Black bars are positions of absorption lines such as obtained from PGOPHER. Right graph: Lorentzian HWHM plotted as a function of the pressure

At the end of the scans, the absorption cross-section of the line at 7000.28 cm^{-1} was determined using the kinetic method (described with Equation 33 to Equation 35) by measuring four HO_2 decays using four initial concentrations of $(COCl)_2$ and O_2, varying between $[(COCl)_2] = 1.4\times10^{14}$ to 9.7×10^{14} cm^{-3} and $[O_2] = 9.7\times10^{16}$ to 4.5×10^{17} cm^{-3}. The HO_2 concentration has simultaneously been quantified on the second cw-CRDS path at 6638.58 cm^{-1}. From these experiments, the slope m is plotted as a function of the intercept I, as shown in Figure 55.

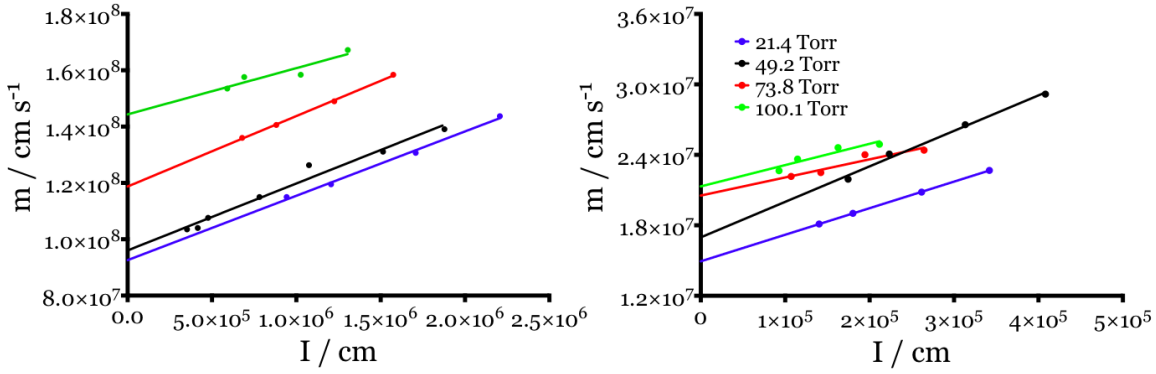

Figure 55: Plot of the slope m as a function of the intercept I obtained by the linear regression of the data of kinetics measurements at different pressures at 6638.58 cm^{-1} (left) and at 7000.28 cm^{-1} (right). Extrapolation to I = 0 leads to $m_{[HO_2]_0\to\infty} = 2k / \sigma$

With the extrapolation of the linear regression to an infinite concentration of HO_2 (when I=0) it is possible to determine the absorption cross-section for each pressure using $m_{I=0} = 2k(R\ 24)/\sigma_\lambda$ and using a rate constant of the HO_2 self-reaction $k(R\ 24) \approx 1.6\times10^{-12}$ cm^3 s^{-1} ($k(R\ 24)$ was calculated for each pressure using Equation 30). The peak absorption cross-sections of the two HO_2 lines obtained for 20, 50, 75 and 100 Torr are listed in Table 7. Using the value of broadening coefficient, the absorption cross-sections were then calculated at the same pressures than the measured absorption cross-sections and found to be accurate with less than 5% difference.

Table 7: Absorption cross-sections for two HO_2 lines at 7000.28 cm^{-1} and 6638.58 cm^{-1} obtained from kinetic measurement method at 21.4, 49.2, 73.8, 100.1 Torr

P / Torr	$\sigma_{(HO2,\ 6638.58\ cm\text{-}1)}$ / 10^{-19} cm^2	$\sigma_{(HO2,\ 7000.28\ cm\text{-}1)}$ / 10^{-19} cm^2
21.4	0.35	2.14
49.2	0.33	1.88
73.8	0.27	1.56
100.1	0.22	1.5

4.4 DO_2 spectrum and absorption cross-section determination

4.4.1 Measurement of the DO_2 spectrum

The DO_2 spectrum has been obtained through the same reaction sequence (R 31) to (R 33) as HO_2, but using CD_3OD as precursor instead of CH_3OH. During the data treatment, it turned out that a part of the observed absorption lines were identical with HO_2 lines. As described previously, the presence of HO_2 radicals can be explained by a fast D/H exchange of the –OD in CD_3OD with H_2O, which is always present in low concentrations in the reaction cell and also on the walls of the Teflon tubing, leading to the partial conversion of CD_3OD to CD_3OH. Thus, reaction with Cl atoms leads to the formation of CD_2OH and the subsequent reaction with O_2 will

finally produce HO_2 instead of the desired DO_2. The measured absorption spectrum was therefore the sum of HO_2 and DO_2 spectra instead of pure DO_2, which was extracted by subtracting the HO_2 spectrum. The zoom of two portions of the spectrum are illustrated in Figure 56: the dashed blue lines represents the initially measured spectrum such as obtained from the kinetics traces described above for HO_2, the black line represents the pure HO_2 spectrum such as obtained in the previous section, and finally the red line represents the pure DO_2 spectrum, obtained after subtraction of the HO_2 spectrum, multiplied by a factor such as to bring HO_2 transitions to zero, without getting a negative absorbance.

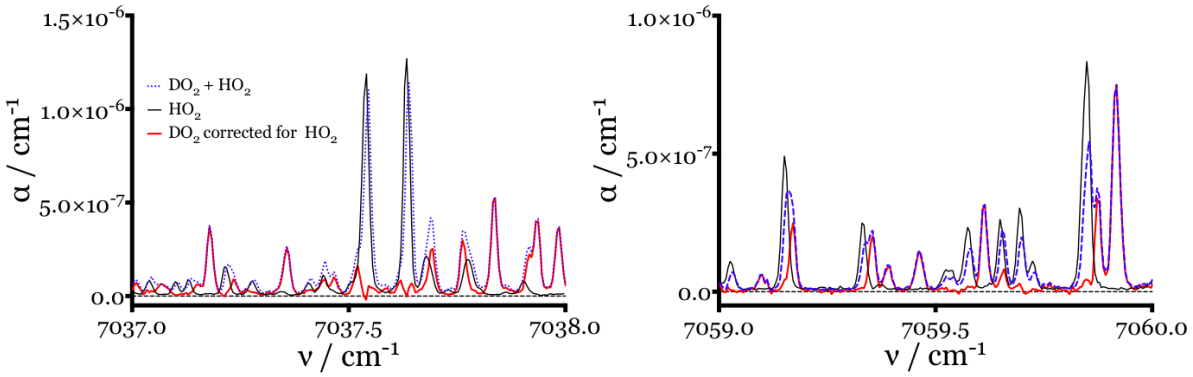

Figure 56: A zoom of two regions of the entire DO_2 spectrum (7037 to 7038 and 7059 to 7060 cm^{-1}). Dashed blue line: initially measured absorption spectrum of DO_2, contaminated with HO_2, black line: pure HO_2 spectrum, red line: pure DO_2 spectrum

This multiplication factor used to subtract the HO_2 spectrum changed over the measurement period (of nearly four days), probably because the water absorbed on the Teflon tube or flowing into the cell through leaks was slowly transformed into HDO and D_2O and thus the D/H exchange became less important with time. This exchange effect can be visualized in Figure 57 where, on the left graph, a line of DO_2 at 7022.98 cm^{-1} was scanned twice a day to check if the concentration of DO_2 did not change during the four days of the full scan measurement. The right graph shows the maximum of absorbance of that line taken from each scan as a function of the total measurement time. It can be seen that after a rapid change during the first hours at

the beginning of the measurement period, the concentration of DO_2 was rather stable after the first day. From the known absorption cross-sections of HO_2, the residual concentration of HO_2 has been calculated to be $(5.3\pm0.3)\times10^{12}$ cm^{-3}, which can be compared with the DO_2 concentration $[DO_2] = 7.0\times10^{12}$ cm^{-3} (see below). Thus, only 57% of Cl atoms were converted to DO_2.

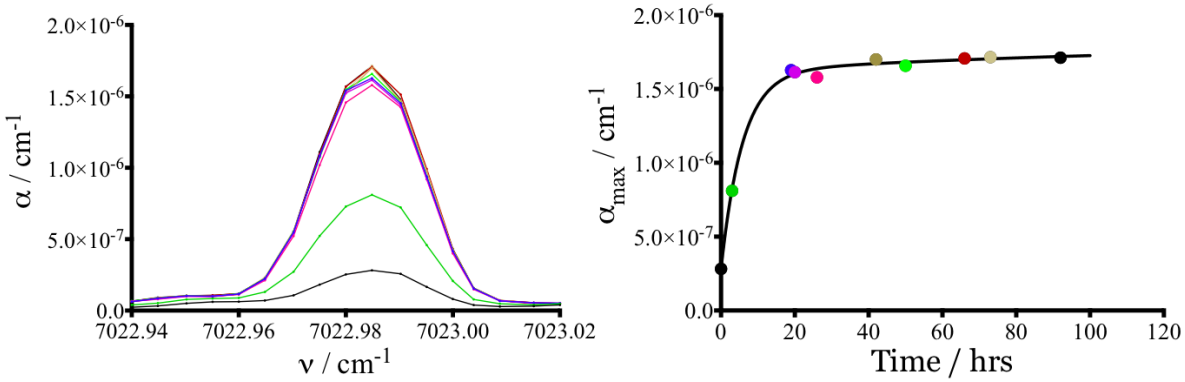

Figure 57: Left graph: DO_2 absorption line at 7022.98 cm^{-1}, scanned twice per day during the full spectra measurement to check the stability of $[DO_2]$. Right graph: maximum of absorption for each individual spectrum at 7022.98 cm^{-1} as a function of the full spectrum measurement time

Therefore, the full spectrum was treated by cutting it into small portions and adapting the multiplication factor accordingly. In good agreement with Figure 57, a higher multiplication factor for subtraction of the HO_2 spectrum was needed for the first parts of the spectrum, i.e. a larger fraction of the initial Cl atoms were converted to HO_2 instead of DO_2 on the first day. To take into account this fact, the DO_2 absorbances of the total spectrum in Figure 61 have been corrected accordingly, supposing that the overall radical concentration, i.e. the initial Cl atom concentration, was stable over the entire measurement period.

4.4.2 Calibration of the DO_2 spectrum

The calibration of the DO_2 spectrum is less straightforward than the calibration described above for the HO_2 spectrum. This is due to the difficulty of getting pure DO_2, and hence the remaining fraction of HO_2 needs to be determined simultaneously. As for the calibration of the HO_2 spectrum, the chlorine concentration was initially converted to HO_2 by addition of CH_3OH, and HO_2 was scanned between 6638.15 and 6638.27 cm^{-1} as shown in Figure 58. Chlorine is estimated to react totally to give HO_2, and thus at the maximum of the HO_2 peak $[HO_2] = [Cl] = 3.17\times10^{12}$ cm^{-3}.

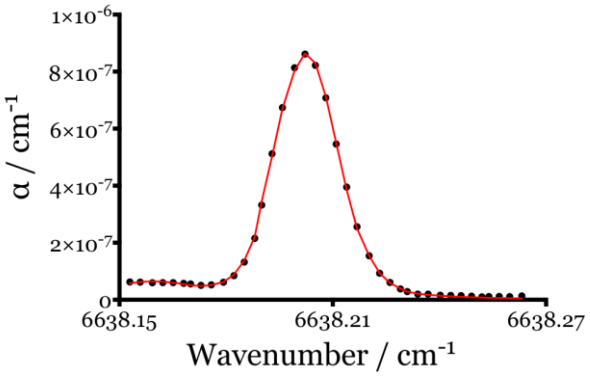

Figure 58: Scan of the HO_2 absorption coefficient between 6638.15 and 6638.27 cm^{-1}. $[HO_2] = 3.17\times10^{12}$ cm^{-3} at the maximum of the peak

Once finished, the CH_3OH flow was turned off and the main helium flow was bypassed through a glass bottle containing D_2O with the goal of replacing as much as possible of the adsorbed H_2O by D_2O. After around 30 minutes, CD_3OD was added and nine DO_2 absorption lines were scanned on one cw-CRDS path. As for HO_2, some of the DO_2 lines are selected according to some criterions to determine their absorption cross-sections σ. The criterions of selection were to have a strong absorption and to be isolated enough from the neighboring lines to avoid any problems of shouldering and having no overlap with HO_2 lines. All the selected peaks were scanned with a resolution of 0.003 cm^{-1} and are presented in Figure 59. These

absorption lines were fitted to a Voigt profile from which the value of absorption coefficient at the maximum of the absorption line was obtained.

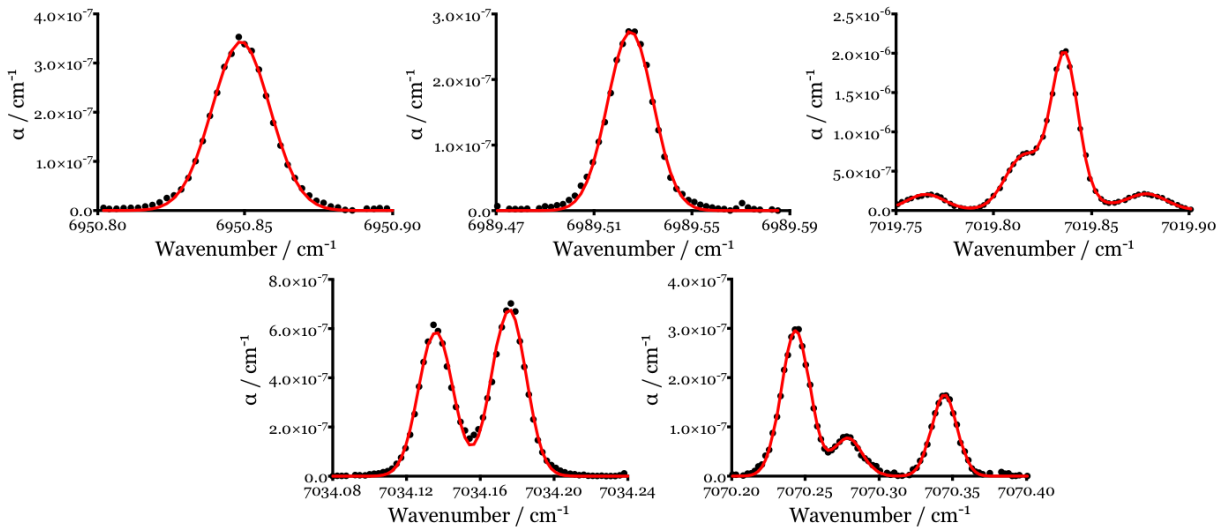

Figure 59: Absorption coefficient of selected DO_2 peaks in eight different wavelength regions. The red full lines are a Voigt adjustment

The remaining HO_2 concentration was simultaneously quantified at 6638.21 cm^{-1} on the second cw-CRDS path at the beginning and at the end of the different scans. The initial and final HO_2 concentrations were similar and equals to 3.50×10^{11} cm^{-3}, so $(COCl)_2$ and the D/H exchange rate did not vary during the scans. The DO_2 concentration was then calculated as the difference between the initial Cl-atom concentration found in presence of CH_3OH and the remaining HO_2 concentration with CD_3OD. This way, 89% of the initial Cl atoms were converted to DO_2, whereas only 57% were converted during the measurement of the full spectrum. Unfortunately, this problem was not highlighted during the measurement of the spectrum and D_2O was not added to the cell. The absorption cross-section of the DO_2 lines have then to be multiplied by a factor of 1.11 in order to have the same amount of chlorine converted to DO_2 or to HO_2, and thus to be able to calibrate the absorption cross-section of DO_2 with the absorption cross-section of HO_2 at 6638.21 cm^{-1}. The absorption cross-section of the selected DO_2 peaks thus measured are listed in Table 8.

Table 8: Absorption cross-section at 50 Torr helium for nine selected lines of DO_2, obtained by simultaneous quantification of the residual HO_2 concentration through the well characterized absorption line at 6638.205 cm^{-1} and the absorbance such as obtained during the measurement of the full spectrum at 20 Torr.

ν / cm^{-1}	α / cm^{-1} at 50 Torr	σ / cm^2 at 50 Torr	α / cm^{-1} full spectrum
6950.85	3.45×10^{-7}	1.21×10^{-19}	8.9×10^{-7}
6989.52	2.78×10^{-7}	9.70×10^{-20}	7.25×10^{-7}
7019.83	8.28×10^{-7}	2.97×10^{-19}	1.98×10^{-6}
7022.98	7.17×10^{-7}	2.51×10^{-19}	1.72×10^{-6}
7034.13	5.88×10^{-7}	2.05×10^{-19}	1.43×10^{-6}
7034.18	6.82×10^{-7}	2.38×10^{-19}	1.61×10^{-6}
7070.24	2.97×10^{-7}	1.04×10^{-19}	7.57×10^{-7}
7070.28	8.03×10^{-8}	2.80×10^{-20}	2.19×10^{-7}
7070.34	1.72×10^{-7}	6.00×10^{-20}	4.62×10^{-7}

In Figure 60 are plotted the absorbance from the full DO_2 spectrum as a function of the absolute absorption cross-section obtained from the scans for the nine lines summarized in Table 8. From the slope of the linear regression it is possible to deduce the concentration of DO_2 radicals during the measurement of the full spectrum to be $[DO_2] = (6.9\pm0.1)\times10^{12}$ cm^{-3}, and this value has been used to convert the absorbances of the full spectrum into absolute absorption cross-section in Figure 61. As for HO_2, the given error is statistical only and other sources of error have to be taken into account: variability of DO_2 concentration during the entire measurement period and uncertainty of the absorption cross-section of the HO_2 line at 6638.205 cm^{-1} used for calibration. A total uncertainty of 20% is estimated.

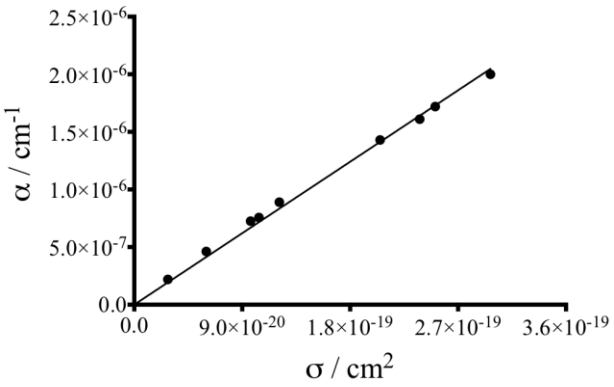

Figure 60: Absorption coefficient α measured during the full scan as a function of the absorption cross-section σ obtained from the comparison with the measured absorption line at 6638.21 cm^{-1}

Similar to the HO_2 case, the DO_2 spectrum was simulated by the Gerätezentrum "Cologne Center for Terahertz Spectroscopy" with the program PGOPHER [95], using the accurate spectroscopic parameters for the 000-000 vibrational band of the electronic transition $^2A' \leftarrow {}^2A''$ provided in the literature [90]. These simulations are compared to the measured data in Figure 61.

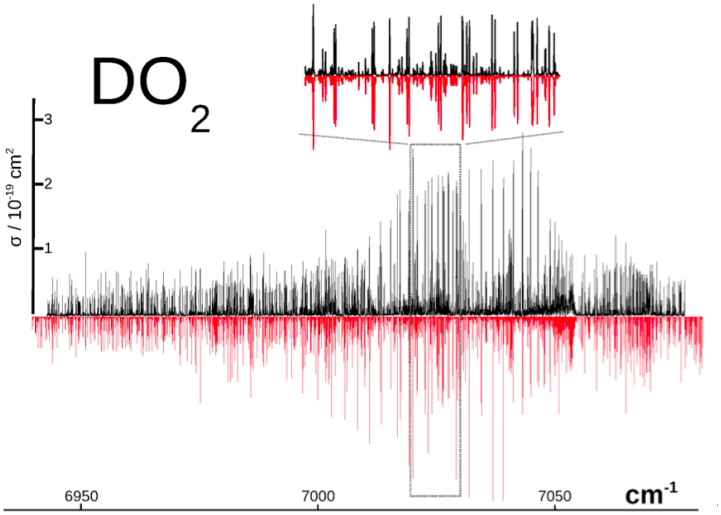

Figure 61: Measured (black upper trace) and simulated (red lower trace) spectra of DO_2 for the 000-000 band of the $^2A' \leftarrow {}^2A''$ electronic transition. The simulation has been performed with PGOPHER [95], based on the accurate molecular constant given in the literature [90]. The zoom in the range 7019.5 to 7030 cm^{-1} shows a strong part Q-branch transitions of the sub-band $K_a' = 1 \leftarrow K_a'' = 0$ as well as the $K_a' = 0 \leftarrow K_a'' = 1$ sub-bands, which show up in pairs belonging to the two spin manifolds F_1 and F_2

As for HO_2, general parameters like the internal temperature, the average linewidth, and the calibration of the used diode laser could be checked. For the DO_2 data set, the intensity distribution corresponds to a fitted temperature of about T = 300 K, a temperature close to room temperature as expected, and slightly below the temperature for HO_2. The difference is within the experimental uncertainty, especially as only the central portion of the transition has been measured. The obtained line width and the small shift of laser wavelength are very similar to the HO_2 case (0.019 cm^{-1} and 0.003 to 0.005 cm^{-1}, respectively)

4.4.3 Pressure broadening of the DO_2 absorption cross-sections

The pressure broadening with helium has been investigated for two absorption lines, the most intense line in the full spectrum range at 7019.83 cm^{-1} and another intense line at 7022.98 cm^{-1} used in this work to check the stability of the DO_2 concentration during the full scan and also already employed for kinetic measurement in previous studies [93]. As for HO_2, the broadening of the DO_2 line at 7019.83 cm^{-1} has been investigated by two different methods: the absorption line has been scanned at four different pressures and the broadening coefficient has been obtained by fitting the absorption lines to a Voigt profile, and for each pressure the peak absorption cross-section has been measured using the kinetic method. This kinetic method has been described previously with the Equation 32 to Equation 35 and is based on determining the time resolved decays of DO_2 radicals. The major removal mechanisms for DO_2 were the self-reaction and diffusion:

$$DO_2 + DO_2 \rightarrow D_2O_2 + O_2 \qquad \text{(R 34a)}$$

$$DO_2 + DO_2 + M \rightarrow D_2O_2 + O_2 (+ M) \qquad \text{(R 34b)}$$

$$DO_2 \rightarrow \text{diffusion} \qquad \text{(R 35)}$$

If the dominant process of consumption of DO_2 is the self-reaction (R 34) then the decay function for radical-radical reactions can be expressed as:

$$\frac{1}{[DO_2]_t} = \frac{1}{[DO_2]_0} + \left(\frac{k_{diff}}{[DO_2]_0} + 2k_{(\mathrm{R\ 34})}\right) t \qquad \text{Equation 36}$$

with $[DO_2]_t$ is the radical concentration at time t after the photolysis pulse and $[DO_2]_0$ is the initial radical concentration at time zero

Plotting $1/[DO_2]_t = f(t)$ results in a slope of $m = (k_{diff}/[DO_2]_0 + 2k)$ and an intercept of $I = 1/[DO_2]_0$. Extrapolation of the slope to infinite $[DO_2]_0$ allows dispensing with the diffusion part, and thus determining the rate constant of the reaction (if the absorption cross-section is known) or the absorption cross-section (if the rate constant is known). In the case of DO_2 two complications arise: first, the rate constant of DO_2 self-reaction is not well-known and only four determination of k(R 34) can be found in the literature [83], [101]–[103] with values varying by more than a factor of three from 4.4 to 14.3×10^{-13} cm^3 s^{-1}, and second, a low concentration of HO_2 was always present and the rate constant for the cross-reaction $HO_2 + DO_2$ is not known and thus it is not possible to estimate the loss of DO_2 through the reaction with HO_2.
The DO_2 lines at 7019.83 cm^{-1} have been scanned at 13.3, 51.9, 79.8 and 98.3 Torr with a resolution of 0.001 cm^{-1} in left graph of Figure 62. This absorption line represents the convolution of two perfectly overlapping lines of same intensity, and even at low pressure no deconvolution could be observed. This absorption line has thus been fitted as one line to a Voigt profile using the Fityk software, leading to the Lorentzian broadening parameter, which has been plotted as a function of the pressure in right graph of Figure 62. A linear regression leads to a broadening coefficient of $\gamma = 0.04382$ cm^{-1} atm^{-1}.

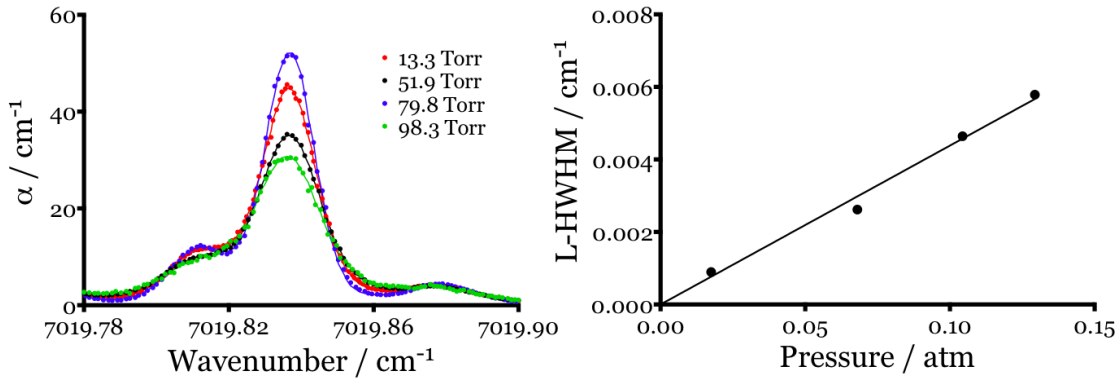

Figure 62: Left graph: absorption spectrum of DO_2 at 7019.83 cm^{-1} for different pressures between 13 and 98 Torr of He. Dots: experimental values, full lines: fits to Voigt profiles. Right graph: Lorentzian HWHM plotted as a function of the pressure

At the end of each scan at each pressure, the absorption cross-section of the line at 7019.83 cm^{-1} was determined using the kinetic method (described with Equation 33 to Equation 35) by measuring four DO_2 decays using four initial concentrations of $(COCl)_2$, varying between $[(COCl)_2] = 3.8\times10^{14}$ to 6.5×10^{14} cm^{-3}, $[O_2] = 1.2\times10^{17}$ cm^{-3}, $[CD_3OD] = 8.6\times10^{14}$ cm^{-3} and a photolysis energy around 60 mJ cm^{-2}. The HO_2 concentration has simultaneously been quantified on the second cw-CRDS path at 6638.58 cm^{-1}. The ratio of HO_2/DO_2 was always small and similar for all pressures (≈ 6% HO_2), therefore to determine the pressure dependence of the peak absorption cross-section it is approximated that the possible impact of HO_2 on the DO_2 decay is the same for all pressures. The Figure 63 shows the DO_2 and HO_2 concentration time profiles at 51.9 Torr for different initial concentrations of $(COCl)_2$.

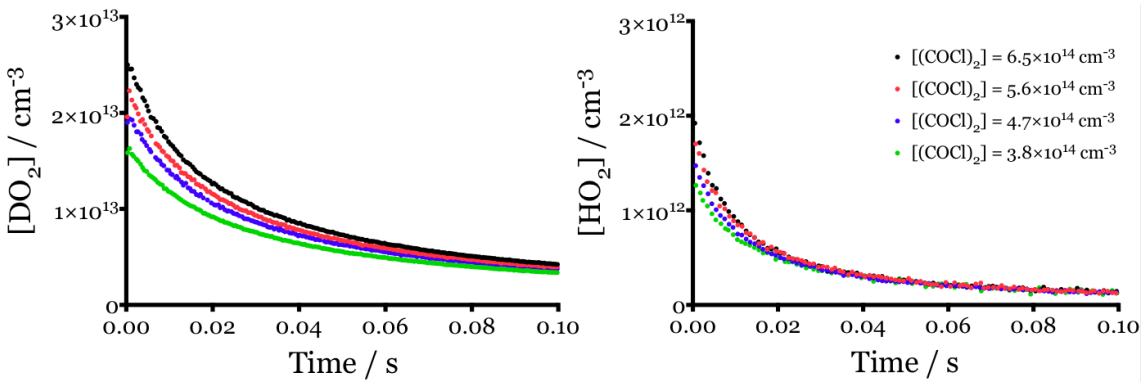

Figure 63: DO_2 and HO_2 concentration time profiles obtained at 51.9 Torr for different $(COCl)_2$ concentrations. Absorption coefficients α have been converted to absolute concentrations by using $\sigma_{7019.83\ cm-1} = 2.97\times10^{-19}$ cm² for DO_2 and $\sigma_{6638.21\ cm-1} = 2.72\times10^{-19}$ cm² for HO_2

From these experiments, the slope m is plotted as a function of the intercept I, as shown in Figure 64. The peak absorption cross-section at 50 Torr has been determined in the above section to be $\sigma_{7019.83\ cm-1} = 2.97\times10^{-19}$ cm², and hence a rate constant can in principle be extracted from an extrapolation to I = 0, i.e. to an infinite DO_2 concentration. This leads to a rate constant of DO_2 self-reaction of k(R 34) = 6.2×10^{-13} cm³ s⁻¹, in good agreement with the values found in the literature: [103] $k_{DO_2+DO_2} = 8.93 \times 10^{-13}$ cm³ s⁻¹, [83] $k_{DO_2+DO_2} = 4.4\times10^{-13}$ cm³ s⁻¹ (measured between 6 and 15 Torr) and [81], [101] $k_{DO_2+DO_2} = 4.9\times10^{-13}$ cm³ s⁻¹, while the other value is more than a factor of 2 higher [102] $k_{DO_2+DO_2} = 1.43\times10^{-12}$ cm³ s⁻¹. However, as explained above, a systematic error can arise from the presence of HO_2 in the reaction cell (which might also have happened in the cited work, but was undetected), and therefore the absolute value of the rate constant should be taken with caution.

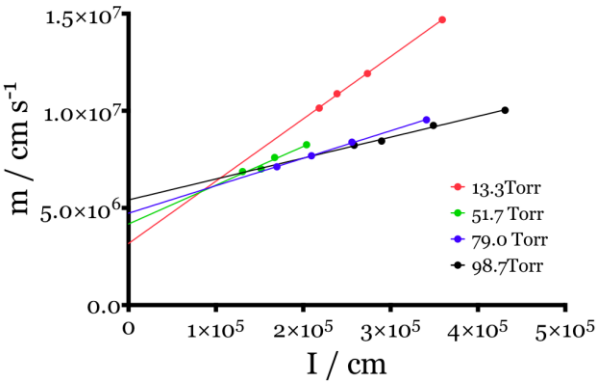

Figure 64: The slope m as a function of intercept I for DO_2 obtained at 7019.83 cm^{-1} between 13.3 and 98.7 Torr and at four $(COCl)_2$ concentrations for each pressure. Extrapolation to I = 0 leads to $m_{[DO_2]_0 \to \infty} = 2k/\sigma$

From other studies [81] it can be deduced that the rate constant is only very slightly pressure dependent. An increase of less than 3% can be estimated under these experimental conditions between 13 to 100 Torr helium. Therefore, the change in the intercept with pressure as shown in Figure 64 is in good approximation directly proportional to the change in the peak absorption cross-section. Taking the value at 50 Torr as reference, the absorption cross-sections $\sigma_{7019.83\ cm\text{-}1}$ = 3.91, 2.97, 2.62 and 2.29×10^{-19} cm^2 can be deduced at 13.3, 51.7, 79.3 and 98.3 Torr, respectively. These values are summarized in Table 9.

This result can be compared with the values obtained by the scanning method. Using the value of broadening coefficient, the absorption cross-sections were then calculated at the same pressures than the measured absorption cross-sections. All the values are summarized in Table 9: the Lorenztian HWHM, the area A and the heights H obtained from the fit of the fully scanned lines using the Fityk program (note that the DO_2 concentration for the scans at different pressures was arbitrary, therefore the absolute values of A and H are also arbitrary). The line strengths S has then been calculated from the area A and heights H, using the absolute absorption cross-section σ for scaling. The consistency has been checked by calculating the peak absorption cross-sections for all for pressures using the Voigt expression with γ_{HWHM} = 0.04382 cm^{-1} atm^{-1} and the average value of the line strengths S = 6.69×10^{-21} cm. The

agreement is excellent with less than 2% difference in the peak absorption cross-sections obtained by both methods.

Table 9: Parameters obtained from a fit using Fityk to a Voigt profile of the scanned lines (Lorentzian HWHM, peak area, peak heights) and peak absorption cross-sections from kinetic measurements for the line at 7019.83 cm^{-1}.

P /Torr	Lorenztian HWHM / cm^{-1}	A / arb. Units	H / arb. Units	σ / cm^2 from kinetic	S / cm	σ / cm^2 from Voigt fit
13.3	8.95×10^{-4}	5.97×10^{-8}	3.37×10^{-6}	3.91×10^{-19}	6.92×10^{-21}	3.84×10^{-19}
51.7	2.62×10^{-3}	1.32×10^{-7}	6.17×10^{-6}	2.97×10^{-19}	6.36×10^{-21}	3.00×10^{-19}
79.3	4.64×10^{-3}	8.90×10^{-8}	3.40×10^{-6}	2.62×10^{-19}	6.86×10^{-21}	2.57×10^{-19}
98.3	5.79×10^{-3}	3.44×10^{-8}	1.19×10^{-6}	2.29×10^{-19}	6.64×10^{-21}	2.33×10^{-19}

A second DO_2 absorption line at 7022.98 cm^{-1} has been scanned at four pressures between 20 and 77 Torr, as shown in Figure 65. After a simulation by the software PGOPHER, it was seen that this line is a convolution of two individual transitions N K_a K_c J = 17 1 17 16.5 ← 17 0 17 16.5 at 7022.982 cm^{-1} and N K_a K_c J = 17 1 17 17.5 ← 17 0 17 17.5 at 7022.991 cm^{-1}, not resolved under the experimental conditions. In a first attempt, the lines have been fitted by the Fityk software to two individual lines with the Doppler width fixed to the theoretical value. These fits lead to very reasonable results: the positions of the two lines were separated by 0.0104 to 0.0111 cm^{-1}, very close to the predicted value given by PGOPHER (0.009 cm^{-1}). The linestrength of the line at 7022.991 cm^{-1} was always slightly higher (between 60-62 % of the total linestrength), also in agreement with the predictions of PGOPHER. The pressure broadening was $\gamma_{7022.982\ cm\text{-}1}$ = 0.0287 cm^{-1} atm^{-1} and $\gamma_{7022.991\ cm\text{-}1}$ = 0.0468 cm^{-1} atm^{-1}. However, to facilitate the extrapolation of peak absorption cross-sections at different pressures, it was more convenient to treat the convolution as one single line. A single Voigt fit reproduces the shape pretty well, as shown in Figure 65.

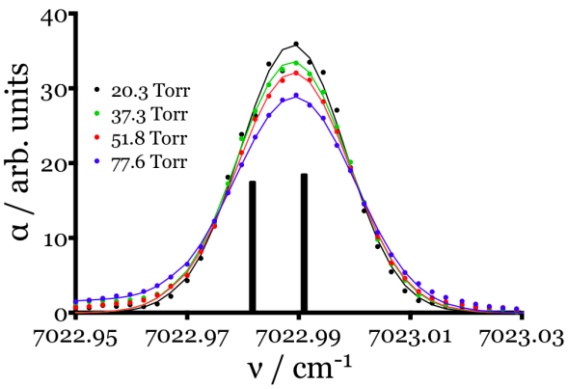

Figure 65: Absorption lines at 7022.98 cm^{-1}, scanned at four different pressures: dots are experimental data, full line shows a Voigt fit to a single line. Black bars are positions of absorption lines such as obtained from PGOPHER

The line strength has been obtained as $S = 7.65\times10^{-21}$ cm, while the pressure broadening at a given pressure is $\gamma = 4.834\times10^{-5} \times p/\text{Torr} + 2.16\times10^{-3}$ cm^{-1}. These parameters have no physical meaning but can be used to extrapolate the absorption cross-sections at different pressures. For the four pressures in this work the values of absorption cross-sections 2.85, 2.66, 2.51 and 2.33×10^{-19} cm^2 are obtained for 20, 37, 52 and 77 Torr helium, respectively. Because it is a convolution of two lines, the peak absorption cross-section at 7022.98 cm^{-1} is less sensitive to pressure broadening. Indeed, extrapolated from 13 to 98 Torr, the peak absorption cross-section of this line decreases by only 27%, while it decreases by 42% for the line at 7019.83 cm^{-1}.

4.5 Determination of the rate constants of DO_2+DO_2 and HO_2+DO_2 reactions

The rate constant of DO_2 self-reaction determined in the previous section does not take into account the presence of HO_2 and the loss of DO_2 through the reaction with HO_2. During the measurements of HO_2 and DO_2 presented in Figure 63, the concentrations of radicals were low and the loss of radicals through other processes such as diffusion was high, and thus it was not straightforward to model these different processes in order to verify the rate constant of DO_2 self-reaction as well as

the rate constant of the cross-reaction HO_2 + DO_2. To increase the concentration of radicals and also to avoid any secondary reactions with photolysis products, the wavelength of the excimer laser was change to 350 nm and Cl_2 was used instead of $(COCl)_2$ to produce the chlorine atoms. The needed DO_2 concentration was too high to be measured on the previously calibrated lines due to saturation and thus another small and isolated line from other DO_2 or HO_2 lines was selected at 7021.15 cm^{-1} for the DO_2 measurements. First, using a rather small concentration of chlorine, two DO_2 lines were scanned in the same conditions at 50 Torr at 7021.15 cm^{-1}, and at 7022.98 cm^{-1}, which has been previously calibrated. The two lines were fitted to a Voigt profile and the maximum of absorption was obtained. At the end of the scans, kinetic measurements were performed at the maximum of each peak with a longer accumulation. The kinetic measurements are presented in Figure 66.

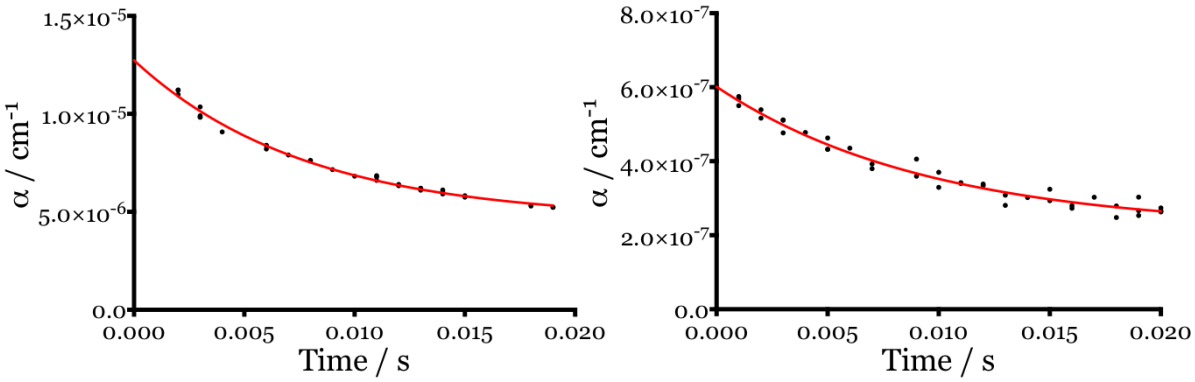

Figure 66: Kinetics measurements at 50 Torr at 7022.98 cm^{-1} (left) and 7021.15 cm^{-1} (right) for $[Cl_2] = 7\times10^{14}$ cm^{-3}, giving $[Cl] = 3.1\times10^{14}$ cm^{-3} with a photolysis energy of 150 mJ cm^{-2}. The absorption coefficient α plotted as a function of the photolysis delay. Red full lines are obtained by fitting the data with an exponential decay

An absorption cross-section of $\sigma_{DO2,\ 7022.98\ cm\text{-}1} = 1.22\times10^{-20}$ cm^2 is obtained with the two methods. The results are presented in Table 10.

Table 10: DO_2 absorption coefficient and absorption cross-section from Voigt profiles and kinetics measurements at 50 Torr helium at 7021.15 cm^{-1} and 7022.98 cm^{-1}

ν / cm^{-1}	α_{scan} / cm^{-1} at 50 Torr	$\alpha_{kinetic}$ / cm^{-1} at 50 Torr	σ / cm^2 at 50 Torr
7021.15	6.13×10^{-7}	6.16×10^{-7}	1.22×10^{-20}
7022.98	1.27×10^{-5}	1.27×10^{-5}	2.51×10^{-19}

The concentration of chlorine was then increased and the rate constants of DO_2 self-reaction and of the HO_2 + DO_2 reaction were determined by measuring three HO_2 and DO_2 decays using three initial concentrations of Cl_2, varying between $[Cl_2] = 3.61\times10^{15}$ to 5.96×10^{15} cm^{-3}, $[O_2] \approx 1\times10^{17}$ cm^{-3}, $[CD_3OD] \approx 5\times10^{14}$ cm^{-3}. The photolysis energy has been around 150 mJ cm^{-2}, giving Cl atoms varying between $[Cl] = 1.60\times10^{14}$ to 2.60×10^{14} cm^{-3}. Under these conditions, DO_2 and HO_2, which is formed due to the D/H exchange, are produced after few microseconds with the DO_2 concentration roughly ten times higher than the HO_2 concentration. The three sets of simultaneous measurements of DO_2 and HO_2 are presented in Figure 67.

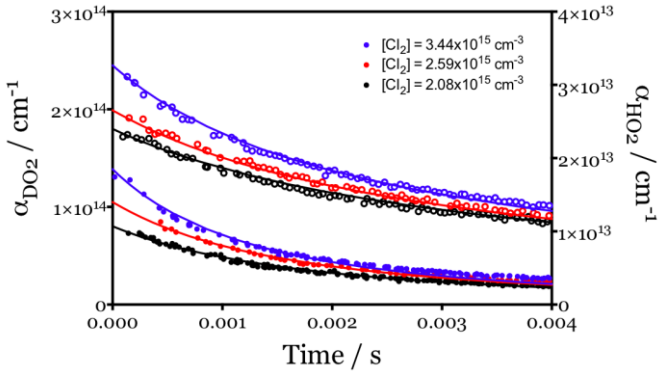

Figure 67: DO_2 (left y-axis, open dots) and HO_2 (right y-axis, full dots) concentration time profiles obtained at 47 Torr helium for different Cl_2 initial concentrations. Absorption coefficients α have been converted to absolute concentrations by using $\sigma_{7021.15\ cm\text{-}1} = 1.22\times10^{-20}$ cm^2 for DO_2 and $\sigma_{6638.21\ cm\text{-}1} = 2.72\times10^{-19}$ cm^2 for HO_2

The experimental data in Figure 67 have been simulated using a simple mechanism listed in Table 11. The diffusion process represents only a minor contribution for DO_2 and HO_2 radical losses. The diffusion is taken into account in the mechanism as a

unimolecular reaction and can be obtained experimentally by fitting the decay at long reaction time, and for all the experiments $k_{diff,DO2}$ = 6 s^{-1} and $k_{diff,HO2}$ = 7 s^{-1} can be found in agreement with the value determined previously [75].

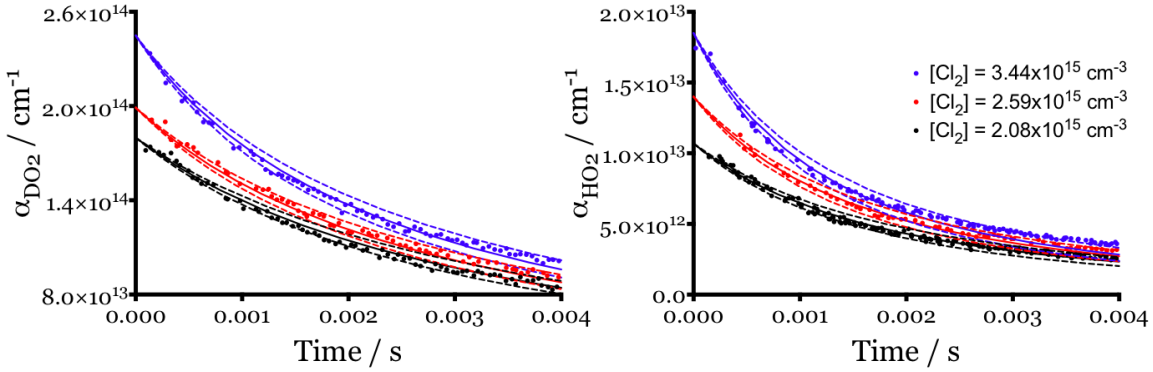

Figure 68: Left graph: DO_2 concentration time profile from Figure 67. Lines show the trace using the rate constants from Table 11. The rate constant (R 34) has been varied between 6.3×10^{-13} (upper dashed lines) and 7.7×10^{-13} cm^3 s^{-1} (lower dotted lines). Right graph: HO_2 concentration time profile from Figure 67. The rate constant (R 36) has been varied between 2.7×10^{-12} (upper dashed lines) and 3.3×10^{-12} cm^3 s^{-1} (lower dotted lines)

The left graph of Figure 68 shows the impact of (R 34), varied between 6.3×10^{-13} and 7.7×10^{-13} cm^3 s^{-1}: increasing k(R 34) leads to a fast DO_2 decay and a lower DO_2 concentration, while it has no significant effect on HO_2 that is not shown here for better clarity. Lowering k(R 34) has the contrary effect. The right graph of Figure 68 shows the impact of (R 36), varied between 2.7×10^{-12} and 3.3×10^{-12} cm^3 s^{-1}: as for DO_2 increasing k(R 36) leads to a fast HO_2 decay and a lower HO_2 concentration, while it has no significant effect on DO_2 that is also not shown here for better clarity, and lowering k(R 36) has the contrary effect.

Thus, the DO_2 and HO_2 decay profiles were very sensitive to the rate constant of the reactions (R 34) and (R 36) and only the values k(R 34) = $(7.0\pm1.0)\times10^{-13}$ cm^3 s^{-1} and k(R 36) = $(3.0\pm0.5)\times10^{-12}$ cm^3 s^{-1} were able to reproduce the experimental data for the three chlorine concentrations. The error has been estimated from varying the rate constants in the model (5%), and increased by 10% due to an uncertainty in the DO_2 and HO_2 radical concentrations.

Table 11: Reaction mechanism used to fit the DO_2 and HO_2 concentration time profiles

No.	Reaction	Rate constant / $cm^3\ s^{-1}$	Reference
(R 34)	$DO_2 + DO_2 \rightarrow D_2O_2 + O_2$	7×10^{-13}	This work
(R 36)	$DO_2 + HO_2 \rightarrow$ products	3×10^{-12}	This work
(R 24)	$HO_2 + HO_2 (+M) \rightarrow H_2O_2 + O_2$	1.6×10^{-12}	[69]
(R 29)	$HO_2 \rightarrow$ diffusion	7	This work
(R 35)	$DO_2 \rightarrow$ diffusion	8	This work

The rate constant k(R 34) is in perfect agreement with earlier results determined using the kinetic method (where k(R 34) = 6.2×10^{-13} $cm^3\ s^{-1}$), confirming that the presence of HO_2 had a minor impact during the measurement with the kinetic method. The value of the rate constants of cross-combination reactions are often estimated using the geometric mean rule [104]:

$$k_{AB} = 2(k_{AA}k_{BB})^{1/2} \qquad \text{Equation 37}$$

With k_{AB} the rate constant of the A+B cross-reaction and k_{AA} and k_{BB} the rate constants of the A+A and B+B self-reactions, respectively

Thus, according to the geometric mean rule a value of k(R 36) = 2.1×10^{-13} $cm^3\ s^{-1}$ can be calculated, which is in good agreement with the value obtained by the model.

4.6 Conclusion

During the data analysis of the CD_3OD and CH_3OH spectrum in the spectral range 6957 to 7077 cm^{-1}, a good part of the observed absorption peaks were due to the presence of HDO and H_2O. The presence of these radicals results from the fact that a fast D/H exchange of the –OD in CD_3OD with H_2O leads to the partial conversion of CD_3OD to CD_3OH and to HDO. Therefore, the CH_3OH and CD_3OD pure spectra were obtained by extracting H_2O and HDO lines.

After the measurement of CD_3OD and CH_3OH spectra, a part of the work was concentrated on the transition from the electronic ground state $^2A''$ into the $^2A'$ excited state ($^2A'' \leftarrow {}^2A'$) of HO_2 and DO_2 radicals, and in particular on their vibrational 000–000 bands. The absorption profiles of HO_2 and DO_2 following the 248 nm photolysis of $(COCl)_2$ in presence of methanol and oxygen have been measured by a combination of laser photolysis with time resolved cw-CRDS. First the relative absorption spectrum of both species was measured in the same spectral range 6957 to 7077 cm^{-1}, and then the absorption cross-sections of few intense and isolated selected lines have been measured to convert the absorption coefficient into absorption cross-section for the entire spectrum. Absolute absorption cross-sections have been obtained through either measuring kinetic decays and retrieving the initial concentration from known rate constants or by comparison with the well-known absorption cross-section of an HO_2 transition in the vibrational overtone region. The strongest absorption cross-sections at 50 Torr helium are $\sigma_{7000.28\ cm^{-1}} = 2.12\times10^{-19}$ cm^2 for HO_2 and $\sigma_{7019.83cm^{-1}} = 2.97\times10^{-19}$ cm^2 and $\sigma_{7022.98cm^{-1}} = 2.51\times10^{-19}$ cm^2 for DO_2. The spectrum has been simulated using the spectroscopic data from earlier papers [89], [90] and reproduced very well the measurements.

The pressure broadening of the HO_2 line at 7000.28 cm^{-1} and of the DO_2 line at 7022.98 cm^{-1} was investigated at different pressures between 10 and 100 Torr helium. These lines were then reproduced by a fit to a Voigt profile using Fityk software. A line strength $S_{HO2\ 7000.28cm^{-1}} = 4.0\times10^{-21}$ cm and a broadening of $\gamma_{HO2\ 7000.28cm^{-1}} = 4.0\times10^{-5} \times$ p/Torr + 9.02×10^{-4} cm^{-1} and a line strength $S_{DO2\ 7022.98cm^{-1}} = 7.65\times10^{-21}$ cm and a broadening of $\gamma_{DO2\ 7022.99cm^{-1}} = 4.834\times10^{-5} \times$ p/Torr + 2.16×10^{-3} cm^{-1} were retrieved. These two parameters can be used in future application to extrapolate the absorption cross-section at different pressures.

Due to the H/D exchange during the study of DO_2 lines, a small amount of HO_2 was always found. To take into account the presence of HO_2 during the measurement of the rate constant of the DO_2 self-reaction, the loss of DO_2 through the reaction with HO_2 has also to be determined by measuring the rate constant of the $HO_2 + DO_2$. The concentration time profiles of HO_2 and DO_2 were followed after the photolysis of Cl_2.

These profiles were then simulated using a simple mechanism and only the rate constants $k_{DO2+DO2} = (7.0\pm1.0)\times10^{-13}$ cm^3 s^{-1} and $k_{HO2+DO2} = (3.0\pm0.5)\times10^{-12}$ cm^3 s^{-1} were able to reproduce the experimental data. The cross-reaction HO_2 + DO_2 is even faster than the HO_2 self-reaction and thus theoretical studies should be performed in order to explain this discrepancy.

Chapter 5 On the CH_3OH+F reactions: rate constants and product yields

5.1 The present understanding of the CH_3OH+F reactions

H-abstraction by fluorine atoms with methanol is known as an efficient method for the production of either free radicals or rovibrationnaly excited HF molecules and has been the subject of several studies. The reaction of F atoms with CH_3OH is highly exothermic and due to the presence of nonequivalent hydrogen atoms on the CH_3-group and the OH-group it leads to the formation of both methoxy, CH_3O, and hydroxymethyl, CH_2OH, through the following competiting reaction channels

$$CH_3OH + F \rightarrow CH_3O + HF \quad \text{(R 37a)}$$

$$\rightarrow CH_2OH + HF \quad \text{(R 37b)}$$

with -128.7 and -166.8 kJ mol^{-1} for (R 37a) and (R 37b), respectively. The two primary formed radical products in the reaction (R 37) may initiate different subsequent reactions. Therefore, the knowledge of the branching ratio is of fundamental importance for laboratory studies. The H-abstraction from the CH_3-group is thermodynamically favored against the H-abstraction from the OH-group, and together with the presence of three equivalent H atoms at the CH_3 group, a high yield or even the exclusive formation of CH_2OH is observed in the reaction of CH_3OH with Cl [105], Br [106], [107], H atoms [108] or OH [105] radicals. Likewise, only a low yield of methoxy radical is expected through the reaction (R 37). However, several experimental studies [105], [109]–[112] over the last 30 years have shown anomalously high CH_3O yields, varying between 0.4 and 0.6. Theoretical studies were able to explain this unexpected high yield through the conclusion that this reaction proceeds through the formation of intermediate complexes, and predicted an even higher CH_3O yield of 0.59 [113] and 0.7 [114].

Most of the above cited studies [105], [109], [111], [112] have been performed in a discharge-flow technique, where F atoms have been generated through a microwave discharge of F_2 and the reaction products have been detected either by LIF for CH_3O or by mass spectrometry for both CH_3O and CH_2OH radicals. Only one study [110] has used pulse radiolysis combined with UV absorption spectroscopy for radical detection.

During this thesis, the yields of CH_2OH and CH_3O were determined in a more direct way. F atoms have been generated through photolysis of XeF_2 at 248 nm and the yields of CH_2OH and CH_3O have then been determined by converting both radicals into HO_2 radicals through their reaction with O_2

$$CH_3O + O_2 \rightarrow HO_2 + CH_2O \qquad \text{(R 38)}$$

$$CH_2OH + O_2 \rightarrow HO_2 + CH_2O \qquad \text{(R 39)}$$

Both radicals can easily be distinguished by taking advantage of the fact that the reaction of $CH_2OH + O_2$ is with $k(R\ 39) = 9.6\times10^{-12}$ cm^3 s^{-1} roughly 5000 times faster than the reaction of $CH_3O + O_2$ with $k(R\ 38) = 1.9\times10^{-15}$ cm^3 s^{-1} [115]. Therefore, using different O_2 concentrations allows distinguishing unequivocally CH_2OH from CH_3O. This is a very direct determination of the ratio of both reaction products, as no absolute concentrations are needed to be measured and no comparison to other reactions is necessary. Using this method, the ratio between both reaction paths is directly obtained.

Under low O_2 concentration, the photolysis of XeF_2 leads after a very short time to a mixture of nearly equal amounts of HO_2, which is obtained in (R 39), and CH_3O. If the rate constant of the HO_2 self-reaction is well known [69], the rate constants of the CH_3O self-reaction or the $CH_3O + HO_2$ cross-reaction are not determined. The rate constant of the CH_3O self-reaction has been estimated [116] to be a very fast with 1×10^{-10} cm^3 s^{-1} and to lead to the formation of CH_2O and CH_3OH. Few experimental determinations [117]–[122] obtain lower values between 1.1 and 3.8×10^{-11} cm^3 s^{-1} for the CH_3O self-reaction, mostly from fitting reaction systems to complex mechanisms. The reaction between CH_3O and HO_2 radicals has received even less attention, and no

experimental determination of the rate constant is available. An estimation from [116] predicts a rate constant of only 5×10^{-13} cm^3 s^{-1} with CH_2O and H_2O_2 being the reaction products. A theoretical investigation of this reaction by [123] predict this time CH_3OH and O_2 to be the major products, but still only with a low calculated rate constant in agreement with the previous estimation [116], even though their calculations predict the reaction to proceed through a submerged barrier.

In the following chapter it will be shown that measuring time-resolved HO_2 profiles at different O_2 concentrations will allow retrieving the yield of CH_3O and CH_2OH in the reaction of F atom with methanol following the photolysis of XeF_2. The rate constants of both CH_3O self-reaction and CH_3O + HO_2 cross-reaction will then be experimentally determined using low O_2 concentrations and it will be shown that the shape of the HO_2 profiles is very sensitive to the rate constants of both reactions. Not surprisingly for radical-radical reactions, fast rate constants have been obtained for both reactions. While the agreement with literature data for the CH_3O self-reaction was found satisfying, the rate constant for the reaction of CH_3O + HO_2 differed by several orders of magnitude with the two only literature values. In order to better understand this strong disagreement, this reaction was again investigated by theoretical methods in collaboration with L. Vereecken.

5.2 Experimental characterization of the CH_3OH+F reaction

5.2.1 Radical generation

During this work, the radicals were generated through pulsed laser photolysis of XeF_2 at 248 nm, leading to F atoms, which in the presence of CH_3OH will generate CH_3O and CH_2OH radicals. Trace amount of water are always present in the photolysis cell, and thus the generation of low concentration of OH radicals through the reaction

$$H_2O + F \rightarrow OH + HF \qquad (R\ 40)$$

cannot be avoided.

XeF_2 is a solid and stable compound and its photochemistry has attracted much attention [124]–[127] as source of F atoms and its co-fragment XeF. The total bond energy in XeF_2 is 265 kJ mol^{-1}, with 252 kJ mol^{-1} located in the first XeF bond [128]. Following the 248 nm photolysis with an energy of 482 kJ mol^{-1}, the XeF fragment decays on the nanosecond time scale to Xe and F, resulting on our experimental time scale in the immediate formation of two F atoms. A fresh mixture of XeF_2 diluted in helium was prepared once per day by introducing a few crystals, typically between 0.3 to 0.5 g, into a homemade double wall Teflon bag. The Teflon bag contains two Teflon Swagelock connectors and was flushed with helium between new fillings. The crystals were introduced under a hood through one of the connectors without taking any precautions such as absence of humidity. The bag was then filled with helium through a calibrated flowmeter, with typically around 50 L. The sublimation of XeF_2 leads to homogeneous mixtures at atmospheric pressure with all the crystals disappearing within a few minutes. The bag contains then less than 1 Torr of XeF_2, well below the XeF_2 vapor pressure ≈ 5 Torr [128]. The flow injected from the bag to the photolysis cell was regulated by a Teflon needle valve and the flow rate was determined through measurement of the pressure increase in a known volume. Typical XeF_2 concentrations in the photolysis cell were 0.5 - 8×10^{14} cm^{-3}, leading to initial F atoms concentrations of 0.5 - 10×10^{12} cm^{-3} using photolysis energies of 10 - 90 mJ cm^{-2}. All experiments have been carried out at a total pressure of 50 Torr helium and at T = 295K, with a photolysis repetition rate of 0.3 Hz. Methanol was introduced into the reaction cell by passing a calibrated flow through a glass bottle containing liquid CH_3OH, thermostated in a water bath to 15°C. The concentrations of methanol were calculated to be around (1-2)$\times10^{15}$ cm^{-3} from the vapor pressure, the total pressure within the glass bottle and total flow rates. F atoms react mostly through (R 37), with only minor contribution through (R 40). The rate constant for the reaction of F atoms with CH_3OH being fast with k(R 37) = 1.6×10^{-10} cm^3 s^{-1} [110], F atoms react immediately on the experimental time scale. O_2 concentrations have been varied between 4.0×10^{14} and 1.2×10^{18} cm^{-3}. The HO_2 radicals are thus formed nearly instantaneously on the experimental time scale through the reaction of $CH_2OH + O_2$ even at the lowest O_2 concentration with $k'(R\ 39)_{,min}$ = 3840 s^{-1}, while for the CH_3O +

O_2 reaction CH_3O radicals are stable on the experimental time scale at the lowest O_2 concentration with $k'(R\ 38)_{,min}$ = 0.8 s^{-1} and is converted to HO_2 only on the millisecond time scale at the highest O_2 concentrations with $k'(R\ 38)_{,max}$ = 2280 s^{-1}.

5.2.2 Determination of the CH_3O/CH_2OH yield

The yield of CH_3O and CH_2OH in the reaction of F atoms with methanol following the photolysis of XeF_2 has been determined on several days by varying the O_2 concentrations while keeping all other parameters including the XeF_2 concentration and the photolysis energy constant. The Figure 69 shows a typical experiment performed during one day where a stable concentration of $[XeF_2]_0 \approx 1\times10^{14}$ cm^{-3} has been photolysed, leading to an initial concentration of F atoms around 2×10^{12} cm^{-3} with a photolysis energy of 90 mJ cm^{-2}, and in large excess of CH_3OH with $[CH_3OH] = 2.7\times10^{15}$ cm^{-3}. The concentration of O_2 has been varied between 1.3×10^{15} and 1.1×10^{18} cm^{-3} while keeping the total flow constant by modulating the additional flow of He. For all O_2 concentrations a rapid formation of HO_2 is observed and can be attributed to the fast reaction (R 39). For the lowest O_2 concentration (black dots in Figure 69) it can be observed that the reaction (R 38) is too slow to have any impact on the HO_2 profile and the slow decay is mostly due to the HO_2 self-reaction and/or a fast reaction between HO_2 and the remaining CH_3O, while diffusion out for the photolysis volume plays only a minor role on this time scale.

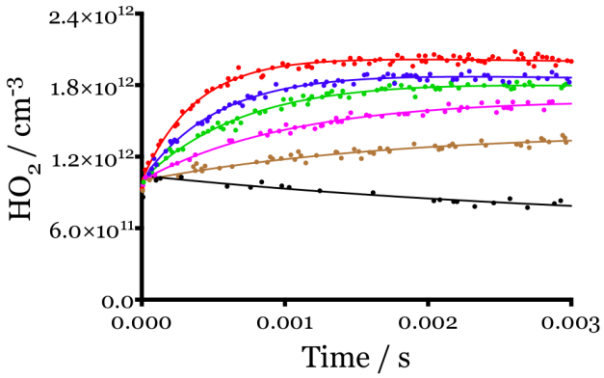

Figure 69: HO_2 concentration time profiles for different O_2 concentrations following the 248 nm photolysis of XeF_2 in excess methanol: $[XeF_2]_0 \approx 1\times10^{14}$ cm^{-3}, $E_{248nm} \approx 90$ mJ cm^{-2}, $[F]_0 \approx 2\times10^{12}$ cm^{-3}, $[CH_3OH] = 2.7\times10^{15}$ cm^{-3}, $[O_2]$ = 11.4, 8.6, 5.8, 3.0, 1.4 and 0.02×10^{17} cm^{-3} from top to bottom.

The formation rate of the secondary HO_2 as well as the maximum HO_2 concentration increases with increasing O_2 concentration. The full lines in Figure 69 correspond to an association-dissociation fit of the HO_2 concentration time profile between 0 and 10 ms, i.e. assuming a pseudo-first order formation and consumption of HO_2 radicals.

$$[HO_2] = [HO_2]_{ini}\, e^{-k_{slow}t} + [HO_2]_{sec}\, \frac{k_{fast}}{k_{slow}-k_{fast}} (e^{-k_{fast}t} - e^{-k_{slow}t}) \qquad \text{Equation 38}$$

From these fits, the initial HO_2 concentration $[HO_2]_{ini}$ can be obtained as the intercept and is attributed to the HO_2 formed through the reaction (R 39), i.e. from CH_2OH, while the amplitude of the association reaction $[HO_2]_{sec}$ can be attributed to the HO_2 formation through the reaction (R 38), i.e. from CH_3O. The decay rate of the HO_2 concentration k_{slow}, which is barely visible in Figure 69 even for the highest O_2 concentration, was always slow with $k_{slow} \approx 10$ s^{-1}. The rate of formation k_{fast} should correspond in a first approximation to the reaction of CH_3O with O_2: in Figure 70 are plotted the HO_2 formation rates k_{fast} as a function of O_2 concentration for all experiments carried out on different days with different initial XeF_2 concentrations.

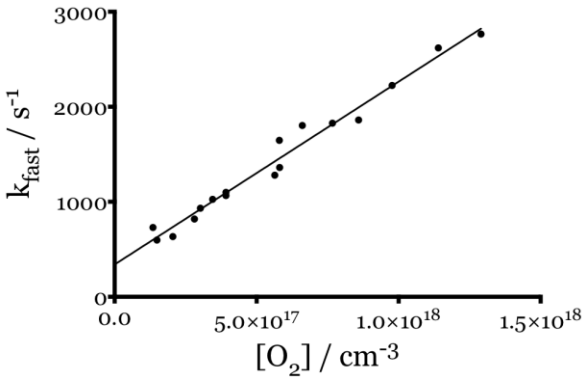

Figure 70: HO_2 formation rates k_{fast} as a function of O_2 concentration

The slope of the linear regression, corresponding to the rate constant of the reaction $CH_3O + O_2$, is with k(R 38) = $(1.92\pm0.08)\times10^{-15}$ cm^3 s^{-1}, in perfect agreement with literature values [115]. The given uncertainty is statistical only with the 95% confidence interval.

The yield of CH_2OH and CH_3O has been deduced from experiments such as shown in Figure 69: in Figure 71 are plotted the ratios of $[HO_2]_{sec}$ / ($[HO_2]_{sec}$ + $[HO_2]_{ini}$), i.e. the CH_3O yields, as a function of O_2 concentration for all series of experiments. Each color indicates a different day of experiment with a different initial F atom concentration. It can be seen that the HO_2 formation from CH_3O increases with increasing O_2 and this effect is more and more pronounced with increasing initial F atom concentration. For the highest F atom concentration (black dots in Figure 71 with [F] ≈ 7×10^{12} cm^{-3}) even at $[O_2]$ = 1×10^{18} cm^{-3} the CH_3O yield is well below 0.4, while at the lowest F atom concentrations (red dots with [F] ≈ 1×10^{12} cm^{-3}) the maximal CH_3O yield is already reached even at O_2 concentrations below 2×10^{17} cm^{-3}.

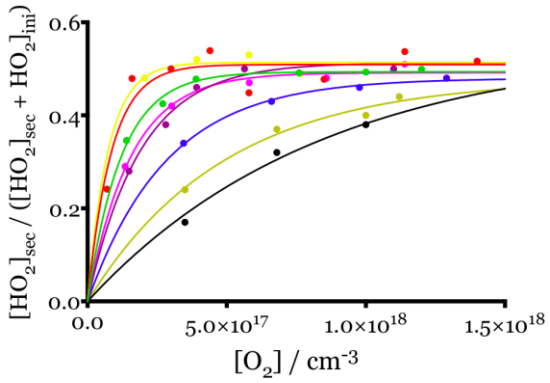

Figure 71: Secondary HO_2 formation yield as a function of O_2 concentration for different initial F atom concentrations. Initial F atom concentrations are 1 (yellow), 1.3 (red), 1.4 (magenta), 2 (green and pink), 4 (blue), 5.2 (brown) and 7×10^{12} cm^{-3} (black). Full lines are fits to an exponential association, forced through 0.

A fit to an exponential association through all data sets leads to an average maximal CH_3O-yield at infinite O_2 concentration of ϕ_{CH_3O} = 0.504±0.013, in excellent agreement with the averaged literature value of 0.52. The observation that the CH_3O yield apparently increases with increasing O_2 concentration is a strong indication that CH_3O radicals react through another reaction path that competes to its reaction with O_2. This effect is more pronounced with increasing radical concentration and therefore a radical-radical reaction can be suspected. Two reactions are primary candidates: the self-reaction of CH_3O and the reaction of CH_3O with HO_2.

5.2.3 Determination of the CH_3O self-reaction and CH_3O+HO_2 reaction rate constants

From the above experiments on the measurement of CH_3O yield it became clear that CH_3O radicals have a competing reaction pathway besides their reaction with O_2. Both possible self-reaction of CH_3O and the reaction of CH_3O with HO_2

$$CH_3O + CH_3O \rightarrow \text{product} \qquad \text{(R 41)}$$

$$CH_3O + HO_2 \rightarrow \text{product} \qquad \text{(R 42)}$$

have been studied. An initial estimation using the above literature values k(R 41) = (1.1 – 3.8) $\times 10^{-11}$ cm^3 s^{-1} shows that only a rather high rate constant can have an impact on the HO_2 profile such as seen in Figure 69. Taking the example of the green dots in Figure 71 where $[CH_3O] \approx [HO_2] \approx 1\times10^{12}$ cm^{-3}, the competing reaction path becomes negligible only above around $[O_2] \approx 3\times10^{17}$ cm^{-3}, i.e. at $k'_5 = 570$ s^{-1}. From this estimation it can be deduced that the competing reaction must be very fast, a rate constant around 1×10^{-11} cm^3 s^{-1} or below for (R 41) or (R 42) should make these reactions negligible at much lower $[O_2]$. In order to determine k(R 41) and k(R 42), several series of experiments at low O_2 concentrations have been carried out. Under these conditions, HO_2, which is generated from CH_2OH, and CH_3O is generated in nearly equal concentrations. Two series of experiments are shown in Figure 72 using the same four different XeF_2 concentrations for each series. The photolysis energies were 90 and 12 mJ cm^{-2} for the left and right graph, respectively.

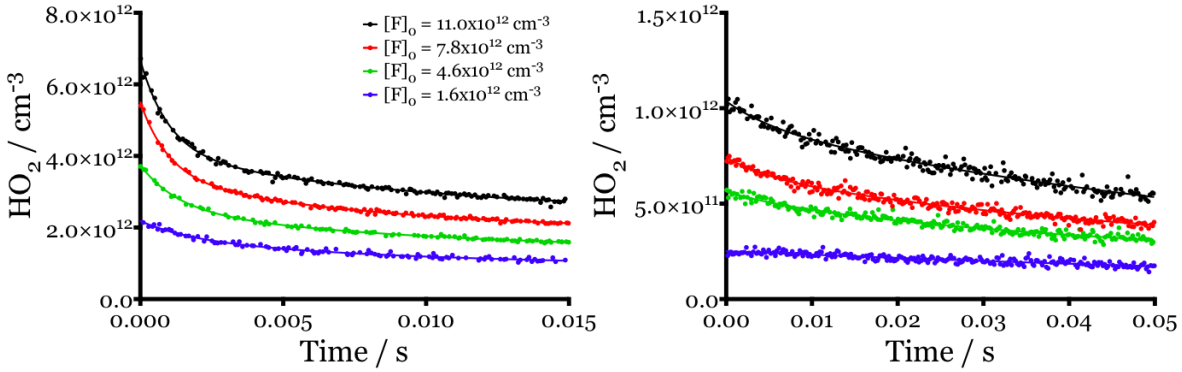

Figure 72: HO_2 concentration time profiles using $[CH_3OH] = 1.4\times10^{15}$ cm^{-3}, $[O_2] = 1.2\times10^{16}$ cm^{-3} and $[XeF_2] = 5.5$ (black), 3.9 (red), 2.3 (green), 0.8×10^{14} cm^{-3} (blue). Photolysis energy was 90 (left graph) and 12 mJ cm^{-2} (right graph). Full lines represent fit to bi-exponential decay. The different time scales should be noted: left graph up to 15 ms, right graph up to 50 ms

For each XeF_2 conditions, HO_2 radicals decay perfectly along a bi-exponential function as presented by the full lines in Figure 72. It was first suspected that the HO_2 decay was governed by the formation of a weakly bound addition complex between HO_2 and XeF_2. This suspicion has been dispersed through experiments with identical

XeF_2 concentrations but different photolysis energies, i.e. different radical concentrations, as shown on the left and right graphs in Figure 72. It can be clearly seen from a comparison between the two graphs that the HO_2 decays are influenced by the radical concentrations, while the influence of the XeF_2 is negligible: slow and nearly identical HO_2 decays are observed in the presence of varying XeF_2 concentrations at low photolysis energies. Therefore, in order to understand the origin of the HO_2 decay, a model presented in Table 12 has been developed and the HO_2 traces with the highest initial radical concentrations in left graph of Figure 72 have been simulated. These simulations are shown in Figure 73 omitting the green trace for improved clarity. The interaction of (R 41) and (R 42) results in a nearly perfect bi-exponential decay showing that the HO_2 profiles are very sensitive to the rate constants of k(R 41) and k(R 42). Indeed, a fast reaction between CH_3O and HO_2 (R 42) decreases rapidly the HO_2 concentration, while at the same time an also fast CH_3O self-reaction (R 41) decreases its concentration and, with this, decreases also the rate of (R 42).

The left graph of Figure 73 depicts the influence of CH_3O self-reaction (R 41) on the HO_2 profile. A higher rate constant for k(R 41), increased from 7 to 9×10^{-11} cm^3 s^{-1}, leads to clearly higher HO_2 concentrations at longer reaction times. This is due to the fact that through a faster CH_3O decay by self-reaction less HO_2 disappears through CH_3O + HO_2 reaction (R 42). In the same manner, decreasing the rate constant from 7 to 5×10^{-11} cm^3 s^{-1} leads to a lower HO_2 concentration at longer reaction times due to a higher CH_3O concentration available for reaction with HO_2. The right graph of Figure 73 shows the impact of the reaction of CH_3O + HO_2 (R 42) on the HO_2 profile: lowering k(R 42) from 11 to 9×10^{-11} cm^3 s^{-1} leads not only to a slower HO_2 decay, but also to higher HO_2 concentrations at long reaction times. Increasing k(R 42) from 11 to 13×10^{-11} cm^3 s^{-1} has the contrary effect.

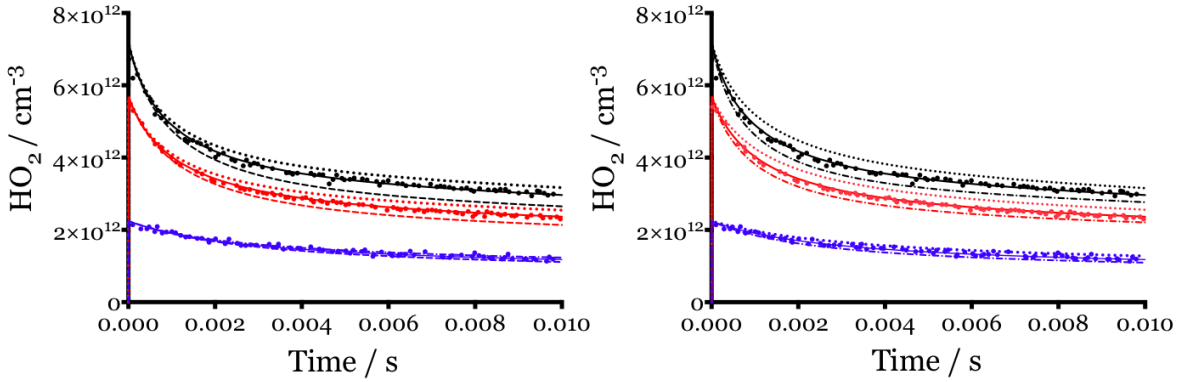

Figure 73: HO_2 concentration time profiles from the left graph of Figure 72 (the green trace is omitted for clarity). Traces obtained using model and rate constants from Table 12. On left graph: the rate constant of CH_3O self-reaction has been varied between 5×10^{-11} cm^3 s^{-1} (lower, dashed-dotted lines) and 9×10^{-11} cm^3 s^{-1} (upper, dotted lines). On right graph: the rate constant of CH_3O + HO_2 reaction has been varied between 9×10^{-11} cm^3 s^{-1} (upper, dotted lines) and 13×10^{-11} cm^3 s^{-1} (lower, dashed-dotted lines)

While increasing k(R 41) or decreasing k(R 42) both lead to higher HO_2 concentrations, HO_2 profiles are only well reproduced within a small range of both rate constants. The effects for both rate constants are clearly visible for the two higher radical concentrations in black and red in Figure 73, while for low radical concentrations in blue the influence of both rate constants is very minor.

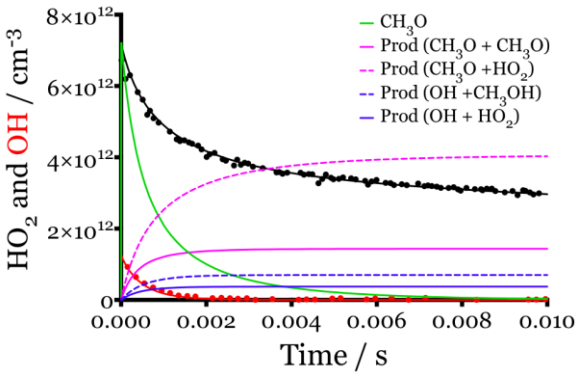

Figure 74: Measured (dots) and modeled (full and dashed lines) concentration time profiles from Figure 73. Traces obtained using model and rate constants from Table 12. OH (red), HO_2 (black), CH_3O (green), product of CH_3O + CH_3O (full pink line), product of CH_3O + HO_2 (dashed pink line), product of OH + CH_3OH (dashed blue line) and product of OH + HO_2 (full blue line)

Figure 74 illustrates the different reaction products for the experiment with the highest radical concentration corresponding to the black profile in left graph of Figure 73. The green line represents the modeled CH_3O profile and it can be seen that its concentration decays much faster and steeper then the HO_2 concentration due to the two parallel reaction paths. OH radicals were always present in the reaction system due to the reaction of F atoms with residual H_2O. Their concentration time profile was always measured simultaneously by cw-CRDS at 7028.83 cm^{-1} and thus their chemistry was taken into account. The major fate of OH radicals in the experimental system is reaction with CH_3OH, generating an HO_2 radical presented by a dashed blue line. However, the impact on the HO_2 profile is attenuated by the competing reaction of OH with HO_2 presented in full blue line. The magenta dashed line represents the product of the (R 42), and it can be seen that this is the major loss for HO_2 radicals. The full magenta line represents the product of the CH_3O self-reaction showing that this reaction rapidly decreases the CH_3O concentration in the beginning of the reaction and thus slows down the HO_2 decay.

Table 12: Reaction mechanism used to model the HO_2 time profiles at different initial F atom concentrations

No.	Reaction	k / cm^3 s^{-1}	Reference
(R 37a)	$F + CH_3OH \rightarrow CH_3O + HF$	8.37×10^{-11}	This work and [110]
(R 37b)	$\rightarrow CH_2OH + HF$	8.23×10^{-11}	This work and [110]
(R 40)	$F + H_2O \rightarrow OH + HF$	1.4×10^{-11}	[129]
(R 39)	$O_2 + CH_2OH \rightarrow CH_2O + HO_2$	9.6×10^{-12}	[115]
(R 38)	$O_2 + CH_3O \rightarrow CH_2O + HO_2$	1.9×10^{-15}	[115]
(R 41)	$CH_3O + CH_3O \rightarrow$ products	7.0×10^{-11}	This work
(R 42)	$CH_3O + HO_2 \rightarrow$ products	1.1×10^{-10}	This work
(R 24)	$HO_2 + HO_2 \rightarrow H_2O_2 + O_2$	1.6×10^{-12}	[69]
(R 43)	$OH + CH_3OH \rightarrow CH_2OH + H_2O$	9.6×10^{-13}	[130]
(R 27)	$OH + HO_2 \rightarrow H_2O + O_2$	1.02×10^{-10}	This work and [75]
(R 29)	$HO_2 \rightarrow$ diffusion	7	This work

The HO_2 concentration time profiles measured during different series of experiments with varying XeF_2 concentration or photolysis energy could be very well reproduced by a simple mechanism using the rate constants k(R 41) = (7.0±1.4)×10^{-11} cm^3 s^{-1} and k(R 42) = (1.1±0.2)×10^{-10} cm^3 s^{-1}. The error has been estimated from varying the rate constants in the model by 10%, and increased by another 10% due to an uncertainty in the absorption cross-section of HO_2 used to calculate the radical concentrations. The same set of rate constants also allows reproducing the O_2 dependence of the CH_3O yields such as shown in Figure 71.

The values can be compared with the sparse data available in the literature, where the rate constant k(R 41) of the CH_3O self-reaction has been determined experimentally several times [117]–[122] with values between 1.1 an 3.8×10^{-11} cm^3 s^{-1}, while a theoretical study [116] evaluated the rate constant to 1×10^{-10} cm^3 s^{-1}. The value obtained during this work is a factor of 2 to 7 faster than the experimental values, but in good agreement with the estimation. No clear reason can be given for the discrepancy. However the earlier works mostly extracted the rate constant from complex mechanism, while in the current work the reaction system is rather simple and the HO_2 profiles are very sensitive to this rate constant. For the rate constant of CH_3O + HO_2 cross-reaction, the disagreement between this study and the only estimation [116] and theoretical estimation [123] is around 3 orders of magnitude. In order to understand this huge disagreement, theoretical calculations have been carried out by L. Vereecken at the Institut für Energie und Klimaforschung in Forschungszentrum Jülich for this reaction.

5.3 Theoretical investigation of the reaction for CH_3O+HO_2

Ab initio calculations have been carried out to obtain the structural parameters of the triplet and singlet potential energy surface (PES) for the CH_3O + HO_2 reaction. Earlier theoretical studies have already characterized this PES [123], but this study shows some additional pathways, while the main reaction pathways are directly comparable

to the literature data. The rate coefficient for the barrierless formation of the triplet pre-reactive complex CH_3O--HOO was calculated as k(300K) = 6.3×10^{-11} cm^3 s^{-1}. An H-abstraction in this complex rapidly produces CH_3OH + $^3O_2$ over a low-lying transition state. This channel competes with redissociation of the complex to the free reactants. A unified treatment [123] of these two sequential steps reveals that redissociation is only a minor channel, owing to the low energy of the competing H-migration transition state, and an effective rate coefficient for methanol formation on the triplet PES is found to be k(300K) = 6.0×10^{-11} cm^3 s^{-1}.

A rate coefficient of k(300K) = 2.5×10^{-11} cm^3 s^{-1} is obtained for the formation of the singlet PES pre-reactive complex. It should be noted that this channel has a priori only a third of the probability of the triplet channel owing to the multiplicities of the electronic spin in reactants and transition state. To assess the products formed in this channel two scenarios are considered, where the first scenario assumes that the pre-reactive complex is well defined. Calculations indicate that CH_3OH + $^1O_2$ formation carries 87 % of the reaction flux at a pressure of 50 Torr He, with most of the remainder, ~10% redissociating to the free reactants. CH_2O + HOOH and stabilized CH_3OOOH are formed in very minor yields near 1.5%, and dissociation to CH_3O_2 + OH is negligible. In 1 atm of N_2 bathgas, CH_3OOOH stabilization increases somewhat to 8%, but CH_3OH + O_2 remains the main product at 80% yield, with still about 10% of redissociation to CH_3O + HO_2. In the second scenario, it is considered that the pre-reactive complex is but a shoulder on the energy profile on the reaction path, with barrierless recombination to CH_3OOOH as the main entrance channel. In this scenario, and at a pressure of 50 Torr of He, it is predicted 89% dissociation of ROOOH to CH_3OH + $^1O_2$, with the remainder redissociating to the free reactants. In 1 atm of N_2 bath gas, it is predicted 15 % of ROOOH formation, 9% of redissociation, and a 76% CH_3OH + $^1O_2$ yield. Thus, both scenarios lead to identical results, within the uncertainties of the analysis, indicating that the presence or absence of the singlet pre-reactive complex has little impact on the rate coefficient or the product distribution.

An overall rate coefficient of k(300K) = 8.3×10^{-11} cm^3 s^{-1}, virtually independent of pressure, is obtained with $CH_3OH + O_2$ as the main product. CH_3OOOH stabilization is expected to be minor with less than 5% overall yield as is formation of CH_2O + HOOH. These results are in excellent agreement with the experimental data, given an a priori uncertainty of at least a factor of 2 on the theory-predicted rate coefficient. Changing the alkyl substrate R in the RO alkoxy radical reactant is not expected to have significant impact on the reaction rate. The main product is likewise expected to remain ROH + O_2, though stabilization of the ROOOH adduct will increase in importance when the R-group becomes larger. However, this product is only formed on the singlet surface, which is predicted to contribute only ~30% to the total reaction rate. This puts an upper limit on the yield of the trioxide product.

These predictions are in clear disagreement with the predictions of the previous literature study [123], where a low rate coefficient for this reaction of 1×10^{-13} cm^3 s^{-1} is predicted. The reason for the discrepancy is not clear, as the PES calculated during this work is comparible with theirs on all major pathways, and the rate coefficients are obtained as expected by chemical intuition for barrierless radical-radical reactions with submerged transition states for subsequent product formation. Exploratory calculations using the energetic data from these authors yielded rate coefficients that are about a factor 10^3 higher than reported, suggesting a computational error in their kinetic analysis.

5.4 Conclusion

The yields of CH_3O and CH_2OH from the reaction of F atoms with CH_3OH have been determined by converting both radicals into HO_2, and taking advantage of their very different rate constants with O_2. Nearly equal amounts of both radicals with a slight excess of CH_3O (ϕ_{CH_3O} = 0.504±0.013) have been found, in agreement with earlier works in the literature and theoretical studies of the reaction mechanism.

In the same reaction system, the rate constant of the CH_3O self-reaction as well as of the reactions between CH_3O + HO_2 has been determined. The HO_2 concentration time profiles measured during different series of experiments with varying XeF_2 concentration or photolysis energy could be very well reproduced by a simple mechanism using the rate constants $k_{CH3O+CH3O}$(R 41) = (7.0±1.4)×10^{-11} cm^3 s^{-1} and $k_{CH3O+HO2}$(R 42) = (1.1±0.2)×10^{-10} cm^3 s^{-1}.

While the rate constant of CH_3O + CH_3O has already been determined a few times and the results obtained in this work are in reasonable agreement with the available literature data, this is the first determination of the rate constant for the reaction of CH_3O + HO_2. Only one estimation and a theoretical calculation are available, with however a rate constant of 3 orders of magnitude lower. Therefore, this reaction has been re-examined by theoretical methods, and a fast rate constant, in agreement with the experimental determination, has been obtained. No valid reason for the huge disagreement could be identified. The thus determined yields and rate constants could now be used for the determination of F atom concentration after their conversion into HO_2 radicals, which can be measured using their well characterized absorption cross-sections.

Chapter 6 The reactions between $C_xH_{2x+1}O_2$ + OH (x=1 to 4): rate constants, product yields, and atmospheric implications

6.1 The present understanding of the $C_xH_{2x+1}O_2$ + OH (x=1 to 4) reactions

Peroxy radicals (HO_2 and RO_2, where R represents a carbon chain) play a central role in the chemistry of the Earth's atmosphere and are key species in combustion processes. In the atmosphere, their subsequent chemistry is in the center of the cycling of reactive radicals and on the formation of tropospheric ozone and other important secondary pollutants. In the troposphere, peroxy radicals are generated in the photochemical oxidation of all hydrocarbon species as shown in the reaction scheme in Figure 75.

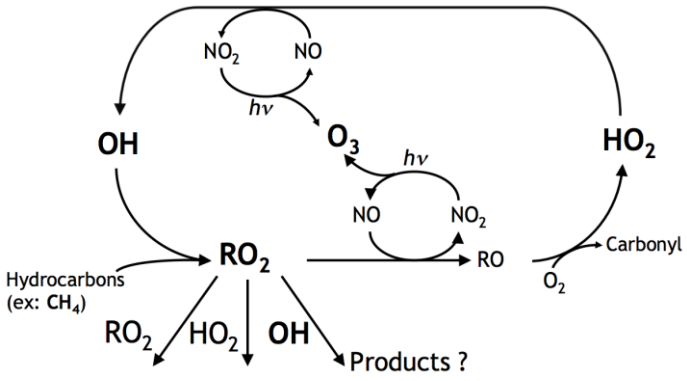

Figure 75: Simplified schematic diagram of the most common reactions of peroxy radicals in the troposphere

The subsequent fate of peroxy radicals depends on the air quality. In polluted environment, thus in presence of high NO_X (= NO + NO_2) concentrations due to anthropogenic activities, they will rapidly react with NO to form NO_2 and alkoxy

radicals RO. The NO_2 will be photolysed and will form a first molecule of ozone O_3. The RO coproduct can further react with O_2 to form a carbonyl compound (aldehyde or ketone) together with HO_2. The reaction of HO_2 with NO recycles the OH radical and produces NO_2, finally leading to the formation of a second O_3 molecule. The OH can generate another RO_2 by reaction with a hydrocarbon RH. Under conditions of low NO_X concentration (<30 ppt), which occur in unpolluted troposphere, reactions between peroxy radicals are significant and are important considerations when determining local ozone production rates. The RO_2 self- or cross-reactions with HO_2 or other peroxy radicals play a larger role and lead mostly to chain termination and radical removal and to the formation of stable products [2].

Until recently, only the reactions with other RO_2 radicals or with HO_2 were taken into account in detailed atmospheric chemistry models such as Master Chemical Mechanism (MCM) [131]. However, a new reaction pathway has been suggested as a possible competitive fate for RO_2 in clean environments: the reaction with OH radicals. In a modeling study [61], the impact of including the reaction between RO_2 and OH on the composition of the Marine Boundary Layer (MBL) was investigated. Different scenarios were run using the BAMBO based on the MCM, and their model showed that, depending on the rate constant and on the reaction products, this type of reaction could have a strong influence on the concentration of several trace species. The following possible products of the reaction with OH were simulated giving for the simplest peroxy radical CH_3O_2:

$$CH_3O_2 + OH \rightarrow CH_2OO + H_2O \qquad \text{(R 44a)}$$

$$\rightarrow CH_3O + HO_2 \qquad \text{(R 44b)}$$

$$\rightarrow CH_3OH + O_2 \qquad \text{(R 44c)}$$

For all the scenarios, they found only a small, negligible effect on the mixing ratios of O_3, NO_X, OH and other trace gas species in the MBL. However, a substantial increase in the mixing ratio of HCOOH was observed if the major reaction pathway was the formation of Criegee radical (R 44a), from 0.16 ppt in absence of (R 44) to 25.5 ppt

with the largest rate constant scenario. If the major pathway was (R 44c), a strong increase in the mixing ratio of CH_3OH was observed, from 37 ppt in absence of (R 44) to 294 ppt with the largest rate constant scenario. And finally, the impact on stable species was the smallest if the reaction (R 44b) was the major pathway. Ab initio calculations [132], [133] predict the pathway (R 44b) to be the major reaction, with possible minor contributions of (R 44c). Very recently a study [133] has implemented the title reaction into a global atmospheric chemistry model and has shown, that a yield of around 18% for (R 44c) could explain a large missing source of methanol over remote oceans. It seems therefore important to determine experimentally the product distribution of (R 44).

The rate constant has been measured recently for the first time for the two simplest peroxy radicals

$$CH_3O_2 + OH \rightarrow \text{products} \qquad \text{(R 44)}$$

$$C_2H_5O_2 + OH \rightarrow \text{products} \qquad \text{(R 45)}$$

Large rate constants k(R 44) = $(2.8\pm1.4)\times10^{-10}$ cm^3 s^{-1} and k(R 45) = $(1.2\pm0.3)\times10^{-10}$ cm^3 s^{-1} have been measured for CH_3O_2 by Bossolasco et al. [134] and $C_2H_5O_2$ [59], respectively. With such fast rate constants, these reactions can become competitive to the other reaction paths as peroxy radical sink. CH_3O_2 is a very important radical particularly over the tropical oceans, where a large fraction of the global CH_4 emission is processed [135]. Neglecting an important path for this radical might therefore lead to a bias in HO_X concentration, CH_4 lifetime or O_3 formation and destruction rate. Integration of the rate constant k(R 44) into the MCM model [60] showed that up to 30% of all CH_3O_2 would react through this channel under remote marine conditions such as found at Cape Verde [136]. In a recent study of Yan et al. [137], the rate constant k(R 44) has been remeasured with k(R 44) = $(8.7\pm1.7)\times10^{-11}$ cm^3 s^{-1} at 298 K, more than a factor of 3 slower than the previous measurement of Bossolasco et al. [134]. With such a slow rate constant, (R 44) would play a less important role as sink of CH_3O_2 radicals in remote environments and would have only a small impact on the CH_3OH concentration, even with a high yield. This makes clear that it is important to

improve the knowledge of this class of reactions by remeasuring the rate constants as well as identifying the reaction products.

In the current chapter, new experiments for determining the reactivity of CH_3O_2, $C_2H_5O_2$ and the next larger peroxy radicals, $C_3H_7O_2$ and $C_4H_9O_2$, with OH radicals are presented. Experiments have been carried out using different precursors than in the previous studies. Experiments for the determination of the yields of the possible products have also been carried out. The results of the experiments on the reaction (R 44) have been implemented into a box model utilizing the MCM, and the impact on the composition of the remote atmosphere has been determined. In addition, the absorption cross-section of CH_3O_2, a parameter on which the rate constant k(R 44) directly depends in our experiment, has also been remeasured because available literature data were not in agreement. All experiments have been carried out at a total pressure of 50 Torr helium and at T = 295 K, with a photolysis repetition rate of 0.3 Hz.

6.2 Experimental characterization of the CH_3O_2+OH reaction

In the previous study of Bossolasco et al. [134], CH_3O_2 radicals were generated by the photolysis of CH_3I at 248 nm in the presence of an excess of O_2, while OH were generated by simultaneous photolysis of H_2O_2. CH_3O_2 radicals had been generated in a large excess over OH, ensuring pseudo-first order conditions for OH radicals. It was then only necessary to determine exponential decay rates of OH radicals in the presence of known concentrations of CH_3O_2 radicals. The absolute concentration of CH_3O_2 was quantified by cw-CRDS at 7489.16 cm^{-1} with an absorption cross-section σ determined previously [19] based on the kinetic method described above. The relative OH concentration was obtained from high repetition rate LIF with a 100 μs time resolution. A detailed kinetic model including the reaction of I atoms, which was co-generated at equal concentration with CH_3O_2 during the photolysis of CH_3I, with CH_3O_2 had been employed to take into account the possible impact of I atoms on

CH_3O_2 concentration [138]. However, no information could be found on the reaction between I atoms and OH radicals. Only low CH_3O_2 concentrations were used (up to 10^{13} cm^{-3}) and thus only low concentrations of I atoms were present. Given the very fast rate constant k(R 44), only a rate constant in the 10^{-10} cm^3 s^{-1} range would make a possible reaction of I atoms with OH competitive with CH_3O_2 for the OH decay. Given the low pressure in these experiments (50 Torr He) it was supposed that a possible reaction of I atoms with OH radicals would be too slow to have an impact on the OH decay and so this reaction was not added to the model. Using a large range of precursor concentrations and photolysis energies, consistent and reproducible results were obtained, leading to the very fast rate constant of k(R 44) = $(2.8\pm1.4)\times10^{-10}$ cm^3 s^{-1}.

Later [59], the rate constant of $C_2H_5O_2$ + OH was determined k(R 45) = $(1.2\pm0.3)\times10^{-10}$ cm^3 s^{-1} and found to be two times slower than k(R 44). However $C_2H_5O_2$ radicals could not be quantified by cw-CRDS as CH_3O_2 because the absorption lines of $C_2H_5O_2$ were out of the reach of the laser diode and, in addition, their absorption cross-sections in the near infrared are not well known. Thus another strategy had been adopted for $C_2H_5O_2$ radicals: they were generated by the reaction of Cl atoms, which were produced by the 248 nm photolysis of $(COCl)_2$, with C_2H_6. The initial concentration of Cl atoms was determined from back-to-back experiments by first converting them by reaction with CH_3OH into HO_2, which can be quantified by cw-CRDS on the well-characterized absorption line at 66388.205 cm^{-1} [64], [70], [73], and then to $C_2H_5O_2$ by reaction with C_2H_6. This method cannot be applied for measuring k(R 44) because the reaction of Cl atoms with CH_4 is only 15 times faster than the reaction of OH radicals with CH_4 (compared to a much higher ratio of ~ 240 for C_2H_6) [115] and would thus lead to a competition between CH_4 and CH_3O_2 for OH radicals. Hence, the two different approaches used to measure the rate constant k(R 44) and k(R 45) could have been biased through two sources of systematic errors that could occur:

(i) The quantification of the CH_3O_2 concentration relies on the determined value of the absorption cross-section of CH_3O_2, while the quantification of the $C_2H_5O_2$

concentration relies on the much better known absorption cross-section of HO_2. To rule out any error due to the CH_3O_2 quantification, the CH_3O_2 absorption cross-section has been remeasured during this work using two different methods: the kinetic method described in chapter 4 but using a different I atom free precursor, and a relative method based on comparing the absorbance of CH_3O_2 with the absorbance of HO_2.

(ii) I atoms were present during the measurement of k(R 44), while the coproduct during the measurement of k(R 45) was HCl. To investigate any unidentified bias due to I atoms, the rate constant k(R 44) was determined again by measuring the OH decays in the presence of excess CH_3O_2 radicals, now preparing CH_3O_2 from a different I atoms free precursor.

6.2.1 Absorption Cross-section of CH_3O_2

6.2.1.1 Using the kinetic method on CH_3O_2 self-reaction

The absorption cross-section of CH_3O_2 has been determined previously by using the kinetic method described previously in Equation 31 to Equation 35 and taking advantage of the rather well known rate constant of the self-reaction of CH_3O_2 radicals [115] to determine the initial radical concentration. In the previous study [19], CH_3O_2 was formed following the photolysis of CH_3I in the presence of excess O_2. The main reaction sequence consists of the following reactions:

$$CH_3I + h\upsilon_{248nm} \rightarrow CH_3 + I \qquad \text{(R 46)}$$

$$CH_3 + O_2 (+M) \rightarrow CH_3O_2 \qquad \text{(R 47)}$$

$$2\ CH_3O_2 \rightarrow 2\ CH_3O + O_2 \qquad \text{(R 48a)}$$

$$\rightarrow CH_2O + CH_3OH + O_2 \qquad \text{(R 48b)}$$

$$\rightarrow CH_3OOCH_3 + O_2 \qquad \text{(R 48c)}$$

The rate constant of the reaction (R 47) is pressure dependent and has been measured in the low-pressure limit [139] (1-6 Torr of helium and argon) as well as in the high-pressure limit [140]. Using an extrapolation of both results with k_o and k_∞, a rate constant of $k(R\ 47)_{,50Torr\ He} = 1.4\times10^{-13}$ cm^3 s^{-1} is calculated. Under the O_2 concentrations used in the previous work, which are roughly the same during this work with $0_2 \approx 4.7\times10^{17}$ cm^{-3}, the reaction (R 47) is therefore completed in a few 10 µs. The fast CH_3 self-reaction with $k_{CH3+CH3} = 5.99\times10^{-11}$ cm^3 s^{-1} is also non-negligible especially under high radical concentrations. However this reaction takes place on a very short time scale and thus CH_3 as well as the product C_2H_6 do not influence the CH_3O_2 decay but only result in a lower initial concentration of CH_3O_2. The recommended values [115] at 298 K of the rate constant is $k(R\ 48) = 3.5\times10^{-13}$ cm^3 s^{-1} with a branching ratio k(R 48a)/k(R 48) = 0.37. The CH_3O formed during the reaction (R 48a) reacts with O_2, which induces secondary reactions:

$$CH_3O + O_2 \rightarrow CH_2O + HO_2 \qquad (R\ 38)$$

$$CH_3O_2 + HO_2 \rightarrow CH_3OOH + O_2 \qquad (R\ 49a)$$

$$\rightarrow CH_2O + H_2O + O_2 \qquad (R\ 49b)$$

The recommended values [115] for the rate constants at 298 K are $k(R\ 38) = 1.9\times10^{-15}$ cm^3 s^{-1} and $k(R\ 49) = 5.2\times10^{-12}$ cm^3 s^{-1}. These two reactions lead to an acceleration of the CH_3O_2 decay rate. The apparent "observed" rate constant $k(R\ 48)_{obs}$ of the self-reaction taking into account an additional decay of CH_3O_2 radicals through reaction with the reaction product HO_2 has been recommended [115] as $k(R\ 48)_{obs} = 4.8\times10^{-13}$ cm^3 s^{-1}. CH_3O_2 decays through self-reaction as well as through diffusion out of the photolysis volume. The diffusion can be well approximated in the current setup [23] as an exponential loss k_{diff}, and with this the CH_3O_2 concentration time profile can be described by the following equation using the approximation that the CH_3O_2 self-reaction is the major loss process:

$$\frac{1}{[CH_3O_2]_t\,\sigma} = \frac{1}{[CH_3O_2]_0\,\sigma} + \left(\frac{k_{diff}}{[CH_3O_2]_0\,\sigma} + \frac{2k(\mathrm{R\ 48})_{obs}}{\sigma}\right)t \qquad \text{Equation 39}$$

A plot of Equation 39 results then in a straight line with the slope m = (k_{diff} /[CH_3O_2]$_0$ σ + 2k(R 48)$_{obs}$/σ) and the intercept I = 1/[CH_3O_2]$_0$ σ. Therefore, measuring kinetic decays at different initial CH_3O_2 concentrations allows distinguishing between losses due to self-reaction and losses due to diffusion. Plotting m as a function of I and extrapolating toward I = 0, i.e. for an infinite CH_3O_2 concentration, allows retrieving a value of the absorption cross-section. This procedure also minimizes possible uncertainties introduced through the approximation of the diffusion process to an exponential decay. Doing so, $\sigma_{CH3O2,7489.16cm-1}$ = (3.4±0.4) ×10^{-20} cm² was previously obtained [19], a value two to three times higher than the only two earlier determinations [18], [141], even though the same approach was used.

The determination of the rate constant k(R 44) of the reaction CH_3O_2 + OH directly depends on the absorption cross-section of CH_3O_2, and using the smaller value of σ_{CH3O2} from earlier works [18], [141] would lead to a rate constant k(R 44) a factor of two to three smaller and thus in much better agreement not only with the rate constant k(R 45) of the reaction $C_2H_5O_2$ + OH, but also in perfect agreement with the rate constant k(R 44) such as obtained very recently by Yan et al. [137]. Therefore, it seems important to repeat the determination of σ_{CH3O2} by using another I atom free precursor.

The photolysis of XeF_2 in presence of CH_4 and an excess O_2 was thus used for the generation of CH_3O_2 radicals through the reactions:

$$XeF_2 + h\upsilon_{248nm} \rightarrow 2\ F + Xe \qquad (R\ 50)$$

$$CH_4 + F \rightarrow CH_3 + HF \qquad (R\ 51)$$

followed by the reaction sequence (R 47)-(R 49) detailed above. The typical XeF_2 concentrations in the photolysis cell were 0.6 - 7×10^{14} cm^{-3}, leading to initial F atoms concentration of 1-10×10^{12} cm^{-3} using a photolysis energy of 100 mJ cm^{-2}. An attempt of quantifying the reaction product HF by cw-CRDS at 7618.519 cm^{-1} [26] following the XeF_2 photolysis failed due to the presence of too much HF already present in the photolysis cell before the photolysis pulse, probably already generated within the Teflon bag due to the presence of water, leading to a saturation of the absorption line.

With a line strength of S = 4.62×10^{-20} cm, the peak absorption cross-section can be estimated to be $\sigma \approx 2\times10^{-18}$ cm² under low-pressure conditions. It can therefore be calculated that a concentration of 5×10^{12} cm^{-3}, i.e. around 1% of the initial XeF_2, would already lead to a very strong absorption. The XeF_2 concentration was nevertheless rather stable from the Teflon bag with the ratio of measured to expected radical concentration decaying only slowly, with ~ 5%/hour or less. HF does not absorb at 248 nm and is rather unreactive at ambient temperature. Therefore, its presence in the photolysis cell is not thought to interfere with the reaction system. High CH_4 concentrations have been used with $[CH_4] = 5\times10^{15}$ cm^{-3} in order to minimize any OH formation in the competing reaction of F atoms with residual H_2O present in the photolysis cell. However, any OH that is formed would react within the first few milliseconds with CH_3O_2, while the CH_3O_2 decays have been fitted in Equation 39 between 5 and 50 ms. A plot of the slope m as a function of I is presented in Figure 76. An extrapolation of the linear regression toward I = 0, i.e. to an infinite CH_3O_2 concentration, results in $m = (2.8\pm0.3)\times10^7$ cm s^{-1}. Thus, using the value of $k(R\ 48)_{obs} = 4.8\times10^{-13}$ cm^3 s^{-1}, the absorption cross-section $\sigma_{CH3O2,7489.16cm-1} = (3.4\pm0.4)\times10^{-20}$ cm² is obtained and is in perfect agreement with the previous determination [19]. The slight difference in the slope, with 14.5 s^{-1} in this work and 26.3 s^{-1} in the previous work, represents probably the different geometrical outline of the current experiment compared to the outline used previously [19]: a larger excimer pulse is now used, with 2.5 cm instead of 2 cm, leading to a slower loss of radicals due to diffusion in the current experiments.

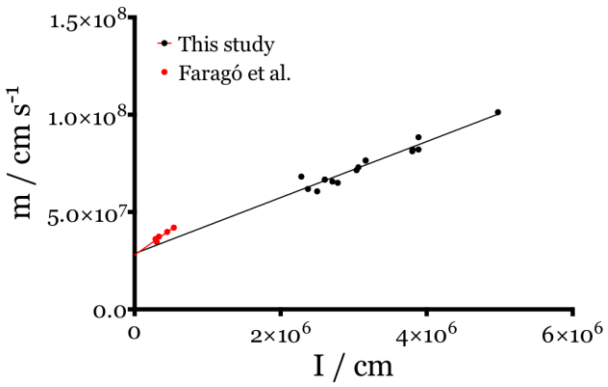

Figure 76:Plot of the slope m as a function of I from Equation 39 for CH_3O_2 decays. Red dots: data from previous studies [19] for the same wavelength using CH_3I as precursor. Black dots: data from this study using F + CH_4 as precursors. All experiments were carried out at 50 Torr helium

From these experiments it can be concluded that the cogenerated I atoms had no impact on the CH_3O_2 decays in the previous study. Even though the CH_3O_2 self-reaction has been studied many times [115] and is believed to be well-known, a doubt might still persist on the accuracy of σ_{CH3O2} determined using the above described method. Therefore, a second approach has been used in this work to measure the absorption cross-section, independent of any uncertainty linked to the kinetic of the CH_3O_2 self-reaction.

6.2.1.2 By direct comparison with HO_2 absorption cross-section

For these experiments, both cw-CRDS paths have been used with one path dedicated to HO_2 radical detection at 6638.205cm^{-1}, while the second path was dedicated to CH_3O_2 radical detection at 7489.16 cm^{-1}. F atoms from the XeF_2 photolysis were used for the radical generation, and were converted in back-to-back experiments either into CH_3O_2 by adding CH_4, or into HO_2 by adding CH_3OH both in a presence of large concentrations of O_2. All other conditions of pressure, photolysis energy and XeF_2 flow were kept constant. This approach was not possible during the previous experiments [19] because the positions of the absorption lines of both species are too

far from each other to be accessible with the same set of cavity mirrors. Changing cavity mirrors involves a vacuum breakdown and alignment of the experiment and can take one day or more, and hence it is not sure to find again the same conditions, especially when using XeF_2 as a radical precursor.

From the ratio of absorbance α for CH_3O_2 and HO_2 measurements, it is possible to deduce the absorption cross-section σ for CH_3O_2 using the well-known absorption cross-section of HO_2. The Figure 77 shows the absorbance α_{HO2} plotted on the left y-axis and α_{CH3O2} plotted on the right y-axis as a function of the time. It can be seen that the signal-to-noise ratio is better for HO_2 than for CH_3O_2 for two reasons: (i) the mirrors used in the HO_2 wavelength range have a higher reflectivity compared to the mirrors for CH_3O_2, leading to $\tau_0 \approx 80$ µs and $\tau_0 \approx 30$ µs respectively, and (ii) the absorption cross-section is roughly ten times higher for HO_2 than for CH_3O_2. It can also be seen that the decay rate of HO_2 is faster compared to CH_3O_2 due to the much faster rate constant of HO_2 self-reaction compared to the CH_3O_2 self-reaction. The HO_2 signal rises within a few milliseconds, due to the fact that the reaction of F atoms with CH_3OH leads to two products, CH_2OH and CH_3O with roughly equal yields [113] as described in the previous chapter: while the reaction $CH_2OH + O_2$ is very fast with $k = 9.6\times10^{-12}$ cm³ s⁻¹, $CH_3O + O_2$ is with $k = 1.65\times10^{-15}$ cm³ s⁻¹ rather slow [115] and a complete conversion takes a few milliseconds in the presence of $[O_2] = 4.7\times10^{17}$ cm⁻³. Under these conditions it can be assumed that identical concentrations of HO_2 and CH_3O_2 are generated. Indeed, taking the secondary reactions $CH_3O + CH_3O$ and $HO_2 + CH_3O$ during the HO_2 measurement into account, induces only a decrease of less than 5% in the final HO_2 initial concentration. Thus, a comparison of $\alpha_{HO2,t=0} = 1.23\times10^{-6}$ cm⁻¹ with $\alpha_{CH3O2,t=0} = 1.51\times10^{-7}$ cm⁻¹ allows calculation of $\sigma_{CH3O2} = (3.33\pm0.17)\times10^{-20}$ cm², using $\sigma_{HO2} = 2.72\times10^{-19}$ cm², in excellent agreement with the value obtained from kinetic measurements $\sigma_{CH3O2} = (3.4\pm0.4)\times10^{-20}$ cm². This seems to exclude any errors in the absorption cross-section of CH_3O_2 having been a source of bias for the measurement of the rate constant k(R 44) of the reaction CH_3O_2 + OH in the earlier experiments of Bossolasco et al. [134].

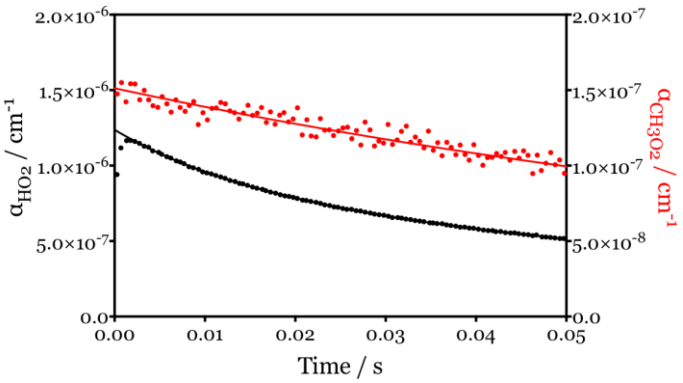

Figure 77: Absorption coefficient α as a function of the photolysis delay following the 248 photolysis of XeF_2 as radical source. Black dots left y-axis: HO_2 radicals generated using 2.8×10^{15} cm^{-3} CH_3OH and 4.7×10^{15} cm^{-3} O_2. Red dots, right y-axis: CH_3O_2 generated radicals using 8.5×10^{15} cm^{-3} CH_4 and 4.7×10^{15} cm^{-3} O_2. H_2O concentration was below 3×10^{14} cm^{-3}, OH was below detection limit

6.2.2 New determination of the rate constant

In the earlier work of Bossolasco et al. [134], the rate constant k(R 44) has been determined through the quantification of time resolved absolute CH_3O_2 concentrations by cw-CRDS and relative OH concentration by LIF. During this work, the same method was used using different precursors: if CH_3O_2 radicals were generated through the CH_3I photolysis in the presence of an excess O_2, thus co-generating I atoms in equal amounts, now CH_3O_2 is generated through the photolysis of XeF_2 in the presence of CH_4, H_2O and O_2 with the co-products being the inert gas Xe and stable molecule HF. CH_3O_2 radicals have thus been generated from the 248 nm of XeF_2 following the reaction sequence (R 47) to (R 51) detailed above, while OH radicals are produced from the reaction of F with H_2O:

$$H_2O + F \rightarrow OH + HF \qquad (R\ 52)$$

The ratio between the initial concentration of CH_3 and OH radicals is given by the ratio of the rates of (R 51) and (R 52), i.e. the products of the rate constants and the corresponding precursor concentration CH_4 or H_2O. The subsequent reaction (R 47)

is under our conditions of oxygen concentration $[O_2] \approx 9\times10^{17}$ cm^{-3} very fast and it can be considered that all CH_3 radicals are converted to CH_3O_2. CH_3O_2 radicals have been quantified on one cw-CRDS absorption path, while OH radicals have been quantified on the second cw-CRDS path but also by LIF. Three days of experiments have been carried out using different ratios for CH_3O_2 and OH. The conditions for all 13 experiments are summarized in Table 13.

Table 13: Experimental conditions for the 3 days of experiments

	[a]CH_4 / 10^{15} cm^{-3}	[b]H_2O / 10^{15} cm^{-3}	[c]XeF_2 / 10^{14} cm^{-3}	[d]CH_3O_2 / 10^{12} cm^{-3}	[e]OH / 10^{11} cm^{-3}	CH_3O_2 / OH	[f]k'_{OH} / s^{-1}
Day 1	31.6	5.44	1.55	2.5	1.0	26.3	513
	23.6	10.5	2.99	5.0	5.1	9.9	909
	45.1	10.5	2.99	5.0	2.6	19.4	1037
	13.5	10.5	2.99	5.2	8.6	6.1	944
	9.67	14.5	4.11	7.0	22	3.2	1140
Day 2	0.33	1.23	3.24	4.6	36	1.3	682
	0.58	1.23	3.24	4.9	23	2.2	803
	0.54	1.23	3.24	5.1	25	2.0	837
	0.60	1.23	3.24	5.8	25	2.3	886
	3.11	1.23	3.23	6.0	5	12.0	920
Day 3	1.00	0.39	1.94	4.5	3.8	12.0	832
	0.82	0.84	3.72	8.6	14	5.8	1362
	0.86	0.75	4.17	9.3	16	5.9	1508
	0.66	1.22	6.04	12.7	38	3.3	2002

[a] measured, [b] measured in-situ by cw-CRDS or extrapolated from XeF_2 flow, [c] estimated (see text), [d] measured by cw-CRDS, [e] estimated from $[CH_4]$ and $[H_2O]$, measured by cw-CRDS on day 3, [f] obtained from fit to single exponential decay of OH profiles over 3 to 5 ms.

The Figure 78 shows the results of the experiment 1, 2 and 4 of the day 3 with the OH decays in the left graph and the simultaneously obtained CH_3O_2 signal in the right graph. The experiments were carried out with constant photolysis energy of 130 mJ

cm^{-2} and constant CH_4 flow, while increasing the XeF_2 concentration through an increase of the gas flow from the Teflon bag. The H_2O concentration in the Teflon bag was always higher than the H_2O concentration of the helium (alphagaz 2) used to fill the Teflon bag due to the permeability of Teflon to the H_2O present in ambient air. During the experiments presented in Figure 78, the presence of around 1.3 Torr H_2O in the Teflon bag was determined by quantifying the H_2O concentration in the photolysis cell by cw-CRDS. It was therefore not necessary to add additional water because OH radicals were already generated in sufficient amount. Changing the CH_4 concentration was used to vary the ratio between OH and CH_3O_2. It can be seen that the CH_3O_2 concentration is not constant, but decreases on the time scale of the OH decays, while it decays slower after OH radicals have reacted away. This is especially visible at the highest radical concentration (blue dots), which was also the experiment with the highest OH to CH_3O_2 ratio due to very high XeF_2 flow and with this a higher H_2O concentration, and at constant CH_4 flow with increasing total flow thus decreasing CH_3O_2 precursor. Under this condition, CH_3O_2 concentration was not in large excess, but only a few times higher than the initial OH concentration.

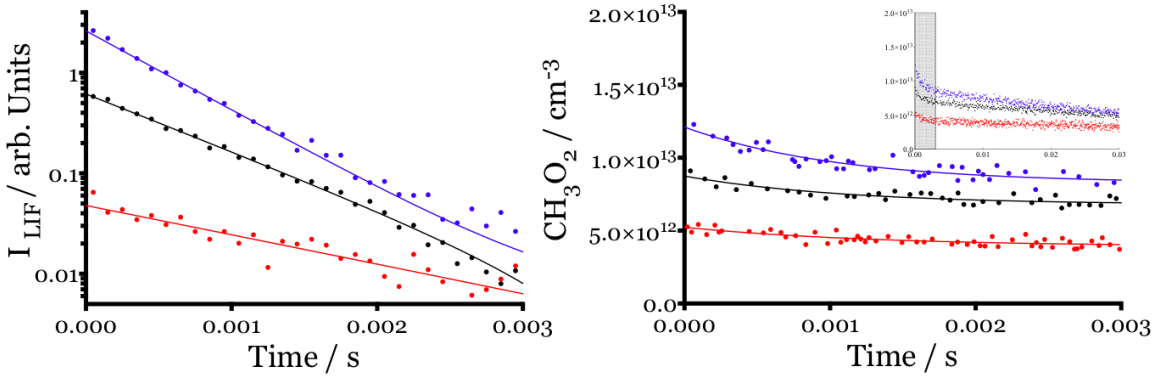

Figure 78: Experiments 1 (red), 2 (black) and 4 (blue) of day 3 in Table 13 with estimated $[XeF_2]$ = 1.9, 3.7 and 6.0×10^{14} cm^{-3}, and decreasing $[CH_4]$ = 10, 8.2 and 6.6×10^{14} cm^{-3}, from bottom to top and using a photolysis energy = 130 mJ cm^{-2}. Left graph: OH decays on a logarithmic scale obtained by LIF, estimated initial OH concentrations were $[OH]_0$ = 0.4, 1.4 and 3.8×10^{12} cm^{-3}, from bottom to top. Right graph: CH_3O_2 concentration time profiles on a linear scale: the inset shows the signals on a longer time scale (30 ms)

During the three days of experiments, OH concentrations have been estimated from CH_4 and H_2O concentrations, whereby the order of magnitude can be verified by comparison with the CH_3O_2 decay for the lowest CH_3O_2 to OH ratio. The last day, OH concentrations have also been quantified by cw-CRDS on the line at 7028.83 cm^{-1} [75] (characterized in previous chapter) and the OH concentrations have been found in good agreement with the estimations. An excellent agreement was also found between OH profiles obtained by cw-CRDS and by LIF, shown in Figure 79 for experiment 4 on day 3. The decay rates obtained by fitting both profiles to a single exponential decay over 5 ms result in (2002±59) and (1922±111) s^{-1} for the measurement obtained by LIF and cw-CRDS, respectively.

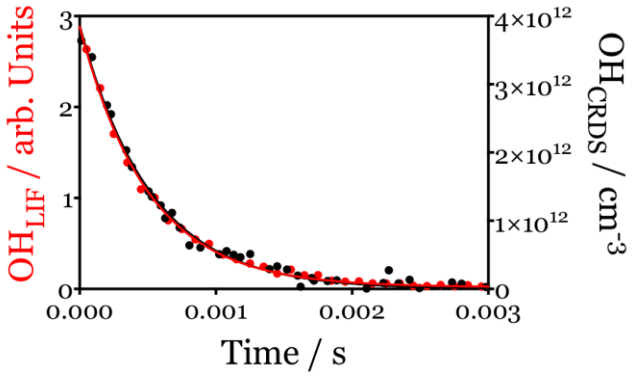

Figure 79: OH decays as a function of the photolysis delay obtained by LIF (red dots left y-axis, in arbitrary units) and cw-CRDS (black dots right y-axis, in absolute concentration using the absorption cross-section obtained from previous chapter σ_{OH} = 1.54×10^{-19} cm^2 [75])

Considering pseudo-first order conditions, the OH decay rate as a function of the initial CH_3O_2 concentration was plotted in Figure 80 for all 13 experiments. A linear regression leads to a rate constant of k(R 44) = $(1.60\pm0.06)\times10^{-10}$ cm^3 s^{-1} with the uncertainty being statistical only with the 95% confidence interval indicated by the dashed line. The intercept of the regression is with (129±56) s^{-1} only slightly above the expected decay rate for OH due to losses through diffusion out of the photolysis volume (15 - 25 s^{-1}) and losses due to reaction with the precursor CH_4 (≈ 10 s^{-1}). Other than the statistical uncertainty, an error in the absorption cross-section of CH_3O_2 has

to be considered. The uncertainty in $\sigma_{CH_3O_2}$ is considered to be less than 10%, which leads to rate constant of reaction CH_3O_2 + OH k(R 44) = (1.6±0.4)×10^{-10} cm^3 s^{-1}.

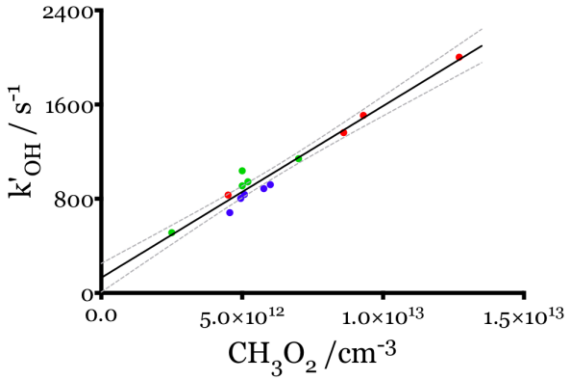

Figure 80: Pseudo first-order decay rate of OH radicals as a function of the initial CH_3O_2 concentration at 50 Torr helium. Different colors indicate experiments from different days with green dots: day 1, blue dots: days 2, and red dots: day 3. Experimental conditions as presented in Table 13

The value of the rate constant obtained during this work is nearly a factor of 2 lower than the value obtained previously by Bossolasco et al. [134], but closer to the value obtained for the reaction of $C_2H_5O_2$ + OH [59], supporting the suspicion that the presence of I atoms may accelerate the OH decays. Two hypotheses could be brought up to explain this phenomenon: (i) the 248 nm photolysis of alkyliodide leads to the formation of electronically excited I atoms I($^2P_{1/2}$) [142]–[144] with an energy gap between electronically excited I($^2P_{1/2}$) and ground state I($^2P_{3/2}$) being 7603 cm^{-1}, which is a close energy match to the second harmonic of OH vibration. Also, efficient quenching rates have been measured for collision of I($^2P_{1/2}$) with several molecules containing an OH group, i.e. H_2O, CH_3OH, C_2H_5OH, etc. [145]. It is therefore plausible that I($^2P_{1/2}$) will also be quenched in collision with OH radicals and possibly even more efficient because a chemical bonding can be formed between I and OH and can enhance the efficiency of energy transfer. The difference between the rate constant k(R 44) obtained using the two different precursors is 1.2×10^{-10} cm^3 s^{-1} and would therefore indicate a quenching rate of I($^2P_{1/2}$) with OH radicals near collision frequency. Such collision would bring the ground state OH(v = 0) into vibrationally

excited OH(v = 2), and thus prevent the detection of OH radicals by the LIF technique because only the OH(v = 0) are detected in the current detection scheme. This will result in an additional decay of the LIF signal of OH and will thus result in an increase in the apparent rate constant. Attempts have been made to detect OH(v = 2) by LIF but were not successful, possibly for several reasons. First, the expected OH(v = 2) concentration would be low because OH(v = 2) radicals reacts probably as fast OH(v = 0) with CH_3O_2 radicals and can also possibly be quenched to OH(v = 1). Therefore, only a small steady-state concentration of OH(v = 2) can be expected. Second, the LIF system, with the dye laser and the detection scheme containing the interference filter, was optimized for the detection of OH(v = 0), which makes it even more difficult to detect possible low OH(v = 2) concentration. (ii) Another way to explain the large difference between the rate constants for CH_3O_2 + OH when using the different precursors would be the hypothesis of a fast chemical reaction between OH and I atoms. However, no data on this possible reaction were found in the current literature. This reaction is difficult to study directly experimentally, because the reaction of OH radicals with I_2 molecules is extremely fast with 2.1×10^{-10} cm^3 s^{-1} [146], preventing the use of I_2 as precursor for I atoms.

The value of the rate constant k(R 44) = $(1.6\pm0.4)\times10^{-10}$ cm^3 s^{-1} determined during this study is in much better agreement with recently determined value k(R 44) = $(8.7\pm1.4)\times10^{-11}$ cm^3 s^{-1} of Yan et al. [137] than the earlier determination k(R 44) = $(2.8\pm1.4)\times10^{-10}$ cm^3 s^{-1} of Bossolasco et al. [134] whose given error bar was a result of the uncertainty in the CH_3O_2 absorption cross-section value and did not reflect the uncertainty in the measurements. Given the confirmation of the CH_3O_2 absorption cross-section in this work, which include a direct comparison with the HO_2 absorption cross-section and thus being independent of the rate constant of the CH_3O_2 self-reaction, the error limit should be drastically reduced but it seems now clear that the previous experiments were biased through the presence of I atoms. The other value of the rate constant of Yan et al. [137] is still nearly a factor of 2 lower than the present determination and the difference cannot be explained satisfactorily by experimental uncertainty. In their experiments, they generated CH_3O_2 and OH radicals by simultaneous photolysis of CH_3COCH_3 and N_2O at 193 nm in the presence of H_2O and

O_2. Their initial radical concentrations were 10 to 50 times higher than in the current study, and the rate constant has been extracted by fitting UV-absorption traces to a complex mechanism containing 46 reactions. The residuals show that the non-exponential OH decays are well reproduced by the mechanism. A sensitivity study has been carried out by the authors identifying 14 reactions as important, being mostly radical-radicals reactions. Assigning errors of ±20% or ±50% to the rate constants of the important reactions depending on the degree of knowledge of the reactions and assuming statistical independence of their errors, the authors obtained a combined error for k(R 44) of ±5%. No convincing reasons can be given at this point for the disagreement. The impact of the reaction (R 44) as sink for CH_3O_2 radicals in remote atmospheres directly depends on the rate constant k(R 44), and the persisting difference of nearly a factor of 2 would make a non-negligible difference in atmospheric chemistry models. It seems therefore indispensable to determine again the rate constant k(R 44) using yet another technique. However, in order to evaluate the impact of this reaction on the composition of the atmosphere it is also essential to identify the reaction products.

6.2.3 The yield of HO_2 as a product of the reaction

The CH_3O_2 and OH radicals have been generated from the 248 nm photolysis of XeF_2 following the reaction sequence (R 47) to (R 52) detailed above. As for the measurement of the rate constant, CH_3O_2 radicals have been quantified on one cw-CRDS absorption path, while HO_2 and OH radicals have been quantified sequentially on the second cw-CRDS path. A total of four experiments have been carried out at changing XeF_2 concentration, all at a total pressure of 50 Torr and 295 K. The initial radical concentrations were between 1-12×10^{12} cm^{-3} with ratios of CH_3O_2/OH between 2 and 9. The concentrations of the radicals and stable species are summarized in Table 14.

Table 14: Initial concentrations of stables species and maximum radical concentrations from cw-CRDS measurements.

O_2 / 10^{18} cm^{-3}	He / 10^{17} cm^{-3}	CH_4 / 10^{15} cm^{-3}	[a] XeF_2 / 10^{14} cm^{-3}	[b] CH_3O_2 / 10^{12} cm^{-3}	[b] OH / 10^{12} cm^{-3}	[b] $HO_{2,max}$ / 10^{12} cm^{-3}
1.30	3.0	1.00	1.94	4.3	0.45	0.58
1.11	5.0	0.82	3.72	8.2	1.7	2.2
1.06	5.5	0.86	4.17	8.9	1.9	2.4
0.86	7.6	0.66	6.04	12.1	4.8	5.2

[a] estimated from weighted XeF_2 in Teflon bag, [b] as obtained from cw-CRDS measurements using the absorption cross-sections given below

The line strength of a ground state $X^2\Pi_{1/2}$ transition of OH radicals in the near infrared region at 7028.831 cm^{-1} has been previously determined to be S = 4.07 ×10^{-21} cm, with a peak absorption cross-section at 50 Torr helium of $\sigma_{OH,50Torr\ He}$ = (1.54±0.1)×10^{-19} cm². The current work has been carried out in the presence of high O_2 concentrations, between 25 to 40 Torr, the complement to 50 Torr being mostly helium from the XeF_2 flow. Therefore, the peak absorption cross-section will be lower due to an increase in the pressure broadening of O_2 compared to He. From the pressure broadening coefficient determined in chapter 3 with γ_{coll}^{O2} = 0.049 cm^{-1} atm^{-1} it is possible to calculate the absorption cross-section of OH in oxygen: from the line strength and considering a Voigt profile, a value of $\sigma_{OH,50Torr\ O2}$ = 1.16×10^{-19} cm² is obtained. Taking into account the varying He/O_2 ratios, the peak absorption cross-section for the different experiments varied between (1.23–1.34)×10^{-19} cm². The average value of σ_{OH} = 1.27×10^{-19} cm² has then been used in Equation 22 to convert the absorption coefficient α_{OH} into OH concentration, taking into account an estimated uncertainty of 20% for this absorption cross-section. The absorption cross-sections of σ_{HO2} = 2.72×10^{-19} cm² (determined in chapter 3) and σ_{CH3O2} = 3.4×10^{-20} cm² (determined in this chapter) have been used to calculate the concentrations of HO_2 and CH_3O_2, respectively. This HO_2 line has an absorption cross-section nearly two times higher than surrounding lines and is probably the convolution of two nearly perfectly overlapping transition. As a result, the pressure broadening in helium [73]

or in oxygen [71] is very small. The uncertainty of σ_{HO_2} is thus estimated to be less than 10%.

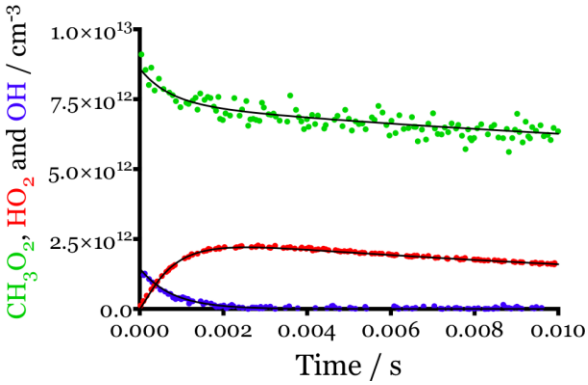

Figure 81: Absolute concentration of CH_3O_2 (green dots), HO_2 (red dots) and OH (blue dots) following the photolysis of [XeF_2] = 3.7×10^{14} cm^{-3} in presence of [CH_4] = 8.2×10^{14} cm^{-3}, [H_2O] = 7×10^{14} cm^{-3}, [He] = 5.0×10^{17} cm^{-3} and [O_2] = 1.1×10^{18} cm^{-3}. Absorption cross-sections of $\sigma_{CH_3O_2}$ = 3.33×10^{-20} cm², σ_{HO_2} = 2.72×10^{-19} cm² and σ_{OH}=1.27×10^{-19} cm² have been used for conversion of absorbances α for the three species. The black lines represent adjustment to the model described in Table 15

The Figure 81 presents the concentration time profiles of all three species, i.e. CH_3O_2, OH and HO_2, obtained during the second experiment of Table 14 at 50 Torr total pressure, using the following concentrations: [XeF_2] = 3.7×10^{14} cm^{-3}, [CH_4] = 8.2×10^{14} cm^{-3}, [H_2O] = 7×10^{14} cm^{-3}, [He] = 5.0×10^{17} cm^{-3} and [O_2] = 1.1×10^{18} cm^{-3}. It can be seen that the initial fast decay in CH_3O_2 concentration is on the same order of magnitude than the decay of the initial OH concentration. It can also be seen that the maximum HO_2 concentration is slightly higher than the initial OH concentration, suggesting a high yield of HO_2 radicals produced from the (R 44). In order to determine the HO_2 yield, Φ_{HO_2}, the concentration time profiles of the three species have been adjusted to a simple model, with the reactions and rate constants shown in Table 15.

Table 15: Reaction mechanism used to fit CH_3O_2, OH and HO_2 concentration time profiles

No.	Reaction	Rate constant / $cm^3\ s^{-1}$	Reference
(R 44a)	$CH_3O_2 + OH \rightarrow CH_2OO + H_2O$	0	This work
(R 44b)	$\rightarrow HO_2 + CH_3O$	$(1.35\pm0.3)\times10^{-10}$	
(R 44c)	$\rightarrow$ products *	$(0.25\pm0.3)\times10^{-10}$	
(R 47)	$CH_3 + O_2 (+M) \rightarrow CH_3O_2$	1.4×10^{-13} **	[139], [140]
(R 38)	$CH_3O + O_2 \rightarrow CH_2O + HO_2$	1.92×10^{-15}	[115]
(R 48a)	$2\ CH_3O_2 \rightarrow 2\ CH_3O + O_2$	1.3×10^{-13}	[115]
(R 48b/c)	$\rightarrow$ products	2.2×10^{-13}	[115]
(R 49	$CH_3O_2 + HO_2 \rightarrow$ products	5.2×10^{-12}	[115]
(R 24)	$HO_2 + HO_2 (+M) \rightarrow$ products	1.6×10^{-12}	[69]
(R 41)	$CH_3O + CH_3O \rightarrow$ products	7×10^{-11}	This work
(R 42)	$CH_3O + HO_2 \rightarrow$ products	1.1×10^{-10}	This work
(R 27)	$OH + HO_2 \rightarrow$ products	1.02×10^{-10}	This work
(R 29)	$HO_2 \rightarrow$ diffusion	$8 - 22\ s^{-1}$	This work

* no informations can be obtained about the products from the current experiment. ** rate constant in 50 Torr helium

All four experiments were very well reproduced with the mechanism and rate constants from Table 15, i.e. Φ_{HO2} = 0.85. The uncertainty of the rate constant k(R 38), leading to formation of a second HO_2 radical, is given [115] with ±50%. However, the O_2 concentration during the experiments was high, thus this reaction was not the rate limiting step and an uncertainty on the value of k(R 38) had only a very minor impact on the HO_2 profile. Also, the reaction of CH_3O with OH was probably not important, even though the rate constant is not well known. Taking an estimated rate constant [112] of $k_{CH3O+OH} = 3\times10^{-11}\ cm^3\ s^{-1}$, even under the most unfavorable conditions with high radical and low O_2 concentration, only 1% of the initial OH radicals would react with CH_3O. However, the reaction of CH_3O with HO_2 is taken into account using the rate constant determined previously and around 7% of the

maximum HO_2 reacts through this reaction, increasing slightly the Φ_{HO2} for the reaction (R 44). The influence of (R 48) and (R 49) are very limited at short reaction times, and therefore any uncertainty of k(R 48) and k(R 49) would have a negligible influence on the retrieval of Φ_{HO2}. Equally, the uncertainty of k(R 27) has only a limited influence on Φ_{HO2}: while the reaction itself consumes around 10% of the initial OH radicals at the experiment with the highest initial radical concentration, the estimated error of 15% on k(R 27) would lead to a change of less than 3% in Φ_{HO2}.

The major uncertainty in the value of Φ_{HO2} comes from uncertainties in the absorption cross-sections used in Equation 22 to convert the absorbance α_{OH} and α_{HO2} into absolute concentrations. While the absorption cross-section of HO_2 radicals is well determined and the uncertainty is estimated to be less than 10%, σ_{OH} has only been determined once from this study. Additionally, the value of the absorption cross-section of OH used in this work needs to take into account the increased pressure broadening by the high O_2 concentrations. Therefore, the uncertainty on the OH absorption cross-section is estimated to be 20%. The impact of this uncertainty on the retrieved Φ_{HO2} is illustrated in the left graph of Figure 82, using the same OH and HO_2 profiles measured during the experiment shown in Figure 81. The Figure 82 is zoomed on OH and HO_2 profiles only, so that the CH_3O_2 profile is not shown. The black lines show the model using $\sigma_{OH} = 1.27\times10^{-19}$ cm², while for the blue and red lines the absorption cross-section for OH has been varied by 20%, with σ_{OH} = 1.06 and 1.53×10^{-19} cm² for the red and blue lines respectively. The lower limiting value of σ_{OH} leads to higher OH concentration (not plotted in Figure 82 for clarity) and the model allows a good reproduction of OH and HO_2 profiles, but in order to make up for the higher initial OH concentration, the yield of HO_2 radicals must be decreased to Φ_{HO2} = 0.67. The higher value for σ_{OH} leads to lower OH concentrations (also not plotted) and also allows a satisfactory reproduction of the HO_2 profile, now with Φ_{HO2} = 0.96.

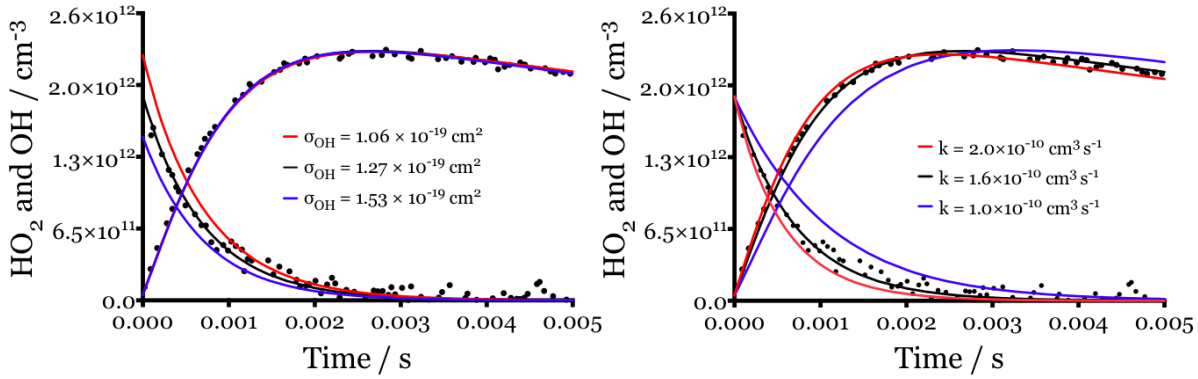

Figure 82: Concentration time profiles of OH (decaying) and HO_2 (rising) from the experiment in Figure 81 and reproduced with the model in Table 15. Left graph: influence of the 20% uncertainty of σ_{OH} on the HO_2 concentration time profile: OH concentrations obtained by using σ_{OH}=1.27×10^{-19} cm² (black line), using σ_{OH} decreased by 20% (red line), or using σ_{OH} increased by 20% (blue line) (the corresponding experimental OH data are not plotted for clarity). Φ_{HO2} = 0.67, 0.8 and 0.96 for the red, black and blue lines, respectively. Right graph: impact of the rate constant k(R 44) on both profiles: all rate constants as in Table 15, only k(R 44) has been changed

The right graph of Figure 82 shows the sensitivity of the experimental data to the rate constant k(R 44), whereby the total value has been varied between 1 and 2×10^{-10} cm^3 s^{-1}. In order to reproduce the absolute HO_2 concentration, k(R 44b) and k(R 44c) have to be adjusted to 9 and 1, 12.5 and 3.5, and 15 and 5×10^{-11} cm^3 s^{-1} for the blue, black and red lines, respectively. The blue line represents the upper limit of the rate constant recently published by Bossolasco et al. [133]. A change in k(R 44) has a strong impact on the predicted HO_2 profile in the current experiment. Not only would the rise time of HO_2 slow down with a decrease in k(R 44), but the final maximum HO_2 concentration would also decrease. This is because the conversion of OH into HO_2 through (R 44) is not only governed by Φ_{HO2}, but also by the rate constant k(R 44): a lower rate constant leads to a lower conversion because competing reactions gain in importance, especially the fast reaction (R 27). The black line shows the best fit for both species with k(R 44) = 1.6×10^{-10} cm^3 s^{-1}. The red lines correspond to the model using k(R 44) = 2×10^{-10} cm^3 s^{-1}: OH and HO_2 profiles are barely reproduced with this faster rate constant, and the retrieved HO_2 yield would be slightly smaller with Φ_{HO2} = 0.75. A decrease to k(R 44) = 1×10^{-10} cm^3 s^{-1} in blue lines results in a very

poor reproduction the OH and HO_2 profiles: the decay and rise profiles are too slow for both species. With this rate constant, Φ_{HO2} would rise to Φ_{HO2} = 0.9 because other loss reactions, especially (R 27), gain in importance. Thus, the determination of the HO_2 yield at a total pressure of 50 Torr O_2 and He shows that HO_2 is the major product with Φ_{HO2} = 0.85±0.15.

6.2.4 Determination of an upper limit for the yield of Criegee intermediates CH_2OO

In addition to this work, the reaction of CH_3O_2 with OH radicals was also investigated by time-resolved broadband cavity-enhanced UV spectroscopy by the Combustion Research Facility in Sandia National Laboratories to test the possibility of formation of formaldehyde oxide CH_2OO through the reaction (R 44a). The experimental apparatus developed at Sandia National Lab has been described in detail previously [144], [145], and only a brief account is given here. The continuous-wave broadband optical buildup cavity was configured to simultaneously probe the spectral range λ = 300–450 nm with average effective path length of ~40 m and spectral resolution of 1.5 nm. The optical cavity was integrated into a gas phase flow reactor with independent control over the experimental temperature, pressure, and sample mixture composition. All experiments were performed at T = 293 K and total P = 30 Torr, and transient UV spectra were recorded with time resolution of 30 μs. Because XeF_2 was not available to initiate the reaction, the reaction sequence was initiated by 266 nm photolysis of acetone vapor in He bath gas in the presence of 2.5 Torr O_2, [O_2] = 8.25×10^{16} cm^{-3}.

Small Criegee intermediates such as formaldehyde oxide were recently shown [149] to have very strong UV absorption bands in the 300–400 nm range with peak absorption cross-sections of the B ← X transition of ~1×10^{-17} cm^2. Thus, UV absorption is a sensitive detection method for Criegee intermediates, and their experiment has a detection limit for CH_2OO below ~5×10^8 cm^{-3}. Using the lower limit

for the determined OH concentration and the upper limit for measured CH_2OO concentration, an upper limit of Φ(R 44a) < 0.05 was found. This result is in very good agreement with theoretical calculations [132], [133], but also with the recent finding by Yan et al. [137], who also determined an upper limit of Φ(R 44a) < 0.05 for the formation of the Criegee intermediate in (R 44).

6.2.5 Modeling and atmospheric implications

In order to evaluate the impact of the HO_2 production from the reaction (R 44) on the composition of the atmosphere under clean, low NO_X conditions, the results of these experiments have been implemented into a box model utilizing the MCM v3.2 by University of Leeds. The model was constrained using field data containing gas phase composition (including halogen oxides IO and BrO concentrations), photolysis rate and meteorological parameters from a field campaign [136] at the Cape Verde Atmospheric Observatory (CVAO), which took place in 2007. This model has been described previously and was used to calculate OH and HO_2 concentrations for comparison with those measured at CVAO [150]. Inclusion of the reaction (R 44b) in the model has a substantial impact on the predicted CH_3O_2 levels by decreasing them by ~30% during the afternoon. Taking into account the HO_2 and CH_3O productions from (R 44b), the model predicts ~20% more HO_2 at CVAO. This increase in the modeled HO_2 further enhances the destruction of CH_3O_2 by increasing the loss of CH_3O_2 via the reaction with HO_2 by 15%, which is the dominant CH_3O_2 sink, accounting for 50% of the total CH_3O_2 destruction in this environment.

Tropospheric ozone is an important greenhouse gas and in remote oceanic regions, integrating (R 44b) into the model impacts also on its formation and destruction paths. At conditions such as found at the CVAO, ozone production via reaction of peroxy radicals with NO is small, and ozone is typically destroyed during the day via photochemical reactions and deposition. HO_2 accounts for 9% of the daily ozone destruction cycle observed at CVAO. As the reaction of CH_3O_2 with O_3 is significantly

slower than the reaction of HO_2 with O_3, an additional source of HO_2 from reaction (R 44b) may influence the modeled estimations of ozone destruction, noted dO_3. The reaction of HO_2 with ozone proceeds ~17% faster when (R 44b) is included. The reactions of HO_2 with IO and BrO are also enhanced by ~18% and this serves to further increase dO_3. Considering all the net ozone destroying reactions, it is estimated that (R 44b) enhances dO_3 by ~4%. Reaction (R1b), also serves to modify ozone production (noted pO_3) by a reduction in the rate of CH_3O_2 + NO reaction and an enhancement in the rate of HO_2 + NO reaction. Overall pO_3 is predicted to decrease modestly by ~75 pptv per day when (R 44b) is considered. Thus, taking both the changes in pO_3 and dO_3 into account, this study suggests that tropospheric ozone in remote regions will be over-estimated by ~6% by models which do not consider the reaction of CH_3O_2 with OH. Remote oceanic regions cover approximately two thirds of the Earth's surface and so omission of the reaction of CH_3O_2 with OH yielding HO_2 may lead to significant over-predictions in tropospheric ozone on a global scale.

Global models generally under predict the concentration of CH_3OH compared to the measurements. In a recent work of [133] it was proposed that a significant yield of CH_3OH in (R 44) could help to explain this discrepancy. The best estimate from their theoretical calculations predict yields for CH_3OH and for the stabilized CH_3OOOH between 0.05 and 0.1, but each with a margin of error of a factor ~3.5. This is in perfect agreement with the measurements presented in this work. However, in order to best reproduce measured CH_3OH concentrations, a yield of 18% and 21% for CH_3OH and CH_3OOH respectively would be needed. This scenario leaves a yield of 61% for HO_2 formation through (R 44). However, in their model they used for their model the previously determined rate constant by Bossolasco et al [134], which is a factor of 2 higher than the revised one from this work, and hence they overestimate the overall importance of (R 44). As a result, the CH_3OH yield would need to be increased even further in order to bring into agreement the CH_3OH predictions with measurements, leading consequently to an even lower value for the HO_2 yield. While a yield of 61% HO_2 would be within the error limit of the current work, an even higher value is not in agreement with the above presented measurements. However, it has to be noted that the current measurement of the HO_2 yield have been carried out at low

pressure in 50 Torr helium and O_2 and that the product distribution might change with pressure. Therefore, product distributions should be determined at higher pressures in order to find out if the reaction (R 44) could be a significant source of CH_3OH in the remote troposphere. The present set-up is not very suitable for this task, because the absorption lines of OH and HO_2 suffer from broadening, making their detection at higher pressure less sensitive. Also, the uncertainty of the yield would increase if the absorption cross-sections of HO_2 and OH are not well known. The better way would be the direct detection of CH_3OH, but unfortunately the cw-CRDS set-up is not sensitive to this species.

6.3 Experimental characterization of the reactions of C_2-C_4 peroxy radicals with OH radicals

Experiments have been dedicated to the reactivity of $C_2H_5O_2$ and the next larger peroxy radicals $C_3H_7O_2$ and $C_4H_9O_2$. The experiments have been carried out using three different precursors: the corresponding alkyliodides for the study of $C_2H_5O_2$, 1-$C_3H_7O_2$ or 2-$C_3H_7O_2$ using C_2H_5I, 1-C_3H_7I or 2-C_3H_7I respectively, or the reaction of either Cl atoms or F atoms with the corresponding hydrocarbon C_2H_6, C_3H_8 or C_4H_{10} to generate $C_2H_5O_2$, $C_3H_7O_2$ and $C_4H_9O_2$, respectively. From these measurements, the rate constants of the three peroxy radicals with OH have been measured as well as the yield of HO_2 formation for each reaction.

6.3.1 Determination of the rate constant using different precursors

6.3.1.1 Rate constants of $C_XH_{2X+1}O_2$ + OH from Cl + $C_XH_{(2X+2)}$ precursors

The reaction was initiated by the 248 nm photolysis of $(COCl)_2$ in the presence of excess C_2H_6, C_3H_8 or C_4H_{10} and high concentrations of O_2. OH was simultaneously

generated by the photolysis of H_2O_2, leading to the formation of two OH radicals, leading to the reactions of OH with the three peroxy radicals

$$C_2H_5O_2 + OH \rightarrow \text{products} \quad \text{(R 45)}$$

$$C_3H_7O_2 + OH \rightarrow \text{products} \quad \text{(R 53)}$$

$$C_4H_9O_2 + OH \rightarrow \text{products} \quad \text{(R 54)}$$

They have been studied at 298 K and 50 Torr total pressure under pseudo-first order conditions using an excess of peroxy radicals over OH radicals. The relative concentration of OH radicals has been measured by the high repetition rate LIF. However, while the absorption cross-sections of HO_2 and CH_3O_2 radicals in the infrared region are well known and therefore these radicals can be quantified directly by cw-CRDS, for other peroxy radicals only their relative spectra are known in this wavelength range. Therefore, the concentrations of these peroxy radicals have been determined indirectly. To do so, the initial Cl atom concentration has been quantified in back-to-back experiments by converting them either to HO_2 radicals, which can be quantified, or to the peroxy radicals. For that, $(COCl)_2$ has first been photolysed in the presence of excess CH_3OH and O_2, thus transforming them quantitatively into HO_2 radicals through the reaction sequence (R 32)-(R 33). HO_2 radicals can be quantified with good precision on the well-characterized line at 6638.205 cm^{-1}. Then, CH_3OH has been replaced by one of the studied hydrocarbons, leading to the formation of peroxy radicals through the reactions:

$$Cl + RH \rightarrow R + HCl \quad \text{(R 55)}$$

$$R + O_2 (+M) \rightarrow RO_2 (+M) \quad \text{(R 56)}$$

It is then supposed that the concentration of the corresponding peroxy radical is equal to the concentration of HO_2 measured just before. The O_2 concentration was 2.7×10^{17} cm^{-3} for all experiments, leading to very fast formation of all peroxy radicals within a few tens of microseconds and can be considered instantaneous on the time scale of the experiments. While for C_2H_6, only one isomer can be formed, two different peroxy

radicals can be formed for the two larger hydrocarbons: 1- and 2-propylperoxy and 1- and 2-butylperoxy. A higher yield for the abstraction of the secondary H atom can be expected, leading to the formation of the 2-peroxy, with ratios of 0.57/0.43 and 0.70/0.30 for propane and butane [151], respectively. In the current experiment, it is not possible to distinguish between both radicals, and therefore only the average rate constant has been determined.

The Figure 83 shows the experimental data such as obtained during the measurement using propane as hydrocarbon. The left graphs shows the HO_2 concentration time profile obtained in the presence of CH_3OH for six different $(COCl)_2$ concentrations. The right graph shows the OH decays on a logarithmic scale, obtained for the same $(COCl)_2$ concentrations but replacing CH_3OH by an excess propane. It can be seen that OH decays exponentially over at least two orders of magnitude, while HO_2 concentration is nearly unchanged on this time scale. The HO_2 decay is mostly due to self-reaction and given the low HO_2 concentration, only a slow decay is expected. This is also the case for the decay of peroxy radicals due to their even lower self-reaction. A simple model shows that for the highest peroxy radical concentration with $[C_3H_7O_2]$ = 1.4×10^{13} cm^{-3} and even for the fastest reacting peroxy radical ($k_{1\text{-}C_3H_7O_2}$ = 3.84×10^{-13} cm^3 s^{-1}) only around 1% of the peroxy radicals have decayed within the first millisecond, i.e. the time where 90% of the OH radicals have reacted. This estimation certainly justifies the assumption of pseudo-first order conditions.

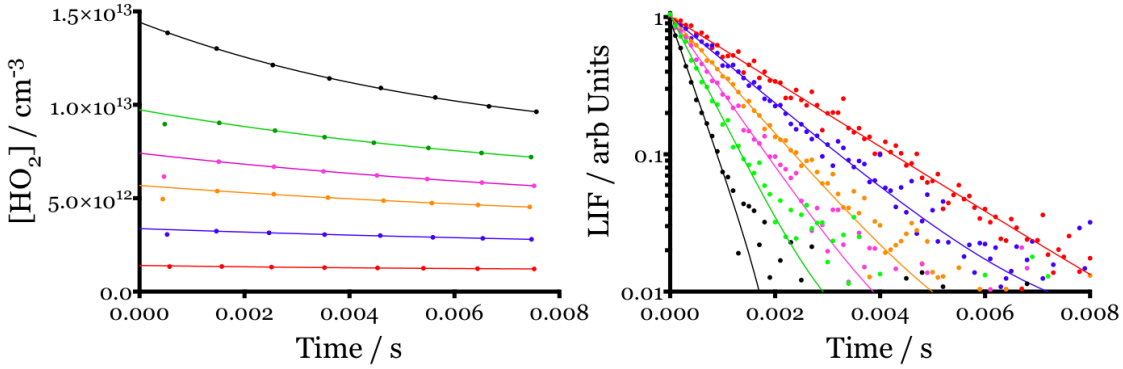

Figure 83: Left graph: HO_2 concentration time profile used to quantify the initial Cl atom concentration through extrapolation of the decay to time zero using $[CH_3OH] = 2\times10^{14}$ cm^{-3}, $[O_2] = 2.7\times10^{17}$ cm^{-3} and $[(COCl)_2]$ increasing from $(0.4\text{-}3.5)\times10^{14}$ cm^{-3}, from bottom to top. Right graph: OH decays for the reaction of $C_3H_7O_2$ with OH in the same conditions as left graph, but replacing CH_3OH by $[C_3H_8] = 3.1\times10^{14}$ cm^{-3}

The pseudo-first order decay rates k_{obs}, obtained from fitting OH profiles to a single exponential decay in the right graph, are then plotted against the HO_2 concentration obtained from extrapolation to t = 0 s from a single exponential fit between 1 and 10 ms in the left graph. This plot is shown in Figure 84 for all three peroxy radicals. By assuming that Cl atoms are converted quantitatively into the same concentration of peroxy radicals than into HO_2 radicals, the slopes of the three plots lead to the sought-after rate constants of the reaction between OH radicals and the peroxy radicals.

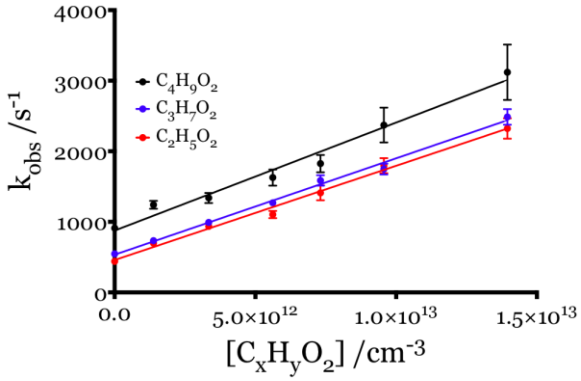

Figure 84: Plot of the pseudo-first order OH decay rate k_{obs} as a function of the peroxy radical concentration for all three species

The following rate constants are thus obtained:

$C_2H_5O_2$ + OH k(R 45) = (1.3±0.3)×10^{-10} cm^3 s^{-1}

$C_3H_7O_2$ + OH k(R 53) = (1.4 ±0.3)×10^{-10} cm^3 s^{-1}

$C_4H_9O_2$ +OH k(R 54) = (1.5 ±0.3)×10^{-10} cm^3 s^{-1}

The given error bar includes a small statistical error given by the 95% confidence interval and an additional error of 10% due to uncertainties in the quantification of the peroxy radical concentrations. This error is due to the uncertainty in the absorption cross-section of HO_2. The intercept of these graphs represent the decay of OH obtained in the absence of $(COCl)_2$ and corresponds to the reaction of OH with H_2O_2 as well as with the peroxy radical precursor. These concentrations do not change during one series of measurements. The concentrations of hydrocarbons used in these experiments were 3.5, 3.1 and 2.9×10^{14} cm^3 for C_2H_6, C_3H_8 and C_4H_{10}, respectively. Multiplying these concentrations with the corresponding known rate constant for the reaction of OH radicals with the hydrocarbon leads to pseudo-first order decays of 86, 339 and 686 s^{-1} for the three species [115]. These values have been plotted in Figure 85 as a function of the intercept from Figure 84. The two data points at zero correspond to the OH decay rates measured in the absence of any hydrocarbon, i.e. only with H_2O_2 obtained at the beginning and the end of the experiment. The full line presents a linear regression with a slope forced to 1, and shows a good agreement between decay rate calculated from added hydrocarbon concentration and decay rate obtained extrapolation of RO_2 + OH measurements.

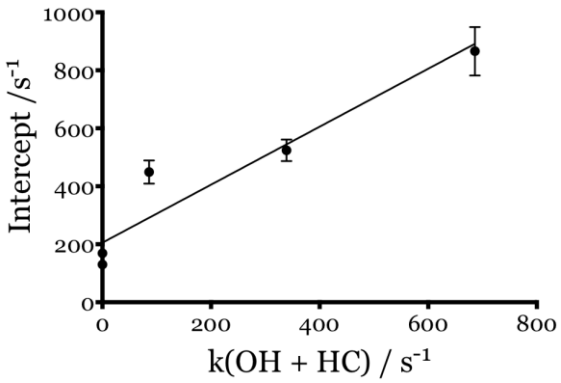

Figure 85: Intercepts from Figure 84 plotted as a function of the calculated pseudo-first order decay rate of the reaction of OH with the three hydrocarbon precursors alone. The two points at x = 0 are the decay rates that have been obtained in the beginning and at the end of the experiment with H_2O_2 alone

6.3.1.2 Rate constants of $C_XH_{2X+1}O_2$ + OH from C_XH_YI precursors

For the determination of the rate constant RO_2 + OH using alkyliodides as precursor, a different strategy has been adapted to overcome the absence of a direct quantification method for the larger peroxy radicals. For these experiments, well-characterized mixtures of CH_3I, C_2H_5I, i-C_3H_7I and n-C_3H_7I have been prepared in glass balloons. First, experiments have been carried out using CH_3I as precursor with a quantification of CH_3O_2 radicals using cw-CRDS. Immediately after, experiments have been carried out using the same flow of another alkyliodide: knowing the mole fractions of the different alkyliodide mixtures as well as the absorption cross-sections of the different iodides at 248 nm, the ethyl- and propylperoxy concentrations have been calculated relative to CH_3O_2 when keeping all other parameters such as laser power, O_2, He and H_2O_2 concentration constant. The concentration of oxygen used for the determination of the rate constants were $[O_2] = 4.8\times10^{17}$ cm^{-3} for propyl peroxy and 5.4×10^{17} cm^{-3} for methyl and ethyl peroxy. Alkyliodide concentrations have been varied between $(1–5)\times10^{14}$ cm^{-3}, and with a photolysis laser energy of around 20 mJ cm^{-2} the obtained initial concentrations of peroxy were between $(2\text{-}10)\times10^{12}$ cm^{-3}. The experimental conditions of all experiments are tabulated in Table 16.

Table 16: Experimental conditions for all peroxy radicals [115], [152], [153]

	σ_{CxHyI} / 10^{-19} cm²	$[C_xH_{2x+1}O_2]$ / $[CH_3O_2]$	$k_{CxHyI+OH}$ / 10^{-13} cm³s⁻¹	$[RI]_{max}\times$ k_{RI+OH} / s⁻¹	k_{RO2+OH} / 10^{-10} cm³ s⁻¹ Non-corr.	corrected*
CH_3I	8.2	1.00	0.72	36	2.9±0.2	
C_2H_5I	8.7	1.05	3.4–7.7	170–385	3.33	3.15
1-C_3H_7I	12	1.42	12.3–25	615–1250	3.01	2.49
2-C_3H_7I	10	1.23	12.9–16	645–800	3.34	2.97

* Slope such as obtained when taking into account the upper limit of the rate constant for the reaction between RI and OH

All the experiments have been carried out on two days with on the first day $C_2H_5O_2$ radicals measured relative to CH_3O_2, and on the second day 1- and 2-$C_3H_7O_2$ radicals measured again relative to CH_3O_2. In Figure 86 are plotted the pseudo-first order decay rates of OH radicals as a function of the peroxy concentrations. The CH_3O_2 data from day 1 are presented as full black symbols and the data from day 2 as open circles. Both days, the rate constant is found to be (2.9±0.2)×10⁻¹⁰ cm³ s⁻¹, in agreement with the previously determined value of Bossolasco et al. [134].

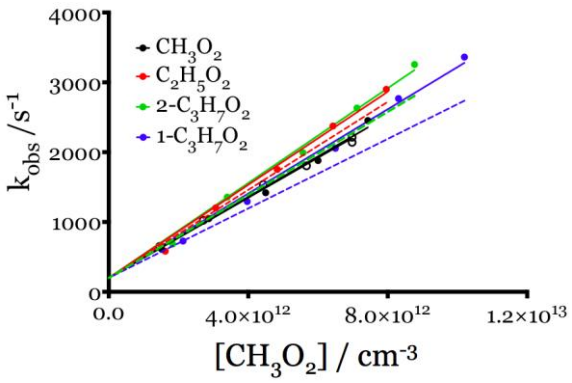

Figure 86: Pseudo-first order decay rates of OH radicals as a function of peroxy radical concentrations. The concentrations of the peroxy radicals have been calculated relative to the measured CH_3O_2 concentrations by cw-CRDS from known precursor concentrations and absorption cross-sections. Full lines represent linear regression of experimental data, dashed line take into account a correction of the reaction between OH radicals and the alkyliodides

The concentrations of $C_2H_5O_2$ and 1- and 2-$C_3H_7O_2$ have been calculated relative to the measured CH_3O_2 concentrations. The slopes for all three radicals are slightly steeper than for CH_3O_2. However the loss of OH radicals due to the reaction with the precursors C_2H_5I and C_3H_7I should be determined. In the case of CH_3O_2 this reaction does not play a role, with a rate constant of CH_3I + OH being 0.72×10^{-13} cm^3 s^{-1}, a pseudo-first order rate constant of 36 s^{-1} is obtained for the highest CH_3I concentration, a little more than 1% of the total OH reactivity. This value increases for the other peroxy radicals with pseudo-first order rate constants of up to 1250 s^{-1} for 1-propylperoxy radical. The values corrected for the upper limit of the RI + OH rate constants are given in Table 16 and are shown as dashed line in Figure 86.

The uncertainties of the absolute values of the rate constants of RO_2 + OH for the higher peroxy radicals are larger than for the method using Cl + RH as precursor given (i) the relative method based on ratios of absorption cross-sections of the different alkyliodides at 248 nm and (ii) added uncertainties for the corrections due to the reaction of RI + OH. However, the rate constants are significantly larger using alkyliodides as precursor compared to the reaction of Cl atoms with hydrocarbons and thus reinforce the earlier suspicion that the presence of I atoms leads to a faster decay of OH radicals. The hypothesis have been brought up previously that electronically excited I atoms, such as formed during alkyliodide photolysis, would be quenched in collision with OH radicals, whereby OH radicals would be excited from v = 0 to v = 2 and thus prevent the detection of OH radicals by the LIF technique where only OH(v = 0) are detected. However, the series of experiments presented in this work does not strongly support this hypothesis in regard of the known yield of I($^2P_{1/2}$) reported in the literature for the different precursors: the I($^2P_{1/2}$) yield measured [154] in C_2H_5I photolysis at 248 nm is found to be around 0.7, very close to the value for CH_3I. The I($^2P_{1/2}$) yields have also been measured [155] at 222 (266) nm to be 0.63 (0.79), 0.57 (0.72) and 0.40 (0.44) for CH_3I, C_2H_5I and 2-C_3H_7I, respectively. The determined I($^2P_{1/2}$) yield of 1-C_3H_7I at 222 nm was found [156] with a significantly higher value at 0.54 compared to 2-C_3H_7I. From these results a slower OH decay would be expected for propylperoxy radicals compared to methyl and ethyl, and an even slower for 2-$C_3H_7O_2$ compared to 1-$C_3H_7O_2$ because less I($^2P_{1/2}$) would be available for collision

with OH in the case of i-$C_3H_7O_2$. However, this was not observed during the experiments and 2-C_3H_7I as precursor tends to result in a faster OH decay. The hypothesis of a fast chemical reaction between OH and I atoms is thus the most likely to explain the large difference between the rate constants for RO_2 + OH when using the different precursors. A systematic error as explanation for the very fast rate constants obtained when using RI as precursor due to this fast reaction is very unlikely, because photolysis repetition rates were always very low, at 0.2 Hz generally, and flow rates were set to assure renewal of the gas mixture between two photolysis shots. Bossolasco et al. [134] have carried out experiments varying flow rates and photolysis frequencies in a large range and have not observed any systematic variation of the rate constant for the reaction CH_3O_2 + OH.

6.3.2 The yield of HO_2 as a product of the reaction

As for the reaction CH_3O_2 + OH, the HO_2 yield Φ_{HO2} for the reaction of the C_2-C_4 peroxy radicals with OH reactions should also be determined in order to determine the impact of these reactions on the composition of the remote atmosphere. To do so, three different approaches have been used with different precursors, with first the study of the $C_2H_5O_2$ radicals from the photolysis of $(COCl)_2$ and the resulting reaction of Cl atom with C_2H_6, and then from the photolysis of XeF_2 and the resulting reaction of F atoms with C_2H_6, C_3H_8 and C_4H_{10} to this time study all three peroxy radicals.

6.3.2.1 The use of C_2H_6+Cl as precursor: measurement of HO_2 yield

The reaction was initiated by the 248 nm photolysis of $(COCl)_2$ in the presence of excess C_2H_6 and two different concentration of O_2, a low one with the oxygen coming only from the leaks $[O_2] = 1.5\times10^{15}$ cm^{-3} and a high one with $[O_2] = 7.7\times10^{17}$ cm^{-3}. OH was simultaneously generated by the photolysis of H_2O_2, leading to the formation of

two OH radicals. The study was focused only on the ethyl peroxy radicals because for C_2H_6 only one isomer can be formed, while for C_3H_8 and C_4H_{10} two isomers can be formed, which could complicate the study. HO_2 radicals were detected by cw-CRDS and OH radicals were detected by cw-CRDs as well as by LIF. H_2O_2 was first photolysed alone in order to determine the initial H_2O_2 concentration from the OH and HO_2 concentration time profiles and was found to be $[H_2O_2] = 6.7\times10^{13}$ cm^{-3}. Ethane was then added to the mixture and its concentration was verified by the change in the OH decay, which will now react with H_2O_2 but also with C_2H_6. A concentration of $[C_2H_6] = 2\times10^{14}$ cm^{-3} was found. Finally, $(COCl)_2$ was also added and the OH and HO_2 concentration time profiles obtained for the two initial concentrations of O_2 are presented on the left graph in Figure 87 by plotting the decay of OH and the formation of HO_2 radicals as a function of the time. The OH and peroxy radicals reacts though the reaction:

$$C_2H_5O_2 + OH \rightarrow HO_2 + C_2H_5O \qquad \text{(R 45a)}$$

$$C_2H_5O_2 + OH \rightarrow \text{products} \qquad \text{(R 45b)}$$

followed in presence of O_2 by the reaction:

$$C_2H_5O + O_2 \rightarrow HO_2 + CH_3CHO \qquad \text{(R 57)}$$

The rate constant of (R 57) being $k(R\ 57) = 8.1\times10^{-15}$ cm^3 s^{-1} it is possible to separate the first HO_2 formed directly by (R 45a) and the second HO_2 formed through (R 57). Indeed at the low oxygen concentration $[O_2] = 1.5\times10^{15}$ cm^{-3} (R 57) is slow ($k(R\ 57)_{obs} \approx 12$ s^{-1}) and only the first HO_2 will be formed, while at the higher oxygen concentration $[O_2] = 7.7\times10^{17}$ cm^{-3} (R 57) is fast ($k(R\ 57)_{obs} \approx 6200$ s^{-1}) and the first and the second HO_2 will be detected. It can be expected that the ratio of overall HO_2 concentration over the initial HO_2 concentration should be at maximum 2. At the end of the experiment, ethane was replaced by methanol in order to determine the chlorine and thus the peroxy radical concentration as explained above, a peroxy radical concentration of $[C_2H_5O_2] = 8.9\times10^{12}$ cm^{-3} was found for the experiment in Figure 87.

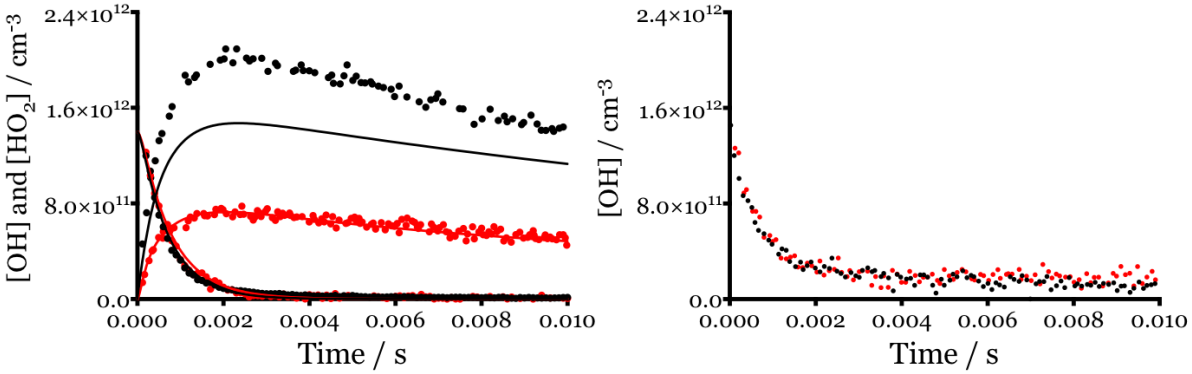

Figure 87: Left graph: OH by LIF (decaying) and HO_2 (rising) concentration time profiles for two different initial [O_2] (in red low, in black high) and using the same photolysis energy 72 mJ cm^{-2}. The full lines represent the result from the model to retrieve the HO_2. Right graph: corresponding online OH by cw-CRDS

The relative OH signals measured by LIF have been converted into concentration by applying a conversion factor in order to match the initial concentrations measured by LIF and by cw-CRDS. On right graph in Figure 87 the OH signal measured online by cw-CRDS for the two different concentrations of oxygen is presented. It can be seen that the signal does not decay to zero. This is not observed when OH is detected by LIF and therefore it can be concluded that the absorption is due to another species absorbing at the same wavelength than OH and that the signal does not stem from a recycling of OH. Only OH measured by LIF was used in the study to avoid any interference from this species. The experimental data in Figure 87 have been simulated using a simple mechanism. It can be seen that the fast decay of OH concentration is on the same order of magnitude than the rise of HO_2 concentration. It can also be seen that the maximum HO_2 concentration for the highest oxygen concentration is almost 2.5 times higher than the HO_2 concentration at low O_2. In order to determine the HO_2 yield Φ_{HO_2}, the concentration time profiles of the OH and HO_2 species have been adjusted to a simple model, with the reactions and rate constants listed in Table 17.

Table 17: Reaction mechanism used to fit OH and HO_2 concentration time profiles

No.	Reaction	Rate constant / $cm^3\ s^{-1}$	Reference
(R 58)	$Cl + C_2H_6 \rightarrow C_2H_5 + HCl$	5.8×10^{-11}	[157]
(R 59)	$OH + C_2H_6 \rightarrow C_2H_5 + H_2O$	2.33×10^{-13}	[158]
(R 60)	$Cl + C_2H_5 \rightarrow$ products	5.8×10^{-10}	[159]
(R 61)	$OH + C_2H_5 \rightarrow$ products	1×10^{-10}	[160]
(R 26)	$H_2O_2 + OH \rightarrow HO_2 + H_2O$	1.7×10^{-12}	[69]
(R 62)	$Cl + C_2H_5O_2 \rightarrow$ products	7.7×10^{-11}	[161]
(R 44a)	$C_2H_5O_2 + OH \rightarrow HO_2 + C_2H_5O$	0.65×10^{-10}	This work
(R 44b)	$\rightarrow$ products	0.65×10^{-10}	
(R 63a)	$C_2H_5 + O_2$ (+M) $\rightarrow C_2H_5O_2$	5×10^{-12}	[162]
(R 63b)	$\rightarrow HO_2 + C_2H_4$	2.5×10^{-13}	
(R 57)	$C_2H_5O + O_2 \rightarrow C_2H_4O + HO_2$	8.1×10^{-15}	[163]
(R 64a)	$2\ C_2H_5O_2 \rightarrow 2\ C_2H_5O + O_2$	4.8×10^{-14}	[164]
(R 64b)	$\rightarrow$ products	2.8×10^{-14}	
(R 65)	$C_2H_5O_2 + HO_2 \rightarrow$ products	7.8×10^{-12}	[164]
(R 24)	$HO_2 + HO_2$ (+M) $\rightarrow$ products	1.6×10^{-12}	[69]
(R 66)	$C_2H_5O + C_2H_5O \rightarrow$ products	7×10^{-11}	This work*
(R 67)	$C_2H_5O + HO_2 \rightarrow$ products	1.1×10^{-10}	This work*
(R 68)	$C_2H_5O_2 + C_2H_5O \rightarrow$ products	1.5×10^{-11}	[164]
(R 27)	$OH + HO_2 \rightarrow$ products	1.02×10^{-10}	This work
(R 29)	$HO_2 \rightarrow$ diffusion	$8 - 22\ s^{-1}$	This work

* values estimated similar to $k_{CH3O+CH3O}$ (R 41) and $k_{CH3O+HO2}$ (R 42)

The experiment at low oxygen concentration was very well reproduced with the mechanism and rate constants from Table 17, i.e. Φ_{HO2} = 0.5, which is almost two times lower than the Φ_{HO2} found for CH_3O_2 + OH reaction. Even at low oxygen concentration, $C_2H_5O_2$ radicals were formed in less than 100 µs. The HO_2 concentration resulting from reaction (R 63b) was measured to be ~ 3% of the initial

$C_2H_5O_2$. This value is in good agreement with previous work [162]. The rate constant of the reaction of C_2H_5O with OH is not well known, however estimating the rate constant [116] to $k_{C2H5O+OH} = 3\times10^{-11}$ cm^3 s^{-1} it can be seen that this reaction is not important even under the most unfavorable conditions (high radical and low O2 concentration) where only 1% of the initial OH radicals would react with C_2H_5O. The HO_2 decay at long reaction times is mainly influenced by reactions (R 65) and (R 67) whereby the last one is not known. Indeed, few values are found in the literature for k(R 65) varying between 0.49 and 1.1×10^{-11} cm^3 s^{-1} [16], [165], but no values are found for k(R 67). These two rate constants could be determined in the future using this experimental setup in order to model more precisely this experiment. However, it is not possible to model the HO_2 profile for the high oxygen concentration condition using this model: the model always underestimates the concentration of HO_2, i.e. there is apparently more than one HO_2 radical formed in (R 57). Few hypothesis can be brought up in order to explain this discrepancy: (i) the model underestimates the first HO_2, i.e. the yield would be higher than $\Phi_{HO2} = 0.5$ to reproduce the second HO_2 (ii) a fast reaction between $C_2H_5O_2$ and Cl leading to the formation of C_2H_5O without formation of the initial HO_2, but with the sequential to HO_2 at high O_2 (iii) another species formed at high O_2 absorbs at this wavelength, or (iv) there is recycling of HO_2 at high O_2 concentration.

In Figure 88, (i) the model has been adjusted to reproduce the HO_2 concentration time profile at high O_2 concentration by increasing the yield to $\Phi_{HO2} = 0.9$. Doing so, the oxygen concentration in the low oxygen conditions has to be decrease by a factor of 10 to $[O_2] = 1.5\times10^{14}$ cm^{-3} compared to the calculated oxygen concentration (1.5×10^{15} cm^{-3}). The OH decay and the HO_2 increase are too slow and are no more reproduced in this condition. This is due to the fact that at such a low oxygen concentration, the $C_2H_5O_2$ radicals are formed in few msec, while for concentrations of O_2 higher than 10^{15} cm^{-3} $C_2H_5O_2$ radicals are formed after less than 100 µs. Thus, the discrepancy seems to be in the formation of the second HO_2 and not in the initial HO_2.

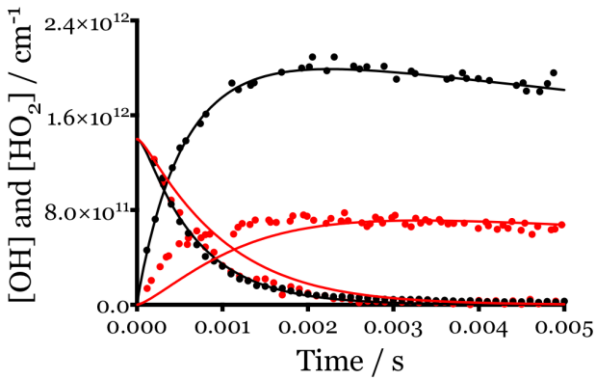

Figure 88: OH by LIF (decaying) and HO_2 (rising) concentration time profiles from Figure 87 for two different initial [O_2] (in red low, in black high) and using the same photolysis energy 72 mJ cm^{-2}. The model has been adjusted to reproduce the second HO_2

It is however unlikely that the O_2 concentration is not well measured, therefore other unknown reactions might play some role. Further experiments need to be carried out to understand this phenomenon.

In order to verify the hypothesis (ii) and (iii), a second experiment presented in Figure 89 was performed by keeping all the parameters constants but increasing the initial concentration of ethane by a factor 30 with [C_2H_6] = 7.3×10^{15} cm^{-3} and using three O_2 concentration with [O_2] = 5.5×10^{15} cm^{-3}, 4.6×10^{17} cm^{-3} and 1.1×10^{18} cm^{-3}. The offline signals of both OH and HO_2 have been measured.

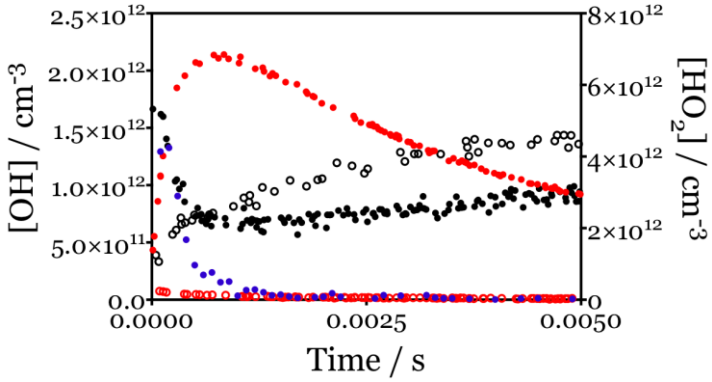

Figure 89: Left graph, left y-axis: OH concentration time profile measured by cw-CRDS (black dots online at 7028.83 cm^{-1}, black open dots offline at 7028.89 cm^{-1}) and by LIF (blue dots) converted into concentration from cw-CRDS by applying a factor taking into account the initial offline OH, right y-axis: HO_2 concentration time profile measured by cw-CRDS (red dots online at 6638.21 cm^{-1}, red open dots offline at 6638.3 cm^{-1}). Only the OH and HO_2 signals for the highest O_2 are shown

An offline measurement of OH showed that this species was formed directly after the photolysis pulse and increased roughly at the same rate than the HO_2 decay and stayed in the cell for a long time, suggesting a reaction of HO_2 maybe with the peroxy radical, leading to the formation of this stable species. However, it was not possible to identify it. The offline measurement of HO_2 did not show any absorption except just after the photolysis pulse. This absorption has a small impact on the rate constant k(R 63b) by reducing it only by less than 5%. This invalidates the assumption of a species formed at high O_2 concentration absorbing at the same wavelength than HO_2.

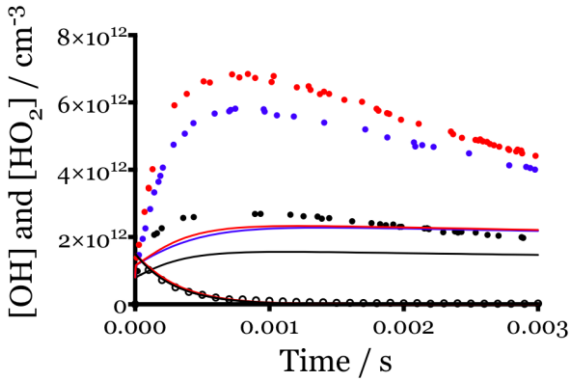

Figure 90: OH by LIF (open dots decaying) and HO_2 (rising) concentration time profiles from Figure 89 for three different O_2 concentrations: 5.5×10^{15} cm^{-3} (black), 4.6×10^{17} cm^{-3} (blue) and 1.1×10^{18} cm^{-3} (red). The full lines represent the result from the model

In Figure 90 it can be seen that the maximum HO_2 concentration for the highest oxygen concentration is again also almost 2.7 times higher than for the low oxygen concentration. In the case of a fast reaction between $C_2H_5O_2$ and Cl this ratio would have changed by changing the ratio of $C_2H_5O_2/C_2H_6$, because at higher C_2H_6 concentrations of the fraction of Cl reaction with $C_2H_5O_2$ would decrease and the interference should decrease. This is not the case here. However, contrary to the lower C_2H_6 concentration, it is not possible to simulate the OH and HO_2 profiles using the model in Table 17. Even for the lowest oxygen concentration the maximum of HO_2 concentration is already higher than initial OH concentration, reinforcing the

hypothesis (iv) of an unknown recycling of HO_2 involving C_2H_6 when using $(COCl)_2$ as precursor. This hypothesis cannot be verified in the current experiment due to the too few information about the chemistry of chlorine species with peroxy radicals and these reactions should be investigated first.

6.3.2.2 The use of C_2H_6+F as precursor: measurement of HO_2 yield

A second approach was used to determine the HO_2 yield Φ_{HO2} from the 248 nm of XeF_2 in presence of hydrocarbon and water to generate the peroxy radicals and OH radicals from following the reaction sequence detailed below:

$$XeF_2 + h\upsilon_{248nm} \rightarrow 2\ F + Xe \qquad \text{(R 50)}$$

$$RH + F \rightarrow R + HF \qquad \text{(R 51)}$$

$$H_2O + F \rightarrow OH + HF \qquad \text{(R 52)}$$

$$R + O_2\ (+M) \rightarrow RO_2 \qquad \text{(R 47)}$$

$$RO_2 + OH \rightarrow HO_2 + RO \qquad \text{(R 69a)}$$

$$RO_2 + OH \rightarrow \text{products} \qquad \text{(R 69b/c)}$$

As for the previous measurement, HO_2 and OH radicals have been quantified sequentially by cw-CRDS. Experiments have been carried out at a total pressure of 50 Torr using four different hydrocarbons, methane, ethane, propane and butane, and for each hydrocarbon two concentration of oxygen, one low at 1.2×10^{16} cm^{-3} and one high at 8.0×10^{17} cm^{-3}, while keeping the XeF_2 concentration and all other parameters constant by adjusting the concentration of the bath helium gas. Before adding each hydrocarbon, XeF_2 has been photolysed only in presence of H_2O to determine the initial concentration of F atoms, assuming that under these conditions all F atoms will be converted into OH. The difference between OH concentration with only H_2O and

with H_2O + hydrocarbon will thus be a good estimation of the concentration of the peroxy radicals. The initial radical concentrations obtained for OH and RO_2 in presence of hydrocarbon were around 1.6×10^{12} cm^{-3} and between 4.8 - 5.5×10^{12} cm^{-3} respectively, with ratios of RO_2/OH around 3 to 4. Knowing the HO_2 yield Φ_{HO2} in the case of methane, it is thus possible to determine the relative Φ_{HO2} for the three other hydrocarbons. The concentrations of the radicals and stable species are summarized in Table 18.

Table 18: Experimental conditions for all peroxy radicals

	O_2 / cm^{-3}	RH / cm^{-3}	F / cm^{-3}	$[HO_2]_{max}$ / cm^{-3}	$[OH]_{t=0}$ / cm^{-3}	$[RO_2]$ / cm^{-3}
H_2O	1.2×10^{16}	0	1.1×10^{13}	-	9.9×10^{12}	-
CH_4	1.2×10^{16}	4.6×10^{14}	1.1×10^{13}	1.1×10^{12}	1.5×10^{12}	8.3×10^{12}
CH_4	8.0×10^{17}	4.6×10^{14}	1.1×10^{13}	1.9×10^{12}	1.5×10^{12}	8.3×10^{12}
H_2O	1.2×10^{16}	0	1.1×10^{13}	-	7.0×10^{12}	-
C_2H_6	1.2×10^{16}	2.1×10^{14}	1.1×10^{13}	7.0×10^{11}	1.6×10^{12}	5.5×10^{12}
C_2H_6	8.0×10^{17}	2.1×10^{14}	1.1×10^{13}	1.4×10^{12}	1.6×10^{12}	5.5×10^{12}
H_2O	1.2×10^{16}	0	1.1×10^{13}	-	6.3×10^{12}	-
n-C_3H_8	1.2×10^{16}	2.6×10^{14}	1.1×10^{13}	3.5×10^{11}	1.5×10^{12}	4.8×10^{12}
n-C_3H_8	8.0×10^{17}	2.6×10^{14}	1.1×10^{13}	4.2×10^{11}	1.5×10^{12}	4.8×10^{12}
H_2O	1.2×10^{16}	0	1.1×10^{13}	-	8.1×10^{12}	-
n-C_4H_{10}	1.2×10^{16}	1.2×10^{14}	1.1×10^{13}	1.1×10^{11}	1.6×10^{12}	6.5×10^{12}
n-C_4H_{10}	8.0×10^{17}	1.2×10^{14}	1.1×10^{13}	1.6×10^{11}	1.6×10^{12}	6.5×10^{12}

The Figure 91 presents the concentration time profiles of OH and HO_2, obtained during the experiments presented in Table 18. It can be seen that the decay in OH concentration is on the same timescale than the increase of HO_2 concentration. The relative HO_2 yield at low O_2 compared to the HO_2 yield in the methane case is 60% of

the initial OH concentration in the case of ethane, while it decreases to 30% and 9% for propane and butane respectively, suggesting a lower yield of HO_2 radicals produced from the (R 69a) for longer hydrocarbons. Contrarily to the experiment using Cl + C_2H_6 as precursors, the ratio of $[HO_2]/[OH]$ is this time at maximum double between the low and high oxygen concentrations suggesting that the Cl atoms had an impact on the level of maximum HO_2 concentration by maybe recycling HO_2 at high oxygen concentration. Experiments should be performed using Cl + C_3H_8/C_4H_{10} to verify this is also the case for other peroxy radicals. In order to determine the HO_2 yield Φ_{HO_2}, the concentration time profiles of the OH and HO_2 species have been adjusted to a simple model in the case of ethane with the reactions and rate constants shown in Table 19.

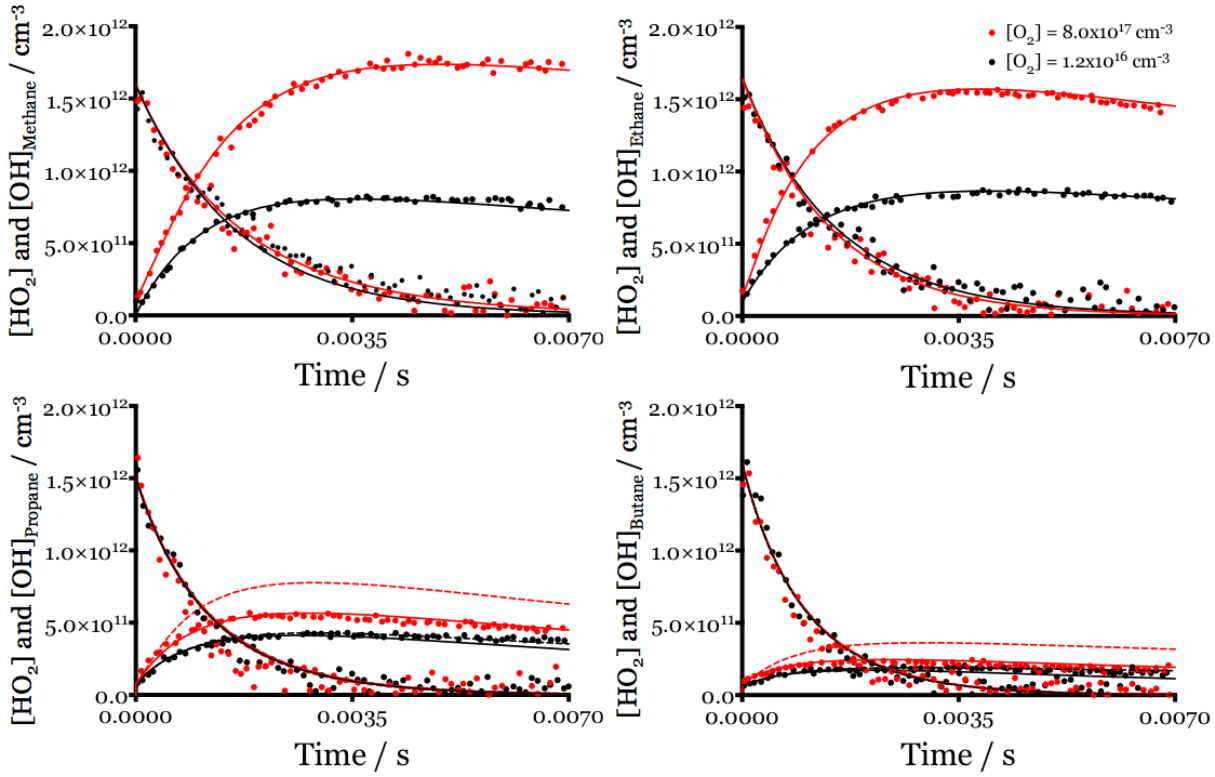

Figure 91: HO_2 rising and OH decaying concentration time profiles for two different initial $[O_2]$ (in red high, in black low) using different hydrocarbon: methane, ethane, propane or butane. Full lines: model from Table 19 excluding (R 70), dotted lines: including (R 70)

Table 19: Reaction mechanism used to fit OH and HO_2 concentration time profiles in the case of $C_2H_5O_2$ + OH from F + C_2H_6 precursors

No.	Reaction	Rate constant / cm^3 s^{-1}	Reference
(R 51)	F + RH → R + HF	6.3×10^{-11} CH_3	[129], [166],
		1.1×10^{-10} C_2H_5	[167]
		4.8×10^{-11} n-C_3H_7	
		2.4×10^{-11} i-C_3H_7	
		3.3×10^{-11} 1-C_4H_9	
		2.2×10^{-11} sec-C_4H_9	
(R 59)	OH + RH → R + H_2O	6.3×10^{-15} CH_4	[158]
		2.3×10^{-13} C_2H_6	
		1.1×10^{-12} C_3H_8	
		2.3×10^{-12} C_4H_{10}	
(R 52)	F + H_2O → OH + HF	1.4×10^{-11}	[129]
(R 61)	OH + R → products	1.2×10^{-10} CH_3	[160], [168],
		1.0×10^{-10} C_2H_5	estimated for
		1.0×10^{-10} C_3H_7	C_3H_8 and
		1.0×10^{-10} C_4H_9	C_4H_{10}
(R 44a)	RO_2 + OH → HO_2 + RO	$\Phi_{HO_2, CH_4} = 0.90$	This work
(R 44b)	→ products	$\Phi_{HO_2, C_2H_6} = 0.55$	
		$\Phi_{HO_2, C_3H_8} = 0.24$	
		$\Phi_{HO_2, C_4H_{10}} = 0.07$	
(R 63a)	R + O_2 (+M) → RO_2	1.4×10^{-13} CH_3	[162], [169]
		5.0×10^{-12} C_2H_5	
		6.0×10^{-12} n-C_3H_7	
		8.3×10^{-12} i-C_3H_7	
		7.5×10^{-12} 1-C_4H_9	
		1.7×10^{-11} sec-C_4H_9	

(R 63b)	→ HO_2 + products	4×10^{-15} CH_3	estimated
		1.5×10^{-14} C_2H_5	from $[HO_2]_{t=0}$
		5×10^{-14} C_3H_7	
		1.4×10^{-14} C_4H_9	
(R 15)	RO + O_2 → HO_2 + products	1.9×10^{-15} CH_3	[115]
		8.1×10^{-15} C_2H_5	
		1.0×10^{-14} n-C_3H_7	
		7.0×10^{-15} i-C_3H_7	
		1.4×10^{-14} 1-C_4H_9	
		7.7×10^{-15} sec-C_4H_9	
(R 9a)	2 RO_2 → 2 RO + O_2	1.3×10^{-13} CH_3	[2], [115],
		4.8×10^{-14} C_2H_5	[170],
		2×10^{-13} n-C_3H_7	estimated for
		6.6×10^{-16} i-C_3H_7	C_3H_7 and C_4H_9
		2.7×10^{-13} 1-C_4H_9	isomers
		4.7×10^{-14} sec-C_4H_9	
(R 9b)	→ products	2.2×10^{-13} CH_3	[2], [115],
		2.8×10^{-14} C_2H_5	[170],
		1×10^{-13} n-C_3H_7	estimated for
		4.4×10^{-16} i-C_3H_7	C_3H_7 and C_4H_9
		1.3×10^{-13} 1-C_4H_9	isomers
		2.3×10^{-14} sec-C_4H_9	
(R 10)	RO_2 + HO_2 → products	5.2×10^{-12} CH_3	[2], [171]
		7.8×10^{-12} C_2H_5	
		9.1×10^{-12} C_3H_7	
		9.5×10^{-12} C_4H_9	
(R 24)	HO_2 + HO_2 (+M) → products	1.6×10^{-12}	[69]
(R 66)	RO + RO → products	7.0×10^{-11}	This work*
(R 67)	RO + HO_2 → products	1.1×10^{-10}	This work*

(R 68)	RO_2 + RO → products	1.5×10^{-11}	[164] estimated from C_2H_6
(R 27)	OH + HO_2 → products	1.02×10^{-10}	This work
(R 29)	HO_2 → diffusion	8 – 22 s^{-1}	This work
(R 70)	C_3H_7O → other processes	10000 s^{-1}	This work
	C_4H_9O → other processes	15000 s^{-1}	

* values estimated similar to $k_{CH3O+CH3O}$ (R 41) and $k_{CH3O+HO2}$ (R 42)

The methane and ethane experiments with two different oxygen concentration were very well reproduced with the mechanism and rate constants from Table 19, i.e. $\Phi_{HO2,\ CH4}$ = 0.90 and $\Phi_{HO2,\ C2H4}$ = 0.55. The value $\Phi_{HO2,\ C2H4}$ is similar to the one determined using Cl atoms as precursor. The uncertainty of the rate constants k(R 15), leading to formation of the second HO_2 radical, is given [115] with ±50%. However, the highest O_2 concentration used during the experiments was high enough so that the value of k(R 15) had only a very minor impact on the HO_2 profiles. The reaction of RO with OH may have an importance depending on their rate constants for the lowest concentration of oxygen, even though the rate constant is not well known. However, taking an estimated rate constant [116] from the reaction CH_3O + OH with $k_{CH3O+OH}$ = 3×10^{-11} cm^3 s^{-1} under the low O_2 concentration, only 1% of the initial OH radicals would react with RO. The reactions of RO + HO_2 and RO + RO were taking into account using the measured values of the rate constants from CH_3O + HO_2 and CH_3O + CH_3O reactions defined in chapter 5. These two reactions did not play any role under the highest oxygen concentration. However, under the lowest oxygen concentration, these reactions played a minor role in the maximum value of HO_2 where around 10% of the maximum HO_2 would reaction through this reaction. The influence of (R 27), (R 9) and (R 10) are very limited at short reaction times and even though the value of their rate constants are not well known in the case of propane and butane, they have a negligible influence on the retrieval of Φ_{HO2}. In the case of propane and butane, in absence of any literature data, the formation of the two

isomers has been determined from the number of H atoms available for the reaction of H-abstraction through reaction (R 51). Thus, ratios of n-C_3H_7/i-C_3H_7 = 2 and 1-C_4H_9/sec-C_4H_9 = 1,5 were calculated. The model does not reproduce the HO_2 profile for the highest oxygen concentration, while for the lowest O_2 concentration the HO_2 profiles are reproduced using $\Phi_{HO2,\ C3H8}$ = 0.24 and $\Phi_{HO2,\ C4H10}$ = 0.07. The mechanism for conversion of RO to HO_2 depends on the length and on the structure of the R group. For high O_2 concentrations, CH_3O and C_2H_5O radicals are almost exclusively converted into HO_2 by reaction with O_2. However for more complex RO radicals such as C_3H_7O and C_4H_9O, these radicals can undergo other loss processes, involving isomerization in the case of C_4H_9O, thermal decomposition or reaction with other species. These different processes thus consume C_3H_7O and C_4H_9O, which are not converted into the second HO_2. A rate loss of 10000 and 15000 s^{-1} is needed to be used in the model for C_3H_7O and C_4H_9O respectively to reproduce the HO2 profile at high O_2 concentration. As discussed above, the major uncertainty in the values of Φ_{HO2} comes mainly from uncertainties in the values of OH and HO_2 absorption cross-sections. Thus, the determination of the HO_2 yield from the three experiments at a total pressure of 50 Torr shows that HO_2 is one of the major products with Φ_{HO2} = 0.55±0.10 for $C_2H_5O_2$, and minor products with Φ_{HO2} = 0.24±0.10 and Φ_{HO2} = 0.07±0.07 for $C_3H_7O_2$ and $C_4H_9O_2$, respectively.

Aside from this experimental investigation on the dependence of HO_2 yield on the size of the hydrocarbon chain, theoretical calculations have been performed by L. Vereecken at the Institut für Energie und Klimaforschung in Forschungszentrum Jülich. Recent studies [133], [172] on the CH_3O_2 + OH and $C_2H_5O_2$ + OH shows that the reactions proceed near-exclusively by the formation of an ROOOH trioxide intermediate, whose lowest-lying fragmentation channel is the formation of RO + HO_2, in agreement with the measurements of high yields of HO_2 as discussed above, and predicted an alcohol + O_2 channel with minor yield.

$$RO_2 + OH \rightarrow ROOOH^* \rightarrow RO{-}HO_2 \rightarrow RO + HO_2 \quad \text{(R 69a)}$$

$$\rightarrow RO{-}HO_2 \rightarrow ROH + O_2 \quad \text{(R 69b)}$$

$$\xrightarrow{+M} \text{ROOOH thermalized} \quad \text{(R 69c)}$$

Qualitative theoretical analysis of the pressure-dependent yields of the HO_2 + RO products and thermalized ROOOH adduct in the RO_2 + OH reaction have been determined as a function of the substrate R.

The (R 69a) reaction sequence is largely independent of the alkyl group in the reactants. In all cases, the exothermic product channel allows for direct dissociation of chemically activated ROOOH adducts. The collision number, and stabilization rates remain comparable across all ROOOH adducts considered. However, the excess energy available to the trioxide adduct is distributed across all degrees of freedom, the number of which increase significantly for larger R-substrates. This slows down the rate of dissociation, such that the competition of collisional energy loss becomes more important as the R-group becomes larger. Table 20 and Table 21 list the results of the calculations for all RO_2 radicals considered. As expected, redissociation of the trioxide adduct to the reactants is negligible in all cases. In the experimental conditions of 50 Torr He in Table 20, fragmentation to RO + HO_2 is the dominant path for CH_3O_2 and $C_2H_5O_2$, with the near-complete conversion to CH_3O + HO_2 in the CH_3O_2 + OH reaction being in agreement with earlier experimental work. For $C_3H_7O_2$ and $C_4H_9O_2$, the importance of the collisional stabilization of the ROOOH increases in importance, and for alkyl-groups larger than C_4H_9, it is expected that the yield of HO_2 becomes very minor. While the absolute values in Table 20 rely on the calibration of the theoretical predictions to the experimental HO_2 yield in the $C_2H_5O_2$ + OH reaction, the predicted trend as a function of the R-substrate relative to this reference reaction is solely the result of the changing molecular properties as derived from the quantum chemical predictions. The good agreement of the predicted HO_2 yields compared to the experimental results thus supports the experimental observations and indicates that the product yield trends are mostly due to changes in the fragmentation rate of the ROOOH intermediate.

In the atmosphere, at a higher pressure of 760 Torr and with the more efficient N_2 and O_2 colliders, an increased yield of stabilized ROOOH is predicted as shown in Table 21. While fragmentation to CH_3O + HO_2 remains the dominant product channel in the CH_3O_2+OH reaction, peroxy radicals with 2 or more carbons are predicted to undergo mostly collisional stabilization of the trioxide intermediate. In these conditions, kinetic models will have to incorporate the secondary chemistry of the trioxide to express the impact of the title reactions. The predictions at 760 Torr still benefit from the calibration of the ratio of dissociation to collisional stabilization for the $C_2H_5O_2$ + OH reaction in atmospheric conditions, as changing the bath gas is equivalent to a relative rate increase, which is more reliable than a priori absolute estimates. Despite this, the predictions are still expected to carry a sizable uncertainty, which can be as high as a factor of 1.5 on the product yields.

Table 20: Product yields of the RO_2+OH reactions at 298K and 50 Torr He as a function of the alkyl group R.

Alkyl group R	Redissociation to RO_2 + OH	Fragmentation to RO + HO_2 measured / theory	Stabilisation of ROOOH
CH_3	1.5%	(85±15)% / 98%	0.004%
C_2H_5	2.2%	(55±10)% / 57% [a]	40%
n-C_3H_7	0.7%	(24±10)% / 17%	81%
n-C_4H_9	1.6%	(7±7)% / 4%	96%

[a] Calibrated approximately against the experimental HO_2 yield.

Table 21: Product yields of the RO_2+OH reactions at 298K and 760 Torr N_2 as a function of the alkyl group R.

Alkyl group R	Redissociation to RO_2 + OH	Fragmentation to RO + HO_2	Stabilisation of ROOOH
CH_3	1.2%	91%	8%
C_2H_5	0.5%	11%	89%
n-C_3H_7	0.08%	1.5%	98%
n-C_4H_9	0.01%	0.3%	99.7%

6.4 Conclusion

The absorption cross-section of CH_3O_2 at 7489.16 cm^{-1} was determined using two different methods, first using the kinetic method by taking advantage of the known value of the rate constant for the self-reaction, then by direct comparison with the well-characterized HO_2 absorption cross-section at 6638.21 cm^{-1}. Both methods gave a similar value of $\sigma_{CH3O2,7489.16cm-1}$ = (3.4±0.4) ×10^{-20} cm^2 in perfect agreement with the previously measured value [19].

Knowing the absorption cross-section of CH_3O_2, the rate constant of the reaction CH_3O_2 + OH has been determined using F atoms from XeF_2 photolysis as a precursor for the simultaneous generation of both radicals. CH_3O_2 and OH radicals were quantified by cw-CRDS in the near-infrared region. The rate constant has been found with (1.6±0.4)×10^{-10} cm^3 s^{-1}, nearly a factor of 2 slower than an earlier determination of Bossolasco et al. [134] but nearly a factor of 2 faster than a very recent determination of Yan et al. [137]. It is suspected that the earlier, very fast value was biased through two possible processes: (i) excited I atoms generated during the photolysis of CH_3I as precursor for CH_3O_2 radicals could be quenched in collision with OH, leading to vibrationally excited OH(v = 2) radicals, which were not detected by the LIF system, or (ii) a very fast reaction between I atoms and OH radicals, the second assumption being the most plausible. However, no explanation can be given concerning the disagreement with the slower rate constant and more experiments are needed using another technique to resolve this disagreement. Two different experimental techniques have been used to determine the products of this reaction. The HO_2 yield has been obtained by simultaneous time-resolved measurements of the absolute concentration of HO_2 by cw-CRDS and the possible formation of a Criegee intermediate has been measured by broadband cavity enhanced UV absorption. A yield of Φ_{HO2} = (0.85±15) and an upper limit for $\Phi_{Criegee}$ < 0.05 has been determined for this reaction, suggesting a possible minor yield of methanol or stabilized trioxide as a product. The impact of this reaction on the composition of the remote marine boundary layer has been determined by implementing these findings into a box model

utilizing the Master Chemical Mechanism v3.2, and constraining the model for conditions found at Cape Verde Atmospheric Observatory in the remote tropical Atlantic Ocean. Inclusion of the CH_3O_2 + OH reaction into the model results in up to 30% decrease in the CH_3O_2 radical concentration while the HO_2 concentration increased by up to 20%. Production and destruction of O_3 are also influenced by these changes, and the model indicates that taking into account this reaction leads to a 6% decrease of O_3.

The rate constants for the reaction of three peroxy radicals ($C_2H_5O_2$, n-$C_3H_7O_2$ and n-$C_4H_9O_2$) with OH have been measured using different precursors. Peroxy radicals have been prepared by either the reaction of Cl atoms with C_2H_6, C_3H_8 or C_4H_{10} or through the photolysis of the corresponding alkyliodide. Using Cl atoms, rate constants of 1.3, 1.4 and 1.5×10^{-10} cm^3 s^{-1} have been found for $C_2H_5O_2$, n-$C_3H_7O_2$ and n-$C_4H_9O_2$, respectively. Experiments using the 248 nm photolysis of the corresponding alkyliodides as precursor enhances the rate constants by a factor of two, bringing up the hypothesis of a very fast reaction between I atoms and OH radicals. Two different precursors were used to determine the HO_2 yield: the reaction of Cl atoms with C_2H_6 or the reaction of F atoms with C_2H_6 in the case of ethane, and F atoms with C_3H_8 and C_4H_{10} for propane and butane. Even if a strange behavior was observed in the case of chlorine for high oxygen concentration leading to too much HO_2, a yield of $\Phi_{HO2,ethane}$ = (0.55±10) $\Phi_{HO2,propane}$ = (0.24±0.10) and $\Phi_{HO2,butane}$ = (0.07±0.07) was found for the three peroxy radicals. Theoretical calculation realized at 50 Torr helium and at 760 Torr nitrogen agrees with the experimentally determined yields with the fragmentation to RO + HO_2 as dominant path for CH_3O_2 and $C_2H_5O_2$ (only at 50 Torr but minor at 760 Torr for $C_2H_5O_2$), with the near-complete conversion to CH_3O + HO_2 in the CH_3O_2 + OH reaction. For $C_3H_7O_2$ and $C_4H_9O_2$, the collisional stabilization of the ROOOH increases in importance, and for alkyl-groups larger than C_4H_9, it is expected that the yield of HO_2 becomes very minor.

Conclusion and further work

While the influence of RO_2 in polluted environments is well known and numerous experimental results are available, the reaction scheme in clean environment is much less known. Under low NO_x conditions the RO_2 self- and cross-reactions become predominant and RO_2 can also react with OH radicals. However, until recently no experimental or theoretical data were found in the literature about RO_2 + OH reactions and these reactions were not included in atmospheric chemistry models. Their impact on atmospheric chemistry is however critically dependent on the nature and yields of the products. This thesis was focused on kinetic studies of relevant reactions including OH, HO_2 and RO_2 radicals to better understand their oxidation mechanisms in low NO_x environment. After a short overview of the role of peroxy radicals in the photochemistry of the troposphere highlighting the role of HO_2 radicals as intermediates of reactions and their interconversion with OH radicals, existing techniques used for the detection of these three radicals were described briefly taking into account the strengths and weaknesses of each technique. Two well-known techniques, namely Laser Induced Fluorescence (LIF, for OH radical) and continuous-wave Cavity Ring-Down Spectroscopy (cw-CRDS, for OH, HO_2 and RO_2 radicals) coupled to a laser photolysis reaction have been used as the measurement tools for the kinetic in the framework of this thesis and the characterization of each technique has been developed.

In the Chapter 3, the absorption time profiles of OH and HO_2 following the 248 nm photolysis of H_2O_2 have been measured on two cw-CRDS absorption paths. Taking advantage of the well-known absorption cross-sections of HO_2 radicals at 6638.21 cm^{-1}: (i) the absorption cross-section of two H_2O_2 lines have been determined, (ii) the rate constant of the reaction between OH and HO_2 was determined with $k = (1.02\pm0.06)\times10^{-10}$ cm^3 s^{-1}, which is in good agreement with current recommendations by IUPAC, and (iii) the peak absorption cross-section of OH at 7028.831 cm^{-1} has been determined at 50 Torr helium to be $\sigma_{OH} = (1.54\pm0.1) \times 10^{-19}$ cm^2. The broadening

coefficient of this line has been determined between 10 and 90 Torr in helium, oxygen and nitrogen. Knowledge of this absorption cross-section and these broadening coefficient will allow easy quantification of OH radicals in future experiments with the goal of studying branching ratios of atmospherically important reactions.

In the Chapter 4, the absorption profiles of HO_2 and DO_2 following the 248 nm photolysis of $(COCl)_2$ in presence of (deuterated) methanol and oxygen have been measured in the spectral range 6957 to 7077 cm^{-1}. First the relative absorption spectrum of both species was measured in this spectral range, and then the absorption cross-section of few intense and isolated selected lines have been measured. The strongest absorption cross-sections at 50 Torr helium are $\sigma_{7000.28\ cm^{-1}} = 2.12\times10^{-19}$ cm^2 for HO_2 and $\sigma_{7019.83cm^{-1}} = 2.97\times10^{-19}$ cm^2 and $\sigma_{7022.98cm^{-1}} = 2.51\times10^{-19}$ cm^2 for DO_2. The pressure broadening of the HO_2 line at 7000.28 cm^{-1} and of the DO_2 line at 7022.98 cm^{-1} was investigated at different pressure between 10 and 100 Torr helium. Due to the H/D exchange during the study of DO_2 lines, a small amount of HO_2 was always found. To take into account the presence of HO_2 during the measurement of the rate constant of the DO_2 self-reaction, the loss of DO_2 through the reaction with HO_2 has also to be determined by measuring the rate constant of the HO_2 + DO_2. The rate constants $k_{DO2+DO2} = (7.0\pm1.0)\times10^{-13}$ cm^3 s^{-1} and $k_{HO2+DO2} = (3.0\pm0.5)\times\times10^{-12}$ cm^3 s^{-1} were determined. The cross-reaction HO_2 + DO_2 is even faster than the HO_2 self-reaction and thus theoretical studies should be performed in order to explain this discrepancy. Knowledge of these HO_2 and DO_2 absorption cross-sections and broadening coefficients will allow the measurement of H-abstraction reactions by using partially deuterated species forming HO_2 and DO_2 and by measuring the yield of these two radicals.

In Chapter 5, the yields of CH_3O and CH_2OH from the reaction of F atoms with CH_3OH have been determined by converting both radicals into HO_2 taking advantage of the very different rate constants with O_2. Nearly equal amounts of both radicals with a slight excess of CH_3O ($\phi_{CH_3O} = 0.504\pm0.013$) have been found. In the same reaction system, the rate constant of the CH_3O self-reaction as well as of the reactions between CH_3O + HO_2 has been determined with $k_{CH3O+CH3O} = (7.0\pm1.4)\times10^{-11}$ cm^3 s^{-1}

and $k_{CH3O+HO2}$ = (1.1±0.2)×10^{-10} cm^3 s^{-1}. While the rate constant of CH_3O + CH_3O has already been determined a few times, this was the first determination of the rate constant for the reaction of CH_3O + HO_2. Only an estimation and a theoretical calculation are available, with however a rate constant of 3 orders of magnitude lower. Therefore, this reaction has been re-examined by theoretical methods, and fast rate constant, in agreement with the experimental determination, has been obtained with no valid reason explaining the huge disagreement. The thus determined yield and rate constants could now be used for the determination of F atom concentration after their conversion into HO_2 radicals, which can be measured using their well characterized absorption cross-sections.

Finally, in the Chapter 6 the absorption cross-section of CH_3O_2 at 7489.16 cm^{-1} was determined using two different methods (a kinetic method or by direct comparison with HO_2) leading to $\sigma_{CH3O2,7489.16cm-1}$ = (3.4±0.4) ×10^{-20} cm^2. Knowing the absorption cross-section of CH_3O_2, the rate constant of the reaction CH_3O_2 + OH has been determined with (1.6±0.4)×10^{-10} cm^3 s^{-1}, nearly a factor of 2 slower than an earlier determination of Bossolasco et al. [134] but nearly a factor of 2 faster than a very recent determination of Yan et al. [137]. The disagreement with the other rate constants needs to be explained using another technique. A yield of Φ_{HO2} = (0.85±20) and an upper limit for $\Phi_{Criegee}$ < 0.05 has been determined for this reaction, suggesting a possible minor yield of methanol or stabilized trioxide as a product. Inclusion of this reaction into the MCM model results in up to 30% decrease in the CH_3O_2 radical concentration while the HO_2 concentration increased by up to 20%. Production and destruction of O_2 are also influenced by these changes, and the model indicates a 6% decrease of O_3. The rate constants for the reaction of $C_2H_5O_2$, n-$C_3H_7O_2$ and n-$C_4H_9O_2$ radicals with OH have been measured and rate constants of 1.3, 1.4 and 1.5×10^{-10} cm^3 s^{-1} have been found for $C_2H_5O_2$, n-$C_3H_7O_2$ and n-$C_4H_9O_2$, respectively. Experiments using the 248 nm photolysis of the corresponding alkyliodides as precursor enhances the rate constants by a factor of two, bringing up the hypothesis of a very fast reaction between I atoms and OH radicals. Yields of $\Phi_{HO2,ethane}$ = (0.55±10) $\Phi_{HO2,propane}$ = 0.24±0.10 and $\Phi_{HO2,butane}$ = 0.07±0.07 were found for the three peroxy radicals, which were in agreement with theoretical calculation. A strange behavior was

observed when using Cl + C_2H_6 as precursors of this reaction in the case of high oxygen concentration leading to too much HO_2. Further studies need to be performed to explain this discrepancy. Taking advantage of the absorption cross-section of DO_2, C_2D_5I could also be used as precursor and the HO_2 yield could be determined through the reaction of $C_2D_5O_2$ + OH leading to HO_2 and C_2D_5O which will be converted to DO_2 by reaction with O_2.

If the chemistry of CH_3O_2 and $C_2H_5O_2$ radicals in low NO_x environment starts to be well known, only few studies have been performed on $C_3H_7O_2$ and $C_4H_9O_2$ radicals and almost no studies exist for bigger peroxy radicals. This setup can be used in the future to measure a wide range of radical-radical reactions. However, sometimes it is not always possible to find the precursors that could be photolysed at the same wavelength to initiate the reaction. A second photolysis laser could be added to the setup to do so. For example, it may be possible to measure the rate constant of the reaction OH + I by photolysing first H_2O_2 at 248 nm in presence of I_2, which does not absorb at this wavelength, to extract the concentration of I_2 using the known rate constant OH + I_2. Then, a second photolysis laser around 530 nm would be synchronized with the first photolysis laser to photolysed I_2. Knowing the photolysis energy, it would be possible to extract a possibly fast rate constant of OH + I. This reaction may explain the discrepancy between the rate constants using precursors containing or not I atoms.

Bibliography

[1] J. H. Seinfeld and S. N. Pandis, *Atmospheric Chemistry and Physics: From Air Pollution to Climate Change*. John Wiley & Sons, 2016.

[2] J. J. Orlando and G. S. Tyndall, "Laboratory studies of organic peroxy radical chemistry: an overview with emphasis on recent issues of atmospheric significance," *Chem. Soc. Rev.*, vol. 41, no. 19, pp. 6294–6317, Sep. 2012.

[3] D. Stone, L. K. Whalley, and D. E. Heard, "Tropospheric OH and HO_2 radicals: field measurements and model comparisons," *Chemical Society Reviews*, vol. 41, no. 19, pp. 6348–6404, 2012.

[4] D. E. Heard and M. J. Pilling, "Measurement of OH and HO_2 in the Troposphere," *Chem. Rev.*, vol. 103, no. 12, pp. 5163–5198, Dec. 2003.

[5] B. J. Finlayson-Pitts and J. N. P. Jr, *Chemistry of the Upper and Lower Atmosphere: Theory, Experiments, and Applications*. Academic Press, 1999.

[6] L. K. Whalley *et al.*, "Quantifying the magnitude of a missing hydroxyl radical source in a tropical rainforest," *Atmos. Chem. Phys.*, vol. 11, no. 14, pp. 7223–7233, Jul. 2011.

[7] C. M. Mihele and D. R. Hastie, "The sensitivity of the radical amplifier to ambient water vapour," *Geophys. Res. Lett.*, vol. 25, no. 11, pp. 1911–1913, Jun. 1998.

[8] L. Reichert, M. D. Andrés Hernández, D. Stöbener, J. Burkert, and J. P. Burrows, "Investigation of the effect of water complexes in the determination of peroxy radical ambient concentrations: Implications for the atmosphere," *J. Geophys. Res.*, vol. 108, no. D1, p. 4017, Jan. 2003.

[9] K. Miyazaki, A. E. Parker, C. Fittschen, P. S. Monks, and Y. Kajii, "A new technique for the selective measurement of atmospheric peroxy radical concentrations of HO_2 and RO_2 using a denuding method," *Atmos. Meas. Tech.*, vol. 3, no. 6, pp. 1547–1554, Nov. 2010.

[10] F. L. Eisele and J. D. Bradshaw, "The Elusive Hydroxyl Radical Measuring OH in the Atmosphere," *Anal. Chem.*, vol. 65, no. 21, p. 927A–939A, Nov. 1993.

[11] C. A. Cantrell *et al.*, "Peroxy radical observations using chemical ionization mass spectrometry during TOPSE," *J. Geophys. Res.*, vol. 108, no. D6, p. 8371, Mar. 2003.

[12] G. M. Wolfe *et al.*, "Missing peroxy radical sources within a summertime ponderosa pine forest," *Atmos. Chem. Phys.*, vol. 14, no. 9, pp. 4715–4732, May 2014.

[13] H.-P. Dorn, U. Brandenburger, T. Brauers, and M. Hausmann, "A New In Situ Laser Long-Path Absorption Instrument for the Measurement of Tropospheric OH Radicals," *J. Atmos. Sci.*, vol. 52, no. 19, pp. 3373–3380, Oct. 1995.

[14] H. Fuchs *et al.*, "Comparison of OH concentration measurements by DOAS and LIF during SAPHIR chamber experiments at high OH reactivity and low NO concentration," *Atmos. Meas. Tech.*, vol. 5, no. 7, pp. 1611–1626, Jul. 2012.

[15] D. Amedro, K. Miyazaki, A. Parker, C. Schoemaecker, and C. Fittschen, "Atmospheric and kinetic studies of OH and HO_2 by the FAGE technique," *Journal of Environmental Sciences*, vol. 24, no. 1, pp. 78–86, Jan. 2012.

[16] T. J. Wallington, P. Dagaut, and M. J. Kurylo, "UV absorption cross sections and reaction kinetics and mechanisms for peroxy radicals in the gas phase," *Chem. Rev.*, vol. 92, no. 4, pp. 667–710, Jun. 1992.

[17] O. J. Nielsen, M. S. Johnson, T. J. Wallington, L. K. Christensen, and J. Platz, "UV absorption spectra of HO_2, CH_3O_2, $C_2H_5O_2$, and $CH_3C(O)CH_2O_2$ radicals and mechanism of the reactions of F and Cl atoms with $CH_3C(O)CH_3$," *Int. J. Chem. Kinet.*, vol. 34, no. 5, pp. 283–291, Jan. 2002.

[18] M. B. Pushkarsky, S. J. Zalyubovsky, and T. A. Miller, "Detection and characterization of alkyl peroxy radicals using cavity ringdown spectroscopy," *The Journal of Chemical Physics*, vol. 112, no. 24, pp. 10695–10698, Jun. 2000.

[19] E. P. Faragó, B. Viskolcz, C. Schoemaecker, and C. Fittschen, "Absorption Spectrum and Absolute Absorption Cross Sections of CH_3O_2 Radicals and CH_3I Molecules in the Wavelength Range 7473–7497 cm^{-1}," *The Journal of Physical Chemistry A*, vol. 117, no. 48, pp. 12802–12811, Dec. 2013.

[20] S. N. Mikhailenko, W. Le, S. Kassi, and A. Campargue, "Weak water absorption lines around 1.455 and 1.66μm by CW-CRDS," *Journal of Molecular Spectroscopy*, vol. 244, no. 2, pp. 170–178, Aug. 2007.

[21] S. Kassi, D. Romanini, A. Campargue, and B. Bussery-Honvault, "Very high sensitivity CW-cavity ring down spectroscopy: Application to the a1Δg(0)–X3Σg-(1) O_2 band near 1.58μm," *Chemical Physics Letters*, vol. 409, no. 4, pp. 281–287, Jun. 2005.

[22] O. M. Lyulin, A. Campargue, D. Mondelain, and S. Kassi, "The absorption spectrum of acetylene by CRDS between 7244 and 7918cm^{-1}," *Journal of Quantitative Spectroscopy and Radiative Transfer*, vol. 130, pp. 327–334, Nov. 2013.

[23] C. Jain, P. Morajkar, C. Schoemaecker, B. Viskolcz, and C. Fittschen, "Measurement of Absolute Absorption Cross Sections for Nitrous Acid (HONO) in the Near-Infrared Region by the Continuous Wave Cavity Ring-Down Spectroscopy (cw-CRDS) Technique Coupled to Laser Photolysis," *J. Phys. Chem. A*, vol. 115, no. 39, pp. 10720–10728, Oct. 2011.

[24] M. K. Sprague, L. A. Mertens, H. N. Widgren, M. Okumura, S. P. Sander, and A. B. McCoy, "Cavity Ringdown Spectroscopy of the Hydroxy-Methyl-Peroxy Radical," *J. Phys. Chem. A*, vol. 117, no. 39, pp. 10006–10017, Oct. 2013.

[25] P. S. Thomas and T. A. Miller, "Cavity ringdown spectroscopy of the NIR A-X electronic transition of allyl peroxy radical ($H_2CCH–CH_2OO·$)," *Chemical Physics Letters*, vol. 491, no. 4, pp. 123–131, May 2010.

[26] L. S. Rothman *et al.*, "The HITRAN2012 molecular spectroscopic database," *Journal of Quantitative Spectroscopy and Radiative Transfer*, vol. 130, pp. 4–50, Nov. 2013.

[27] M. D. A. Hernández *et al.*, "Marine boundary layer peroxy radical chemistry during the AEROSOLS99 campaign: Measurements and analysis," *J. Geophys. Res.*, vol. 106, no. D18, pp. 20833–20846, Sep. 2001.

[28] G. D. Edwards *et al.*, "Chemical Ionization Mass Spectrometer Instrument for the Measurement of Tropospheric HO_2 and RO_2," *Anal. Chem.*, vol. 75, no. 20, pp. 5317–5327, Oct. 2003.

[29] T. Brauers, M. Hausmann, A. Bister, A. Kraus, and H.-P. Dorn, "OH radicals in the boundary layer of the Atlantic Ocean: 1. Measurements by long-path laser absorption spectroscopy," *J. Geophys. Res.*, vol. 106, no. D7, pp. 7399–7414, Apr. 2001.

[30] D. Mihelcic *et al.*, "Peroxy radicals during BERLIOZ at Pabstthum: Measurements, radical budgets and ozone production," *J. Geophys. Res.*, vol. 108, no. D4, p. 8254, Feb. 2003.

[31] I. Johnson and M. Davidson, "Jablonski Energy Diagram." [Online]. Available: http://www.olympusmicro.com/primer/java/jablonski/jabintro/.

[32] G. P. Smith and D. R. Crosley, "A photochemical model of ozone interference effects in laser detection of tropospheric OH," *J. Geophys. Res.*, vol. 95, no. D10, pp. 16427–16442, Sep. 1990.

[33] G. G. Guilbault, *Practical Fluorescence, Second Edition*. CRC Press, 1990.

[34] S. Forget, "Optique des Lasers et Faisceaux Gaussiens." [Online]. Available: http://www.optique-ingenieur.org/fr/cours/OPI_fr_M01_C03/co/OPI_fr_M01_C03_web.html.

[35] D. Z. Anderson, J. C. Frisch, and C. S. Masser, "Mirror reflectometer based on optical cavity decay time," *Appl. Opt., AO*, vol. 23, no. 8, pp. 1238–1245, Apr. 1984.

[36] A. O'Keefe and D. A. G. Deacon, "Cavity ring- down optical spectrometer for absorption measurements using pulsed laser sources," *Review of Scientific Instruments*, vol. 59, no. 12, pp. 2544–2551, Dec. 1988.

[37] K. K. Lehmann, "Ring-down cavity spectroscopy cell using continuous wave excitation for trace species detection," US5528040 A, 18-Jun-1996.

[38] A. E. Parker, C. Jain, C. Schoemaecker, P. Szriftgiser, O. Votava, and C. Fittschen, "Simultaneous, time-resolved measurements of OH and HO_2 radicals by coupling of high repetition rate LIF and cw-CRDS techniques to a laser photolysis reactor and its application to the photolysis of H_2O_2," *Applied Physics B*, vol. 103, no. 3, pp. 725–733, Jun. 2011.

[39] O. Votava, M. Mašát, A. E. Parker, C. Jain, and C. Fittschen, "Microcontroller based resonance tracking unit for time resolved continuous wave cavity-ringdown spectroscopy measurements," *Review of Scientific Instruments*, vol. 83, no. 4, p. 43110, 2012.

[40] J. Thiebaud and C. Fittschen, "Near infrared cw-CRDS coupled to laser photolysis: Spectroscopy and kinetics of the HO_2 radical," *Applied Physics B*, vol. 85, no. 2–3, pp. 383–389, Nov. 2006.

[41] *Sirah Dye Laser: Service Manual: Pulse Dye Laser*. 2009.

[42] L. S. Rothman *et al.*, "The HITRAN 2004 molecular spectroscopic database," *Journal of Quantitative Spectroscopy and Radiative Transfer*, vol. 96, no. 2, pp. 139–204, Dec. 2005.

[43] S. Dusanter, D. Vimal, P. S. Stevens, R. Volkamer, and L. T. Molina, "Measurements of OH and HO_2 concentrations during the MCMA-2006 field campaign–Part 1: Deployment of the Indiana University laser-induced fluorescence instrument," *Atmospheric Chemistry and Physics*, vol. 9, no. 5, pp. 1665–1685, 2009.

[44] P. P. Morajkar, "Application of laser photolysis coupled to time resolved optical detection methods to study the kinetics and spectroscopy of atmospherically relevant species," Thesis, Université Lille 1, 2012.

[45] Y.-C. Wang, L.-H. Shyu, and C.-P. Chang, "The Comparison of Environmental Effects on Michelson and Fabry-Perot Interferometers Utilized for the Displacement Measurement," *Sensors*, vol. 10, no. 4, pp. 2577–2586, Mar. 2010.

[46] W. W. Chow and S. W. Koch, *Semiconductor-Laser Fundamentals*. 2010.

[47] R. Paschotta, *Field guide to lasers*. Bellingham, Wash: SPIE Press, 2008.

[48] J. Chaithanya, "Laser photolysis coupled to detection by LIF and cw-CRDS: Application to spectroscopic and kinetic studies of OH, HO_2 and HONO," Thesis, Université Lille 1, 2011.

[49] J. Nocedal and S. Wright, *Numerical Optimization*. Springer Science & Business Media, 2006.

[50] C. B. M. Groß, T. J. Dillon, G. Schuster, J. Lelieveld, and J. N. Crowley, "Direct Kinetic Study of OH and O_3 Formation in the Reaction of $CH_3C(O)O_2$ with HO_2," *J. Phys. Chem. A*, vol. 118, no. 6, pp. 974–985, Feb. 2014.

[51] J. Thiebaud, F. Thévenet, and C. Fittschen, "OH Radicals and H_2O_2 Molecules in the Gas Phase near to TiO_2 Surfaces," *J. Phys. Chem. C*, vol. 114, no. 7, pp. 3082–3088, Feb. 2010.

[52] S. A. Carr *et al.*, "Experimental and Modeling Studies of the Pressure and Temperature Dependences of the Kinetics and the OH Yields in the Acetyl + O_2 Reaction," *J. Phys. Chem. A*, vol. 115, no. 6, pp. 1069–1085, Feb. 2011.

[53] F. A. F. Winiberg *et al.*, "Pressure-dependent calibration of the OH and HO_2

channels of a FAGE HOx instrument using the Highly Instrumented Reactor for Atmospheric Chemistry (HIRAC)," *Atmos. Meas. Tech.*, vol. 8, no. 2, pp. 523–540, Feb. 2015.

[54] Y. Sadanaga *et al.*, "Development of a measurement system of OH reactivity in the atmosphere by using a laser-induced pump and probe technique," *Review of Scientific Instruments*, vol. 75, no. 8, pp. 2648–2655, Aug. 2004.

[55] A.-L. Holloway *et al.*, "Rate coefficients for the reactions of OH radicals with the keto/enol tautomers of 2,4-pentanedione and 3-methyl-2,4-pentanedione, allyl alcohol and methyl vinyl ketone using the enols and methyl nitrite as photolytic sources of OH," *Journal of Photochemistry and Photobiology A: Chemistry*, vol. 176, no. 1, pp. 183–190, Dec. 2005.

[56] A. S. Hasson, G. S. Tyndall, and J. J. Orlando, "A Product Yield Study of the Reaction of HO_2 Radicals with Ethyl Peroxy ($C_2H_5O_2$), Acetyl Peroxy ($CH_3C(O)O_2$), and Acetonyl Peroxy ($CH_3C(O)CH_2O_2$) Radicals," *J. Phys. Chem. A*, vol. 108, no. 28, pp. 5979–5989, Jul. 2004.

[57] T. J. Dillon and J. N. Crowley, "Direct detection of OH formation in the reactions of HO_2 with $CH_3C(O)O_2$ and other substituted peroxy radicals," *Atmos. Chem. Phys.*, vol. 8, no. 16, pp. 4877–4889, Aug. 2008.

[58] E. Assaf, B. Song, A. Tomas, C. Schoemaecker, and C. Fittschen, "Rate Constant of the Reaction between CH_3O_2 Radicals and OH Radicals Revisited," *J. Phys. Chem. A*, vol. 120, no. 45, pp. 8923–8932, Nov. 2016.

[59] E. P. Faragó, C. Schoemaecker, B. Viskolcz, and C. Fittschen, "Experimental determination of the rate constant of the reaction between $C_2H_5O_2$ and OH radicals," *Chemical Physics Letters*, vol. 619, pp. 196–200, Jan. 2015.

[60] C. Fittschen, L. K. Whalley, and D. E. Heard, "The Reaction of CH_3O_2 Radicals with OH Radicals: A Neglected Sink for CH_3O_2 in the Remote Atmosphere," *Environ. Sci. Technol.*, vol. 48, no. 14, pp. 7700–7701, Jul. 2014.

[61] A. T. Archibald, A. S. Petit, C. J. Percival, J. N. Harvey, and D. E. Shallcross, "On the importance of the reaction between OH and RO_2 radicals," *Atmosph. Sci. Lett.*, vol. 10, no. 2, pp. 102–108, Apr. 2009.

[62] P. F. Bernath and R. Colin, "Revised molecular constants and term values for

the X2Π and B2Σ+ states of OH," *Journal of Molecular Spectroscopy*, vol. 257, no. 1, pp. 20–23, Sep. 2009.

[63] D. Romanini and K. K. Lehmann, "Ring- down cavity absorption spectroscopy of the very weak HCN overtone bands with six, seven, and eight stretching quanta," *The Journal of Chemical Physics*, vol. 99, no. 9, pp. 6287–6301, Nov. 1993.

[64] J. Thiebaud, S. Crunaire, and C. Fittschen, "Measurements of Line Strengths in the $2\nu^1$ Band of the HO_2 Radical Using Laser Photolysis/Continuous Wave Cavity Ring-Down Spectroscopy (cw-CRDS)," *The Journal of Physical Chemistry A*, vol. 111, no. 30, pp. 6959–6966, Aug. 2007.

[65] W. Ludwig, B. Brandt, G. Friedrichs, and F. Temps, "Kinetics of the Reaction C_2H_5 + HO_2 by Time-Resolved Mass Spectrometry," *J. Phys. Chem. A*, vol. 110, no. 9, pp. 3330–3337, Mar. 2006.

[66] Z. Hong, A. Farooq, E. A. Barbour, D. F. Davidson, and R. K. Hanson, "Hydrogen Peroxide Decomposition Rate: A Shock Tube Study Using Tunable Laser Absorption of H_2O near 2.5 μm," *J. Phys. Chem. A*, vol. 113, no. 46, pp. 12919–12925, Nov. 2009.

[67] G. L. Vaghjiani and A. R. Ravishankara, "Photodissociation of H_2O_2 and CH_3OOH at 248 nm and 298 K: Quantum yields for OH, O(3P) and H(2S)," *The Journal of Chemical Physics*, vol. 92, no. 2, pp. 996–1003, Jan. 1990.

[68] J. Thiebaud, A. Aluculesei, and C. Fittschen, "Formation of HO_2 radicals from the photodissociation of H_2O_2 at 248nm," *The Journal of Chemical Physics*, vol. 126, no. 18, p. 186101, May 2007.

[69] R. Atkinson *et al.*, "Evaluated kinetic and photochemical data for atmospheric chemistry: Volume I - gas phase reactions of O_X, HO_X, NO_X and SO_X species," *Atmos. Chem. Phys.*, vol. 4, no. 6, pp. 1461–1738, Sep. 2004.

[70] Y. Tang, G. S. Tyndall, and J. J. Orlando, "Spectroscopic and Kinetic Properties of HO_2 Radicals and the Enhancement of the HO_2 Self Reaction by CH_3OH and H_2O," *J. Phys. Chem. A*, vol. 114, no. 1, pp. 369–378, Jan. 2010.

[71] H. Bouzidi, C. Fittschen, P. Coddeville, and A. Tomas, "Photolysis of 2,3-pentanedione and 2,3-hexanedione: Kinetics, quantum yields, and product study in a simulation chamber," *Atmospheric Environment*, vol. 82, pp. 250–257, Jan. 2014.

[72] N. Ibrahim, J. Thiebaud, J. Orphal, and C. Fittschen, "Air-broadening coefficients of the HO_2 radical in the $2\nu_1$ band measured using cw-CRDS," *Journal of Molecular Spectroscopy*, vol. 242, no. 1, pp. 64–69, Mar. 2007.

[73] P. Morajkar, A. Bossolasco, C. Schoemaecker, and C. Fittschen, "Photolysis of CH_3CHO at 248 nm: Evidence of triple fragmentation from primary quantum yield of CH_3 and HCO radicals and H atoms," *The Journal of Chemical Physics*, vol. 140, no. 21, p. 214308, Jun. 2014.

[74] M. Wojdyr, "Fityk: a general-purpose peak fitting program," *J Appl Cryst, J Appl Crystallogr*, vol. 43, no. 5, pp. 1126–1128, Oct. 2010.

[75] E. Assaf and C. Fittschen, "Cross Section of OH Radical Overtone Transition near 7028 cm^{-1} and Measurement of the Rate Constant of the Reaction of OH with HO_2 Radicals," *J. Phys. Chem. A*, vol. 120, no. 36, pp. 7051–7059, Sep. 2016.

[76] A. V. Ivanov, S. Trakhtenberg, A. K. Bertram, Y. M. Gershenzon, and M. J. Molina, "OH, HO_2, and Ozone Gaseous Diffusion Coefficients," *J. Phys. Chem. A*, vol. 111, no. 9, pp. 1632–1637, Mar. 2007.

[77] B. Ghosh, D. K. Papanastasiou, and J. B. Burkholder, "Oxalyl chloride, ClC(O)C(O)Cl: UV/vis spectrum and Cl atom photolysis quantum yields at 193, 248, and 351 nm," *The Journal of Chemical Physics*, vol. 137, no. 16, p. 164315, Oct. 2012.

[78] K. V. Chance *et al.*, "Pressure broadening of the 118.455 cm^{-1} rotational lines of OH by H_2, He, N_2, and O_2," *Journal of Molecular Spectroscopy*, vol. 146, no. 2, pp. 375–380, Apr. 1991.

[79] M. E. Jenkin, R. A. Cox, G. D. Hayman, and L. J. Whyte, "Kinetic study of the reactions CH_3O_2+ CH_3O_2 and CH_3O_2+ HO_2 using molecular modulation spectroscopy," *J. Chem. Soc., Faraday Trans. 2*, vol. 84, no. 7, pp. 913–930, Jan. 1988.

[80] M. J. Elrod, D. L. Ranschaert, and N. J. Schneider, "Direct kinetics study of the temperature dependence of the CH_2O branching channel for the CH_3O_2 + HO_2 reaction," *Int. J. Chem. Kinet.*, vol. 33, no. 6, pp. 363–376, Jun. 2001.

[81] C. C. Kircher and S. P. Sander, "Kinetics and mechanism of hydroperoxo and hydroperoxo-d disproportionations," *J. Phys. Chem.*, vol. 88, no. 10, pp. 2082–2091, May 1984.

[82] B. A. Thrush and G. S. Tyndall, “Reactions of HO_2 studied by flash photolysis with diode-laser spectroscopy,” *J. Chem. Soc., Faraday Trans. 2*, vol. 78, no. 8, pp. 1469–1475, Jan. 1982.

[83] N. A. Martin and B. A. Thrush, “The disproportionation of DO_2 radicals studied by infrared laser spectroscopy,” *Chemical Physics Letters*, vol. 153, no. 2, pp. 200–202, Dec. 1988.

[84] H. E. Hunziker and H. R. Wendt, “Near infrared absorption spectrum of HO_2,” *The Journal of Chemical Physics*, vol. 60, no. 11, pp. 4622–4623, Jun. 1974.

[85] C. A. Taatjes and D. B. Oh, “Time-resolved wavelength modulation spectroscopy measurements of HO_2 kinetics,” *Applied optics*, vol. 36, no. 24, pp. 5817–5821, 1997.

[86] J. D. DeSain, A. D. Ho, and C. A. Taatjes, “High-resolution diode laser absorption spectroscopy of the O–H stretch overtone band (2,0,0)←(0,0,0) of the HO_2 radical,” *Journal of Molecular Spectroscopy*, vol. 219, no. 1, pp. 163–169, May 2003.

[87] A. M. Knepp, G. Meloni, L. E. Jusinski, C. A. Taatjes, C. Cavallotti, and S. J. Klippenstein, “Theory, measurements, and modeling of OH and HO_2 formation in the reaction of cyclohexyl radicals with O_2,” *Phys. Chem. Chem. Phys.*, vol. 9, no. 31, pp. 4315–4331, Aug. 2007.

[88] J. Yi, C. Bahrini, C. Schoemaecker, C. Fittschen, and W. Choi, “Photocatalytic Decomposition of H_2O_2 on Different TiO_2 Surfaces Along with the Concurrent Generation of HO_2 Radicals Monitored Using Cavity Ring Down Spectroscopy,” *J. Phys. Chem. C*, vol. 116, no. 18, pp. 10090–10097, May 2012.

[89] E. H. Fink and D. A. Ramsay, “High-Resolution Study of the $\tilde{A}^2A' \rightarrow \tilde{X}^2A''$ Transition of HO_2: Analysis of the 000–000 Band,” *Journal of Molecular Spectroscopy*, vol. 185, no. 2, pp. 304–324, Oct. 1997.

[90] E. H. Fink and D. A. Ramsay, “High-Resolution Study of the $\tilde{A}^2A' \rightarrow \tilde{X}^2A''$ Transition of DO_2: Analysis of the 000–000 Band,” *Journal of Molecular Spectroscopy*, vol. 216, no. 2, pp. 322–334, Dec. 2002.

[91] N. Kanno, K. Tonokura, A. Tezaki, and M. Koshi, “Water Dependence of the HO_2 Self Reaction: Kinetics of the HO_2–H_2O Complex,” *J. Phys. Chem. A*, vol. 109,

no. 14, pp. 3153–3158, Apr. 2005.

[92] N. Kanno, K. Tonokura, A. Tezaki, and M. Koshi, "Nitrogen- and water-broadening coefficient measurements in the $\tilde{A}^2A' \leftarrow \tilde{X}^2A''$ 000–000 band of HO_2 using high-resolution diode laser two-tone frequency modulation spectroscopy," *Journal of Molecular Spectroscopy*, vol. 229, no. 2, pp. 193–197, Feb. 2005.

[93] E. G. Estupiñán, J. D. Smith, A. Tezaki, S. J. Klippenstein, and C. A. Taatjes, "Measurements and Modeling of DO_2 Formation in the Reactions of C_2D_5 and C_3D_7 Radicals with O_2," *J. Phys. Chem. A*, vol. 111, no. 19, pp. 4015–4030, May 2007.

[94] A. Schocker, M. Uetake, N. Kanno, M. Koshi, and K. Tonokura, "Kinetics and Rate Constants of the Reaction $CH_2OH+O_2 \rightarrow CH_2O+HO_2$ in the Temperature Range of 236–600 K," *J. Phys. Chem. A*, vol. 111, no. 29, pp. 6622–6627, Jul. 2007.

[95] C. M. Western, "PGOPHER: A program for simulating rotational, vibrational and electronic spectra," *Journal of Quantitative Spectroscopy and Radiative Transfer*, vol. 186, pp. 221–242, Jan. 2017.

[96] L. E. Christensen, M. Okumura, J. C. Hansen, S. P. Sander, and J. S. Francisco, "Experimental and ab Initio Study of the $HO_2 \cdot CH_3OH$ Complex: Thermodynamics and Kinetics of Formation," *J. Phys. Chem. A*, vol. 110, no. 21, pp. 6948–6959, Jun. 2006.

[97] L. E. Christensen, "Laboratory studies of atmospherically important gas-phase peroxy radical reactions," Thesis, California Institute of Technology, 2003.

[98] D. Stone and D. M. Rowley, "Kinetics of the gas phase HO_2 self-reaction: Effects of temperature, pressure, water and methanol vapours," *Phys. Chem. Chem. Phys.*, vol. 7, no. 10, pp. 2156–2163, May 2005.

[99] M. Staak, E. W. Gash, D. S. Venables, and A. A. Ruth, "The rotationally-resolved absorption spectrum of formaldehyde from 6547 to 6804 cm^{-1}," *Journal of Molecular Spectroscopy*, vol. 229, no. 1, pp. 115–121, Jan. 2005.

[100] N. Jacquinet-Husson *et al.*, "The 2015 edition of the GEISA spectroscopic database," *Journal of Molecular Spectroscopy*, vol. 327, pp. 31–72, Sep. 2016.

[101] S. P. Sander, M. Peterson, R. T. Watson, and R. Patrick, "Kinetics studies of the hydrogen dioxide + hydrogen dioxide and deuterium dioxide + deuterium dioxide reactions at 298 K," *J. Phys. Chem.*, vol. 86, no. 8, pp. 1236–1240, Apr. 1982.

[102] M. Mozurkewich and S. W. Benson, "Self-Reaction of HO_2 and DO_2: Negative temperature dependence and pressure effects," *Int. J. Chem. Kinet.*, vol. 17, no. 8, pp. 787–807, Aug. 1985.

[103] E. J. Hamilton and R.-R. Lii, "The Dependence on H_2O and on NH_3 of the Kinetics of the self-reaction of HO_2 in the gas-phase formation of $HO_2.H_2O$ and $HO_2{\cdot}NH_3$ complexes," *Int. J. Chem. Kinet.*, vol. 9, no. 6, pp. 875–885, Nov. 1977.

[104] L. J. Garland and K. D. Bayes, "Rate constants for some radical-radical cross-reactions and the geometric mean rule," *J. Phys. Chem.*, vol. 94, no. 12, pp. 4941–4945, Jun. 1990.

[105] S. Dóbé, T. Bérces, F. Temps, H. G. Wagner, and H. Ziemer, "Formation of methoxy and hydroxymethyl free radicals in selected elementary reactions," *Symposium (International) on Combustion*, vol. 25, no. 1, pp. 775–781, Jan. 1994.

[106] S. Dóbé *et al.*, "Direct Kinetic Studies of the Reactions $Br+CH_3OH$ and $CH_2OH+HBr$: The Heat of Formation of CH_2OH," *J. Phys. Chem.*, vol. 100, no. 51, pp. 19864–19873, Jan. 1996.

[107] J. T. Jodkowski, M.-T. Rayez, J.-C. Rayez, T. Bérces, and S. Dóbé, "Theoretical Study of the Kinetics of the Hydrogen Abstraction from Methanol. 2. Reaction of Methanol with Chlorine and Bromine Atoms," *J. Phys. Chem. A*, vol. 102, no. 46, pp. 9230–9243, Nov. 1998.

[108] K. Hoyermann, R. Sievert, and H. G. Wagner, "Mechanism of the reaction of H atoms with methanol," *Berichte der Bunsengesellschaft für physikalische Chemie*, vol. 85, no. 2, pp. 149–153, Feb. 1981.

[109] U. Meier, H. H. Grotheer, and T. Just, "Temperature dependence and branching ratio of the CH_3OH+OH reaction$_3$," *Chemical Physics Letters*, vol. 106, no. 1, pp. 97–101, Apr. 1984.

[110] P. Pagsberg, J. Munk, A. Sillesen, and C. Anastasi, "UV spectrum and kinetics of hydroxymethyl radicals," *Chemical Physics Letters*, vol. 146, no. 5, pp. 375–381, May 1988.

[111] D. J. Bogan, M. Kaufman, C. W. Hand, W. A. Sanders, and B. E. Brauer, "Laser-induced fluorescence study of methoxy radical formation from the reactions of fluorine(^{2}P) atoms with methanol (CH_3OH, CD_3OH, and CH_3OD)," *J. Phys. Chem.*,

vol. 94, no. 21, pp. 8128–8134, Oct. 1990.

[112] J. L. Durant, “Anomalous methoxy radical yields in the fluorine + methanol reaction. 1. Experiment,” *J. Phys. Chem.*, vol. 95, no. 26, pp. 10701–10704, Dec. 1991.

[113] J. T. Jodkowski, M.-T. Rayez, J.-C. Rayez, T. Bérces, and S. Dóbé, “Theoretical Study of the Kinetics of the Hydrogen Abstraction from Methanol. 1. Reaction of Methanol with Fluorine Atoms,” *J. Phys. Chem. A*, vol. 102, no. 46, pp. 9219–9229, Nov. 1998.

[114] W. A. Glauser and M. L. Koszykowski, “Anomalous methoxy radical yields in the fluorine + methanol reaction. 2. Theory,” *J. Phys. Chem.*, vol. 95, no. 26, pp. 10705–10713, Dec. 1991.

[115] R. Atkinson *et al.*, “Evaluated kinetic and photochemical data for atmospheric chemistry: Volume II - gas phase reactions of organic species,” *Atmos. Chem. Phys.*, vol. 6, no. 11, pp. 3625–4055, Sep. 2006.

[116] W. Tsang and R. F. Hampson, “Chemical Kinetic Data Base for Combustion Chemistry. Part I. Methane and Related Compounds,” *Journal of Physical and Chemical Reference Data*, vol. 15, no. 3, pp. 1087–1279, Jul. 1986.

[117] E. Hassinen, J. Koskikallio, and å. Oskarsson, “Flash Photolysis of Methyl Acetate in Gas Phase. Products and Rate Constants of Reactions between Methyl, Methoxy and Acetyl Radicals,” *Acta Chemica Scandinavica*, vol. 33a, pp. 625–630, 1979.

[118] J. Weaver, R. Shortridge, J. Meagher, and J. Heicklen, “The photooxidation of $CD_3N_2CD_3$,” *Journal of Photochemistry*, vol. 4, no. 1, pp. 109–120, Jan. 1975.

[119] M. J. Yee Quee and J. C. J. Thynne, “The Photolysis of Organic Esters,” *Berichte der Bunsengesellschaft für physikalische Chemie*, vol. 72, no. 2, pp. 211–217, Mar. 1968.

[120] M. J. Y. Quee and J. C. J. Thynne, “Photolysis of dimethyl carbonate,” *Trans. Faraday Soc.*, vol. 62, no. 0, pp. 3154–3161, Jan. 1966.

[121] P. Biggs, C. E. Canosa-Mas, J.-M. Fracheboud, D. E. Shallcross, and R. P. Wayne, “Kinetics of the reaction of F atoms with CH_3ONO and CH_3O, and the reaction of CH_3O with a number of hydrocarbons,” *Journal of the Chemical Society, Faraday Transactions*, vol. 93, no. 15, pp. 2481–2486, 1997.

[122] U. Meier, H. H. Grotheer, G. Riekert, and T. Just, “Study of Hydroxyl Reactions with Methanol and Ethanol by Laser-induced Fluorescence,” *Berichte der Bunsengesellschaft für physikalische Chemie*, vol. 89, no. 3, pp. 325–327, Mar. 1985.

[123] S. H. Mousavipour and Z. Homayoon, “Multichannel RRKM-TST and CVT Rate Constant Calculations for Reactions of CH_2OH or CH_3O with HO_2,” *J. Phys. Chem. A*, vol. 115, no. 15, pp. 3291–3300, Apr. 2011.

[124] P. C. Tellinghuisen and J. Tellinghuisen, “Precise Characterization of the B (1/2) and C (3/2) States of XeF from a Deperturbation Analysis of the B → X Spectrum of ^{136}XeF,” *J. Phys. Chem. A*, vol. 106, no. 36, pp. 8317–8322, Sep. 2002.

[125] H. Helm, L. E. Jusinski, D. C. Lorents, and D. L. Huestis, “KrF laser excitation of the D(1/2)←X(1/2) transition of XeF,” *The Journal of Chemical Physics*, vol. 80, no. 5, pp. 1796–1800, Mar. 1984.

[126] G. Black *et al.*, “XeF_2 photodissociation studies. I. Quantum yields and kinetics of XeF(B) and XeF(C),” *The Journal of Chemical Physics*, vol. 75, no. 10, pp. 4840–4846, Nov. 1981.

[127] G. T. Dunning *et al.*, “Dynamics of photodissociation of XeF_2 in organic solvents,” *Physical Chemistry Chemical Physics*, vol. 16, no. 30, pp. 16095–16102, 2014.

[128] P. C. Tellinghuisen, J. Tellinghuisen, J. A. Coxon, J. E. Velazco, and D. W. Setser, “Spectroscopic studies of diatomic noble gas halides. IV. Vibrational and rotational constants for the X, B, and D states of XeF,” *The Journal of Chemical Physics*, vol. 68, no. 11, pp. 5187–5198, Jun. 1978.

[129] R. Atkinson *et al.*, “Evaluated kinetic and photochemical data for atmospheric chemistry: Volume III - gas phase reactions of inorganic halogens,” *Atmospheric Chemistry and Physics Discussions*, vol. 6, no. 2, pp. 2281–2702, Apr. 2006.

[130] A. Parker, C. Jain, C. Schoemaecker, and C. Fittschen, “Kinetics of the reaction of OH radicals with CH_3OH and CD_3OD studied by laser photolysis coupled to high repetition rate laser induced fluorescence,” *React Kinet Catal Lett*, vol. 96, no. 2, pp. 291–297, Apr. 2009.

[131] S. M. Saunders, M. E. Jenkin, R. G. Derwent, and M. J. Pilling, “Protocol for the development of the Master Chemical Mechanism, MCM v3 (Part A): tropospheric

degradation of non-aromatic volatile organic compounds," *Atmos. Chem. Phys.*, vol. 3, no. 1, pp. 161–180, Feb. 2003.

[132] H. Bian, S. Zhang, and H. Zhang, "Theoretical study on the atmospheric reaction of CH_3O_2 with OH," *Int. J. Quantum Chem.*, vol. 115, no. 17, pp. 1181–1186, Sep. 2015.

[133] J.-F. Müller, Z. Liu, V. S. Nguyen, T. Stavrakou, J. N. Harvey, and J. Peeters, "The reaction of methyl peroxy and hydroxyl radicals as a major source of atmospheric methanol," *Nat Commun*, vol. 7, Oct. 2016.

[134] A. Bossolasco, E. P. Faragó, C. Schoemaecker, and C. Fittschen, "Rate constant of the reaction between CH_3O_2 and OH radicals," *Chemical Physics Letters*, vol. 593, pp. 7–13, Feb. 2014.

[135] S. Kirschke *et al.*, "Three decades of global methane sources and sinks," *Nature Geoscience*, vol. 6, no. 10, pp. 813–823, 2013.

[136] L. K. Whalley *et al.*, "The chemistry of OH and HO_2 radicals in the boundary layer over the tropical Atlantic Ocean," *Atmos. Chem. Phys.*, vol. 10, no. 4, pp. 1555–1576, Feb. 2010.

[137] C. Yan, S. Kocevska, and L. N. Krasnoperov, "Kinetics of the Reaction of CH_3O_2 Radicals with OH Studied over the 292–526 K Temperature Range," *J. Phys. Chem. A*, vol. 120, no. 31, pp. 6111–6121, Aug. 2016.

[138] T. J. Dillon, M. E. Tucceri, and J. N. Crowley, "Laser Induced Fluorescence Studies of Iodine Oxide Chemistry: The Reactions of IO with CH_3O_2, CF_3O_2 and O_3," *Phys. Chem. Chem. Phys.*, vol. 8, no. 44, pp. 5185–5198, Nov. 2006.

[139] E. A. Selzer and K. D. Bayes, "Pressure dependence of the rate of reaction of methyl radicals with oxygen," *J. Phys. Chem.*, vol. 87, no. 3, pp. 392–394, Feb. 1983.

[140] R. X. Fernandes, K. Luther, and J. Troe, "Falloff Curves for the Reaction CH_3 + O_2 (+ M) → CH_3O_2 (+ M) in the Pressure Range 2–1000 Bar and the Temperature Range 300–700 K," *J. Phys. Chem. A*, vol. 110, no. 13, pp. 4442–4449, Apr. 2006.

[141] D. B. Atkinson and J. L. Spillman, "Alkyl Peroxy Radical Kinetics Measured Using Near-infrared CW–Cavity Ring-down Spectroscopy," *J. Phys. Chem. A*, vol. 106, no. 38, pp. 8891–8902, Sep. 2002.

[142] A. T. J. B. Eppink and D. H. Parker, "Energy partitioning following

photodissociation of methyl iodide in the A band: A velocity mapping study," *The Journal of Chemical Physics*, vol. 110, no. 2, pp. 832–844, Dec. 1998.

[143] A. T. J. B. Eppink and D. H. Parker, "Methyl iodide A-band decomposition study by photofragment velocity imaging," *The Journal of Chemical Physics*, vol. 109, no. 12, pp. 4758–4767, Sep. 1998.

[144] G. N. A. Van Veen, T. Baller, A. E. De Vries, and M. Shapiro, "Photofragmentation of CF_3I in the A band," *Chemical Physics*, vol. 93, no. 2, pp. 277–291, Feb. 1985.

[145] I. I. Gonzalez Liz, F. Castano, E. Martinez, and M. N. Sanchez Rayo, "The collisional quenching of $I(5^2P_{12})$ by the molecules H_2O, CH_2OH, C_2H_5OH, HCOOH and CH_3COOH by time-resolved emission ($I(5^2P_{12}) \rightarrow I(5^2P_{32}) + h\nu$, $\lambda = 1.315$ μm) following pulsed-laser photolysis," *Journal of Photochemistry and Photobiology A: Chemistry*, vol. 55, no. 3, pp. 275–282, Jan. 1991.

[146] M. K. Gilles, J. B. Burkholder, and A. R. Ravishankara, "Rate coefficients for the reaction of OH with Cl_2, Br_2, and I_2 from 235 to 354 K," *Int. J. Chem. Kinet.*, vol. 31, no. 6, pp. 417–424, Jan. 1999.

[147] L. Sheps and D. W. Chandler, "Time-Resolved Broadband Cavity-Enhanced Absorption Spectroscopy for Chemical Kinetics," Sandia National Laboratories: Livermore, CA, SAND2013-2664, 2013.

[148] L. Sheps, A. M. Scully, and K. Au, "UV absorption probing of the conformer-dependent reactivity of a Criegee intermediate CH_3CHOO," *Phys. Chem. Chem. Phys.*, vol. 16, no. 48, pp. 26701–26706, Nov. 2014.

[149] L. Sheps, "Absolute Ultraviolet Absorption Spectrum of a Criegee Intermediate CH_2OO," *J. Phys. Chem. Lett.*, vol. 4, no. 24, pp. 4201–4205, Dec. 2013.

[150] J. D. Lee *et al.*, "Reactive Halogens in the Marine Boundary Layer (RHaMBLe): the tropical North Atlantic experiments," *Atmos. Chem. Phys.*, vol. 10, no. 3, pp. 1031–1055, Feb. 2010.

[151] G. S. Tyndall, J. J. Orlando, T. J. Wallington, M. Dill, and E. W. Kaiser, "Kinetics and mechanisms of the reactions of chlorine atoms with ethane, propane, and n-butane," *Int. J. Chem. Kinet.*, vol. 29, no. 1, pp. 43–55, Jan. 1997.

[152] S. Zhang, R. S. Strekowski, A. Monod, L. Bosland, and C. Zetzsch,

"Temperature-Dependent Kinetics Study of the Reactions of OH with C_2H_5I, n-C_3H_7I, and iso-C_3H_7I," *J. Phys. Chem. A*, vol. 116, no. 38, pp. 9497–9506, Sep. 2012.

[153] E. S. N. Cotter, C. E. Canosa-Mas, C. R. Manners, R. P. Wayne, and D. E. Shallcross, "Kinetic study of the reactions of OH with the simple alkyl iodides: CH_3I, C_2H_5I, 1-C_3H_7I and 2-C_3H_7I," *Atmospheric Environment*, vol. 37, no. 8, pp. 1125–1133, Mar. 2003.

[154] Y. Tang, W.-B. Lee, Z. Hu, B. Zhang, and K.-C. Lin, "Productions of I, I*, and C_2H_5 in the A-band photodissociation of ethyl iodide in the wavelength range from 245 to 283 nm by using ion-imaging detection," *The Journal of Chemical Physics*, vol. 126, no. 6, p. 64302, Feb. 2007.

[155] S. Uma and P. K. Das, "Production of $I^*(^2P_{1/2})$ in the ultraviolet photodissociation of α - branched alkyl iodides," *The Journal of Chemical Physics*, vol. 104, no. 12, pp. 4470–4474, Mar. 1996.

[156] S. Uma and P. K. Das, "I∗ production from n-alkyl iodides at 222 nm," *Chemical Physics Letters*, vol. 241, no. 4, pp. 335–338, Jul. 1995.

[157] M. G. Bryukov, I. R. Slagle, and V. D. Knyazev, "Kinetics of Reactions of Cl Atoms with Ethane, Chloroethane, and 1,1-Dichloroethane," *J. Phys. Chem. A*, vol. 107, no. 34, pp. 6565–6573, Aug. 2003.

[158] L. N. Krasnoperov and J. V. Michael, "Shock Tube Studies Using a Novel Multipass Absorption Cell: Rate Constant Results For OH + H^2 and OH + C^2H^6," *J. Phys. Chem. A*, vol. 108, no. 26, pp. 5643–5648, Jul. 2004.

[159] P. W. Seakins, E. L. Woodbridge, and S. R. Leone, "A laser flash photolysis, time-resolved Fourier transform infrared emission study of the reaction Cl + C_2H_5 → HCl(v) + C_2H_4," *J. Phys. Chem.*, vol. 97, no. 21, pp. 5633–5642, May 1993.

[160] K. Fagerström, A. Lund, G. Mahmoud, J. T. Jodkowski, and E. Ratajczak, "Kinetics of the gas-phase reaction between ethyl and hydroxyl radicals," *Chemical Physics Letters*, vol. 208, no. 3, pp. 321–327, Jun. 1993.

[161] M. M. Maricq, J. J. Szente, E. W. Kaiser, and J. Shi, "Reaction of Chlorine Atoms with Methylperoxy and Ethylperoxy Radicals," *J. Phys. Chem.*, vol. 98, no. 8, pp. 2083–2089, Feb. 1994.

[162] E. P. Clifford, J. T. Farrell, J. D. DeSain, and C. A. Taatjes, "Infrared

Frequency-Modulation Probing of Product Formation in Alkyl + O_2 Reactions: I. The Reaction of C_2H_5 with O_2 between 295 and 698 K," *J. Phys. Chem. A*, vol. 104, no. 49, pp. 11549–11560, Dec. 2000.

[163] W. B. DeMore *et al.*, "Chemical Kinetics and Photochemical Data for Use in Stratospheric Modeling. Evaluation No. 12," Jan. 1997.

[164] A. C. Noell, L. S. Alconcel, D. J. Robichaud, M. Okumura, and S. P. Sander, "Near-Infrared Kinetic Spectroscopy of the HO_2 and $C_2H_5O_2$ Self-Reactions and Cross Reactions," *J. Phys. Chem. A*, vol. 114, no. 26, pp. 6983–6995, Jul. 2010.

[165] F. F. Fenter, V. Catoire, R. Lesclaux, and P. D. Lightfoot, "The ethylperoxy radical: its ultraviolet spectrum, self-reaction, and reaction with hydroperoxy, each studied as a function of temperature," *J. Phys. Chem.*, vol. 97, no. 14, pp. 3530–3538, Apr. 1993.

[166] A. Persky, "The temperature dependence of the rate constant for the reaction $F+C_2H_6$," *Chemical Physics Letters*, vol. 380, no. 3, pp. 286–291, Oct. 2003.

[167] R. Pearson, J. Cowles, G. Hermann, D. Gregg, and J. Creighton, "Relative performance of a variety of NF_3 + hydrogen-donor transverse-discharge HF chemical-laser systems," *IEEE Journal of Quantum Electronics*, vol. 9, no. 9, pp. 879–889, Sep. 1973.

[168] M. Sangwan, E. N. Chesnokov, and L. N. Krasnoperov, "Reaction CH_3+OH Studied over the 294–714 K Temperature and 1–100 bar Pressure Ranges," *J. Phys. Chem. A*, vol. 116, no. 34, pp. 8661–8670, Aug. 2012.

[169] T. M. Lenhardt, C. E. McDade, and K. D. Bayes, "Rates of reaction of butyl radicals with molecular oxygen," *The Journal of Chemical Physics*, vol. 72, no. 1, pp. 304–310, Jan. 1980.

[170] B. G. Glover and T. A. Miller, "Near-IR Cavity Ringdown Spectroscopy and Kinetics of the Isomers and Conformers of the Butyl Peroxy Radical," *J. Phys. Chem. A*, vol. 109, no. 49, pp. 11191–11197, Dec. 2005.

[171] H. Hou, J. Li, X. Song, and B. Wang, "A Systematic Computational Study of the Reactions of HO_2 with RO_2: The HO_2+$C_2H_5O_2$ Reaction," *J. Phys. Chem. A*, vol. 109, no. 49, pp. 11206–11212, Dec. 2005.

[172] Y. Liu, L. Chen, D. Chen, W. Wang, F. Liu, and W. Wang, "Computational study

on mechanisms of $C_2H_5O_2$+OH reaction and properties of $C_2H_5O_3H$ complex," *Chem. Res. Chin. Univ.*, vol. 33, no. 4, pp. 623–630, Aug. 2017.

Nomenclature

BVOC: Biogenic Volatile Organic Compounds

PERCA: Peroxy Radical Chemical Amplifier

PerCIMS, ROxMas: Peroxy Radical Chemical Ionization Mass Spectroscopy

DOAS: Differential Optical Absorption Spectroscopy

FAGE: Fluorescence Assay by Gas Expansion

AOM: Acousto-Optic Modulator

cw-CRDS: continuous-wave Cavity Ring-Down Spectroscopy

DFB: Distributed Feed-Back

FSR: Free Spectral Range

G-FWHM: Gaussian Full-Width at Half-Maximum

L-HWHM: Lorentzian Half-Width at Half-Maximum

LIF: Laser Induced Fluorescence

MBL: Marine Boundary Layers

MCM: Master Chemical Mechanism

PM: PhotoMultiplier

CVAO: Cape Verde Atmospheric Observatory

PES: Potential Energy Surface

List of Reactions

$O_3 + h\upsilon_{<310nm} \rightarrow O(^1D) + O_2(^1\Delta_g)$ (R 1)

$O(^1D) + M \rightarrow O(^3P) + M$ (R 2)

$O(^1D) + H_2O \rightarrow 2\ OH$ (R 3)

$O(^3P) + O_2\ (+ M) \rightarrow O_3$ (R 4)

$OH + CO + O_2 \rightarrow HO_2 + CO_2$ (R 5)

$OH + RH + O_2 \rightarrow RO_2 + H_2O$ (R 6)

$RO_2 + NO \rightarrow RO + NO_2$ (R 7)

$HO_2 + NO \rightarrow OH + NO_2$ (R 8)

$RO_2 + RO_2 \rightarrow 2\ RO + O_2$ (R 9)

$HO_2 + RO_2 \rightarrow ROOH + O_2$ (R 10)

$HO_2 + HO_2 \rightarrow H_2O_2 + O_2$ (R 11)

$HO_2 + OH \rightarrow HO_2 + O_2$ (R 12)

$NO_2 + OH\ (+ M) \rightarrow HNO_3$ (R 13)

$RO_2 + NO \rightarrow RO + HO_2$ (R 14)

$RO + O_2 \rightarrow R'O + HO_2$ (R 15)

$HO_2 + NO \rightarrow OH + NO_2$ (R 16)

$OH + CO \rightarrow H + CO_2$ (R 17)

$H + O_2\ (+M) \rightarrow HO_2$ (R 18)

$OH + SO_2\ (+M) \rightarrow HSO_3$ (R 19)

$HSO_3 + O_2 \rightarrow SO_3 + HO_2$ (R 20)

$SO_3 + 2\ H_2O \rightarrow H_2SO_4 + H_2O$ (R 21)

HO_X or RO_X + Reactant → Products 1 (R 22)

HO_X or RO_X + Reference → Products 2 (R 23)

$HO_2 + HO_2\ (+M) \rightarrow H_2O_2 + O_2$ (R 24)

$H_2O_2 + h\nu_{248nm} \rightarrow 2\ OH$ (R 25)

$H_2O_2 + OH \rightarrow HO_2 + H_2O$ (R 26)

$HO_2 + OH \rightarrow O_2 + H_2O$ (R 27)

$OH + OH\ (+M) \rightarrow H_2O_2$ (R 28)

$HO_2 \rightarrow$ diffusion (R 29)

$OH \rightarrow$ diffusion (R 30)

$(COCl)_2 + h\upsilon_{248nm} \rightarrow 2\ Cl + 2\ CO$ (R 31)

$Cl + CH_3OH \rightarrow CH_2OH + HCl$ (R 32)

$CH_2OH + O_2 \rightarrow HO_2 + CH_2O$ (R 33)

$DO_2 + DO_2 \rightarrow D_2O_2 + O_2$ (R 34a)

$DO_2 + DO_2 + M \rightarrow D_2O_2 + O_2\ (+ M)$ (R 34b)

$DO_2 \rightarrow$ diffusion (R 35)

$DO_2 + HO_2 \rightarrow$ products (R 36)

$CH_3OH + F \rightarrow CH_3O + HF$ (R 37a)

$\rightarrow CH_2OH + HF$ (R 37b)

$CH_3O + O_2 \rightarrow HO_2 + CH_2O$ (R 38)

$CH_2OH + O_2 \rightarrow HO_2 + CH_2O$ (R 39)

$H_2O + F \rightarrow OH + HF$ (R 40)

$CH_3O + CH_3O \rightarrow$ product (R 41)

$CH_3O + HO_2 \rightarrow$ product (R 42)

$OH + CH_3OH \rightarrow CH_2O + H_2O$ (R 43)

$CH_3O_2 + OH \rightarrow CH_2OO + H_2O$ (R 44a)

$\rightarrow CH_3O + HO_2$ (R 44b)

$\rightarrow CH_3OH + O_2$ (R 44c)

$C_2H_5O_2 + OH \rightarrow$ products (R 45)

$CH_3I + h\upsilon_{248nm} \rightarrow CH_3 + I$ (R 46)

$CH_3 + O_2\ (+M) \rightarrow CH_3O_2$ (R 47)

$2\ CH_3O_2 \rightarrow 2\ CH_3O + O_2$ (R 48a)

$\rightarrow CH_2O + CH_3OH + O_2$ (R 48b)

$\rightarrow CH_3OOCH_3 + O_2$ (R 48c)

$CH_3O_2 + HO_2 \rightarrow CH_3OOH + O_2$ (R 49a)

$\rightarrow CH_2O + H_2O + O_2$ (R 49b)

$XeF_2 + h\upsilon_{248nm} \rightarrow 2\ F + Xe$ (R 50)

$CH_4 + F \rightarrow CH_3 + HF$ (R 51)

$H_2O + F \rightarrow OH + HF$ (R 52)

$C_3H_7O_2 + OH \rightarrow$ products (R 53)

$C_4H_9O_2 + OH \rightarrow$ products (R 54)

$Cl + RH \rightarrow R + HCl$ (R 55)

$R + O_2\ (+M) \rightarrow RO_2\ (+M)$ (R 56)

$C_2H_5O + O_2 \rightarrow HO_2 + CH_3CHO$ (R 57)

$Cl + RH \rightarrow R + HCl$ (R 58)

$OH + C_2H_6 \rightarrow C_2H_5 + H_2O$ (R 59)

$Cl + C_2H_5 \rightarrow$ products (R 60)

$OH + C_2H_5 \rightarrow$ products (R 61)

$Cl + C_2H_5O_2 \rightarrow$ products (R 62)

$C_2H_5 + O_2\ (+M) \rightarrow C_2H_5O_2$ (R 63a)

$\rightarrow HO_2 + C_2H_4$ (R 63b)

$2\ C_2H_5O_2 \rightarrow 2\ C_2H_5O + O_2$ (R 64a)

$\rightarrow$ products (R 64b)

$C_2H_5O_2 + HO_2 \rightarrow$ products (R 65)

$C_2H_5O + C_2H_5O \rightarrow$ products (R 66)

$C_2H_5O + HO_2 \rightarrow$ products (R 67)

$C_2H_5O_2 + C_2H_5O \rightarrow$ products (R 68)

$RO_2 + OH \rightarrow ROOOH^* \rightarrow RO{-}HO_2 \rightarrow RO + HO_2$ (R 69a)

$\rightarrow RO{-}HO_2 \rightarrow ROH + O_2$ (R 69b)

$\xrightarrow{+M}$ ROOOH thermalized (R 69c)

$RO \rightarrow$ other processes (R 70)

List of Tables

List of Figures